Phase Transitions in Nanoscale Designed Magnetic Thin Films

eman ta zabal zazu

Universidad del País Vasco
Euskal Herriko Unibertsitatea

Mikel Quintana Uriarte

Ph.D. Thesis

2023

Supervised by:

Dr. Andreas Berger

Hell yeah, I remember Aurora,
Take me now, we can spin the sun around,
And the stars will all come out,
Then we'll turn and come back down...

Aurora – Foo Fighters

Abstract

The general occurrence of thermodynamic phase transitions (TPT) in matter, associated with abrupt changes of certain physical quantities in such systems, is of upmost relevance, both in their pure fundamental understanding, but also in terms of technological applications. Examples of technologically relevant TPT include the superconducting phase transition, used, for example, to reduce the energy consumption in magnetic resonance imaging techniques, or phase changing materials, used in computer cooling systems or thermal energy storage.

Ferromagnetic (FM) materials are another type of systems undergoing TPTs. In these materials, a TPT is known to occur in a specific temperature called the Curie temperature T_C, bellow which the system exhibits an ordered FM phase. At temperatures below T_C, two equivalent FM states can be found in absence of an external magnetic field, also separated by a different type of TPT. The occurrence of such TPTs in ferromagnets and the associated FM states are also relevant in widespread technological applications involving magneto-caloric refrigeration or magnetic recording media.

In general, thin film research and technologies involving FM materials have historically considered abrupt interfaces mainly. Such abrupt interfaces induce and/or enhance effects required, for example, in the electronic read-out of such FM states. However, gradual changes in the physical properties of thin films are also known to improve their performance in certain conditions.

In this regard, gradual changes in the exchange coupling strength are known to influence the occurrence of the TPT in FM thin films. Here, separate Quasi-PM/FM phases can coexist in the same ferromagnetic thin film. Such formation of separate phases in the same film can furthermore be controlled by means of temperature upon suitable design of the exchange-graded profiles. Thus, exchange-graded FM thin films are a novel tool that can lead to potentially relevant technological applications upon suitable design of such exchange coupling strength profile.

Parallel, the occurrence of TPT is associated to thermodynamic equilibrium conditions in which all thermodynamic quantities remain constant in time. However, phase transitions are also known to happen in systems that are far from equilibrium in presence of a time-dependent driving force that initiates the dynamic trajectory or pattern. Indeed, these so-called dynamic phase transitions (DPT) have been known to exist in FM materials as well. However, their experimental

verification has only been possible recently, by means of specifically designed experiments. The understanding of DPTs is crucial in non-equilibrium physics because of their similarities with respect to the TPT. Such similarities allow for the use of methodologies for dynamical states and systems that were originally devised for TPTs only.

In this thesis, a series of investigations related to the occurrence of phase transitions in nanoscale-designed ferromagnetic materials are explained in a comprehensive manner, and associated scientific conclusions are drawn. More specifically, relevant aspects related to the two aforementioned phenomena are explored, namely, the occurrence of phase transitions in exchange-graded FM materials, and the occurrence of dynamic phase transitions in FM thin films.

In Chapter 1, the main theoretical aspects of this thesis are discussed. These include the key ideas of ferromagnetism, together with a review of the most important aspects of TPTs in FM materials. In Chapter 2, the main experimental techniques employed in this work are explained.

Chapters 3-6 represent the main results of this thesis. Chapters 3 and 4, explain the fabrication and structural and magnetic characterization of thin films exhibiting exchange-graded ferromagnetic properties along the film depth. More specifically, Chapter 3 explores the thermodynamic equilibrium behavior of exchange profiles, exhibiting a single FM domain that expands with decreasing temperature. In this work, such type of exchange-graded profiles is shown to bypass universality and, thus, modify the thermodynamic equilibrium critical exponents; a fact that is otherwise basically impossible to control.

In Chapter 4, a more complex exchange-graded profile is designed and investigated. Such profile allows one to create separate FM regions at different depths in the thin film that can interact with each other by means of proximity-induced coupling. Accordingly, such particular sample design is shown to induce strongly temperature dependent coupling or bias fields over extended temperature ranges. The experimental results presented in this chapter demonstrate that such an exchange coupling profile can be used to obtain temperature independent coercivities over large temperature ranges by using otherwise conventional magnetic materials, making them particularly relevant for applications that are relying on stable operation points.

Chapters 5 and 6 explain the here obtained results related to DPTs in FM thin films. In Chapter 5, the first ever experimental quantification of the scaling

behavior in the vicinity of the DPT and associated critical exponents is achieved. This is a major achievement, given that such dynamic critical exponents have been theorized to be of the same universality class of the TPT, but no experimental work had verified such universality. For this work, the dynamic behavior of magnetization in ultrathin FM films with in-plane uniaxial anisotropy has been investigated by means of transverse magneto-optical Kerr effect magnetometry. The here obtained results are compatible with the 2D Ising model, as expected. Interestingly, they are shown to differ from the critical exponents of the TPT, that agree with the 3D Ising model. Such observation points towards fundamentally different length-scales for the dimensional crossover between the dynamic and equilibrium phase transition, an entirely novel fact that has not been explored in the literature so far.

In Chapter 6, the existence of a generalized conjugate field for the dynamic order parameter of the DPT is explored, both theoretically and experimentally. For this purpose, time-dependent magnetic field sequences without half-wave asymmetry are considered in the immediate vicinity of the critical point of the DPT. The here obtained results show that one can construct a generalized conjugate field definition and associated values that allow for a renormalization of the entire dynamic phase space. Furthermore, within the mean-field approximation, the dynamic critical exponents are preserved if one employs the proper renormalized phase space for driving forces that do not have half-wave asymmetry.

In Chapter 7, several concluding remarks and an outlook to the present work are discussed.

Resumen

El fenómeno de las transiciones de fase termodinámicas (TPT, por sus siglas en inglés) en la materia, asociadas con un cambio abrupto en cierta cantidad física, son de una importancia fundamental, tanto en su comprensión teórica como en aplicaciones tecnológicas. Algunos ejemplos significativos de aplicaciones de las TPT incluyen la transición de fase en materiales superconductores, usados, por ejemplo, en la reducción del consumo energético en equipos de resonancia magnética, o los materiales de cambio de fase, empleados en la refrigeración de ordenadores o en almacenamiento térmico de energía.

Los materiales ferromagnéticos (FM) son también un tipo de sistemas en los que pueden observarse TPTs. En estos materiales, un tipo de TPT está determinado por una temperatura especifica, llamada temperatura de Curie T_C, por debajo de la cual el sistema exhibe una fase FM ordenada. A temperaturas inferiores a T_C, el material presenta dos estados equivalentes en ausencia de campo magnético externo, también separados por otro tipo de TPT. Dichas TPT en materiales FM y sus estados magnéticos asociados son relevantes en aplicaciones tecnológicas ampliamente extendidas, como la refrigeración o las memorias magnéticas.

En general, las tecnologías basadas en películas delgadas FM han considerado históricamente interfases abruptas entre capas principalmente. Dichos cambios abruptos inducen y/o amplifican efectos necesarios, por ejemplo, para la lectura y escritura de sus estados magnéticos. Sin embargo, cambios graduales en las propiedades físicas de las películas delgadas pueden mejorar su rendimiento, en determinadas circunstancias.

En este contexto, es bien sabido que cambios graduales en la interacción de intercambio en películas delgadas FM influyen en el fenómeno de la TPT. En estas películas, pueden coexistir diferentes fases quasi-paramagneticas (PM)/FM. No solo eso, dicha separación de fases puede ser controlada con la temperatura, mediante el diseño del perfil de energía de intercambio en la película. Así, películas delgadas FM con intercambio-gradual, son una herramienta novedosa con potenciales aplicaciones tecnológicas mediante el diseño de dichos perfiles.

Paralelamente, el fenómeno de la TPT está asociado con el equilibrio termodinámico, en el que todas las cantidades permanecen constantes en el tiempo. Sin embargo, las transiciones de fase pueden ocurrir en sistemas que se encuentran lejos del equilibrio termodinámico en presencia de una fuerza dependiente del

tiempo. De hecho, las llamadas transiciones dinámicas de fase (DPT), son bien conocidas en materiales FM. Sin embargo, su verificación experimental sólo ha sido posible recientemente, mediante experimentos diseñados *exprofeso*. Comprender las DPTs es crucial en la física del no-equilibrio termodinámico, debido a sus similitudes con respecto a las TPT. Dichas similitudes permitirían usar metodologías originalmente concebidas para las TPT en sistemas dinámicos.

En esta tesis, se llevan a cabo una serie de investigaciones relacionadas con la fenomenología de las transiciones de fase en películas delgadas FM diseñadas en la nanoescala. Más concretamente, se investigan aspectos relevantes de los dos fenómenos previamente mencionados, es decir, las transiciones de fase en películas delgadas con interacción de intercambio graduada, y transiciones dinámicas de fase en películas delgadas FM.

En el Capítulo 1, se explican los aspectos teóricos principales del ferromagnetismo y se detallan los conceptos clave de las TPT en materiales FM. En el Capítulo 2, se detallan las técnicas experimentales clave para el desarrollo de este trabajo.

Los Capítulos 3-6 presentan los resultados principales de esta tesis. Los Capítulos 3 y 4 explican la fabricación y la caracterización estructural y magnética de películas delgadas con interacción de intercambio gradual. El Capítulo 3 explora el comportamiento termodinámico de cierto perfil de intercambio en el que se forma una única región FM al reducir la temperatura. En este trabajo, se muestra cómo dicho tipo de películas delgadas no sigue la universalidad y, por lo tanto, permiten modificar los exponentes críticos de la TPT; un resultado de otro modo imposible de controlar.

En el Capítulo 4, se presenta e investiga un perfil de intercambio más complejo. Dicho perfil permite crear en la misma película regiones FM separadas a diferentes profundidades, las cuales pueden interactuar entre sí mediante efectos de proximidad. Así, se observa cómo dicho diseño permite crear campos autoinducidos dependientes de la temperatura sobre extensos rangos de temperatura. Los resultados experimentales presentados en este capítulo demuestran que dichos perfiles pueden usarse para obtener campos coercitivos independientes de la temperatura, empleando materiales convencionales y convirtiéndose así en diseños particularmente relevantes para obtener puntos de operación estables en dispositivos.

Los Capítulos 5 y 6 explican los resultados en esta tesis relacionados con las DPT en películas delgadas FM. En el Capítulo 5, se presenta el primer estudio experimental del comportamiento de escala cerca del punto crítico de la DPT. Este es un resultado significativo puesto que los exponentes críticos dinámicos corresponden a la universalidad de la TPT, pero ningún estudio había sido capaz de verificarlos experimentalmente hasta la fecha. Para este proyecto, el comportamiento dinámico de la magnetización ha sido estudiado en películas delgadas FM mediante magnetometría magnetoóptica de efecto Kerr transversal. Los resultados obtenidos son compatibles con el comportamiento del modelo de Ising 2D. Sorprendentemente, los exponentes críticos de la TPT son acordes al modelo de Ising 3D. Dichas observaciones apuntan hacia diferencias fundamentales en el cambio dimensional entre la TPT y la DPT, un aspecto novedoso no investigado en la literatura hasta ahora.

En el Capítulo 6, se investiga la existencia de un campo conjugado generalizado para el parámetro de orden de la DPT, teórica y experimentalmente. Para ello, se consideran secuencias de campo magnético sin antisimetría de onda media, cerca del punto crítico de la DPT. Estos resultados, demuestran que se puede definir un campo conjugado generalizado que permita la renormalización de todo el espacio de fases. Además, dentro de la aproximación del campo medio, se preservan los exponentes críticos dinámicos en el espacio renormalizado, incluso si las señales de campo magnético externo no poseen antisimetría de onda media.

En el Capítulo 7, se extraen varias conclusiones y perspectivas de este proyecto.

Table of Contents

Chapter 1: Fundamental Aspects

In this chapter, the most relevant fundamental aspects for this thesis in the field of ferromagnetism are explained. In Sections 1.1 and 1.2, the basic aspects in ferromagnetism are described. Here, the different energy contributions in the Hamiltonian of a simple ferromagnetic system are discussed in detail. The overall process of magnetization reversal is explained in Section 1.3, together with the magnetization behavior in the context of the macrospin model. Finally, the concept of phase transition is introduced, with particular attention to their occurrence in ferromagnetic materials at exactly the Curie temperature.

1.1 Basic Aspects of Ferromagnetism

Magnetic properties in solids arise mainly due to electronic magnetic moments in the atoms. While protons and neutrons also exhibit nuclear magnetic moments, they are much weaker than electronic ones and they will be neglected in this thesis [1]. In atoms, electrons have certain orbital and spin momenta, that can give rise to a net magnetic moment $\boldsymbol{\mu}$, which is related to the total angular momentum of the electron itself. Filled electronic shells in atoms lead to $\mu = |\boldsymbol{\mu}| = 0$ and the presence of an external magnetic field strength $\boldsymbol{H}$ induces a non-zero $\mu \neq 0$ that will align antiparallel to $\boldsymbol{H}$ in order to minimize the total energy of the system. Half-filled electronic shells however can give rise to a net $\boldsymbol{\mu}$ even in absence of $\boldsymbol{H}$ and will generally align parallel to it[1] [2].

Macroscopically in solids, the quantity employed in the description of the magnetic behavior is the magnetization $\boldsymbol{M}$, which is the magnetic moment per unit volume. In most materials, the interactions between individual magnetic moments are dipolar only and, thus, very so that they cannot induce any significant long-range ordering, even at low temperatures. In this case, thermal disorder makes the

---

[1] These two phenomena are generally known as Larmor diamagnetism and Van-Vleck paramagnetism [1, 2].

electronic magnetic moments to orient randomly, leading to $\boldsymbol{M} = 0$ in absence of an external $\boldsymbol{H}$.

The presence of a non-zero $\boldsymbol{H}$, leads generally to a linear response of $\boldsymbol{M}$ as,

$$\boldsymbol{M} = \chi\ \boldsymbol{H}, \tag{1.1}$$

where χ represents the magnetic susceptibility. Here, if magnetic moments tend to align parallel to $\boldsymbol{H}$, then $\chi > 0$ and the material is paramagnetic. If otherwise magnetic moments align antiparallel with $\boldsymbol{H}$, then $\chi < 0$ and the material is diamagnetic [3].

However, in some materials, different magnetic moments can interact with each other more strongly giving rise to a long-range ordering. Such ordering will lead then to a non-linear $\boldsymbol{M}$ vs. $\boldsymbol{H}$ behavior. This is exactly the case of ferromagnetism which is the main focus of this work.

In ferromagnets, $\boldsymbol{M}$ can be non-zero even in absence of external $\boldsymbol{H}$. Such long-range ordering of magnetic moments and the formation of a ferromagnetic (FM) state happens however only below a material-specific temperature constant T_C called Curie temperature. As the temperature T is increased beyond T_C, the magnetic ordering is lost and $\boldsymbol{M} = 0$ in absence of $\boldsymbol{H}$, leading to a paramagnetic (PM) phase. At exactly $T = T_C$, the system undergoes a thermodynamic phase transition (TPT) [4]. Further details related to this phase transition will be

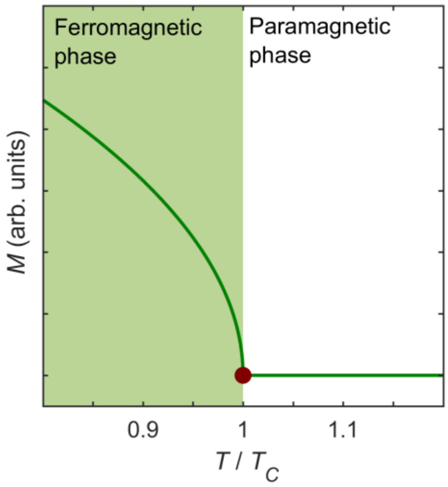

Figure 1.1: Temperature dependence of spontaneous magnetization M in a ferromagnetic material in absence of an external magnetic field H, showing two distinct phases, called ferromagnetic and paramagnetic phase.

explained later in Section 1.4. The physical origin of the necessary strong interaction between magnetic moments is purely quantum-mechanical and will be explained in the following, together with other energy contributions that are relevant in ferromagnetic materials.

1.2 Energy Contributions in Ferromagnetic Materials

1.2.1 Exchange interactions

As stated, the strong interaction between magnetic moments in ferromagnets is of quantum-mechanical nature and is called exchange interaction. Exchange interactions between adjacent moments are due to the combined effect of Coulomb repulsion and Pauli exclusion principle active in between electrons. For instance, a two-electron system exhibits an energy difference between the singlet (E_s) and triplet (E_t) states, exhibit a symmetric or antisymmetric orbital (spatial) part of the electronic wavefunction. Given such energy differences, the ground state of the system is determined by the symmetry of the spin part wavefunction, given that electrons (Fermions) must have an antisymmetric wavefunction [3]. This is true, even if the Hamiltonian does not explicitly depend on the electron spins, i.e., upon neglecting relativistic effects.

In the two-electron system, the Hamiltonian can then be expressed in terms of two dimensionless spin operators $\hat{\boldsymbol{s}}_1$ and $\hat{\boldsymbol{s}}_2$ as,

$$\mathcal{H}_{\mathrm{ex}} = -J\, \hat{\boldsymbol{s}}_1 \cdot \hat{\boldsymbol{s}}_2, \tag{1.2}$$

where $J = E_s - E_t$ is the exchange constant with units of energy. More generally, in a lattice structure the Hamiltonian of the system can be expressed as,

$$\mathcal{H}_{\mathrm{ex}} = -\frac{1}{2}\sum_{i,j} J_{ij}\, \hat{\boldsymbol{s}}_i \cdot \hat{\boldsymbol{s}}_j, \tag{1.3}$$

where J_{ij} represents the exchange interaction between spins in the (i, j) lattice points. Eq. (1.3) is the so-called Heisenberg Hamiltonian [1, 3]. Here, $J_{ij} > 0$ implies a FM ordering, i.e., a parallel alignment of magnetic moments. However, a $J_{ij} < 0$ interaction is also possible and will lead to an antiparallel alignment of magnetic moments, also known as antiferromagnetism. Also, more complex magnetic ordering types, such as ferrimagnetism, can also be explained within the Heisenberg model, but they are not covered here, given that they do not relate to the subjects explored in this thesis. It is worthwhile mentioning that, from the quantum-mechanical perspective, the Heisenberg Hamiltonian is an approximation because, here, only a two-state electron system is considered. Nonetheless, such model works very well in the description of many FM systems.

The Heisenberg model can undergo different types of simplifications [3]. In the most common cases, interactions are only considered in between nearest-neighbors given that exchange interactions decay exponentially with distance and, so, next-to-nearest neighbors interactions are generally much smaller than the ones of nearest-neighbors. Another simplification consists in assuming that each spin in the lattice is one-dimensional and can only take two opposite values such that $\hat{\boldsymbol{s}}_i = \pm 1$. The so-called spin-½ Ising model, that was actually proposed before the Heisenberg model, and has been widely used in statistical physics due to its simplicity. One can have Ising models with larger S-values too.

A different commonly used simplification in the Heisenberg model consists in substituting the spin operators with a classical localized magnetic moment vector with $\boldsymbol{s}_i = \boldsymbol{\mu}_i / \mu_i$ at each lattice point. These $\boldsymbol{s}_i$ vectors are commonly known as spins, but they should not be confused with the electronic spin, given that they are classical vectors.

At this point, it is relevant to mention that conventional ferromagnetic materials, such as Co, Fe, and Ni, are itinerant ferromagnets [5]. This means that the electrons responsible for the magnetism, which are the electrons in the d-bands in 3d transition metal ferromagnets, are rather delocalized. Such itinerant ferromagnetic materials undergo a spontaneous band splitting of spin up and spin down electrons and cause an imbalance in the density of states, giving rise to a net magnetization. So, in the most general case, and particularly in the case of itinerant FM materials, localized spin vectors are significant simplification, and the study of their thermodynamic behaviors would require time-consuming temperature dependent ab-initio calculations. However, Heisenberg models with localized magnetic moments are frequently used to investigate the thermodynamic behaviors of itinerant ferromagnetic materials because they allow for an accurate and simple description of the magnetization behaviors at temperatures close to T_C. In some cases, such local picture can be even more accurately than some ab initio calculations because the collective nature of FM ordering, and especially its thermodynamic behavior, are not very sensitive to the atomic details that generate J [5].

Thus, even if the purely local picture constitutes a relevant approximation in itinerant ferromagnets, it serves its purpose for the description of thermodynamic behaviors of ferromagnetic materials. Throughout this thesis, Heisenberg models with localized magnetic moments and nearest-neighbor interactions are going to be considered.

1.2.2 Magneto-crystalline anisotropy

While the size of M is not generally orientation dependent, its response to an external magnetic field can be anisotropic. Generally, such anisotropy is due to a crystal structure of the material, which is commonly known as magneto-crystalline anisotropy (MCA). MCA arises in crystals due to the crystal field quenching and spin-orbit coupling [3, 5]. On the one hand, orbital angular momenta in the crystal field are quenched and favor certain orbitals depending on the symmetry of the crystal. On the other hand, spin-orbit coupling stabilizes the electronic spins parallel with those orbital states [6]. In sum, the energy of the system is minimized when magnetic moments in the lattice, and thus $\boldsymbol{M}$, are parallel to certain crystallographic direction.

The work here focuses on materials with uniaxial magnetic anisotropy, that is, materials in which magnetic moments are favorably parallel to a single crystallographic axis. Hereby, the MCA Hamiltonian can be expressed as,

$$\mathcal{H}_K = \sum_i k_1 \, [1 - (\boldsymbol{s}_i \cdot \hat{e})^2] + k_2 \, [1 - (\boldsymbol{s}_i \cdot \hat{e})^2]^2 + O\,\{[1 - (\boldsymbol{s}_i \cdot \hat{e})^2]^3\}, \tag{1.4}$$

where $\hat{e}$ is a unit vector that represents the crystallographic direction of the uniaxial anisotropy and k_1 and k_2 are the first- and second-order anisotropy energies [3, 7], with units of energy. In this Hamiltonian, assuming that k_1, $k_2 > 0$ the energy of the system is minimized if $\boldsymbol{s}_i$ are parallel to $\hat{e}$.

The work here focuses on Co and Co-alloys at sufficiently low temperatures, which tend to grow naturally in a hexagonal close packed (hcp) lattice structure. In general, hcp Co tend to exhibit anisotropy densities $k_1 > 0$ and $(k_1 + k_2) > 0$ such that magnetization is favored to be parallel to the c-axis of the hcp lattice structure, which is known as the easy-axis (EA).

1.2.3 Zeeman energy

Magnetic moments in FM materials tend to align parallel to an external magnetic field in order to minimize the energy of the system [1, 3]. This is formally described by the Zeeman energy, which can be expressed as,

$$\mathcal{H}_{\mathrm{Z}} = -\mu_0 \sum_i \boldsymbol{\mu}_i \cdot \boldsymbol{H}_i = -\mu_0 \sum_i \mu_i\, \boldsymbol{s}_i \cdot \boldsymbol{H}_i, \tag{1.5}$$

where μ_0 is the vacuum permeability and $\boldsymbol{H}_i$ denotes the magnetic field strength at the ith lattice point, which in all cases here is going to be considered homogeneous and, thus, identical for all spins in the system. Macroscopically, assuming that all magnetic moments have the same magnitude, the energy density of the Hamiltonian is expressed as,

$$\frac{\mathcal{H}_{\mathrm{Z}}}{V} = -\, \mu_0 M_s^0 \sum_i \boldsymbol{s}_i \cdot \boldsymbol{H}_i, \tag{1.6}$$

where $M_s^0 = \mu / V$ is the maximum magnetic moment per unit volume in the system, that is, the zero-temperature saturation magnetization.

1.2.4 Dipolar interactions

Dipole moments themselves induce magnetostatic fields that play a crucial role in the overall magnetization configuration of a ferromagnetic material [1, 3]. Dipole-dipole interactions can be expressed as dipolar fields acting onto a magnetic moment, such that,

$$\mathcal{H}_{dip} = -\frac{\mu_0}{2} \sum_{i \neq j} \boldsymbol{\mu}_i \cdot \boldsymbol{H}_{ij}^{dip}, \tag{1.7}$$

where $\boldsymbol{H}_{ij}^{dip}$ is the dipolar field induced at the location of $\boldsymbol{\mu}_i$ and being generated by $\boldsymbol{\mu}_j$. $\boldsymbol{H}_{ij}^{dip}$ can be calculated as,

$$\boldsymbol{H}_{ij}^{dip} = \frac{1}{4\pi} \frac{3\, \boldsymbol{r}_{ij} \left(\boldsymbol{\mu}_i \cdot \boldsymbol{\mu}_j \right) - \boldsymbol{\mu}_j \left| \boldsymbol{r}_{ij} \right|^2}{\left| \boldsymbol{r}_{ij} \right|^5}, \tag{1.8}$$

where $\boldsymbol{r}_{ij} = \boldsymbol{r}_i - \boldsymbol{r}_j$ is the vector connecting the ith and jth moments in two different lattice points. One can observe that $\boldsymbol{H}_{ij}^{dip}$ in eq. (1.8) that dipolar interactions are long-range if compared to exchange interactions. Correspondingly here, the consideration of nearest-neighbor interactions alone is insufficient, which makes the calculation of $\boldsymbol{H}_{ij}^{dip}$ more cumbersome.

Given eqs. (1.7-1.8), the magnetostatic energy is minimized if magnetic moments are parallel to the vectors connecting them. Thus, dipole-dipole interactions tend to demagnetize any given structure, which is the reason why dipolar fields are referred to as demagnetizing fields as well. In order to minimize

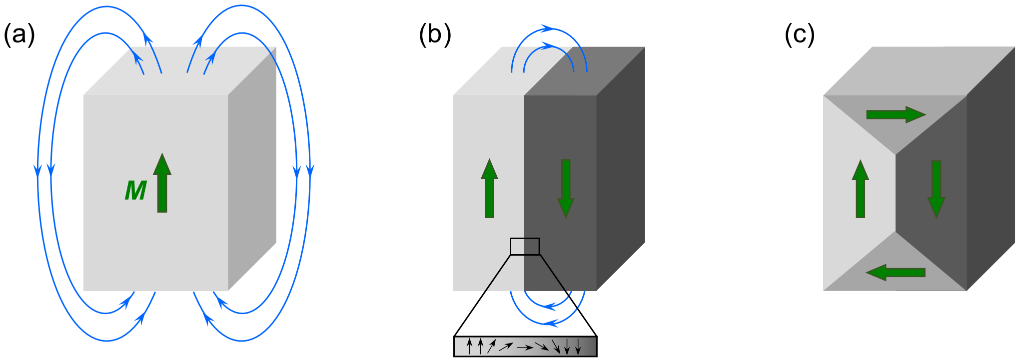

Figure 1.2: Schematic illustrations of the domain formation in ferromagnetic structures. (a) Uniform magnetic state with large stray fields, shown in blue. (b) Two magnetic domains with reduced stray fields. The spin configuration of the transition region between two separate domains, i.e., a domain wall, is shown as a zoom-in. (c) Domain closure in absence of any relevant stray fields.

both $\mathcal{H}_{dip}$ and $\mathcal{H}_{ex}$ at the same time, FM structures can exhibit magnetic domains with different magnetization orientations separated by domain-walls (DW) [8]. Fig. 1.2 shows schematically the domain formation in ferromagnetic materials. In a uniformly magnetized structure, dipolar interactions are relatively large and favor the formation of separate domains with different magnetization vector orientations, which also reduce the stray fields outside the ferromagnet. In a domain-wall, the magnetic moments change in a rather continuous fashion from one direction to the other, as shown schematically in Fig. 1.2(b). The domain-wall width depends on both the exchange energy (increasing the width) and the magnetic anisotropy (decreasing the width) and their typical size in thin film with in-plane magnetization is of the order of ~100 nm [8].

Dipole-dipole interactions are also responsible for the formation of shape anisotropies in any non-spherical shape [9, 10]. In thin film geometries, the thickness of the film is orders of magnitude smaller than the other two lateral dimensions. Then, assuming an infinite film, dipolar interactions tend to align the magnetic moments in the plane of the film. Thus, in a uniformly magnetized film with magnetization $\boldsymbol{M}$, magnetostatic energy can be rewritten as [11],

$$\mathcal{H}_{dip} = \frac{\mu_0}{2} V \, M_s^0 \, [1 - \cos^2 \theta_M], \tag{1.9}$$

where V is the film volume and θ_M is the angle between magnetization and the plane of the film. Eq. (1.9) implies that $\mathcal{H}_{dip}$ is minimized if magnetization is contained in the plane of the film. This specific fact is going to be relevant throughout the entirety of this thesis, because the absence of any relevant dipolar fields leads to a single magnetic domain in thin films and, at the same time, enables simple interpretations and magnetic characterizations of their properties.

1.2.5 Other energy contributions

While the energy contributions explained in Sections 1.2.1-1.2.4 alone will allow for the description of the physical properties in the films in this thesis, there are other interactions between magnetic moments worthwhile mentioning. In thin FM/NM/FM multilayers, the FM layers can couple with each other, even if they are separated by a non-magnetic (NM) spacer layer. Such interaction, known as RKKY interaction, leads then to parallel or antiparallel alignment of the FM layers' moments depending on the thickness of the spacer layer [12, 13]. Such coupling can be expressed as a change in the free energy density difference such that,

$$\Delta\mathcal{F} = -J_{RKKY}\, \widetilde{\boldsymbol{M}}_1 \cdot \widetilde{\boldsymbol{M}}_2, \tag{1.10}$$

where $\widetilde{\boldsymbol{M}}_1$ and $\widetilde{\boldsymbol{M}}_2$ are magnetization vectors normalized to their corresponding saturation, and J_{RKKY} is the interlayer exchange coupling strength, in energy density units. J_{RKKY} has an oscillatory behavior as a function of the thickness of the spacer NM layer, which can then be tuned to control the interaction between $\widetilde{\boldsymbol{M}}_1$ and $\widetilde{\boldsymbol{M}}_2$. The reason for this type of interaction is related to the density of states at the Fermi level of spin-up and spin-down configurations and the density of states of the non-magnetic layer [14, 15]. The RKKY interaction is historically coupled with the development of hard-drive disk (HDD) technologies employing the giant magneto-resistance (GMR). Here, a very large change in the resistance of the FM/NM/FM layers is detected in presence of an external magnetic field that is strong enough to overcome the antiparallel alignment of the two FM layers. Such change in the resistance is due to the different scattering of electrons with spin-up or spin-down.

Another type of interaction worthwhile mentioning is the Dzyaloshinskii-Moriya interaction (DMI), which is a type of antisymmetric exchange interaction that favors a perpendicular alignment of neighboring spins as [16],

$$\mathcal{H}_{DMI} = -\sum_{\{i,\, j\}} \boldsymbol{D}_{ij} \cdot \left(\boldsymbol{s}_i \times \boldsymbol{s}_j\right), \tag{1.11}$$

where $\boldsymbol{D}_{ij}$ is the DMI vector. The DMI induces a chirality in the system whose sign of rotation depends on the DMI vector. This type of interaction can only be present in systems without inversion symmetry, such as materials with non-centrosymmetric lattice structures [17, 18] or surfaces and interfaces [19, 20, 21, 22]. The DMI is currently a phenomenon of increasing relevance because it allows for the formation of structures that are otherwise topologically protected, such as skirmions.

1.3 Magnetization Reversal and Macrospin Model

Considering the previously explained energy terms, the entire Hamiltonian of a ferromagnetic thin film can be described as,

$$\mathcal{H} = \mathcal{H}_{ex} + \mathcal{H}_K + \mathcal{H}_Z + \mathcal{H}_{dip} + \ldots \tag{1.12}$$

In order to find the $\boldsymbol{M}$ state of the ferromagnet, one needs then to minimize $\mathcal{H}$ in eq. (1.12). However, finding such state in a ferromagnet is in general a complex procedure since not all energy contributions can be minimized at the same time and there is a vast number of local minima that the system can occupy temporarily [23]. For example, magnetic anisotropy favors magnetic moments to lie parallel to an EA, while Zeeman energy favors the moments to lie parallel to a certain field direction. Thus, if the external magnetic field is not parallel to the EA, then $\mathcal{H}_K$ and $\mathcal{H}_Z$ cannot be minimized at the same time [24]. Furthermore, at finite temperatures, statistical analysis on the thermal fluctuations and the thermodynamic equilibrium behavior of $\boldsymbol{M}$ must be considered [1, 2, 3].

Such complex energy landscape with multiple local energy minima brings us to the magnetization response of ferromagnets to external magnetic fields. Fig. 1.3 shows schematically the M component parallel to the external magnetic field direction plotted against H in a typical FM material. In presence of a strong enough external magnetic field, all magnetic moments will tend to align parallel to H in

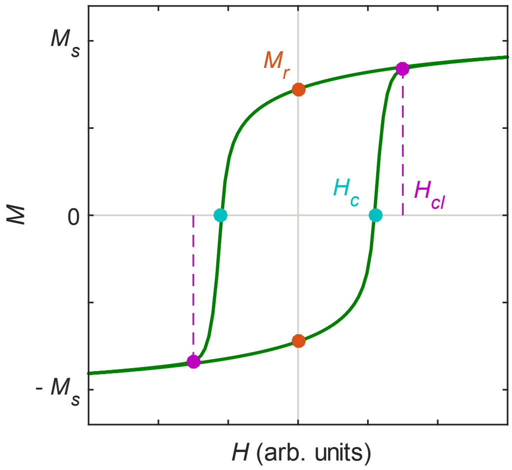

Figure 1.3: Schematic representation of a typical M vs. H hysteresis loop. The colored points represent several relevant points of the hysteresis loop, namely, remanence magnetization M_r (in yellow), coercive field H_c (in light-blue) and closure field H_{cl} (in purple).

order to minimize both the exchange and Zeeman energies, leading to a saturation magnetization value M_s. Upon decreasing the external magnetic field to $H = 0$, certain non-zero remanence magnetization M_r will remain, due to the spontaneous magnetic ordering in absence of H. As H is decreased further, the ferromagnet undergoes a first order phase transition (see Section 1.4) and the stable state of M changes sign because the global energy minimum changes abruptly with the field inversion. However, the system may remain in a metastable state in which H and M are antiparallel, which gives rise to the hysteretic behavior of the M vs. H curve.

By further decreasing H, M might eventually get to the demagnetized state in which $M = 0$, which occurs at the coercive field H_c. Such a state might occur because the average magnetic moment configuration is zero or because M is perpendicular to the external magnetic field. At the closure field, H_{cl}, the two branches of the hysteresis loop overlap with each other. Such reversal occurs with the free energy of the system going from a metastable energy minimum to the global energy minimum. Hereby, in an isolated ferromagnetic system, that is, in presence of an external H only, it must be fulfilled that,

$$M_{inc}(H) = -M_{dec}(-H). \tag{1.13}$$

Such condition is known as the time-reversal symmetry and implies that the hysteresis loop must be antisymmetric with respect to H and centered at $H = 0$[2,3].

The magnetization reversal at large enough opposite field values is in the most general case a non-equilibrium phenomenon that combines many different possible processes involving domain nucleation [25], domain-wall expansion [26] and coherent rotations [27] depending on the specifics of the Hamiltonian of the system, the temperature and the external field dynamics. Such complex reversal is due to the nature of the first order phase transition and the multiple metastable energy minima. Ultimately, all these processes determine the shape of the hysteresis loop.

---

[2] Time-reversal symmetry is true in mayor hysteresis loops only. This is not the case for minor loops, because the actual state inversion is not guaranteed.

[3] Time-reversal symmetry is true in systems without DMI, because this energy contribution favors certain chirality in the magnetization reversal.

In the most general case, because of the complex energy landscape in the magnetization reversal process, a macroscopic characterization of $\boldsymbol{M}$ alone cannot accurately describe the underlaying processes of magnetization reversal. Nonetheless, one can elaborate models that allow for such characterization in certain conditions. For example, in absence of demagnetizing fields, i.e. $\mathcal{H}_{dip} = 0$, domain formation in thermal equilibrium is not favored generally and can occur only for field values in the close vicinity of H_c. In this condition, upon magnetization reversal, only coherent rotations of $\boldsymbol{M}$ should be favored. This is exactly the hypothesis of the macrospin model, also known as the Stoner-Wohlfarth model [28].

The Stoner-Wohlfarth model considers exchange interactions to be much stronger than the rest of energy contributions such that only parallel alignment of magnetic moments is possible. In other words, the model assumes the ferromagnet to be single-domain with $\boldsymbol{M}$ having constant modulus, so that the remaining energy contributions are allowed to affect its orientation only. In this model, originally envisioned for small particles, the $\boldsymbol{M}$ vector direction is then determined by $\boldsymbol{H}$ and the magnetic anisotropy[4]. For the case of thin films with in-plane magnetic anisotropy (and EA), assuming that both $\boldsymbol{H}$ and $\boldsymbol{M}$ are in the plane of the film, the model proposes a free energy density $\mathcal{F}$ as,

$$\mathcal{F} = -\mu_0 H M_s \cos(\varphi) + \mathrm{K}_1 \sin^2(\nu - \varphi) + \mathrm{K}_2 \sin^4(\nu - \varphi), \tag{1.14}$$

where φ is the angle between $\boldsymbol{H}$ and $\boldsymbol{M}$, and ν is the angle between EA and $\boldsymbol{H}$. Here, M_s is the temperature dependent saturation magnetization, and K_1 and K_2 are the temperature dependent anisotropy energy densities. Here, the $\boldsymbol{M}$ vector direction is determined by minimizing $\mathcal{F}$ in eq. (1.14). Fig. 1.4(a) shows schematically the case with $\boldsymbol{H}$ and EA being perpendicular to each other, i.e., $\nu = 90^{\circ}$, with the $\boldsymbol{M}$ vector having certain angle φ with respect to $\boldsymbol{H}$. At this stage, it is instructive to explain the hysteretic behavior of the M component parallel to H, i.e., $M = M_s \cos(\varphi)$, in two different cases, namely, $\nu = 0^{\circ}$, 90°, as shown in Fig. 1.4(b). The $\nu = 0^{\circ}$ case, corresponds to the case with EA and $\boldsymbol{H}$ parallel to each other. In this condition, for any given $|\boldsymbol{H}|$-value, only two states are possible with

---

[4] While dipolar energy is not necessarily null or orientation independent, it typically takes the form of shape anisotropy. Such shape anisotropy does not need to be aligned with the crystallographic axes.

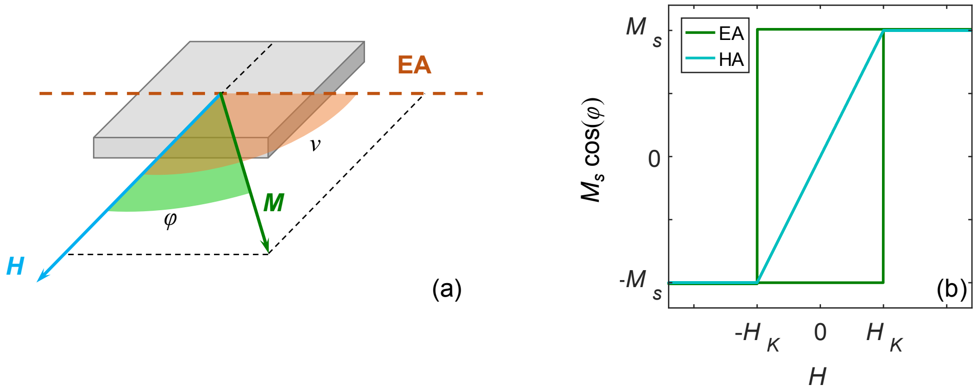

Figure 1.4: (a) Schematic of a ferromagnetic thin film with in-plane uniaxial magnetic anisotropy and EA (in orange) perpendicular to $\boldsymbol{H}$ (in light-blue), with the particular case of $\nu = 90^{\circ}$. The macrospin $\boldsymbol{M}$ vector (in green) has an angle φ with respect to $\boldsymbol{H}$, determined by the interplane between magnetic anisotropy and Zeeman energy. (b) Hysteretic behavior of the magnetization component parallel to $\boldsymbol{H}$ for the cases in which $\boldsymbol{H}$ and EA and parallel and perpendicular to each other.

$\varphi = 0^{\circ}$, 180°. Thus, a rectangular hysteresis loop is obtained, shown in Fig. 1.4(b) by means of the solid-green line. Contrarily, for $\nu = 90^{\circ}$, EA and $\boldsymbol{H}$ are perpendicular to each other. Here, in absence of $\boldsymbol{H}$, $\boldsymbol{M}$ will be parallel to the EA and thus, $M = M_s \cos(\varphi) = 0$. As the field is increased, the $\boldsymbol{M}$ vector will rotate towards $\boldsymbol{H}$ in a continuous fashion as shown in the solid-blue of Fig. 1.4(b). It can be easily shown that M will increase linearly until $M = M_s$. The field value at which $\boldsymbol{M}$ gets parallel to $\boldsymbol{H}$ is called anisotropy field H_K and can be obtained as,

$$H_K = \frac{2K_1 + 4K_2}{\mu_0 M_s}. \tag{1.15}$$

Further details in this regard can be found in Appendix A. It is worthwhile mentioning that when EA and $\boldsymbol{H}$ are parallel, i.e $\nu = 0^{\circ}$, the abrupt magnetization reversal occurs at H_K, at least in a scenario in which thermal fluctuations are not considered. This is because, the metastable energy minimum disappears at $H = H_K$. This is the reason why H_K constitute an upper bound of the coercive field in any ferromagnet with uniaxial magnetic anisotropy. In real thin films, local imperfections and demagnetizing fields contribute to different reversal processes not dominated by a coherent rotation of $\boldsymbol{M}$, at least in the immediate vicinity of H_c.

Experimentally, for the case of a ferromagnetic thin film in which $\boldsymbol{H}$ and EA are aligned parallel, the magnetization reversal generally occurs through the thermal excitation of random nucleation domains with moments parallel to $\boldsymbol{H}$ [25, 26]. Here, thermally activated reversal occurs if the system is likely to overcome the positive energy cost of having a domain with certain domain size, that is, the activation energy barrier. Sufficiently large domains are always favored to expand because of the energy gain due to inverting magnetization into the field direction. This mechanism, thus, cannot be explained by the Stoner-Wohlfarth model, because the model considers a macrospin whose $\boldsymbol{M}$ modulus remain constant.

1.4 Phase Transitions in Ferromagnetic Materials

A phase transition is a singular change of an order parameter (magnetization, fluid density…) upon changing certain control variables in the system, such as the temperature or pressure [3, 4]. Beyond the conventional phase transitions between states of matter (solid-liquid-gas), many different physical systems are known to undergo other phase transitions, that are furthermore essential for their formal understanding [4]. These include the liquid He transition [29, 30], or superconducting materials [31, 32, 33]. Another seminal example of the occurrence of phase transitions in solids is ferromagnetism [4]. Here, the FM-PM transition at the Curie temperature T_C, already mentioned in Section 1.1, is a continuous phase transition of crucial relevance both from a theoretical perspective, but also for applications.

A phase transition is often identified by means of an order parameter, that quantifies the degree of order-disorder in the system. Phase transitions are associated with the changes in the order parameter in thermodynamic equilibrium, that is, in equilibrium between forces in the system such that macroscopic quantities no longer change with time. Nonetheless, phase transitions are also known to happen in non-equilibrium systems, and an example of this will be covered in Chapters 5 and 6.

The abrupt change in the state of a system undergoing a phase transition is due to the occurrence of discontinuities in certain derivative of its free energy $\mathcal{F}$[5]. Hereby, phase transitions were originally classified by Ehrenfest to be first, second or nth order depending on whether the discontinuity occurs at the first, second or nth derivative of $\mathcal{F}$, respectively [34, 35]. Modern classifications prefer to use the terms 'continuous' instead of the original 'second order' to refer to such type of phase transitions[6,7].

---

[5] Throughout this thesis free energy refers to the Helmholtz free energy, defined as $\mathcal{F} = U - TS$, with U being the internal energy and S its entropy.

[6] Later works proved that this classification scheme can be insufficient to account for logarithmic divergences in cases such as the 2D Ising model, as shown by Onsager in 1944 [35].

[7] Here, the terms 'second' and 'continuous' phase transition are going to be used indistinctively to refer to the occurrence of the phase transition of FM materials at T_C.

In ferromagnetic materials specifically, magnetization is the order parameter of a second order phase transition happening at $T = T_C$. Here, the disordered PM with $M = 0$ is separated from the ordered FM phase in which $M \neq 0$. T_C is then the critical point in which the phase transition is second order. Considering statistical mechanics and Boltzmann's distribution [1, 2], the thermodynamic equilibrium behavior of M, as well as the susceptibility χ can be obtained as,

$$M = -\frac{\partial \mathcal{F}}{\partial(\mu_0 H)}, \tag{1.16}$$

$$\chi = -\frac{\partial^2 \mathcal{F}}{\partial(\mu_0 H)^2} = \frac{\partial M}{\partial(\mu_0 H)}. \tag{1.17}$$

Fig. 1.5(a) show the already shown $M(T)$ behavior in the vicinity of T_C superimposed onto $\chi(T)$. Here, one observes that the χ diverges at exactly T_C leading to the occurrence of the continuous phase transition.

An externally applied magnetic field plays the role of the conjugate field of M. This conjugate field allows one to define a (T, H) phase space for the order parameter, M. Fig. 1.5(b), shown as a color-coded map such $M(T, H)$ behavior in the vicinity of T_C. This implies that, in the PM phase, magnetic moments will favorably align with the field, competing against thermal fluctuations and, which in turn will lead to a continuous behavior of $M(H)$, as seen by means of the gradual

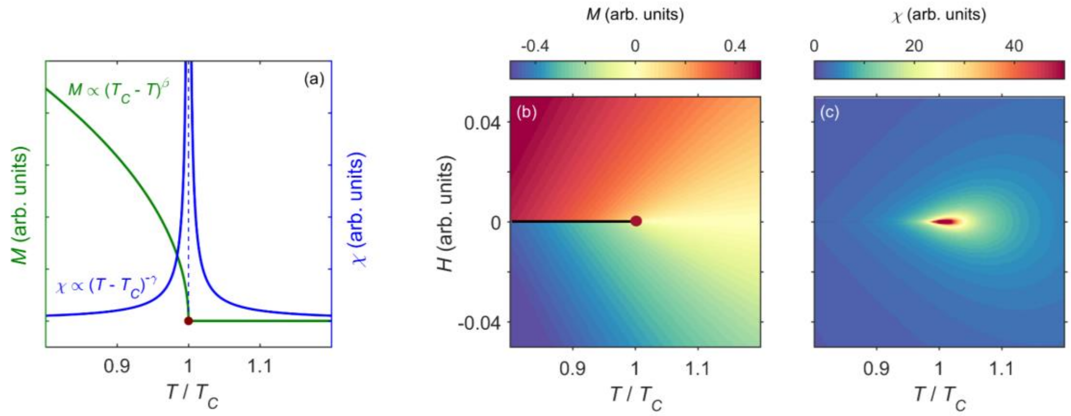

Figure 1.5: (a) M vs. T behavior of a FM material in green, superimposed to the corresponding χ vs. T behavior, in blue, showing susceptibility divergence at $T = T_C$. (b) Color-coded map of the $M(T, H)$ behavior in the vicinity of T_C. The solid-black line corresponds to the first order phase transition, whereas the dark-red dot represents the second order phase transition. (c) Corresponding $\chi(T, H)$ behavior in the same phase space as (b) showing large susceptibilities in the near vicinity of T_C only.

color change for $T/T_C > 1$ in Fig. 1.5(b). In the FM phase, contrarily, the system undergoes a first order phase transition, upon crossing the $H = 0$ line, because here the system abruptly changes its minimum energy state, namely, the moments being positively aligned to negatively aligned. Here, the red and blue regions of the map correspond to the two equivalent FM phases with M being parallel to H, and separated by the first order phase transition at exactly $H = 0$, as indicated by means of the solid-black line. Both FM and PM phases are separated by the continuous phase transition that occurs at exactly T_C, indicated in Fig. 1.5(b) by means of the dark-red point. Fig. 1.5(c) shows the corresponding phase space behavior of $\chi(T, H)$ in the same phase space region as Fig. 1.5(b). Here, one observes that χ diverges only at $T = T_C$, as indicated by the white and red portions of the map.

Another relevant aspect of the occurrence of phase-transitions is the scaling behaviors that the order parameter exhibits in the vicinity of the critical point [4]. Indeed, in the vicinity of T_C, M follows a power-law behavior of the form,

$$M(T \rightarrow T_C,\ H = 0) \propto (T_C - T)^{\beta}, \tag{1.18}$$

where β is a critical exponent [36]. Likewise, at exactly $T = T_C$, M follows a power-law as a function of H as,

$$M(T = T_C,\ H \longrightarrow 0) \propto H^{1/\delta}, \tag{1.19}$$

where δ is another critical exponent. For the discussion here, it will be relevant to define a third critical exponent γ, related to the temperature dependence of χ as,

$$\chi(T \longrightarrow T_C,\ H = 0) \propto (T - T_C)^{-\gamma}, \tag{1.20}$$

which is correlated to β and δ as [37, 38],

$$\gamma = \beta(\delta - 1). \tag{1.21}$$

The relevance of such critical exponents β, γ, δ is that they depend only on the dimensionality of the system, and are otherwise independent from any further details of the constituting materials [4, 35, 39]. A set of exponents is then said to correspond to a certain universality class. This is a major feature in the occurrence of phase transitions because critical exponents allow for the same model description of systems that are completely different as long as they fall into the same universality class.

Eqs. (1.18-1.21) can be combined to a single equation-of-state for the $M(T, H)$ behavior in the vicinity of T_C, first proposed by Arrott and Noakes in 1967 [40]. Such equation-of-state is described as,

$$\left(\frac{H}{M}\right)^{1/\gamma} = \frac{T\text{ - }T_C}{T_1} + \left(\frac{M}{M_1}\right)^{1/\beta}, \tag{1.22}$$

where T_1 and M_1 are material specific constants. Eq. (1.22), encompasses the scaling behaviors of M as a function of T and H and allows for an evaluation of the here described set of exponents in a comprehensive manner. Further details of the scaling behavior described by of eq. (1.22) can be found in Appendix C.

1.4.1 Mean-field models

One relevant approximation to the Hamiltonian of eq. (1.12), particularly in the context of the thermodynamic behavior of $\boldsymbol{M}$ and its associated phase transition, is the mean-field approximation [1, 3, 4]. In this approximation, each spin in the system is affected by an effective field $\boldsymbol{H}_{eff}$ only. Such $\boldsymbol{H}_{eff}$ encompasses all the energy contributions in the Hamiltonian, including the external field $\boldsymbol{H}$, anisotropy energies, and the effective field caused by exchange interactions between neighboring spins in the lattice.

In a Heisenberg (or Ising) system with localized magnetic moments, spins can be expanded as

$$\boldsymbol{s}_i = \langle \boldsymbol{s}_i \rangle + \delta \boldsymbol{s}_i, \tag{1.23}$$

where $\langle \boldsymbol{s}_i \rangle$ represents the average spin, i.e., the magnetization vector, and $\delta \boldsymbol{s}_i$ represents its thermal fluctuations. Hereby, the mean-field approximation, consists of suppressing any second-order fluctuations $O(\delta \boldsymbol{s}_i^2)$ terms in the Hamiltonian caused by exchange and anisotropy energies. Furthermore, in a homogeneous FM system, one can assume translational invariance such that $\langle \boldsymbol{s}_i \rangle = \langle \boldsymbol{s}_j \rangle = \langle \boldsymbol{s} \rangle$. For example, assuming a Hamiltonian with homogeneous exchange and Zeeman energies only[8], the approximation would lead to [1, 3],

$$\begin{aligned}\mathcal{H} &= -J\sum_{\{i,j\}} \boldsymbol{s}_i\boldsymbol{s}_j - \mu_0\,\mu\boldsymbol{H}\sum_{\mathrm{i}} \boldsymbol{s}_i \\ &\approx \frac{Nn_T J\langle \boldsymbol{s}\rangle^2}{2} - \sum_i \left[n_T J\langle \boldsymbol{s}\rangle + \mu_0\,\mu\boldsymbol{H}\right]\cdot \boldsymbol{s}_i, \\ &\approx \frac{Nn_T J\langle \boldsymbol{s}\rangle^2}{2} - \sum_i \mu_0\,\mu\boldsymbol{H}_{\mathit{eff}}\cdot \boldsymbol{s}_i, \end{aligned} \tag{1.24}$$

where N is the total number of spins, n_T is the number of nearest-neighbors and $\boldsymbol{H}_{\mathit{eff}} = [n_T J/\mu_0\mu]\langle \boldsymbol{s}\rangle + \boldsymbol{H}$ is the effective field. This approximation leads to a Hamiltonian that does not depend on spin-spin interactions, but rather in average spin value. One can easily obtain the free energy of the system owning eq. (1.24), such that,

$$\mathcal{F} = -\,k_B T \log \mathcal{Z}, \tag{1.25}$$

where $\mathcal{Z}$ is the canonical partition function of the system and k_B is the Boltzmann constant. Using eq. (1.16), and assuming localized spin vectors one obtains,

$$\frac{\boldsymbol{M}}{M_s^0} = \langle \boldsymbol{s}\rangle = \mathcal{L}\left[\frac{\mu_0\,\mu\left|\boldsymbol{H}_{\mathit{eff}}\right|}{k_B T}\right]\frac{\boldsymbol{H}_{\mathit{eff}}}{\left|\boldsymbol{H}_{\mathit{eff}}\right|}, \tag{1.26}$$

where $\mathcal{L}(\mathrm{x}) = \coth(\mathrm{x}) - 1/\mathrm{x}$ is the Langevin function. Eq. (1.26) provides a closed expression to calculate $\boldsymbol{M}$ in thermodynamic equilibrium, which can be obtained self-consistently. Further details in the calculations related to mean-field models can be found in Appendix B. In the limit of $H = 0$ and $M \to 0$, one can obtain a value for T_C as,

$$T_C = \frac{n_T J}{3k_B}. \tag{1.27}$$

Here, T_C is observed to be proportional to the exchange energy J, meaning that larger exchange energies will require larger thermal fluctuations to drive the

	Mean-field	2D Ising	3D Ising	3D Heisenberg
β	0.5	0.125	0.324	0.362
γ	1	1.75	1.24	1.39
δ	3	15	4.82	4.82

Table 1.1: Summary of the β, γ, δ critical exponents of the TPT in several theoretical models [3].

system into the PM phase. This observation is going to be particularly relevant in Chapters 3 and 4, in the discussion of exchange-graded ferromagnetic materials.

In this approximation, $\boldsymbol{\delta s}_i$ is assumed to be small at all temperatures. However, this is not the case at temperatures close enough to T_C, where thermal fluctuations become very significant. The mean-field approximation leads then to a modification of the magnetization onset at temperatures close to T_C and, thus, a modification of the equilibrium critical exponents. In Table 1.1, such theoretical exponents are shown, for Ising or Heisenberg models with different dimensionalities.

Chapter References

[1] S. Blundell, *Magnetism in Condensed Matter* (Oxford University Press, UK, 2001).

[2] N. W. Ashcroft and N. D. Mermin, *Solid State Physics* (Cengage Learning, Canada, 1976).

[3] R. Skomski, *Simple Models of Magnetism* (Oxford University Press, UK, 2008).

[4] N. Goldenfeld, *Lectures on Phase Transitions and the Renormalization Group* (Addison-Wesley Publishing Company, 1992).

[5] J. Kübler, *Theory of Itinerant Electron Magnetism* (Oxford University Press, UK, 2010).

[6] H. Brooks, *Ferromagnetic anisotropy and the itinerant electron model*, Phys. Rev. **58**, 909 (1940).

[7] E. R. Callen and H. B. Callen, *Anisotropic Magnetization*, J. Phys. Solids **16**, 310 (1960).

[8] A. Hubert and R. Schäfer, *Magnetic Domains. The Analysis of Magnetic Microstructures* (Springer-Verlag Berlin Heidelberg New York, Germany, 1998).

[9] G. Gubbiotti, S. Tacchi, G. Carlotti, P. Vavassori, N. Singh, S. Goolaup, A. O. Adeyeye, A. Stashkevich, and M. Kostylev, *Magnetostatic interaction in arrays of nanometric permalloy wires: A magneto-optic Kerr effect and a Brillouin light scattering study*, Phys. Rev. B **72**, 224413 (2005).

[10] J. M. Porro, A. Bedoya-Pinto, A. Berger, and P. Vavassori, *Exploring thermally induced states in square artificial spin-ice arrays*, New J. Phys. **15**, 055012 (2013).

[11] J. M. D. Coey, *Magnetism and Magnetic Materials* (Cambridge University Press, UK, 2010).

[12] J. P. Liu, E. Fullerton, O. Gutfleisch and D. J. Sellmyer, *Nanoscale Magnetic Materials and Applications* (Springer, Germany, 2009).

[13] J.A.C. Bland and B. Heinrich, *Ultrathin Magnetic Structures III: Fundamentals of Nanomagnetism* (Springer, Germany, 2005).

[14] E. Y. Tsymbal and I. Žutić (edited by), Handbook of Spin Transport and Magnetism (CRC Press, USA, 2012).

[15] G. Varvaro and F. Casoli (edited by) *Ultra-High-Density Magnetic Recording: Storage Materials and Media Designs* (CRC Press, New York, 2016).

[16] E. Y. Vedmedenko, P. Riego, J. A. Arregi, and A. Berger, *Interlayer Dzyaloshinskii-Moriya Interactions*, Phys. Rev. Lett. 122, 257202 (2019).

[17] J.J. Prejean, M.J. Joliclerc and P. Monod, *Hysteresis in CuMn : The effect of spin orbit scattering on the anisotropy in the spin glass state*, J. Phys. **41**, 427-435 (1980).

[18] M. Plumer and M. Walker, *Wavevector and spin reorientation in MnSi*, J. Phys. C: Solid State Phys **14**, 4689 (1981).

[19] U. Gradmann, *Magnetism of surfaces and interfaces*, J. Magn. Magn. Mater. **6**, 173 (1977).

[20] A. Fert and Peter M. Levy, *Role of Anisotropic Exchange Interactions in Determining the Properties of Spin-Glasses*, Phys. Rev. Lett. **44**, 1538 (1980).

[21] A. Crépieux, C. Lacroix, *Dzyaloshinsky–Moriya interactions induced by symmetry breaking at a surface*, J. Magn. Magn. Mater. **182**, 341-349 (1998).

[22] F. Hellman et. al., *Interface-induced phenomena in magnetism*, Rev. Mod. Phys. **89**, 025006 (2017).

[23] A. Kirilyuk, J. Ferré, V. Grolier, J. P. Jamet, and D. Renard, *Magnetization reversal in ultrathin ferromagnetic films with perpendicular anisotropy*, J. Magn. Magn. Mater. **171**, 45 (1997).

[24] P. F. Carcia, *Perpendicular magnetic anisotropy in Pd/Co and Pt/Co thin-film layered structures*, J. Appl. Phys. **63**, 5066–5073 (1988).

[25] A. Aharoni, *Theoretical Search for Domain Nucleation*, Rev. Mod. Phys. **34**, 227 (1962).

[26] X. Zhou, N. Vernier, G. Agnus, S. Eimer, W. Lin, and Y. Zhai, *Highly Anisotropic Magnetic Domain Wall Behavior in In-Plane Magnetic Films*, Phys. Rev. Lett. **125**, 237203 (2020).

[27] Qiang Zhang, A. V. Nurmikko, A. Anguelouch, G. Xiao, and A. Gupta, *Coherent Magnetization Rotation and Phase Control by Ultrashort Optical Pulses in* CrO_2 *Thin Films*, Phys. Rev. Lett. **89**, 177402 (2002).

[28] E. C. Stoner and E. P. Wohlfarth, *A mechanism of magnetic hysteresis in heterogeneous alloys*, Philos. Trans. R. Soc. London **240**, 599 (1948).

[29] D. J. Bishop and J. D. Reppy, *Study of the Superfluid Transition in Two-Dimensional* ^4He *Films*, Phys. Rev. Lett. **40**, 1727 (1978).

[30] D. L. Stein and M. C. Cross, *Phase Transitions in Two-Dimensional Superfluid* ^3He, Phys. Rev. Lett. **42**, 504 (1979).

[31] W. J. Skocpol and M. Tinkham, *Fluctuations near superconducting phase transitions*, Rep. Prog. Phys. **38,** 1049 (1975).

[32] M. Kiometzis, H. Kleinert, and A. M. J. Schakel, *Critical Exponents of the Superconducting Phase Transition*, Phys. Rev. Lett. **73**, 1975 (1994).

[33] R.M. Scanlan, A.P. Malozemoff, and D.C. Larbalestier, *Superconducting materials for large scale applications*, Proceedings of the IEEE 92, 1639-1654 (2004).

[34] G. Jaeger, *The Ehrenfest Classification of Phase Transitions: Introduction and Evolution*, Arch. Hist. Exact Sci. **53**, 51-81 (1998).

[35] L. Onsager, *Crystal Statistics. I. A Two-Dimensional Model with an Order-Disorder Transition*, Phys. Rev. **65**, 117 (1944).

[36] L. P. Kadanoff, W. Götze, D. Hamblen, R. Hecht, E. A. S. Lewis, V. V. Palciauskas, M. Rayl, J. Swift, D. Aspnes, and J. Kane, *Static Phenomena Near Critical Points: Theory and Experiment*, Rev. Mod. Phys. **39**, 395 (1967).

[37] K. Miyatani and K. Yoshikawa, *Kink-Point Locus and Critical Phenomena of YIG and Nickel*, J. Appl. Phys. **41**, 1272 (1970).

[38] K. Ghosh, C. J. Lobb, R. L. Greene, S. G. Karabashev, D. A. Shulyatev, A. A. Arsenov, and Y. Mukovskii, *Critical Phenomena in the Double-Exchange Ferromagnet* $La_{0.7}Sr_{0.3}MnO_3$, Phys. Rev. Lett. **81**, 4740 (1998).

[39] H. W. J. Blote, E. Luijten and J. R. Heringa, *Ising universality in three dimensions: a Monte Carlo study*, J. Phys. A: Math. Gen. **28**, 6289 (1995).

[40] A. Arrott & J. E. Noakes, *Approximate Equation of State For Nickel Near its Critical Temperature*, Phys. Rev. Lett. **19**, 786 (1967).

Chapter 2: Experimental Methods

In this chapter, all the key experimental methods employed in this thesis will be discussed. Firstly, the sample fabrication methods are explained, for which the key technique is sputter deposition. Structural characterization has been conducted mainly by means of X-ray reflectivity (XRR) and X-ray diffraction (XRD) techniques. Finally, magnetic characterization techniques are explored. Such magnetic characterization includes vibrating sample magnetometry (VSM), SQUID magnetometry and transverse magneto-optical Kerr effect (T-MOKE).

2.1 Thin Film Fabrication: Magnetron Sputter Deposition

All the thin films and multilayer fabricated in this work have thicknesses in the range of 0.8-100 nm. In most of the cases, multilayers and alloys with homogeneous and pre-defined inhomogeneous compositions have been fabricated with the purpose of achieving specific structural and/or magnetic properties. In order to fabricate such a wide variety of thin films, sputter deposition has been employed, due to its versatility both technologically and scientifically [1, 2, 3].

Sputter deposition is a physical vapor deposition technique, widely used in modern technologies and scientific research, due to its stable deposition conditions and broad variety of materials that can be deposited. In general, the sputter deposition technique is realized in an ultra-high vacuum (UHV) chamber, where several guns contain the material targets to be deposited. A schematic of the overall process is shown in Fig 2.1. In this UHV chamber, a certain gas pressure is maintained in constant and stable conditions, which is going to be used then to generate a gas plasma [1]. In this work, an inert gas (Ar) is employed in order to avoid unwanted chemical reactions with the material targets or substrate. Nonetheless, reactive gases such as O_2 and N_2 can be employed as well for the generation of oxides and nitrides [4, 5, 6, 7].

A voltage difference between the sputtering gun (anode) and the material target (cathode) is generated by a power supply. Such voltage difference leads to the ionization of the Ar atoms, that subsequently generate a plasma of positively charged Ar^+ ions and free electrons (e^-). The free electrons in the plasma are accelerated by the electric field and generate additional Ar^+ ions or recombine with them, causing stable plasma upon reaching balance between charge losses and generation. The positively charged ions mechanically erode the target surface and cause target atoms to be ejected from the material in all directions. On the opposite side of the chamber, ejected atoms coat in all directions the sample holder, in which the substrate is located, with certain deposition rate on stable pressure and power supply conditions. In general, the target atom flux is not homogeneous. Consequently, points in the substrate that are sufficiently distant from each other can, in principle, exhibit different deposition rates.

For metallic targets, the sputtering process described above is generally conducted with a DC power supply. Semiconductor and insulating materials produce a charge accumulation at the cathode that can impede the plasma discharge and can furthermore severely damage the target due to overheating. In order to avoid such damage and deposit non-metallic materials, a radiofrequency (RF) power supply can be employed. In these conditions, Ar^+ ions will only impact the target surface in the negative half-cycle of the supply and, consequently, the

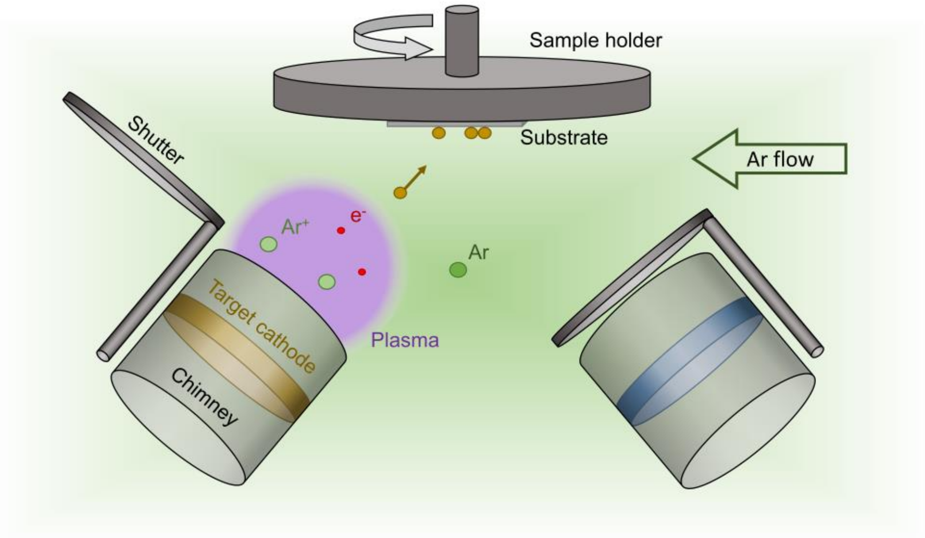

Figure 2.1: Schematic of the sputter deposition procedure showing the plasma composed of Ar^+ ions and free electrons, the guns with material targets and shutters and the substrate in the rotating sample holder.

RF deposition rates are going to be generally smaller. Metallic targets can also employ RF power supplies in order to reduce the overall deposition rates, and therefore, precisely fabricate ultrathin films and multilayers. The deposition rates of each of the materials depend primarily in the number of ions colliding with the target, the cohesion energy of its atoms, and the atomic masses.

Higher plasma densities close to the material targets are generally preferable because low deposition rates due to limited ionization efficiencies of plasma could result in severe limitations in the overall deposition scheme. Following this issue, magnetron sputtering was designed to increase the plasma density and, thus, enhance the overall deposition rates of any given target [8]. In this extension of the conventional sputter deposition, an array of permanent magnets below each target generates a static magnetic field that keeps charged particles confined near the target surface. Such static field traps the free electrons in much longer helicoidal-like trajectories, therefore increasing the probability of electrons colliding Ar atoms and, thus, enhancing plasma density and stability.

In this work, a commercial ATC series UHV sputtering system from AJA International, Inc. Company has been employed, whose key components are shown in Fig 2.2(a). The here employed tool contains a main chamber that is generally in ultra-high vacuum pressure conditions to avoid oxidation of the targets within and maintain very low background gas contaminations during the depositions. Pumping this chamber to UHV conditions takes 24 hours and can lead furthermore to

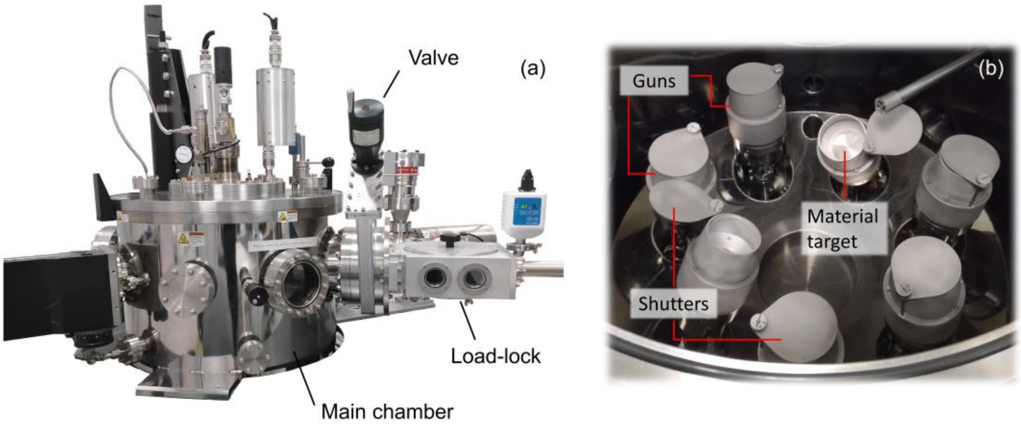

Figure 2.2: (a) Image of the sputtering tool, showing the main chamber, the load-lock, and the separation valve in between. (b) Image from the inside of the main chamber, showing the guns with a material target and the shutters.

modification of the targets' deposition conditions. In order to introduce the substrates inside this chamber without losing UHV conditions, a load-lock is employed, as shown on the right-hand side of Fig. 2.2(a). The load-lock is a chamber of smaller volume connected to the main chamber through a valve. Such load-lock allows one to decrease the pressure to UHV conditions much faster (about two minutes) without perturbing the pressure conditions in the main chamber. Hereby, the sample is located inside the load-lock first and, after achieving high-vacuum conditions, a mechanical arm allows one to introduce the sample holder through the valve into the main chamber, where the deposition procedure is conducted.

Inside the main chamber, seven guns with targets of different materials are kept. Each of these guns can tilt so that each material can points towards the substrate in a reproducible manner, as also shown in Fig 2.2(b). For the sputter tool, 4 DC and 2 RF power supplies are available, which, in the most general case, would allow one to co-sputter up to 6 materials at the same time. This co-sputtering procedure is going to be particularly relevant in Chapter 3 for the fabrication of magnetic alloys. Also, each of the guns has a shutter that can open or close, which allows one to generate and maintain plasma without depositing material onto the substrate. Shutters are particularly useful to clean new targets from possible oxidations, that would otherwise affect the high-quality sample fabrication; this procedure is generally referred to as '*pre-sputtering*'.

In the sputter tool, the position of the substrates and tilt of the guns can be manually controlled from outside the vacuum chamber to ensure reproducible deposition conditions. Furthermore, because deposition rate is not identical in all directions, the sample holder can rotate at a constant rate while depositing in order to average out deposition rate differences in different points of the film and, thus, compensate lateral non-uniformities. All the deposition parameters, such as the gas flow, shutters, deposition power of the supplies and deposition times can be controlled electronically with a PHASE II software, that allow as well to generate complex recipes.

All the samples in this work are fabricated in a constant Ar pressure of 3 mTorr = 0.4 Pa, which leads to optimal deposition rates in the tool [1, 2]. In order to precisely control the thickness of our films, calibration samples are fabricated under certain power conditions and then, their thicknesses and deposition rates are quantified by means of XRR (see Section 2.2.1). In Fig. 2.3, the overall target calibration procedure is shown exemplarily for two distinct materials: Co and Cr. In Fig. 2.3(a), the measured thicknesses of several calibration samples of Co and Cr are shown as a function of the deposition time for a deposition power of 100 W. As clearly observed, larger deposition times lead to larger thickness of the coated layer, implying a linear thickness versus time dependences for both materials, and with null thickness for null deposition time. The linear least-squares fitting, shown as dashed lines, are employed to obtain an accurate deposition rate value. This procedure is repeated for different DC power supply settings. In Fig. 2.3(b), the deposition rate of these two materials is shown as a function of the DC power. Here, a linear dependence of the deposition rate with the power is observed as well over an extended power range, with the slope being a deposition rate ratio. Such target calibration scheme allow one to accurately design thin film, multilayered structures and alloys with well-defined thicknesses and dopant concentrations.

Specifically, in order to fabricate alloy thin films of the form $A_{1-x}B_x$, with x being the dopant concentration of B, a co-sputter procedure is carried out. Here, deposit two distinct materials are deposited at the same time, considering the

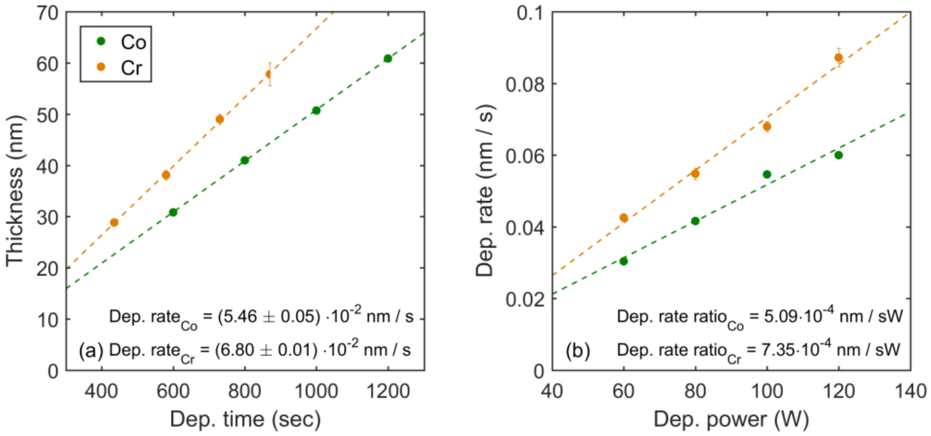

Figure 2.3: (a) Co and Cr thicknesses as a function of the deposition time of several thin films with a DC power of 100 W on naturally oxidized Si wafers. (b) Deposition rate of Co and Cr as a function of the DC power.

relative deposition rates to precisely control the dopant concentration x. Thus, the deposition rates are calculated as,

$$\frac{\text{dep. rate B}}{\text{dep. rate A}} = \frac{x}{1\text{-}x}\frac{\rho_A}{\rho_B}\frac{m_B}{m_A}, \tag{2.1}$$

where, $\rho_{A,B}$ and $m_{A,B}$ are the room temperature densities and standard atomic masses of the materials, respectively. This expression considers the volume ratio per unit cell of the two materials.

2.2 Structural Characterization: X-rays

A relevant portion of this work consists in the investigation of magnetic thin films with specific thicknesses and crystal structures. In order to verify the design of the structural properties of such films, X-ray characterization has been employed throughout this work. In general, X-ray probe techniques are widely used in material science because the photon wavelength λ is comparable to the interatomic distances in matter [9, 10]. Furthermore, X-ray characterization is a nondestructive technique that can be performed under standard environmental conditions.

In X-ray characterization, the X-rays generation is achieved by accelerated electrons that impact inelastically an anode, causing the emission of a certain X-ray spectrum. Such spectrum is composed of a continuous background, known as '*bremsstrahlung*', superimposed to several characteristic lines of the anode material [9]. These discrete lines correspond to the electron transitions from higher energy shells to the lowest K-shell vacancies. In the case of Cu-anodes, the most relevant characteristic lines are the Cu-K_α (λ = 1.54 Å) and Cu-K_β (λ = 1.40 Å). Given the narrow bandwidth and high intensity of the Cu-K_α line, this particular wavelength is most commonly employed for X-ray analysis.

In this work, two different X-ray tools have been employed: a X'Pert PRO PANalytical and a PANalytical EMPIREAN. Both tools have a similar set of optics composed of an incident beam arm with a Cu-anode and a detection arm, both of which can move independently. Furthermore, the sample stage allows for polar and azimuthal rotations of the sample.

2.2.1 X-ray Reflectivity (XRR)

X-ray Reflectivity is a technique commonly used to quantify films and multilayers thicknesses. XRR consists in measuring the intensity of a specularly reflected beam at the surface of a film while varying the grazing incidence and reflected angles ω and θ, respectively, such that $\omega = \theta$[9], as seen in the schematic of Fig 2.4. At each interface of the thin film, there is an electron density change that, ultimately, leads to a change of the complex refractive index N_i, shown on the left-

---

[9] Different X-ray characterization techniques can employ configurations in which $\theta \neq \omega$. For example, this is the case of grazing incidence X-ray diffraction. However, for all considerations here, $\omega = \theta$.

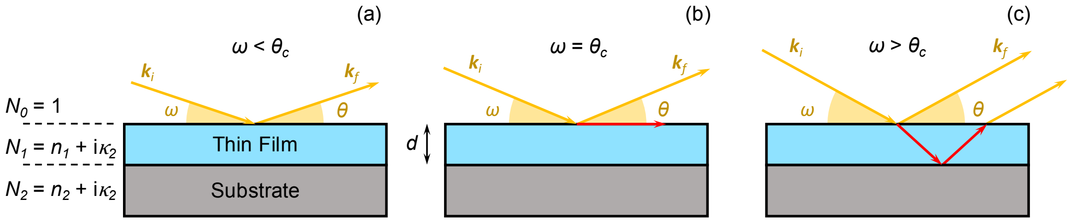

Figure 2.4: Schematics of XRR in a thin film of thickness d, showing an incident X-ray with incident and reflected wavevectors $\boldsymbol{k}_i$ and $\boldsymbol{k}_f$. Each case shows the incident beam angle ω being smaller (a), equal (b) or larger than (c) the critical angle θ_c.

hand side of Fig. 2.4(a). At the X-rays frequency, most materials have a refractive index $n < 1$ and, therefore, total reflection will occur below a certain critical angle θ_c, as shown in Fig. 2.4(a). At exactly θ_c, part of the X-ray intensity continues in a direction tangential to the medium boundary, as schematized in Fig. 2.4(b). For angles above θ_c, part of the X-rays will penetrate in the thin film and reflect at the thin film-substrate interface, as shown in Fig. 2.4(c). The optical path difference leads to an interference pattern, whose constructive and destructive interferences can be calculated as $2d\sin\theta$, being d a single layer thickness.

In Fig. 2.5, the total intensity of the reflected X-rays is represented as a function of 2θ for several Co thin films with different thicknesses. For small enough angles, the total intensity remains basically constant, therefore fulfilling the total reflection condition for $\theta < \theta_c$. For larger θ-values, the interference patterns become apparent by the several maxima and minima in the total intensity; such maxima and minima are commonly known as Kiessig fringes. Furthermore, for different film thicknesses of the Co layer, the periodicity of the fringes varies such that larger thickness, lead to smaller periodicities due to the distinct optical path differences.

One can model the reflectivity pattern to extract, not only the film thickness, but also an accurate estimation of some other relevant structural parameters, such as the roughness of each layer [11], which can be particularly relevant for multilayers with low layer thicknesses. In Fig. 2.5, together with the data, a least squares fit is represented by means of the red solid lines. In all the cases, the model can almost perfectly reproduce the experimentally obtained fringes, with $R^2 > 0.994$ in all the cases, indicating the quality of the model. Such analysis reports in all these cases roughnesses of about 1 nm, that are much smaller than the film thicknesses themselves, verifying the overall quality of the sample growth

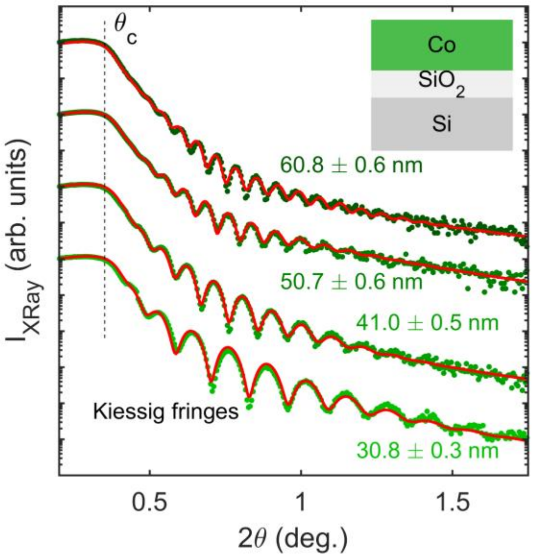

Figure 2.5: XRR intensity patterns of several Co thin films with thicknesses ranging 30-60 nm deposited on top of naturally oxidized Si wafers. For angles $\theta > \theta_c$, X-ray interference leads to the formation of Kiessig fringes that provide information about the film thickness. The red lines represent least-squares fitting in order to extract the actual thickness of the film.

procedure. Throughout the work, thicknesses of calibration samples are calculated with this method in order to obtain accurate deposition rates of the sputtering tool (see Section 2.1).

2.2.2 X-ray Diffraction (XRD)

Given that interatomic distances are comparable to the X-ray wavelengths, optical interferences can lead to diffraction patterns that, at the same time, can provide relevant information about the materials' atomic structure. In a periodic atomic arrangement, assuming elastic X-ray scattering, constructive interference will happen if the total momentum transfer,

$$\boldsymbol{Q}_i = \boldsymbol{k}_f - \boldsymbol{k}_i, \tag{2.2}$$

is a vector of the reciprocal lattice and $|\boldsymbol{Q}_i| = 2\pi/d_i$, where d_i is the distance between atomic planes, and $\boldsymbol{k}_\mathrm{i}$ and $\boldsymbol{k}_\mathrm{f}$ are the diffracted and incident wave-vectors, with angles $\omega = \theta$, as in the XRR case [9, 10, 12, 13]. Such condition, known as the Laue condition, leads to Bragg's law, which states that constructive interference will occur if

$$n\lambda = 2d_i \sin\theta, \tag{2.3}$$

where n is an integer number. Thus, by measuring the total intensity of diffracted light as a function of 2θ, one can identify the crystallographic planes on the structure, which are generally classified using Miller indexes (hkl) [9]. Fig. 2.6(a) shows schematically the incident and diffracted beams together with the total momentum transfer at the surface of a film.

In single-crystal thin film studies, one of the most common procedures is to quantify the crystallographic planes whose vectors are perpendicular to the thin film surface. However, one can also perform non-canonical measurements in conditions in which $\boldsymbol{Q}_i$ is not parallel to the surface. This could be done by considering conditions in which $\omega \neq \theta$ or by rotating the surface normal $\hat{n}$, as schematized in Fig. 2.6(b). This procedure allows one to investigate crystallographic planes that are not parallel to the film surface. The relevance of this type of measurements will become apparent in Chapter 3, where the relative lattice relationships between several layers of a certain multilayer structure is investigated, therefore earning access to the overall epitaxial growth of the structure.

The two different tools employed in this thesis have different sets of optics in the incident and reflected beam arms that can subsequently affect the diffraction results and the interpretation of the data. The incident beam arm of the X'Pert PRO PANalytical tool has a hybrid monochromator that filters all wavelengths except for the Cu-K$_\alpha$ line. This allows for somewhat simpler analysis of the crystallography of the samples. The PANalytical EMPIREAN, on the other hand,

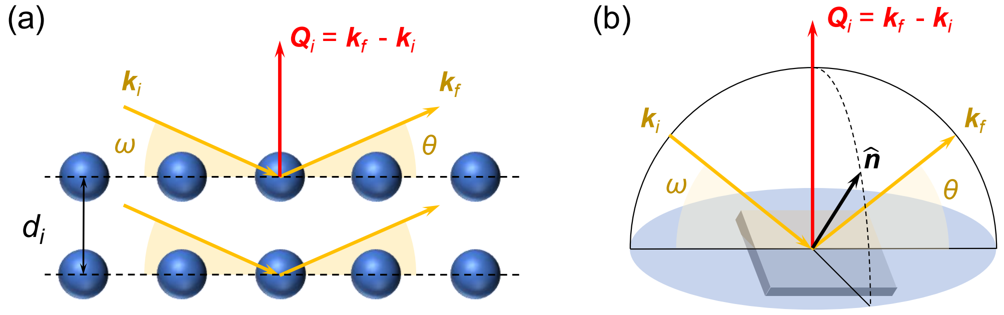

Figure 2.6: (a) Schematic of the XRD measurement scheme showing the incident and diffracted photon momentum $\boldsymbol{k}_i$ and $\boldsymbol{k}_f$, respectively, and the momentum transfer $\boldsymbol{Q}_i$. (b) XRD measurement scheme for quantification of crystallographic planes that are not parallel to the film surface.

has larger beam intensities but does not contain a beam monochromator. Thus, in this particular tool, diffraction measurements can exhibit peaks that correspond to the same crystallographic planes, but different wavelengths, following eq (2.3).

2.3 Magnetic Characterization

In this work several magnetometry techniques have been employed in order to quantify the macroscopic magnetization behavior as a function of different variables, such as external field, temperature, or sample orientation. The first two techniques employed are the vibrating sample magnetometry (VSM) and the superconductive quantum interference device (SQUID) magnetometry, both of which quantify the total moment of the sample. The third technique is the transverse magneto-optical Kerr effect (T-MOKE) magnetometry, which quantifies locally a relative change in magnetization.

2.3.1 Vibrating Sample Magnetometry (VSM)

In a VSM setup, the sample under investigation is located inside the gap of an electromagnet, composed by a suitably designed set of coils, that can generate a homogeneous field in the gap. Then, the magnetized sample vibrates at a constant frequency rate and amplitude, which induces an electric field signal in the detection coils due to Faraday's induction law [14, 15]. The so-induced electric field signals oscillate with the sample vibration frequency and, thus, can be easily isolated from background. The extracted signal is then proportional to the magnetic moment component that is parallel to the field direction. Such total moment is composed of both the moment of the sample and sample holder.

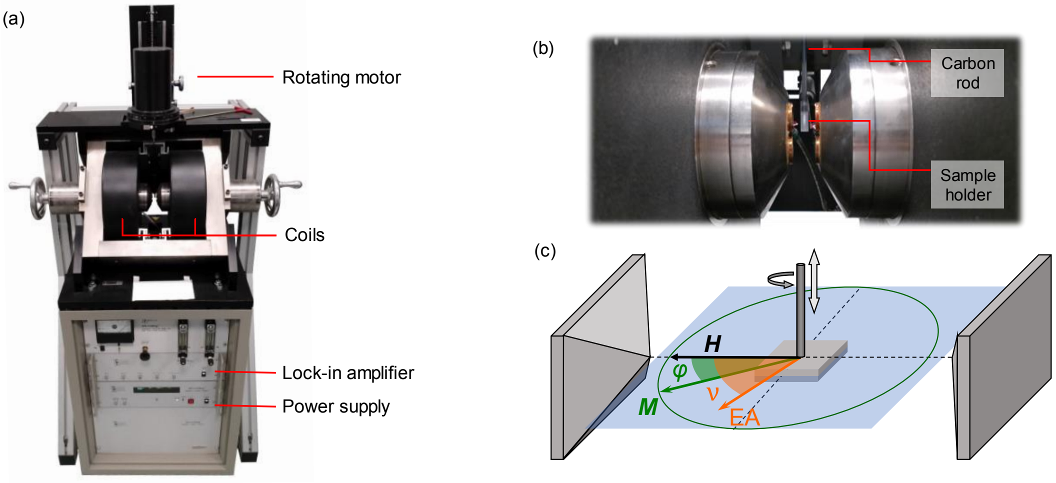

Figure 2.7: (a) Image of the VSM tool showing its key components. (b) Image of the VSM tool showing the detection coils and sample mounting. (c) Schematic of the measuring system, showing the sample vibration and rotation, which allows for the quantification of magnetic anisotropies.

The here utilized tool is a commercial MicroMag Model 3900 VSM System from Princeton Measurements Corporation, shown in Fig 2.7(a). In this work, all the samples are glued with silicone grease to a Kel-F (Plychlorotrifluoroethylene) sample holder, that at the same time is screwed to a carbon rod, as can be observed in Fig. 2.7(b). The tool itself allows for temperature dependent measurements in a range of 300-1000K, even if this specific feature has not been employed in this work.

The maximum field achievable by the coils is 2T. The detection coils send the electric field signal to a lock-in amplifier that extracts the moment component parallel to the field. The rod can rotate in the vertical axis 360º with a precision of better than 1º. Sample holders for in-plane and out-of-plane measurements are available. However, in this work, only in-plane measurements are conducted. This is the most suitable configuration for the type of thin films investigated in this thesis, exhibiting relevant in-plane anisotropies. Such anisotropies can be quantified by means of orientation dependent measurements as shown in the schematic of Fig 2.7(c) (see Chapter 3).

2.3.2 Superconducting Quantum Interference Device (SQUID)

The superconducting quantum interference device (SQUID) is a different type of magnetometer that is extremely sensitive to low magnetic moments [16, 17]. The principle of operation of the SQUID is similar to that of conventional VSM, explained in the previous section, with the main differences being the signal detection system, and the cryogenic temperatures required for the measurement.

Here, the detection coils are a set of superconductors in superconducting phase. These detection coils are inductively coupled by means of a flux transformer to a superconductive ring with two Josephson junctions, as schematized in Fig 2.8(a). The ring itself is in superconducting phase as well and, therefore, any change of magnetic flux leads to small changes in the persistent current in the ring. The changes in the persistent current of the ring are then proportional to the total magnetic moment in the sample. Given the null effective resistance of the ring, the tool allows for extremely low signal detections.

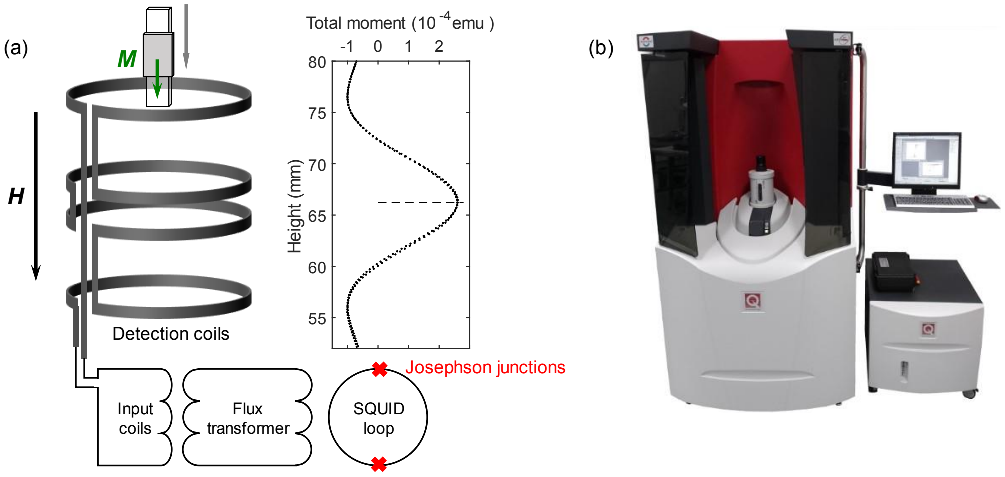

Figure 2.8: (a) Schematic of the SQUID measurement procedure showing the overall superconducting circuit, composed by the detection coils, several flux transformers, and the superconducting ring with two Josephson junctions. The inset figure shows the DC alignment of the sample along the z-axis, which exhibits a maximum in the center of the detection coils. (b) Image of the actual SQUID magnetometer employed.

The system can operate both in DC or VSM modes. In the DC mode, the sample moves continuously along the detection coils, leading to a signal detection as the one shown in the inset of Fig 2.8(a). This mode is used in this work to locate the sample in the center of the detection coils. In the VSM mode, the sample is located in the center of the detection coils and vibrates at a constant rate and amplitude. Then, a lock-in amplifier after the Josephson junction detects the electrical signal that is proportional to the moment component parallel to the direction of the detection coils. The SQUID DC mode is known to exhibit larger signal-to-noise ratios as compared to the VSM mode [16]. However, the DC mode is much more time consuming, particularly, for extensive measurements of the entire M(T, H) phase space, which is why the VSM mode is preferred in this work.

The particular system used in this thesis is a MPSM3 SQUID-VSM EverCool system from Quantum Design, shown in Fig 2.8(b). The inner chamber is filled with liquid He, that allow for magnetic measurements in the T-range of 2-300 K. The generating coils allow for an external magnetic field of ±7 T, applied in the vertical direction, that is also the direction of the detection coils. Samples are fixed in a quartz crystal sample holder with Teflon tape.

2.3.3 Transverse Magneto-Optical Kerr Effect (T-MOKE)

Magneto-optics is a branch of optics that focuses on the effects of polarized light in magnetized matter. Faraday documented in 1845 the first magneto-optical (MO) effect, when observed a polarization change in the transmitted light in a piece of glass subject to a magnetic field [18]. Later, Kerr observed similar polarization changes of reflected light from a piece of steel [19]. The nowadays called magneto-optical Faraday and Kerr effects (MOFE and MOKE, respectively) are the basis of active research in magnetism [20], as they allow for surface detection of magnetization states in thin films accurately using only light, making it suitable, for example, for time-dependent measurements of magnetization [21, 22, 23].

In this thesis, only reflection geometry will be considered and, thus, only MOKE will be discussed for the magnetic characterization. Specifically, MOKE has been employed to characterize the dynamic behaviors of thin films in the presence of time-dependent magnetic fields at room temperature, as will be discussed in Chapter 5.

The microscopic origin of magneto-optical effects resides in light-matter interactions, and the absorption and subsequent emission of photons through an electric dipole transition. More specifically, in magnetized matter, spin-orbit coupling, causes the splitting of electronic p- and d-orbitals. Such splitting ultimately lead to an absorption difference of left- and right-circularly polarized light, which is exactly the origin of MOKE [24, 25].

Macroscopically, light-matter interactions are explained by the electric displacement field $\boldsymbol{D} = \bar{\bar{\varepsilon}}\ \boldsymbol{E}$, where $\boldsymbol{E}$ is the electric field vector and $\bar{\bar{\varepsilon}}$ represents the dielectric permittivity tensor, defined in cartesian coordinates as,

$$\bar{\bar{\varepsilon}} = \begin{pmatrix} \varepsilon_{xx} & \varepsilon_{xy} & \varepsilon_{xz} \\ \varepsilon_{yx} & \varepsilon_{yy} & \varepsilon_{yz} \\ \varepsilon_{zx} & \varepsilon_{zy} & \varepsilon_{zz} \end{pmatrix}. \tag{2.4}$$

Throughout this work only the case of linear optically isotropic medium will be considered even though non-linear optical and magneto-optical effects have been largely documented in literature [26, 27]. Optical isotropy implies that the diagonal elements are identical, with $\varepsilon_{xx} = \varepsilon_{yy} = \varepsilon_{zz}$, being the off-diagonal elements 0. If a material is magneto-optically active, then the off-diagonal elements can become nonzero and, assuming a linear magneto-optical response, the dielectric tensor takes the form,

$$\overline{\overline{\varepsilon}} = N^2 \begin{pmatrix} 1 & iQ_{MO}M_z & -iQ_{MO}M_y \\ -iQ_{MO}M_z & 1 & iQ_{MO}M_x \\ iQ_{MO}M_y & -iQ_{MO}M_x & 1 \end{pmatrix}, \tag{2.5}$$

where N is the complex refractive index, $Q_{MO} << N$ is the magneto-optical coupling constant and $\boldsymbol{M} = (M_x, M_y, M_z)$ the magnetization vector. As observed in eq. (2.5), each magnetization component leads to opposite $\varepsilon_{ij} = -\varepsilon_{ji} \neq 0$.

Following eq. (2.5), three distinct MOKE configurations are described in literature based on the different magnetization components, namely, longitudinal (L-MOKE), transversal (T-MOKE) and polar (P-MOKE), as schematized in Fig 2.9. L-MOKE occurs for $M_x \neq 0$, that is, in the plane of the film and parallel to the plane-of-incidence. T-MOKE refers to the configuration in which $M_y \neq 0$, in the plane of the film and perpendicular to the plane-of-incidence. Finally, P-MOKE is the configuration in which $M_z \neq 0$, perpendicular to the film surface. An arbitrary $\boldsymbol{M}$ vector leads then to a superposition of these cases.

In Jones matrix formalism, the electric field of an incident polarized light beam can be described as,

$$\boldsymbol{E} = \begin{pmatrix} E_s \\ E_p \end{pmatrix}, \tag{2.6}$$

where E_s is the electric field component perpendicular to the plane of incidence and E_p is the component contained in the plane of incidence, being the wave-vector $\boldsymbol{k}$ perpendicular to both components. The electric field vector of reflected light is going to differ both in the amplitude and phase of the incident light. For the case of planar bulk and thin film structures, the resulting reflection matrix can be calculated by Maxwell's equations and the corresponding boundary conditions, and can be expressed as a 2×2 matrix of complex elements as [28],

$$\overline{\overline{R}} = \begin{pmatrix} r_{ss} & r_{sp} \\ r_{ps} & r_{pp} \end{pmatrix}. \tag{2.7}$$

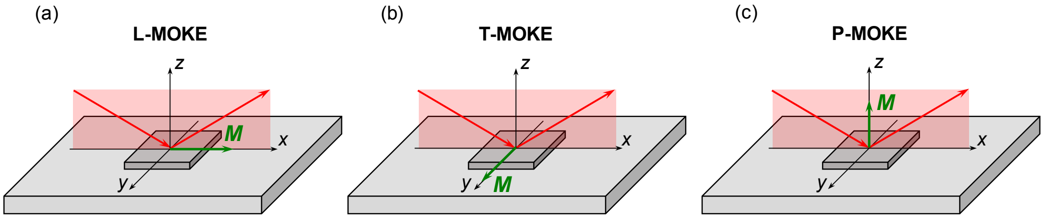

Figure 2.9: Schematic representations of transverse, longitudinal and polar MOKE, respectively, showing the laser plane-of-incidence and the magnetization vector $\boldsymbol{M}$.

Assuming that the MO effects are much smaller than the conventional optical effects, namely, $Q_{MO} << N$, then, $\bar{\bar{R}}$ is expressed as [29, 30, 31],

$$\bar{\bar{R}} = \begin{pmatrix} r_s & \alpha_{MO} + \gamma_{MO} \\ -\alpha_{MO} + \gamma_{MO} & r_p + \beta_{MO} \end{pmatrix} = r_p \begin{pmatrix} \widetilde{r_s} & \widetilde{\alpha_{MO}} + \widetilde{\gamma_{MO}} \\ -\widetilde{\alpha_{MO}} + \widetilde{\gamma_{MO}} & 1 + \widetilde{\beta_{MO}} \end{pmatrix}. \tag{2.8}$$

Here, α_{MO}, β_{MO}, γ_{MO} are the magneto-optical components of L-, T-, and P-MOKE components, respectively, and all matrix elements are complex quantities. Such MO parameters are proportional to their corresponding magnetization components and, thus, they change sign upon magnetization reversal.

If α_{MO}, β_{MO} or γ_{MO} are non-zero, then a change in $\boldsymbol{M}$ will lead to rotation and an ellipticity changes in reflected light (Kerr rotation and Kerr ellipticity). In general, $|\widetilde{\alpha_{MO}}|$, $|\widetilde{\beta_{MO}}|$, $|\widetilde{\gamma_{MO}}| << 1$, and therefore, the ellipticity and rotation changes in the reflected light are going to be small upon magnetization reversal.

In the following, attention will be drawn towards the particular tool that has been employed to characterize magneto-optically the magnetization behaviors of the films. This tool is an ultrasensitive T-MOKE setup, and its key elements are schematically shown in Fig 2.10 [32, 33, 34, 35].

The tool itself is composed of the following elements. The light source is an ultra-low noise laser of wavelength λ = 635 nm (red), 5 mW of output power, and which is placed to generate an angle of incidence of 60º. In the incident beam optics,

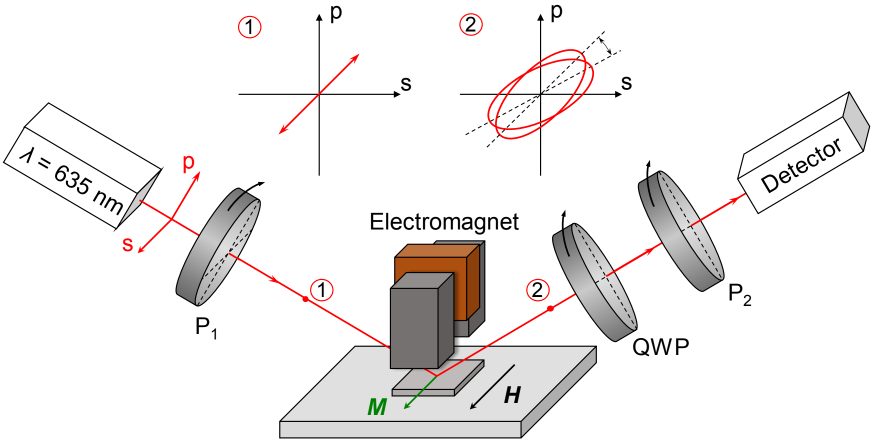

Figure 2.10: Schematic of the ultrasensitive T-MOKE setup showing the laser the first polarizer P_1, the sample located inside the gap of the electromagnet, the quarter-wave plate QWP, the second polarizer P_2 and the detector. The inset figures show the polarization state of light before and after reflection.

a rotatable linear polarizer P_1 allows one to choose linearly polarized with any given s- and p-polarization combinations. Light is then reflected in the sample, which is located inside the gap of an electromagnet. After reflection, light passes through a quarter wave plate QWP and a second polarizer P_2 that ultimately allow for a sensitive polarization analysis. Both optical elements can rotate by means of an electronic motor with a precision better than $2 \cdot 10^{-4}$ degrees. The intensity detector is a low-noise low-offset Si-photodiode with tunable gain. A notch filter attached to the photodetector suppresses all wavelengths of ambient light except for the $\lambda =$ 635 nm to minimize any possible sources of noise in the light intensity signals. The sample can be moved horizontally by means of an xy-stage with a precision better than 10^{-2} mm and can also be rotated with a rotation stage with a precision better than $2 \cdot 10^{-4}$ degrees. The electromagnet in this set-up can produce a time-dependent magnetic field along the transversal direction in a frequency range of 30-300 Hz with magnetic fields up to 60 mT. A hall sensor inside the gap can monitor in real-time the magnetic field signals.

In T-MOKE magnetometry, ellipticity changes, lead to an absolute change in the total intensity in the detector, which allows to define a relative intensity change as,

$$\frac{\Delta I_D}{I_D} = 2\ \frac{I_D(H)\ \text{-}\ I_D(\text{-}H)}{I_D(H) + I_D(\text{-}H)}. \tag{2.9}$$

In eq. (2.8), it is observed that only E_p polarized light contributes to the quantification of the transversal magnetization component, as only r_{pp} depends on β_{MO}. Owning this particular polarization change, a specific detection scheme is employed, in which QWP and P_2 are aligned to establish an extremely sensitive configuration, and with which such transversal polarization changes are very precisely measured. Firstly, a linear combination of incident s- and p-polarized light are selected. The complex diagonal elements in eq. (2.8) will generally give rise to a phase shift between E_s and E_p after reflection, leading in the most general case to elliptically polarized light even without any MOKE contribution. Then, the QWP is aligned such that linear polarized light is obtained after transmission and P_2 is aligned nearly perpendicular to the resulting light polarization, leading to a large reduction of intensity that does not carry magnetic information. Such reduction of the total light intensity in the detector lead to an enhancement of the setup's sensitivity [32]. Previous works showed that optimum $\Delta I_D/I_D$ signals are obtained if P_1 is aligned at 45º with respect to the plane of incidence [32, 33].

Detailed T-MOKE ellipsometry can be used to quantify the full reflection matrix [35]. However, in this work, only the most sensitive magnetization detection scheme is required in order to quantify the dynamic magnetization behavior (see Chapters 5 and 6). For this purpose, stable QWP and P_2 operation points are used to quantify such M(t) behavior in different field conditions. For this purpose, the extinction point is found for each sample by iteratively rotating the QWP and P_2, until minimum intensity is measured in the photodiode. Then, P_2 is rotated 2º away from such extinction point. This procedure allows for optimal $\Delta I_D/I_D$ and signal to noise ratios upon magnetization reversal.

Chapter References

[1] D. L. Smith, *Thin-Film Deposition: Principles and Practice* (McGraw-Hill Inc., New York, 1995).

[2] K. Wasa and S. Haykawa, *Handbook of Sputter Deposition Technology: Principles, Technology and Applications* (Noyes Publication, New Jersey, 1992).

[3] K. Seshan, *Handbook of Thin-Film Deposition Processes and Techniques*, 2nd ed., (Noyes Publications/William Andrew Publishing, Norwich, New York, 2002).

[4] E. Hollands and D. S. Campbell, *The mechanism of reactive sputtering*, J. Mat. Sci. **3**, 544-552 (1968).

[5] W. D. Sproul, D. J. Christie, D. C. Carter, *Control of reactive sputtering processes*, Thin Solid Films **491**, 1-17 (2005).

[6] C. R. Aita, A. J. Purdes, K. L. Lad, and P. D. Funkenbusch, *The effect of* O_2 *on reactively sputtered zinc oxide*, J. Appl. Phys. **51**, 5533 (1980).

[7] M. Futsuhara, K. Yoshioka, O. Takai, *Structural, electrical and optical properties of zinc nitride thin films prepared by reactive rf magnetron sputtering*, Thin Solid Films **322**, 274-281 (1998).

[8] J. A. Thornton, *Magnetron sputtering: basic physics and application to cylindrical magnetrons*, J. Vac. Sci. Technol **15**, 2 (1978).

[9] B. D. Cullity and S. R. Stock, *Elements of X-ray Diffraction* (Prentice Hall, New Jersey, 2001).

[10] E. Zolotoyabko, *Basic Concepts of X-ray Diffraction* (Wiley-VCH, Weinheim, Germany 2004).

[11] E. Chason and T. M. Mayer, *Thin film and surface characterization by specular X-ray reflectivity*, Critical Reviews in Solid State and Material Sciences **22**, 1-67 (1997).

[12] M. Birkholz, *Thin Film Analysis by X-ray Scattering* (Wiley-VCH, Weinheim, Germany, 2006).

[13] N. W. Ashcroft, N. D. Mermin, *Solid State Physics* (Saunders College, Philadelphia, 1976).

[14] S. Foner, *Versatile and sensitive vibrating-sample magnetometer*, Rev. Sci. Instrum. **30**, 548 (1959).

[15] F. Fiorillo, *Measurements of magnetic materials*, Metrologia **47**, S114 (2010).

[16] R. L. Fagaly, *Superconducting quantum interference device instruments and applications*, Rev. Sci. Instrum. **77**, 101101 (2006).

[17] J. Clarke and A. I. Braginski, *The SQUID handbook* (Wiley-VCH, Weinheim, Germany, 2004).

[18] M. Faraday, *Experimental researches in electricity. Nineteenth series*, Phil. Trans. R. Soc. **136**, 1-20 (1846).

[19] J. Kerr, *On rotation of the plane of polarization by reflection from the pole of a magnet*, Phyl. Mag. **3**, 321 (1877).

[20] A. Kimel et. al., *The 2022 magneto-optics roadmap*, J. Phys. D: Appl. Phys. **55**, 463003 (2022).

[21] A. Berger, S. Knappmann, and H. P. Oepen, *Magneto-optical Kerr effect study of ac susceptibilities in ultrathin cobalt films*, J. Appl. Phys. **75**, 5598 (1994).

[22] A. Berger, and M. R. Pufall, *Generalized magneto-optical ellipsometry*, Appl. Phys. Lett. **71**, 965-7 (1997).

[23] A. Berger, M. R. Pufall, *Quantitative vector magnetometry using generalized magneto-optical ellipsometry*, J. Appl. Phys. **85**, 4583-5 (1999).

[24] P. Bruno, Y. Suzuki, and C. Chappert, *Magneto-optical Kerr effect in a paramagnetic overlayer on a ferromagnetic substrate: A spin-polarized quantum size effect*, Phys. Rev. B **53**, 9214 (1996).

[25] J. Hamrle, *Magneto-optical determination of the in-depth magnetization profile in magnetic multilayers*, Ph.D. thesis, University Paris XI, Orsay and Charles University, Prague (2003).

[26] W. Hübner and K.-H. Bennemann, *Nonlinear magneto-optical Kerr effect on a nickel surface*, Phys. Rev. B **40**, 5973 (1989).

[27] D. Budker, W. Gawlik, D. F. Kimball, S. M. Rochester, V. V. Yashchuk, and A. Wels, *Resonant nonlinear magneto-optical effects in atoms*, Rev. Mod. Phys. **74**, 1153 (2002).

[28] Z. Q. Qiu and S. D. Bader, *Surface magneto-optic Kerr effect*, Rev. Sci. Instrum. **71**, 1243 (2000).

[29] S. C. Shin and C. Y. You, *Generalized Analytic Formulae for Magneto-Optical Kerr Effects*, J. Appl. Phys. **84**, 541 (1998).

[30] J. Zak, E. R. Moog, C. Liu, S. D. Bader, *Universal approach to magneto-optics*, J. Magn. Magn. Mater. **89**, 107 (1990).

[31] M. Schubert, T. E. Tiwald, and J. A. Woollam, *Explicit Solutions for the Optical Properties of Arbitrary Magneto-Optic Materials in Generalized Ellipsometry*, Appl. Opt. **38**, 177 (1999).

[32] E. Oblak, P. Riego, L. Fallarino, A. Martínez-de-Guerenu, F. Arizti and A. Berger, *Ultrasensitive transverse magneto-optical Kerr effect measurements by means of effective polarization change detection*, J. Phys. D: Appl. Phys. **50**, 23LT01 (2017).

[33] E. Oblak, P. Riego, A. García-Manso, A. Martínez-de-Guerenu, F. Arizti, I. Artetxe and A. Berger, *Ultrasensitive transverse magneto-optical Kerr effect measurements using an effective ellipsometric detection scheme*, J. Phys. D: Appl. Phys. **53**, 205001 (2020).

[34] C. Martín Valderrama, M. Quintana, A. Martínez-de-Guerenu, T. Yamauchi, Y. Hamada, Y. Kurokawa, H. Yuasa and A. Berger, *Insertion layer magnetism detection and analysis using transverse magneto-optical Kerr effect (T-MOKE) ellipsometry*, J. Phys. D: Appl. Phys. **54**, 435002 (2021).

[35] C. Martín Valderrama, M. Quintana, A. Martínez-de-Guerenu, T. Yamauchi, Y. Hamada, Y. Kurokawa, H. Yuasa and A. Berger, *Sensitivity and reproducibility of transverse magneto-optical Kerr effect (T-MOKE) ellipsometry*, J. Phys. D: Appl. Phys. **55**, 435007 (2022).

Chapter 3: Exchange-Graded Ferromagnetism

In this chapter, the concept of exchange-graded ferromagnetism is explained, with the purpose of showing as a proof-of-concept the capabilities of this type of materials design towards potential thin film applications. Here, by means of specifically designed and fabricated thin films exhibiting exchange-graded profiles (EGPs), general aspects related with the general occurrence of first- and second-order phase transitions are investigated. These studies, conducted mainly by means of SQUID magnetometry, explain how the phase-space behavior of $M(T, H)$ can be modified in the vicinity of the Curie temperature, by means of such properly designed EGPs.

3.1 Introduction to Exchange-graded Ferromagnetism

The presence of abrupt interfaces in thin films is essentially immaterial to nanomagnetism and spin-transport phenomena [1]. interfaces are known to induce and/or enhance many relevant effects required for device applications [2, 3] such as, giant-magnetoresistance (GMR) [4, 5], interface anisotropies [6, 7, 8], or Dzyaloshinskii-Moriya interactions (DMI) [9, 10, 11]. Some of these phenomena are intrinsically related to the symmetry breaking of the lattice structure at the interface.

However, while most research in nanotechnology has searched for extremely abrupt interfaces, controlled gradual changes in the materials compositions and, so, in their physical properties, can potentially enhance specific aspects of the devices' performance [12, 13, 14, 15, 16]. One such exception to the fabrication of thin films with steep interfaces is exchange-spring media [17].

Exchange-spring ferromagnets are structures composed of a soft/hard magnetic bilayer whose phases are exchange-coupled at their interface [18, 19]. In exchange-spring ferromagnetic thin films, the soft magnetic layer basically aids for the reversal of the hard magnetic layer. In a high field regime, the entire bilayer exhibits a uniform magnetic state, parallel to the field direction. Once the external field is reversed, part of the soft layer switches and forms a vertically occurring spiral-like magnetization profile right at the interface with the hard magnetic layer [20]. The formation of such a state aids the reversal of the hard magnetic layer if the field strength decreases further. The overall decrease of coercivity in the hard magnetic layer is of significance in data storage applications, because small ferromagnets carrying magnetic information require high anisotropy to overcome the superparamagnetic limit, while at the same time having small coercivity to promote the read-write cycles [21].

Exchange-spring ferromagnets were initially conceived as bilayers and, thus, exhibiting abrupt interfaces only. However, later works proved that gradient anisotropy energy profiles, in which anisotropy energy actually changes in a continuous fashion along the film depth, can further reduce the switching fields of the hard magnetic layer. Actually, such anisotropy gradients can lead to arbitrarily small switching fields of the hard layer, with the optimum switching field reductions happening with profiles that decrease as $1/z^2$, with z being the depth of the film [22, 23]. Anisotropy graded materials with exchange-spring like effect rapidly became a significant technological advance in HDD technologies, even before the first publication by Goll et. al. [22, 24, 25]. Thus, graded anisotropy media is a clear example of an increase in performance that can be obtained by using gradient structural compositions in thin film technologies. Not only that, but it is also an example of how, the abrupt magnetization reversal happening at the FOPT of ferromagnets can be controlled by suitable sample design.

More recently, compositional gradients are also being designed and employed in the spatial control of saturation magnetization [26, 27]. Such controlled gradient profiles in M_s lead to asymmetric dynamic responses of the ferromagnetic structure, which can promote asymmetric domain-wall expansions [28] and spin-wave dispersion-relations [29]. The research in collective properties of exchange-graded ferromagnetic materials necessarily connects then with the general occurrence of the SOPT at exactly T_C, which is mainly driven by the exchange interaction. In this regard, scientific community has started looking into the potential technological relevance of exchange-graded ferromagnets.

In essence, an exchange-graded ferromagnetic thin film is one in which there is an exchange-graded profile (EGP) with an effective continuous change of the local exchange energy J along a certain direction. Such continuous change in J, can be driven by an average reduction of the local exchange energy due to nonmagnetic dopant concentrations [30], or by spatially varying strain induced effects [31]. In most scientific research on exchange-graded ferromagnetic thin films, gradient properties are considered along the film depth only, due to the excellent control in thin film deposition, while lateral dimensions are kept homogeneous at all depths.

The first steps in this regard were demonstrated by Marcellini et. al. [32], who fabricated high-quality Fe(001)/V(001) multilayers exhibiting T_C-distributions with unexpected temperature dependencies. Later, Le Graët et. al. [33], designed films exhibiting movable AFM-FM phase boundaries in Ir- and Pd-doped FeRh films. A more detailed investigation was conducted by Kirby et. al. [30] on $Ni_{1-x(z)}Cu_{x(z)}$ alloys, that were designed to exhibit linear exchange profiles. Here, the authors studied the depth dependence magnetization profiles of such exchange-graded thin films. In homogeneous FM thin films, the Curie temperature is proportional to exchange coupling strength of the ferromagnets [34]. A spatial gradient of J along the depth of the film will then impact the occurrence of the SOPT in such ferromagnets, at least to some extent. The study by Kirby et. al. [30] showed that an exchange-graded ferromagnetic thin film behaves as composed of virtually independent ferromagnetic layers, each of which exhibiting a local exchange coupling constant J that generate a ‘local’ Curie temperature $T_C^{loc}(z)$ as a function of the depth z of the film.

This is an intriguing result given that, from a thermodynamics perspective, a ferromagnetic material should exhibit only one single T_C. Figs. 3.1(a) show schematically an exemplary EGP with linearly increasing $J(z)$ profile together with

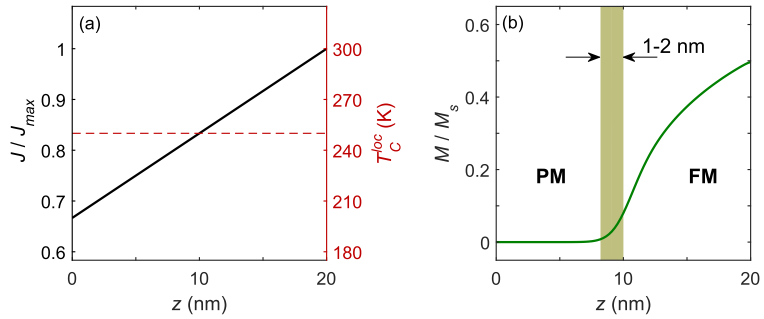

Figure 3.1: (a) Schematic example of a linear $J(z)$ and associated $T_C^{loc}(z)$ profile of a EGP. The dashed-red line corresponds to an exemplarily chosen fixed T. (b) Exemplary $M(z)$ profile at the temperature T, showing two separated regions, a PM and a FM one. The brown region indicates the region of 1-2 nm that separates both magnetic phases.

its associated $T_C^{loc}(z)$. Fig. 3.1(b) shows the subsequent $M(z)$ profile[10] at the temperature indicated in Fig. 3.1(a) by means of the red dashed line. Despite the fact that ferromagnetism is a long-range collective phenomenon, at temperatures in which $T = T_C^{loc}$, the magnetization describes an abrupt spatial onset on the 1-2 nm length-scale [35]. Such an onset will separate an effective PM phase in which $T > T_C^{loc}$ from a FM phase in which $T < T_C^{loc}$. The so-called PM region of the film describes a small but non-zero interface-induced magnetization, which however falls-off exponentially, and at any given temperature. Thus, by increasing or decreasing the temperature, the formation of FM and PM phases will shift accordingly, which provide a relevant degree of freedom in the design of FM phases with temperature.

[10] The here shown profile has been calculated by means of a mean-field model, whose details are explained in Chapter 4 in conjunction with Appendix B.

3.2 Motivation: EGP Description

In Section 3.1, an introduction to the basic aspects of exchange-graded ferromagnetism has been given. The formation of separated FM and PM regions in the same film as a function of the temperature provides a framework that can be relevant both in the context of fundamental research related to the general occurrence of the SOPT, but also for technological applications.

In the following, a particular type of EGPs will be explored with the particular purpose of showing the potential relevance of this type of thin film architectures. Likewise, this chapter will also serve as a basis to describe the particular fabrication procedure of exchange-graded FM thin films, together with their structural analysis.

The EGP explored in this chapter is an inverted V-shape with total thickness d. Such EGP should lead to a $T_C^{loc}(z)$ profile in which the maximum T_C occurs in the center of the EGP and linearly decreases down to a minimum T_C at the bottom and top surfaces of the film. Such $T_C^{loc}(z)$ profile should lead then to the formation and expansion of a single FM region as the temperature is decreased following the explanation in Section 3.1. The fabrication of thin films with such exchange-graded profiles will be conducted on, $\mathrm{Co}_{1-x(z)}\mathrm{Ru}_{x(z)}$ $(10\underline{1}0)$ epitaxial thin films [36]. This type of epitaxial thin films will be shown to exhibit laterally uniform magnetization states, so that the only degree of complexity of its associated magnetism is introduced by the EGP along the depth of the film.

Thus, firstly, the general procedure for the fabrication of such exchange-graded $\mathrm{Co}_{1-x(z)}\mathrm{Ru}_{x(z)}$ $(10\underline{1}0)$ thin films will be explained in a comprehensive manner. Next, in Section 3.4, several results related to these thin film structures will be shown. These include the continuous modification of the thermodynamic equilibrium critical exponents [37], and the realization of thin films exhibiting negligible coercivity [38], in a manner that is similar to that of the exchange-spring effect, and with potential relevance in magneto-caloric applications [39]. Finally, in Section. 3.5, the conclusions and outlook will be drawn.

3.3 Experimental Methods: Fabrication of Epitaxial $Co_{1-x(z)}Ru_{x(z)}$ $(10\underline{1}0)$ Thin Films

In this section, a general fabrication scheme and structural characterization of epitaxially grown thin films exhibiting EGP is explained. For this specific purpose, one requires first an alloy combination A-B such that increasing contents of B lead to an effective reduction of the exchange coupling constant. For this reason, firstly, the structural and magnetic properties of homogeneous $A_{1-x}B_x$ alloy combinations have to be explored, with x being the dopant concentration. Furthermore, for the here conducted type of research, the choice of A and B must be such that other physical properties, such as the crystal structure, in the alloy are not substantially affected by modulating contents of B content.

Parallel, in the introduction in Chapter 1, the existence of magnetostatic fields has been described. Such magnetostatic fields are always present in any ferromagnet and typically lead to the formation of magnetic domains, that can difficult the accessing of stable magnetic states, as well as the characterization of the magnetic behaviors in the vicinity of the SOPT. In general, demagnetizing fields cannot be totally suppressed, but they can be strongly reduced if one considers a ferromagnetic thin film exhibiting in-plane magnetic orientations. Such in-plane geometry can be easily achieved by having thin films with in-plane magnetic anisotropy. For this reason, in this chapter, and throughout this thesis, samples with such magnetic properties are employed.

For the purpose of achieving exchange graded thin films with uniaxial in-plane magnetic anisotropy, hcp $Co_{1-x(z)}Ru_{x(z)}$ $(10\underline{1}0)$ thin films are used in this thesis. Firstly, the exchange coupling of the Co-Ru alloy is known to be reduced for increasing Ru concentrations [36]. Also, Ru is a non-magnetic material that also grows naturally in the hcp crystal structure and has sufficiently similar lattice parameters to those of Co making them suitable materials for the epitaxial growth. Ru also forms a random alloy with Co, such that a wide range of x-concentrations are available without the occurrence of possible segregations [40].

Regarding the specific crystal orientation, both Co and $Co_{1-x}Ru_x$ $(10\underline{1}0)$ films exhibit the crystallographic EA of the hcp lattice structure along the in-plane [0001] direction, as shown schematically in Fig. 3.2(a) [36, 41, 42, 43, 44]. Both Co and

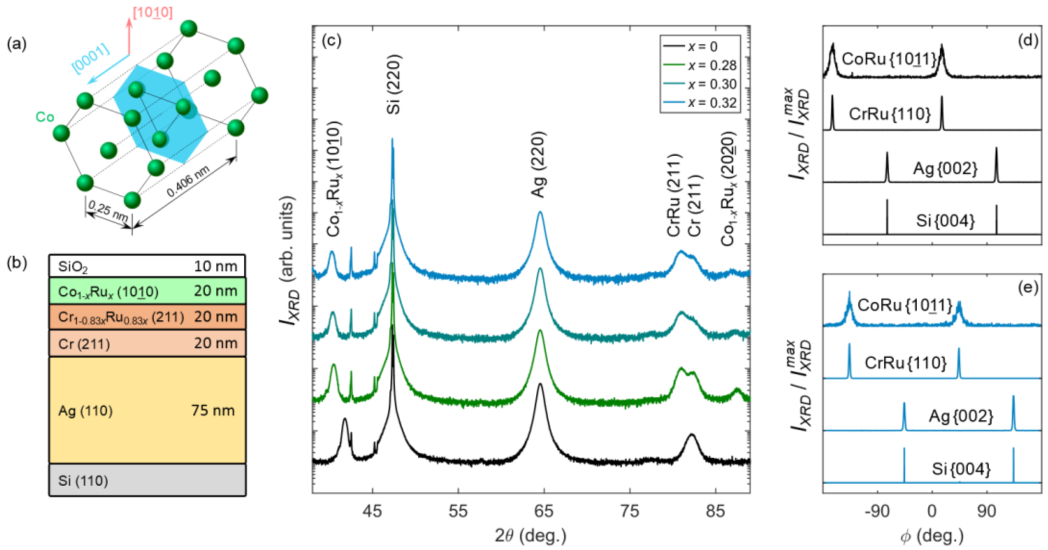

Figure 3.2: (a) Schematic of the hcp Co lattice structure with $(10\underline{1}0)$ surface orientation. Light-blue and pink vectors indicate the [0001] and $[10\underline{1}0]$ directions, respectively. (b) Schematic of the multilayer structure required for the epitaxial growth of homogeneous $Co_{1-x}Ru_x$ $(10\underline{1}0)$ thin films. (c) XRD θ-2θ scans of several thin films with different Ru concentrations x. The solid-black line corresponds to a Co $(10\underline{1}0)$ thin film with $x = 0$ for reference. The non-indexed peaks correspond to the Si (220) peak at different wavelengths and do not correspond to any of the films grown. (d, e) XRD azimuthal scans at the 2θ poles of Si {004}, Ag {002}, Cr {110}, and CoRu $\{10\underline{1}1\}$ for the samples with $x = 0$ and $x = 0.32$, verifying the overall epitaxial growth of the films.

$Co_{1-x}Ru_x$ $(10\underline{1}0)$ thin film structures can be grown epitaxially following specific multilayers sequences on Si (110) wafers [45], shown schematically in Fig. 3.2(b).

Here, Ag(110) and Cr(211) thin films serve as template layers for the epitaxial growth of $Co(10\underline{1}0)$. Details regarding the heteroepitaxial growth of this particular multilayer sequence can be found elsewhere [36, 43]. The epitaxial growth of $Co_{1-x}Ru_x$ $(10\underline{1}0)$ films with $x \neq 0$ has been optimized in the previous works [36] with the addition of a $Cr_{1-y}Ru_y$ (211) layer that accommodates the lattice mismatch between $Co_{1-x}Ru_x$ $(10\underline{1}0)$ and Cr(211) due to the Ru concentrations. Hereby, $Co_{1-x}Ru_x$ $(10\underline{1}0)$ optimally grows on top of $Cr_{1-y}Ru_y$ when $y = x/1.2$ [36].

In order to fabricate the entire structure, single-crystal Si (110) thin films are cleaned in ultrasonic baths with acetone, isopropanol, and deionized water, respectively. Afterwards, native SiO_2 layer is removed by means of hydrofluoric (HF) etching in a bath for 20 minutes and immediately introduced into the vacuum chamber in the sputter deposition tool for the growth of the multilayers, avoiding the oxidation of the Si surface. The fabrication of such thin films is conducted by means of co-sputter deposition (see Chapter 2) using an Ar atmosphere with 0.4

Pa. Following previous works, here 75-nm-thick Ag films, 20-nm-thick Cr and 20-nm-thick $Cr_{1-y}Ru_y$ layers are grown, which serve as template for the epitaxial growth of $Co_{1-x}Ru_x$ $(10\underline{1}0)$ layer. A 10-nm-thick SiO_2 layer is grown on top of the entire structure to avoid the oxidation of the films.

Fig. 3.2(c) shows XRD θ-2θ scans of several exemplary $Co_{1-x}Ru_x$ $(10\underline{1}0)$ samples with homogeneous x-concentrations of Ru, together with the XRD scan of a pure Co $(10\underline{1}0)$ thin film, shown for comparison purposes[11]. Here, one observes the peaks corresponding to each of the crystallographic planes of the intended layers and sequence only, as indicated in the labels. The presence of the second order $Co_{1-x}Ru_x$ $(20\underline{2}0)$ and the absence of peaks corresponding to other crystallographic planes allow one to verify that all the layers have grown in a single crystal manner. The $Co_{1-x}Ru_x$ $(10\underline{1}0)$ peaks shift towards lower 2θ angles for increasing Ru content, which indicates a significant distortion in the lattice parameters of the $Co_{1-x}Ru_x$ films. Nonetheless, despite such epitaxial strain, the samples are single crystal and, thus, such distortion does not influence the quality of the overall epitaxial grown [36]. The peaks at 42.5º and 45.2º correspond to the Si (220) peak at different wavelengths, such as the Cu-K_β line and, so, they are not associated with the grown film.

In order to fully verify the epitaxial growth of the entire multilayer structure, azimuthal ϕ-scans are performed. These measurements are performed at crystal planes that are not perpendicular to the film surface, which provides information about the in-plane crystal structure and relative orientations between layers in the films. Figs. 3.2(d, e) show several exemplary ϕ-scans for the samples with $x = 0$, 0.32. Here the X-ray intensities, normalized to the maximum value in each corresponding measurement are shown. All such ϕ-scans show two well-defined peaks that are 180° apart at positions that match the stereographic projections of their nominal structure [45, 46]. The Si {004} and Ag {002} scans indicate a parallel alignment of the Si and Ag [001] directions. Likewise, the 90° angular shift between the Ag and the Cr/CrRu peaks indicates that the Cr $[1\underline{1}0]$ direction is parallel to the Ag [001] direction, as intended. Finally, the CoRu $\{10\underline{1}1\}$ peaks appear at the

---

[11] The here shown measurements were conducted in the PANalytical EMPIREAN tool (see Chapter 2)

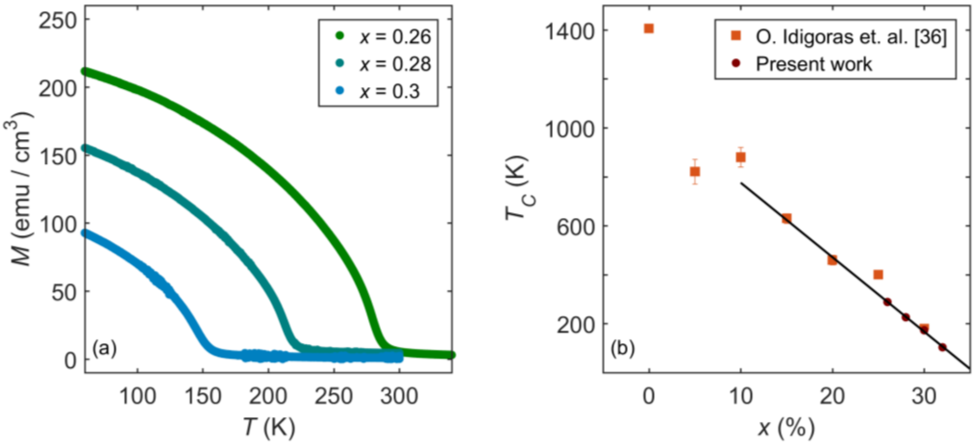

Figure 3.3: (a) SQUID measurements of the $M(T)$ behavior of several uniform $Co_{1\text{-}x}Ru_x$-alloy samples with different Ru concentrations x. (b) T_C vs. x-concentration dependence. The orange squares represent the data from previous works at higher temperatures [36], while the red dots represent here obtained results by means of SQUID magnetometry. The solid black-line represents the linearly decreasing trend of T_C in a broad x-range.

same ϕ-values as those for Cr/CrRu {110}, confirming the in-plane alignment of the CoRu [0001] direction, parallel to the Cr/CrRu $[1\underline{1}0]$ direction, as intended. Therefore, this structural analysis in homogeneous CoRu thin films allow one to verify that the entire structure grows in an epitaxial single-crystal manner [43, 46].

In order to quantify the effective reduction of exchange coupling strength due to increasing Ru concentrations, the Curie temperature of the so grown homogeneous thin films is quantified by means of SQUID magnetometry measurements (see Chapter 2). Fig. 3.3(a) shows the $M(T)$ behavior in three films with different x. The measurements are conducted while decreasing the temperature with a small but non-zero field $\mu_0 H = 5$ mT applied parallel to the EA, that avoids the formation of domains at the ordering temperature. In all the cases, one observes a sharp onset corresponding to T_C, which is of decreasing magnitude with increasing Ru concentrations, as expected. The exact T_C-values are extracted using a least-squares fitting of the experimental magnetization data to a power-law, as explained in Chapter 1, namely,

$$M = M_1 \, (T_C - T)^{\beta}. \tag{3.1}$$

Here, the fitting is repeated self-consistently in the same T/T_C-range. The extracted T_C-values are represented as a function of x in Fig. 3.3(b). In this figure, one observes an almost linearly decreasing $T_C(x)$ behavior, at least in a significant concentration range. Fig. 3.3(b) also shows comparatively the data from prior work, obtained for lower Ru concentrations [36]. The here obtained $T_C(x)$ data for large x-concentrations are fitted to a single line, shown as a solid-black line. Such a least-squares fit matches the experimental data very well, even for lower concentrations. The quality of these preliminary results and the observed linear behaviors now enables the design and fabrication of exchange-graded thin films, as will be explained later. At this point, it is relevant to mention that possible sources of inhomogeneities in these films, such as phase separations are known to occur in Co-Ru alloys, only at larger Ru concentrations and temperatures higher than room temperature [40] and, thus, they are not expected to influence the overall magnetic behavior for the samples fabricated for this thesis.

Another aspect that has been investigated in detail in this work is the uniaxial magnetic anisotropy behavior of homogeneous $Co_{1-x}Ru_x$ (10$\underline{1}$0) thin films. The samples shown in Figs. 3.2 and 3.3 have T_C lower than room temperature, and their magnetic anisotropy behavior cannot be investigated in detail in the SQUID setup. Instead, $Co_{1-x}Ru_x$ (10$\underline{1}$0) thin films with slightly lower x-concentrations have been fabricated, so that they have larger T_C and, thus, their anisotropic behavior can be investigated at room temperature in the VSM, (see Chapter 2) [44].

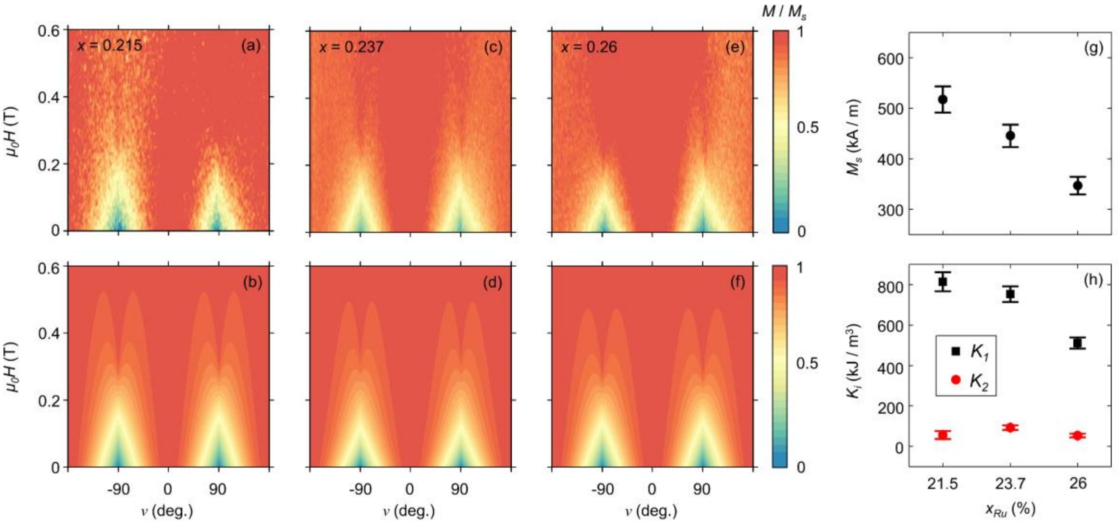

Figure 3.4: (a, c, e) Color-coded maps of the experimentally obtained $M(\nu, H)$ by means of VSM measurements for several x-concentrations. (b, d, f) Color-coded maps of the corresponding least-squares fitting results to the data in (a, c, e). (g) M_s and (h) first- and second-order K_i anisotropy energies as a function of the Ru concentration x.

In this tool, the sample is set inside the gap of the electromagnet such that an in-plane $\boldsymbol{H}$ can be applied. Hysteresis loops of the magnetization component parallel to the field are recorded for different orientations υ between the EA and $\boldsymbol{H}$. The $M(H)$ behavior for each υ is experimentally determined in a decreasing field sequence after first achieving saturation along said magnetic field direction.

Figs. 3.4(a, c, e) show as color-coded maps the $M(\upsilon, H)$ behavior for several samples with three different uniform x-concentrations in samples that are ferromagnetic at room temperature. In all the cases, the expected 180º rotational symmetry of the magnetization behavior is observed. At $\upsilon = 0^{\circ}$ and 180º, the EA and field direction are parallel to each other and, thus, the magnetization vector will remain parallel to this direction, leading to $M = M_s$. Contrarily, at $\upsilon = -90$, 90º, EA and H are perpendicular to each other. Thus, at large enough field values, magnetization will remain parallel to the field direction, but as the field decreases its magnitude, the magnetization vector will rotate continuously towards the EA, as explained in Section 1.3 [42, 43, 44]. The experimental data in the color-maps of Figs. 3.4(a, c, e) can exhibit some asymmetries in their 180º angular symmetry, particularly visible at larger fields by means of the orange regions. This asymmetry is due to small but non-zero misalignments of the surface normal of sample with respect to the vibration direction. Such deviations are in any case small and that do not influence the overall analysis scheme.

In thin films with in-plane uniaxial magnetic anisotropy, demagnetizing fields are negligible in the overall energy contributions of the system. Therefore, magnetization will behave as a macrospin, in which all spin contributions rotate coherently, as explained in Chapter 1. The $M(\upsilon, H)$ behavior can be modeled then by the Stoner-Wohlfarth model [47], assuming that the energy density of the system is given as,

$$\mathcal{F} = -\mu_0 H M_s \cos\varphi + K_1 \sin^2(\nu - \varphi) + K_2 \sin^4(\nu - \varphi)\,, \tag{3.2}$$

where K_1 and K_2 are the first- and second-order anisotropy energy densities and φ is the angle between M and field direction. Details regarding the evaluation of eq. (3.2) can be found in Appendix A. Figs. 3.4(b, d, f) show the least-squares fits of eq. (3.2) to the experimental results in Figs. 3.4(a, c, e), respectively. Here, one observes that all key aspects of the $M(\upsilon, H)$ fits are in excellent agreement with the experimental data. Figs. 3.4(g, h) show the results of M_s and K_1, K_2 vs. x from this analysis conducted at room temperature. Here, M_s decreases in a monotonous manner with increasing Ru concentrations, as expected. K_1 also seem to decrease in a monotonous manner, in agreement with prior experimental works, while K_2 remains always smaller than K_1, but still non-zero [34, 48]. These results imply that the epitaxially grown $Co_{1-x}Ru_x$ $(10\underline{1}0)$ thin films exhibit the expected in-plane uniaxial magnetic anisotropy. Hereby, a simple macrospin behavior is observed in all the films, even with increasing x-concentrations.

Now that the expected structural and magnetic behaviors of homogeneous $Co_{1-x}Ru_x$ $(10\underline{1}0)$ thin films have been verified, the fabrication of exchange-graded thin films is conducted. Fig. 3.5 shows the overall sample fabrication procedure of a particular set of $Co_{1-x(z)}Ru_{x(z)}$ $(10\underline{1}0)$ thin films exhibiting EGPs, as well as the subsequent structural analysis. Fig. 3.5(a) shows the specific multilayer structure employed in the epitaxial growth of these $Co_{1-x(z)}Ru_{x(z)}$ $(10\underline{1}0)$ thin films.

In this chapter, the results from a particular type of exchange-profile are discussed, whose properties are shown in Fig. 3.5(b). It consists of a V-shaped profile, whose maximum and minimum Ru concentrations are kept constant to 32.5% and 37%, while the total thickness of the magnetic layer d is varied. Such thickness ranges d = 10-150 nm. This profile translates into a $J(z)$ profile as

$$J = J_0 \left[1\text{-}\ (s_g|z|)^{\varepsilon}\right], \tag{3.3}$$

where J_0 is the maximum exchange energy at the center $z = 0$ of the ferromagnetic layer and $s_g = (1\text{-}\,T_C^{min}/\,T_C^{max})/(d/2)$ defines the slope of the exchange-profile. Here, $\varepsilon = 1$ is chosen for simplicity, even if the sample type will be shown to be generalizable to $\varepsilon \neq 1$.

Fig. 3.5(c) shows the XRD θ-2θ scans of several exemplary exchange-graded samples with different thicknesses d of the $Co_{1-x(z)}Ru_{x(z)}$ layer. As in the case of homogeneous $Co_{1-x}Ru_x$ thin films, one observes here the peaks corresponding to each of the crystallographic planes of the film only. In all of the samples one observes both the first- and second-order peaks of the $Co_{1-x(z)}Ru_{x(z)}$ layers. Also, their magnitude becomes increasingly large for increasing total thicknesses, which is a good indicator that the entire structure grows in a single crystal manner, even for thicker films. While the homogeneous thin films exhibit a shift of the $Co_{1-x}Ru_x$ peaks for increasing Ru concentrations, here the peaks remain in the same 2θ-values, because the maximum and minimum Ru concentrations are kept constant throughout the entire set of films.

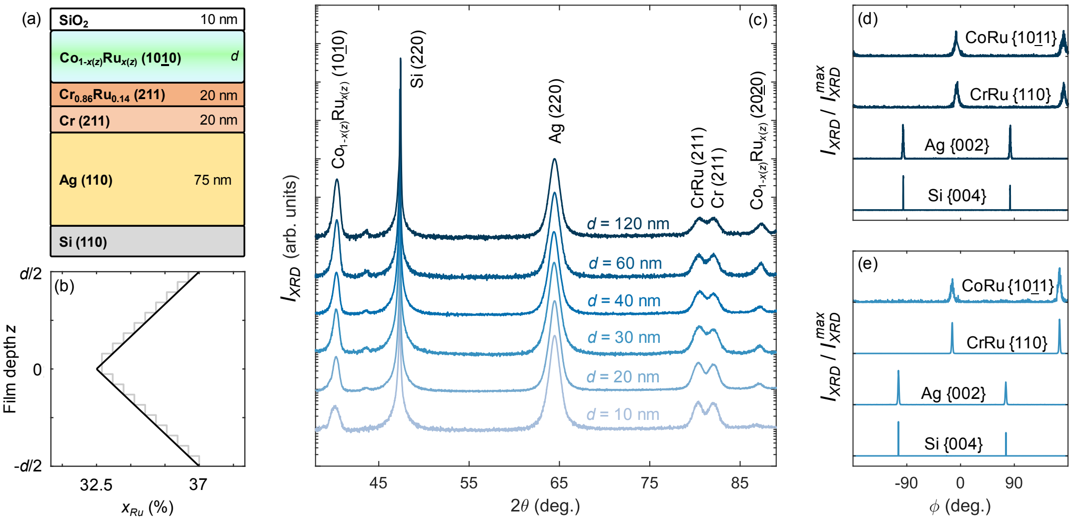

Figure 3.5: (a) Schematic of the overall multilayer sequence employed for the epitaxial growth of $Co_{1\text{-}x(z)}Ru_{x(z)}$ $(10\underline{1}0)$ thin films. (b) Ru concentration x-profile throughout the Co film. The stepwise grey line represents the nominal profile employed with steps of 0.5-1 nm of homogeneous x-concentrations. (c) XRD θ-2θ scans of several thin films with different total thickness of the CoRu layer. (d, e) XRD azimuthal scans at the 2θ poles of Si {004}, Ag {002}, Cr {110}, and CoRu $\{10\underline{1}1\}$ for two exemplary samples with d = 120 nm and d = 30 nm.

In order to verify the epitaxial growth of the entire structure, azimuthal ϕ-scans are performed at the 2θ poles of suitable crystallographic planes, in the same way as explained in conjunction with Fig. 3.2 (d, e). Figs. 3.5(d, e) correspond to this particular analysis conducted for the films with d = 120 nm and d = 30 nm. Here as well, one detects the parallel alignment of the Si {004}/Ag {002} poles, the perpendicular alignment of the Ag {002}/CrRu {110} poles and, finally, the parallel alignment of the CrRu {110}/CoRu $\{10\underline{1}1\}$, verifying the in-plane alignment of the Co [0001] direction [43, 46]. These results allow one to verify the overall epitaxial growth of the entire structure and, particularly, the in-plane alignment of the CoRu{0001}, even for the thicker films.

Therefore, the epitaxial growth of the entire set of single crystal $Co_{1\text{-}x(z)}Ru_{x(z)}$ $(10\underline{1}0)$ thin films is verified. The here shown sample fabrication methodology, is not limited to this particular V-shaped profile, but instead is applicable to more complex $x(z)$ profiles, as will be shown in Chapter 4.

It is relevant to mention at this point that, in principle, unintended intermixing of Ru and Co atoms could occur throughout the depth of the film, which would then lead to substantial modifications of the expected $T_C^{loc}(z)$ profile.

However here, a room temperature deposition process is employed to avoid such intermixing. Furthermore, in samples very similar to the ones here fabricated, the intended nominal profiles on the relevant length-scale were verified by means of polarized neutron reflectometry, with unintended intermixing being limited to below 2 nm in depth [49]. Thus, while a certain level of intermixing is likely to occur, it is limited to length-scales that are significantly smaller than the magnetically relevant profile features of the films.

3.4 Results & Discussion

In Section 3.3, a methodology for the epitaxial growth of $Co_{1\text{-}x(z)}Ru_{x(z)}$ $(10\underline{1}0)$ thin films has been discussed in detail. Here, samples exhibiting V-shaped $x(z)$ profiles have been fabricated, and their structural analysis has been explained in a comprehensive manner. In this section, the results on the thermodynamic behavior of these type of films exhibiting EGPs will be explained in a comprehensive manner [37, 38, 39].

3.4.1 Modification of critical exponents in the equilibrium phase transition

As discussed in Chapter 1, ferromagnetic materials undergo a SOPT at a unique critical point, which is the Curie temperature. Hereby, the $M(T, H)$ behavior in the vicinity of T_C is characterized by scaling behavior associated with several critical exponents that depend solely on the dimensionality of the system [50]. Such universality enables the common description of complex physical systems by means of rather simple models [12].

On the other hand, the fact that such critical exponents depend only on the dimensionality of the system, severely limits the materials design capabilities for specific applications related to the SOPT of ferromagnets. The only seeming, but key, exception to universality is the occurrence of SOPT at interfaces[12] (or surfaces) of 3D magnetic systems. Here, most relevantly, there is a broken symmetry of the 3D lattice structure. In addition, the exchange coupling strength at the interface J_s can differ from that of bulk J_{bulk}. Hereby, tunning J_s can lead to different types of magnetization onsets at the interface in the vicinity of the SOPT, leading to a modification of the surface critical exponents β_s. For example, in a simple cubic Ising-like spin systems, the surface critical exponent $\beta_s \approx 0.78$ for $J_s/J_{bulk} < 1$, and it changes continuously until $\beta_s \approx 0.125$ for $J_s/J_{bulk} > 1.55$ [51]. However, this strategy towards the modification of critical exponents is very limited in practice, given that only few surface exponents can be obtained following this strategy. Furthermore, tuning exchange energies in single atomic layers is not easily achieved in practice [52].

---

[12] Here, interface shall be used to refer to the film layer at which J changes.

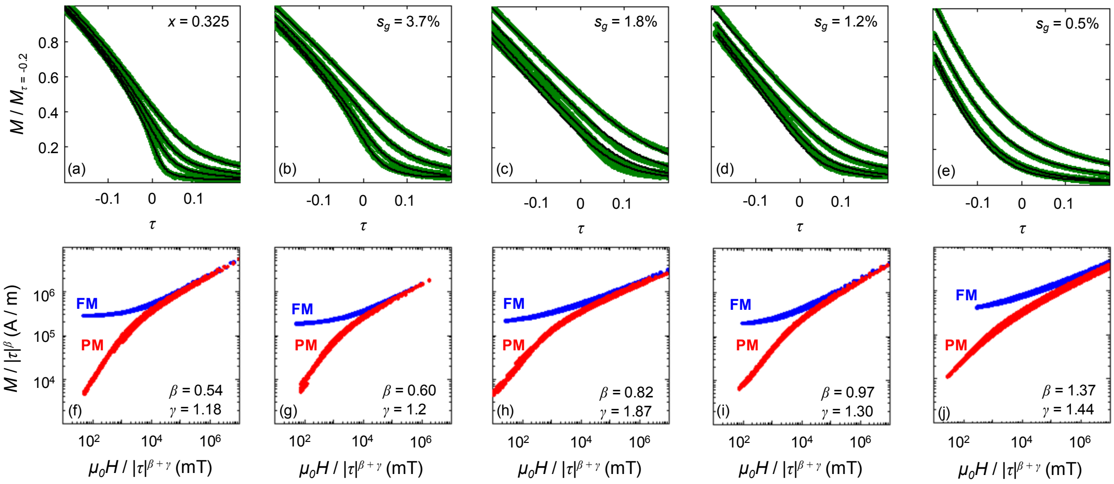

Figure 3.6: (a-e) SQUID magnetometry measurements of the $M(T, H)$ behaviors for a homogeneous Co$_{1\text{-}x}$Ru$_x$ and several Co$_{1\text{-}x(z)}$Ru$_{x(z)}$ thin films with different s_g-values. The green dots represent experimental data whereas solid black lines represent the least-squares fits to eq. (3.4) for each sample. (f-j) Arrott plot of the renormalized $M/|\tau|^{\beta}$ as a function of the renormalized field $\mu_0 H/\tau^{|\beta+\nu|}$ showing the scaling of M. The red (blue) points correspond to the points in the PM (FM) phase.

This discussion connects then with the here explored exchange-graded thin films [32, 53]. Because in these films exchange energy varies in a continuous fashion along the depth of the film, then, such films could be regarded as all-interface materials in which J changes at all depths of the film. In practice, different portions of the films will start to order at different temperatures, leading to a modification of the average $M(T)$ onset [30].

In order to test the impact and potential of this effect, the $M(T, H)$ behavior of the V-shaped Co$_{1\text{-}x(z)}$Ru$_{x(z)}$ (10$\underline{1}$0) thin films is quantified by means of SQUID magnetometry measurements for samples with many different s_g-values [37]. Here, the M component parallel to the EA is measured with decreasing T, and constant positive H applied parallel to the EA as well. Fig. 3.6(a-e) show the $M(\tau = T/T_C - 1 , H)$ behavior, normalized to its value at $\tau = -0.2$, of several exemplary samples, namely, a homogeneous thin film with $x = 32.5\%$ and four graded thin films with different s_g. The measurements are conducted with constant field values of $\mu_0 H =$ 4, 5, 10, 20 mT.

Strictly, the SOPT is never observed in these measurements because in all the cases a small field is applied in order to avoid the formation of domains at the ordering temperature, even if a clear onset occurs in all the samples at $\tau = 0$. More relevantly, though, the $M(T)$ onset is strongly modified in between samples. The homogeneous thin film in Fig. 3.6(a) exhibits a rather steep onset for the $H = 4$ mT curve with a rather concave $M(T)$ behavior in the FM phase. Contrarily, the sample with $s_g = 1.8\%$ seems to exhibit rather linear $M(T)$ curves in the FM phase and the sample with $s_g = 0.5\%$ shows a convex $M(T)$ behavior.

In order to explore the scaling behavior in these films, each of these data sets are now assumed to follow the Arrott-Noakes equation-of-state [50],

$$\left(\frac{H}{M}\right)^{1/\gamma} = \frac{T - T_C}{T_1} + \left(\frac{M}{M_1}\right)^{1/\beta}, \tag{3.4}$$

where T_1 and M_1 are material specific constants. Here, least-squares fits to eq. (3.4) is conducted taking as fitting parameters the critical exponents, material specific constants and T_C. For each sample, the data corresponding to the four different H-values are fitted simultaneously. Furthermore, the fitting is repeated self-consistently in order to quantify the critical regime in the same relative τ-range.

The solid-black lines in Figs. 3.6(a-e) show the results from each of these least-squares fitting procedures. Here, the fit results clearly follow the experimental data in all the cases, even in the samples with lower slopes of the EGP profile where the $M(T, H)$ behaviors are more strongly modified. In all the cases, determination coefficients $R^2 > 0.995$ are obtained, which is a clear indication that scaling is preserved in these EGPs, even if the films exhibit distinct magnetization onset behavior at their respective Curie temperatures T_C.

Following the here conducted fitting procedure, one can now construct the associated Arrott plots, as shown in Figs. 3.6(f-j). Here, the renormalized order parameter $M/|\tau|^{\beta}$ is represented as a function of the renormalized field $H/|\tau|^{\beta+\gamma}$ (see Appendix C). In such data representation, all the experimental data of the equilibrium phase space collapse onto two separate curves, which correspond to the points in the FM (blue) and PM (red) phases. Here, excellent scaling is observed for at least 5 orders of magnitude in the renormalized field, which clearly indicates that the scaling is preserved in all the exchange-graded thin films. This is by itself a non-trivial observation, given that the magnetization onset close to T_C does not need to be described a priori by power-laws of the form of eq. (3.4) because dimensional crossover could make the critical regime extremely small [30, 49].

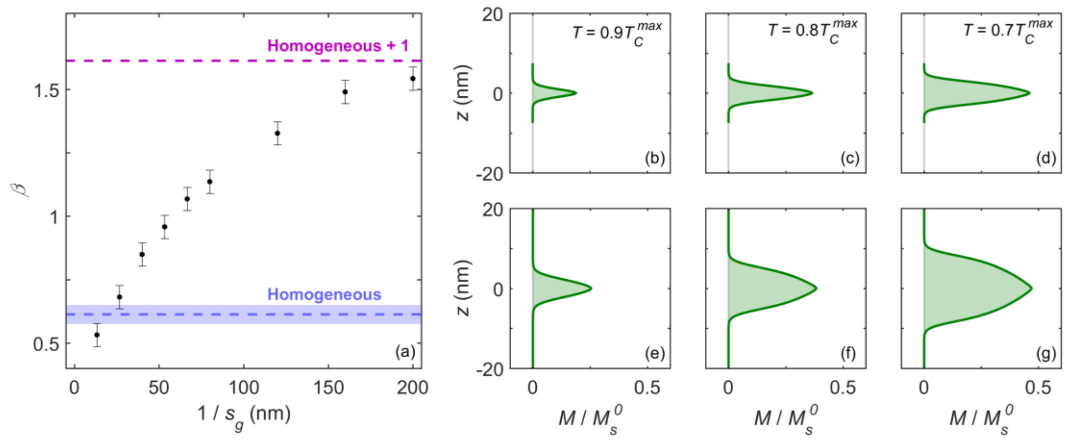

Figure 3.7: (a) Critical exponents β represented as a function of $1/s_g$. The light-purple line indicates the critical exponent of homogeneous Co$_{1\text{-}x}$Ru$_x$ ($10\underline{1}0$) thin films. (b-d) Exemplary magnetization profiles at three different temperatures of a thin film with an EGP exhibiting $1/s_g = 22.5$ nm (d = 15 nm). (e-g) Exemplary magnetization profiles at three different temperatures of a thin film with an EGP exhibiting 1/s$_g$ = 60 nm (d = 40 nm). Magnetization profiles are obtained by means of a mean-field model whose details are explained in Chapter 4.

The measurements and least-squares fits have been repeated for many samples with different total thicknesses and, therefore, different slopes s_g of the EGP. The set of critical exponents β are represented now as a function of $1/s_g$ in Fig. 3.7. The light-purple line indicates the critical exponent β_{hom} of the thin films exhibiting homogeneous J-profiles. Here, despite the fact scaling is preserved in all the Co$_{1\text{-}x(z)}$Ru$_{x(z)}$ ($10\underline{1}0$) thin films, the critical exponents β changes very dramatically for different $1/s_g$ and for decreasing s_g-values of the graded-layer, the exponents seem to approach the $\beta_{hom} + 1$. It is also worthwhile to mention that the critical exponents γ exhibit only a rather modest systematic increase with $1/s_g$.

In order to understand these results that seemingly violate universality, one must have a closer look at the temperature evolution of the magnetization profile along the depth of the film [30, 32, 37]. Figs. 3.7(b-g) shows the $M(z)$ profiles of two different samples with different s_g-values at three different temperatures, with respect to the global Curie temperature $T_C{}^{max} = \max(T_C{}^{loc}(z))$. Such profiles have been obtained by means of mean-field calculations whose details are explained in Chapter 4 in conjunction with Appendix B. One can verify here that exchange-graded profiles exhibit $T_C{}^{loc}(z)$ profiles down to the 1-2 nm length-scale. Hereby, in these V-shaped EGPs, the local magnetization behavior is basically determined by such local $T_C{}^{loc}(z)$. Taking this into consideration, by decreasing the temperature bellow the global $T_C{}^{max}$, only the central portion of the film will start to exhibit a ferromagnetic ordering, as seen in Figs 3.7(b, e). By further decreasing T, larger portions of the film will exhibit a long-range ordering, because locally, $T < T_C^{loc}(z)$. Thus, as T is decreased further, the $M(z, T)$ profile will continue to extend, both in magnitude and along the film depth, as observed in Figs 3.7(c, d, f, g) [53].

For different exchange-gradient profiles with different slopes of the EGP, the temperature evolution of $M(z, T)$ will be different from sample to sample. Given that, here, the maximum and minimum T_C^{loc}-values are kept constants, samples with larger s_g (lower total thickness) will exhibit more abrupt changes in the M behavior for decreasing temperatures. Contrarily, samples with lower s_g (larger total thickness), will order more gradually as T decreases. Such different ordering of the FM region will lead to a continuous modification of β.

To show this, one can consider a $M(z, T)$ profile, in which each layer depends only on the specific J in the layer itself, that is, locally independent layers as [30, 37],

$$M(z,\ T) \propto \begin{cases} \left[T_C^{max}\left(1 - \left(s_g|z|\right)^{\varepsilon}\right) - T\right]^{\beta_{hom}} & \text{for } T < T_C^{max}\left(1 - \left(s_g|z|\right)^{\varepsilon}\right), \\ 0 & \text{for } T \geq T_C^{max}\left(1 - \left(s_g|z|\right)^{\varepsilon}\right). \end{cases} \tag{3.5}$$

Here, the magnetization $M(z, T)$ profile will exhibit a non-zero ordering only for that part of the sample, in which $T < T_C^{loc}(z)$ is fulfilled. This is a significant simplification given that, in reality, the M-profile is not purely local. Indeed, at the film depth in which $T = T_C^{loc}(z)$ magnetization describes an exponentially decreasing onset towards the effective PM region, even if the contribution of such an onset to the total moment in the film is in any case small.

Then, given that the FM portion of the film is determined only by $-\left[(T_C - T)/T_C\ s_g^{\varepsilon}\right]^{1/\varepsilon} \leq z \leq \left[(T_C - T)/T_C\ s_g^{\varepsilon}\right]^{1/\varepsilon}$, then the average $M(T)$ in the film can be calculated as,

$$M(T) \propto \frac{2}{d}\int_0^{\left[\frac{(T_C - T)}{T_C} s_g^{\varepsilon}\right]^{\frac{1}{\varepsilon}}} \mathrm{dz}\ \left\{\left[T_C^{max}\left(1 - \left(s_g|z|\right)^{\varepsilon}\right) - T\right]^{\beta_{hom}}\right\}\ , \tag{3.6}$$

which, by making use of hypergeometric functions, can be rewritten as,

$$M(T) \propto \begin{cases} \dfrac{2\,\tilde{f}}{d \cdot s_g}(T_C - T)^{\beta + 1/\varepsilon} & \text{for } T < T_C^{max}, \\ 0 & \text{for } T \geq T_C^{max}, \end{cases} \tag{3.7}$$

where, $\tilde{f}$ is a hypergeometric function with values in the interval [0,1]. More importantly, one obtains a global $\beta = (\beta_{hom} + 1/\varepsilon)$ which becomes $\beta = \beta_{hom} + 1$ in the case of the here explored films in the limit $s_g \rightarrow 0$, i.e. very shallow gradients [54]. Very high ε-values would lead then to very flat M-profiles in the center of the film and thus, the behavior of a homogeneous FM thin film would be restored. While this limiting case does not explain all intermediate values of β obtained experimentally, it guides an understanding of the underlying physical behavior in these exchange-graded thin films and how their critical behavior is fundamentally different from conventional ferromagnets.

3.4.2 Coercivity Suppression in exchange-graded ferromagnets

In Section 3.4.1, the equilibrium thermodynamic $M(T, H)$ behavior has been investigated in the vicinity of T_C in exchange-graded thin films. Hereby, the here observed modification of the critical exponent β is associated with a spatial evolution of the FM phase, as T decreases [37].

In this regard, it is interesting to consider the thermodynamic behavior of an exchange-graded ferromagnet right at the PM/FM interface after the initial FM state has occurred. In the purely local picture, because $T = T_C^{loc}(z)$ at exactly this boundary, the susceptibility χ at the PM/FM interface should diverge. In realistic magnetization profiles, however, M undergoes an exponentially decreasing onset on the 1-2 nm length-scale, that causes a proximity induce ordering in the adjacent layers [30, 53]. Still, the susceptibility at the PM/FM should exhibit very large values at the positions where $T = T_C^{loc}(z)$ is fulfilled. Thus, the occurrence of the FOPT upon inverting an applied magnetic field could be relevantly modified as

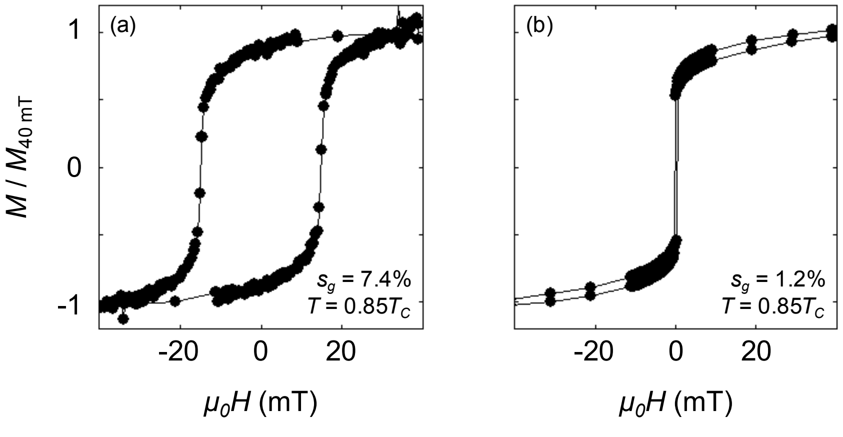

Figure 3.8: $M(0.85\,T_C^{max}, H)$ of two samples with $s_g = 7.4\%$ and 1.2% respectively, showing distinct hysteretic behaviors

well, with the associated $M(H)$ hysteretic behavior exhibiting changed reversal mechanisms over extended temperature ranges, which could provide novel materials designs towards real-life applications [38, 39, 53]. This is exactly the phenomenon investigated in this section, for which the V-shaped $\mathrm{Co}_{1\text{-}x(z)}\mathrm{Ru}_{x(z)}$ $(10\underline{1}0)$ thin films explained in the previous sections are employed.

In order to test this effect, the hysteretic behavior of the $M(H)$ is quantified in all the samples described in Section 3.3 for all temperatures in the relevant T-range, by means of SQUID magnetometry. In Fig. 3.8, the hysteretic behavior of $M(H)$ is shown exemplarily at a $T = 0.85\,T_C{}^{max}$ for two different $\mathrm{Co}_{1\text{-}x(z)}\mathrm{Ru}_{x(z)}$ $(10\underline{1}0)$ thin films with different s_g-values. The M data correspond to the magnetization component parallel to $\boldsymbol{H}$, set along the EA. In both cases, M saturates for sufficiently high H, as expected. Upon decreasing H, the film with $s_g = 7.4\%$ (low thickness), shown in Fig. 3.8(a), M will exhibit a rather steep magnetization reversal at H_c. In contrast, the film with $s_g = 1.2\%$ (large thickness), shown in Fig. 3.8(b), exhibits a negligible coercive field H_c even if a large part of the film is already ferromagnetically ordered. Such film exhibits then a significant remanence with $H_c = 0$ within experimental precision [38].

In order to explore this phenomenon in detail, the hysteresis loops of the exchange-graded FM thin films are measured for different temperatures. Fig. 3.9 show the $H_c(T)$ behaviors extracted from such hysteresis loop measurements of several exemplary samples with different slopes of the EGP. Fig. 3.9(a) shows the H_c vs. T behavior for a homogeneous $\mathrm{Co}_{1\text{-}x}\mathrm{Ru}_x$ $(10\underline{1}0)$ thin film. Here, upon decreasing T below T_C, the entire structure exhibits substantial and nearly uniform FM ordering and H_c starts to increase monotonously. This is because, at lower temperatures, larger fields in the opposite direction are required to induce a domain

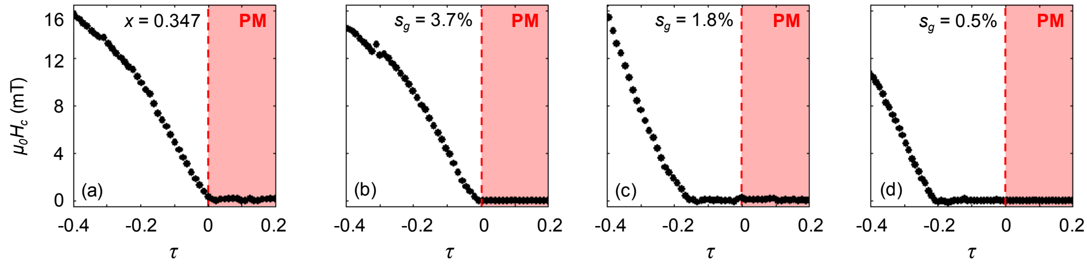

Figure 3.9: Coercive field H_c plotted against the reduced temperature τ for several samples with homogeneous x (a) and distinct s_g-values (b-d), showing the anhysteretic behaviors over extended temperature ranges.

nucleation and subsequent domain-wall expansion. For large slope s of the EGP profile of the $Co_{1-x(z)}Ru_{x(z)}$ films, in Fig. 3.9(b), the $H_c(T)$ behavior is similar to that of homogeneous thin films. However, for decreasing slope s, i.e. larger film thickness, one observes extended temperature ranges in which H_c remains null within the experimental precision, even if at least part of the film is already in its FM state.

For the cases with high-s_g, the $M(z)$ profile is basically completely populated at T_C^{max}, because for such large gradients the total thickness is comparable with the internal magnetic profile width [53]. This is the case of profiles as the ones shown exemplarily in Figs. 3.7(b-d). Therefore, even in the presence of a $M(z)$ profile, a conventional $H_c(T)$ behavior is observed because a collective FM behavior develops in the entire film along its depth. For low-s samples, however, the FM state at $T < T_C^{max}$ forms first in the sample's center, which results in a magnetization profile whose thickness is smaller than the total material thickness [38, 53]. Correspondingly, the central FM region is delimited by two PM regions on its top and bottom, developing a PM/FM/PM-like quasi-multiphase magnetic structure. Furthermore, such PM phases have very large susceptibilities because locally $(T-T_C^{loc})/T_C^{loc} << 1$. Thus, in the presence of a very small magnetic field in the opposite direction, the PM regions in the film will align with H, and the FM state will become unstable, which will aid the magnetization reversal. Upon lowering T below T_C^{min}, the entire film will exhibit a FM state and, thus, no PM region will aid the M reversal. Below this temperature, the film will exhibit a non-zero H_c, as observed in Fig. 3.9 at lower temperatures.

3.5 Conclusions & Outlook

In this chapter, the magnetic properties of exchange-graded ferromagnetic thin films have been described. Such type of ferromagnetic films is demonstrated to exhibit magnetic behaviors that are controllable at the nanometer scale by means of temperature. This in turn allows one to tune macroscopic properties of the film that otherwise cannot be controlled. More specifically, the main focus of this thesis work has been a series of $Co_{1-x(z)}Ru_{x(z)}$ $(10\underline{1}0)$ samples exhibiting V-shaped $x(z)$ profiles. In such films, a FM region is generated in the central layer at temperatures $T < T_C^{max}$, which expands further into the film depth for decreasing temperatures.

Firstly, such films containing EGP have been designed and grown in a single crystal manner such that they exhibit rather simple magnetic behaviors with laterally uniform magnetic states. Despite this fact, it is relevant to remind that there is nothing particular about the here employed materials choice. Indeed, different alloy combinations are also known to allow for depth dependent exchange profiles [14, 30, 35, 46]. Thus, the work here serves merely as a proof-of-concept of the capabilities of such materials design.

In these V-shaped exchange-graded thin films, it has been demonstrated that the global critical exponent β can be modified, due to the broken symmetry at each plane of the structure, and the subsequent spatial evolution of the magnetization profile along the depth of the film. Interestingly, in such films scaling is preserved with modified exponents, which is in and by itself is a nontrivial observation. These experimental results provide key experimental evidence for further theoretical research in the field.

Likewise, such films are shown to exhibit negligible coercivity over extended temperature ranges in the FM state. At intermediate temperatures, the formation of pseudo-PM/FM/PM regions, favors the low-field magnetization reversal due to field induced effects in the PM regions coupling effectively to the FM region. This effect, being similar to that of anisotropy graded materials, offers far broader applicable technological potential beyond the reach of existing materials technologies, that could help in the development of novel heat-assisted magnetic recording-media (HAMR) [55, 56].

In general, the here explored structures offer performance advances in any application relying on strong thermomagnetic response and low magnetic fields. Furthermore, the non-hysteretic behavior over extended temperature ranges superimposed to the broadening of the SOPT make these materials particularly useful for the purpose of enhancing the performance of the magnetocaloric effect (MCE) with applications in magnetic cooling. This is an issue that has also been covered recently by using exchange-graded ferromagnetic thin films with similar properties to the ones here utilized [39].

Finally, the thin films with EGPs envisioned here are designed to exhibit their $T_C^{loc}(z)$ profiles bellow room temperature in order to accurately quantify their M behaviors by means of SQUID measurements. However, such $T_C^{loc}(z)$ can be, in principle, freely chosen for work operations at any given temperature range, which enhances the significance of the here explored phenomena towards real life applications. Nonetheless, it is also worthwhile mentioning that, at higher temperatures, relevant diffusions and atom segregation could lead to an irreversible modification of the overall $x(z)$ profiles and, consequently their thermodynamic properties [40].

Chapter References

[1] J. A. C. Bland and B. Heinrich, Ultrathin Magnetic Structures III: Fundamentals of Nanomagnetism (Springer, Germany, 2005).

[2] E. Y. Tsymbal and I. Žutić, Handbook of Spin Transport and Magnetism (CRC Press, USA, 2012).

[3] F. Hellman et. al., *Interface-induced phenomena in magnetism*, Rev. Mod. Phys. **89**, 025006 (2017).

[4] A. Fert, *Nobel Lecture: origin, development, and future of spintronics*, Rev. Mod. Phys. **80**, 1517 (2008).

[5] P. A. Grünberg, *Nobel Lecture: from spin waves to giant magnetoresistance and beyond*, Rev. Mod. Phys. **80** 1531 (2008).

[6] P. F. Carcia, A. D. Meinhaldt, and A. Suna, *Perpendicular magnetic anisotropy in Pd/Co thin film layered structures*, Appl. Phys. Lett. **47**, 178–180 (1985).

[7] P. F. Carcia, *Perpendicular magnetic anisotropy in Pd/Co and Pt/Co thin-film layered structures*, J. Appl. Phys. **63**, 5066–5073 (1988).

[8] B. N. Engel, C. D. England, R. A. Van Leeuwen, M. H. Wiedmann, and C. M. Falco, *Interface magnetic anisotropy in epitaxial superlattices*, Phys. Rev. Lett. **67**, 1910 (1991).

[9] A. Fert and Peter M. Levy, *Role of Anisotropic Exchange Interactions in Determining the Properties of Spin-Glasses*, Phys. Rev. Lett. **44**, 1538 (1980).

[10] A. Crépieux, C. Lacroix, *Dzyaloshinsky–Moriya interactions induced by symmetry breaking at a surface*, J. Magn. Magn. Mater. **182**, 341-349 (1998).

[11] E. Y. Vedmedenko, P. Riego, J. A. Arregi, and A. Berger, *Interlayer Dzyaloshinskii-Moriya Interactions*, Phys. Rev. Lett. 122, 257202 (2019).

[12] B. Saleh, J. Jiang, R. Fathi, T. Al-hababi, Q. Xu, L. Wang, D. Song and A. Ma, *30 years of functionally graded materials: an overview of manufacturing methods, applications and future challenges*, Composites B **201** 108376 (2020).

[13] W. Li and B. Han, *Research and Applications of Functionally Gradient Materials*, *Conf. Ser.: Mater. Sci. Eng.* **394** 022065 (2018).

[14] L. Fallarino, B. J. Kirby, and E. E. Fullerton, *Graded magnetic materials*, J. Phys. D: Appl. Phys. **54**, 303002 (2021).

[15] J. F. Geisz, R. M. France, K. L. Schulte, M. A. Steiner, A. G. Norman, H. L. Guthrey, M. R. Young, T. Song, and T. Moriarty, *Six-junction III–V solar cells with 47.1% conversion efficiency under 143 Suns concentration*, Nature Energy **5**, 326–335 (2020).

[16] J. P. Liu, E. Fullerton, O. Gutfleisch and D. J. Sellmyer, *Nanoscale Magnetic Materials and Applications* (Springer, Berlin, 2009).

[17] F. Kneller and R. Hawig, *The exchange-spring magnet: a new material principle for permanent magnets*, IEEE Trans. Magn. **27** 3588 (1991).

[18] R. Skomski and J. M. D. Coey, *Giant energy product in nanostructured two-phase magnets*, Phys. Rev. B 48, 15812 (1993).

[19] E. E. Fullerton, J. S. Jiang, and S. D. Bader, *Hard/soft magnetic heterostructures: model exchange-spring magnets*, J. Magn. Magn. Mater. **200**, 392–404 (1999).

[20] R. Röhlsberger, H. Thomas, K. Schlage, E. Burkel, O. Leupold, and R. Rüffer*, Imaging the Magnetic Spin Structure of Exchange-Coupled Thin Films*, Phys. Rev. Lett. **89**, 237201 (2002).

[21] G. Varvaro and F. Casoli (edited by) *Ultra-High-Density Magnetic Recording: Storage Materials and Media Designs* (CRC Press, New York, 2016).

[22] D. Goll, A. Breitling, L. Gu, P. A. van Aken, and W. Sigle, *Experimental realization of graded L1-FePt/Fe composite media with perpendicular magnetization*, J. Appl. Phys. **104**, 083903 (2008).

[23] G. T. Zimanyi, Graded media: Optimization and energy barriers, J. Appl. Phys. 103, 07F543 (2008).

[24] A. Berger, E. E. Fullerton, and B. H. Lengsfield III, *Perpendicular magnetic recording exchange-spring type medium with a lateral coupling layer for increasing intergranular exchange coupling in the lower magnetic layer.* U.S. Patent No 7,588,841 (2009).

[25] A. Berger, H. Van Do, E. E. Fullerton, Y. Ikeda, B. H. Lengsfield III, N. F. Supper, *Perpendicular magnetic recording medium with multiple exchange-coupled magnetic layers having substantially similar anisotropy fields.* U.S. Patent No 7,550,210 (2009).

[26] H. Yang, Y. Li, M. Zeng, W. Cao, W. E. Bailey, and R. Yu, Static and Dynamic Magnetization of Gradient FeNi Alloy Nanowire, Sci. Rep. 6, 20427 (2016).

[27] L. Álvaro-Gómez, S. Ruiz-Gómez, C. Fernández-González, M. Schöbitz, N. Mille, J. Hurst, D. Tiwari, A. De Riz, I. M. Andersen, J. Bachmann, L. Cagnon, M. Foerster, L. Aballe, R. Belkhou, J.-C. Toussaint, C. Thirion, A. Masseboeuf, D. Gusakova, L. Pérez, and O. Fruchart, *Micromagnetics of magnetic chemical modulations in soft-magnetic cylindrical nanowires*, Phys. Rev. B **106**, 054433 (2022).

[28] T. L. Staggers, L. Jacob, S. D. Pollard, *Domain wall velocity asymmetries driven by saturation magnetization gradients without a Dzyaloshinskii-Moriya interaction*, J. Magn. Magn. Mater. **558**, 169500 (2022).

[29] P. Borys, O. Kolokoltsev, N. Qureshi, M. L. Plumer, and T. L. Monchesky, *Unidirectional spin wave propagation due to a saturation magnetization gradient*, Phys. Rev. B **103**, 144411 (2021).

[30] B. J. Kirby, H. F. Belliveau, D. D. Belyea, P. A. Kienzle, A. J. Grutter, P. Riego, A. Berger and C. W. Miller, *Spatial evolution of the ferromagnetic phase transition in an exchange graded film,* Phys. Rev. Lett. **116**, 047203 (2016).

[31] P. Makushko et. al., *Flexomagnetism and vertically graded Néel temperature of antiferromagnetic Cr_2O_3 thin films*, Nature Comm. **13**, 6745 (2022).

[32] M. Marcellini, M. Pärnaste, B. Hjörvarsson, and M. Wolff, *Influence of the distribution of the inherent ordering temperature on the ordering in layered magnets*, Phys. Rev. B **79,** 144426 (2009).

[33] C. Le Graët, T. R. Charlton, M. McLaren, M. Loving, S. A. Morley, C. J. Kinane, R. M. D. Brydson, L. H. Lewis, S. Langridge and C. H. Marrows, *Temperature controlled motion of an antiferromagnet-ferromagnet interface within a dopant-graded FeRh epilayer,* APL Mater. **3**, 041802 (2015).

[34] R. Skomski, *Simple Models of Magnetism* (Oxford University Press, UK, 2008).

[35] B. J. Kirby, L. Fallarino, P. Riego, B. B. Maranville, Casey W. Miller, and A. Berger, *Nanoscale magnetic localization in exchange strength modulated ferromagnets*, Phys. Rev. B **98**, 064404 (2018).

[36] O. Idigoras, U. Palomares, A. K. Suszka, L. Fallarino, and A. Berger, *Magnetic properties of room temperature grown epitaxial* $Co_{1-x}Ru_x$*-alloy films*, Appl. Phys. Lett. **103**, 102410 (2013).

[37] L. Fallarino, E. López Rojo, M. Quintana, J. S. Salcedo Gallo, B. J. Kirby, and A. Berger, *Modifying Critical Exponents of Magnetic Phase Transitions via Nanoscale Materials Design*, Phys. Rev. Lett. **127**, 147201 (2021).

[38] L.Fallarino, M. Quintana, E. López Rojo, and A. Berger, Suppression of Coercivity in Nanoscale Graded Magnetic Materials, Phys. Rev. Appl. **16**, 034038 (2021).

[39] J. S. Salcedo Gallo, A. Berger, M. Quintana, E. Restrepo Parra and L. Fallarino, *Nanoscale control of temperature operation ranges for magnetocaloric applications*, J. Phys. D: Appl. Phys. **54**, 304003 (2021).

[40] Y. Maeda, K. Takei, and D. J. Rogers, *Detection of Compositional Separation in Co-Ru Alloy Magnetic Films*, Jpn. J. Appl. Phys. **32**, 4540 (1993).

[41] O. Idigoras, P. Vavassori, J.M. Porro, and A. Berger, *Kerr microscopy study of magnetization reversal in uniaxial Co-films*, J. Magn. Magn. Mater. **20**, L57-L60 (2010).

[42] O. Idigoras, A. K. Suszka, P. Vavassori, P. Landeros, J. M. Porro, and A. Berger, *Collapse of hard-axis behavior in uniaxial Co films*, Phys. Rev. B **84**, 132403 (2011).

[43] O. Idigoras, A. K. Suszka, P. Vavassori, B. Obry, B. Hillebrands, P. Landeros, and A. Berger, *Magnetization reversal of in-plane uniaxial Co films and its dependence on epitaxial alignment*, J. Appl. Phys. **115**, 083912 (2014).

[44] O. Idigoras, U. Palomares, A. K. Suszka, L. Fallarino, and A. Berger, *Magnetic properties of room temperature grown epitaxial* $Co_{1-x}Ru_x$*-alloy films*, Appl. Phys. Lett. **103**, 102410 (2013).

[45] W. Yang, D. N. Lambeth, and D. E. Laughlin, J. Appl. Phys. **85**, 4723 (1999).

[46] L. Fallarino, B. J. Kirby, M. Pancaldi, P. Riego, A. L. Balk, C. W. Miller, P. Vavassori, and A. Berger, Magnetic properties of epitaxial CoCr films with depth-dependent exchange-coupling profiles, Phys. Rev. B **95**, 134445 (2017).

[47] E. C. Stoner and E. P. Wohlfarth, *A mechanism of magnetic hysteresis in heterogeneous alloys*, Philos. Trans. R. Soc. London **240**, 599 (1948).

[48] E. R. Callen and H. B. Callen, *Anisotropic Magnetization*, J. Phys. Solids **16**, 310 (1960).

[49] L. Fallarino, P. Riego, B. J. Kirby, C. W. Miller, and A. Berger, *Modulation of Magnetic Properties at the Nanometer Scale in Continuously Graded Ferromagnets*, Materials **11(2)**, 251 (2018).

[50] A. Arrott & J. E. Noakes, *Approximate Equation of State For Nickel Near its Critical Temperature*, Phys. Rev. Lett. **19**, 786 (1967).

[51] K. Binder and D. P. Landau, *Crossover Scaling and Critical Behavior at the "Surface-Bulk" Multicritical Point*, Phys. Rev. Lett. **52**, 318 (1984).

[52] S. Langridge, G.M. Watson, D. Gibbs, J. J. Betouras, N. I. Gidopoulos, F. Pollmann, M.W. Long, C. Vettier, and G. H. Lander, *Distinct Magnetic Phase Transition at the Surface of an Antiferromagnet*, Phys. Rev. Lett. **112**, 167201 (2014).

[53] J. S. Salcedo-Gallo, L. Fallarino, J. D. Alzate-Cardona, E. Restrepo-Parra, and A. Berger, *Monte carlo simulations of the thermodynamic behavior of exchange graded ferromagnets*, Phys. Rev. B **103**, 094440 (2021).

[54] D. Belitz, T. R. Kirkpatrick, and R. Saha, *Criticality in Inhomogeneous Magnetic Systems: Application to Quantum Ferromagnets*, Phys. Rev. Lett. **99**, 147203 (2007).

[55] I. L. Prejbeanu, M. Kerekes, R. C. Sousa, H. Sibuet, O. Redon, B. Dieny, and J. P. Nozières, *Thermally assisted MRAM*, J. Phys.: Condens. Matter **19**, 165218 (2007).

[56] D. Weller, G. Parker, O. Mosendz, E. Champion, B. Stipe, X.Wang, T. Klemmer, G. Ju, and A. Ajan, *A HAMR media technology roadmap to an areal density of 4 Tb/in*^{2}, IEEE Trans. Magn. **50**, 1 (2014).

Chapter 4: Magnetic Devices with Exchange-Graded Ferromagnetic Thin Films

In this chapter of the thesis, a novel exchange-graded profile (EGP) is devised in which separate FM portions of the film exhibit a temperature dependent interaction with each other over certain intermediate temperature ranges. Hereby, SQUID magnetometry measurements of epitaxial $Co_{1-x(z)}Ru_{x(z)}$ $(10\underline{1}0)$ films exhibiting such profiles confirm the existence of strongly temperature dependent bias fields that can aid or oppose the magnetization reversal in each one of the FM regions. An atomistic mean-field model is developed for an in-depth understanding of the magnetization profiles of such films as a function of temperature. The here proposed EGP can be utilized to counteract the inherent temperature dependence of coercivity over extended temperature ranges.

4.1 Introduction: EGPs for Magnetic Devices

In Chapter 3, the concept of exchange-graded ferromagnetism has been introduced. The characteristic feature of an exchange-graded ferromagnetic thin film is a gradual change in the local exchange coupling strength along certain direction, such as its depth. Such specifically designed gradual changes lead to the formation of ‘local’ Curie temperature distributions $T_C^{loc}(z)$ [1, 2, 3]. Hereby, at finite temperatures T, the ferromagnetic layer can exhibit separate quasi-PM and FM regions whose effective interfaces occur at depths where $T = T_C^{loc}(z)$ [4].

The key aspect for the formation of separate PM and FM regions is that the depth dependent magnetization profiles can exhibit spatial variations down to the 1-2 nm length-scales, despite the fact that ferromagnetism is a long-range collective phenomenon [1]. This way, the design of particular $T_C^{loc}(z)$ profiles allows to tune specific aspects of FM, such as the equilibrium critical exponents, that are otherwise very difficult or effectively impossible to control [4, 5]. Furthermore, the control of such magnetic properties in the thin films can be of potential technological relevance [6].

This connects with modern electronic and spintronic devices relying on the magnetic states of separate magnetic layer such as in magnetic-tunnel-junction (MTJ) technologies [7, 8]. In spin-orbit torque (SOT) and spin-transfer-torque (STT) magnetic random-access memories (MRAM), for example, relatively high current densities are generally required to switch the magnetic free layer [9, 10, 11]. This, in turn, can lead to relevant self-heating effects, including in devices of ever-decreasing size [12, 13, 14, 15], which can subsequently lead to substantial modifications of the device's ferromagnetic properties. In particular, self-heating effects can influence the magnetization-reversal thresholds that furthermore require overdrive margins to ensure the switching over the entire certified temperature range of operation [16, 17]. Thus, such magnetic devices need to account for the temperature dependence of M in their devices, as well as the subsequent T dependent interactions.

In this regard, while the profile explored in the previous section exhibited a single FM region for decreasing temperatures, more complex $T_C{}^{loc}(z)$ profiles can lead to the formation of separate FM regions over significant temperature ranges, that could, furthermore, interact with each other. Therefore, exchange-graded ferromagnetism offers an excellent framework to explore novel thin film geometries, potentially with improved performances. Such geometries could aid the achievement of stable operation points over extended temperature ranges.

In this chapter of the thesis, one such EGP is devised, with the particular purpose of achieving strongly temperature dependent interactions between FM region in the film in specifically designed T-ranges. For this purpose, a complex $T_C{}^{loc}(z)$ profile is constructed such that, at intermediate temperatures, a FM/PM/FM trilayer can be generated, and in which the effective thickness of the PM regions depends on the temperature. Such profiles will be shown to for such temperature dependent interactions, that allow to compensate the temperature dependence of coercivity over an extended T-range [18].

4.2 Motivation: EGP Description

As explained in the introduction, the EGP profile utilized in Chapter 3 leads to a single FM region in the central portion of the film. For the purpose of investigating the possible interactions between FM regions in the film, a the $T_C^{loc}(z)$ profile has to be designed such that separate FM/PM/FM regions can be generated, at least in a significant temperature range. In the work here, the FM regions are designed such that their magnetic behaviors can be disentangled from each other, given that SQUID magnetometry allows only for an analysis of the total magnetic moment in the film.

Following the aforementioned strategy to create thin films exhibiting temperature independent coercivity, EGPs of the type schematically shown in Fig. 4.1 have been devised in this work. Here, the T_C^{loc} profile is shown as a function of film depth z, which is composed of three different segments. First, a base FM layer is a homogeneous film with large ordering temperature $T_C^{loc} = T_C^B$. The second layer is composed of an EGP structure of thickness d and whose T_C^{loc} decreases linearly from T_C^B to $T_C^G < T_C^B$. Finally, the film has a top homogeneous layer with a constant intermediate $T_C^{loc} = T_C^T$, such that $T_C^G < T_C^T < T_C^B$.

Let us have a preliminary look at the magnetic behavior expected in such film design within the local Curie temperature picture, extensively described in Chapter

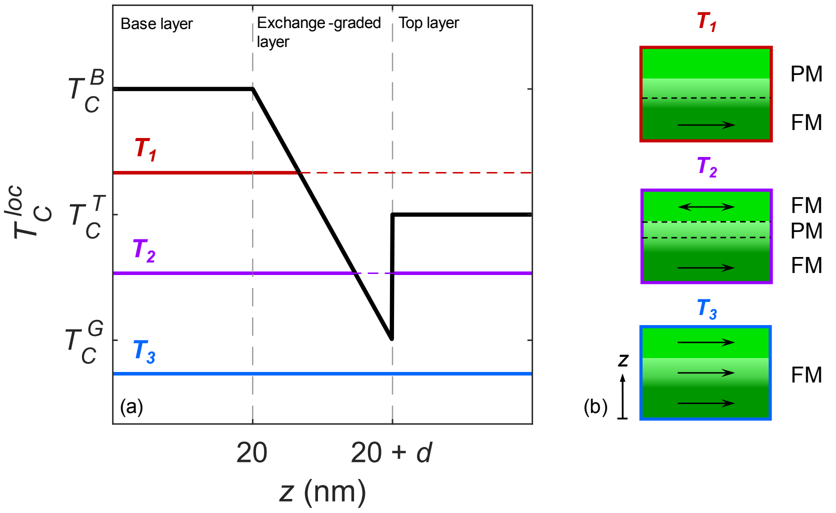

Figure 4.1: (a) Schematic of the particular $T_C^{loc}(z)$ profile under research composed of base and top layers with constant T_C^{loc} separated by a film with an exchange-graded profile. Colored lines indicate FM (solid) and PM (dashed) regions in the film at three distinct temperatures. (b) Schematic of the cross-sections of the films, showing the expected magnetic behaviors.

3. At a certain temperature T_1 such that $T_C^B > T_1 > T_C^T$, symbolized in red in Fig. 4.1, only the base and part of the intermediate exchange-graded layer will be in its FM phase. Accordingly, the magnetic behavior of such FM region should be that of a rather conventional FM phase, also exhibiting a rather conventional single layer behavior and magnetization reversal [4, 5]. At sufficiently low temperatures $T_3 < T_C^G$, shown in blue in Fig. 4.1, the entire film should be in its FM state and exhibit a collective magnetization reversal as well. This is true regardless of the non-homogeneous exchange profile, because $T < T_C^{loc}(z)$ for all depths z.

However, at intermediate temperatures $T_C^T < T_2 < T_C^G$, shown in purple in Fig. 4.1, the film is designed to exhibit two relevantly separated FM regions whose magnetization components should be mostly independent from each other. Here, however, the two separated FM regions at $T = T_2$ could in principle interact with each other due to proximity effects [19, 20]. Hereby, such interaction between FM regions should strongly depend on the thickness and properties of the PM spacer region, and thus also on its precise temperature [21, 22, 23]. Furthermore, the gradient nature of $T_C^{loc}(z)$ should lead to a continuous temperature dependent change in the effective thickness of the PM portion separating both FM phases. Thus, the influence of the FM portions onto each other can be expected to be strongly temperature dependent.

In order to achieve such magnetic behavior, once again $Co_{1-x(z)}Ru_{x(z)}$ $(10\underline{1}0)$ thin films will be fabricated, as explained in Chapter 3. Here as well, the choice of this particular alloy combination is due to basically linearly decreasing $T_C(x)$ dependence and the laterally uniform magnetic states, that make the only degree of complexity in the structure the EGP profile. The specific fabrication methods of thin films exhibiting such complex EGPs are shown in Section 4.3. In Section 4.4, the results regarding the magnetic behavior of these EGP are discussed. These include, firstly, the quantification of the interaction between FM portions in the film, both experimentally and theoretically, discussed in Sections 4.4.1 and 4.4.2, respectively. Then, a particular application of this type of FM thin film geometries is discussed in Section 4.4.3, namely, achieving temperature independent coercivity over an extended temperature range [18].

4.3 Experimental Methods & Samples Fabrication

Following the strategy of Chapter 3, in order to fabricate samples with $T_C^{loc}(z)$ profiles, epitaxial $\mathrm{Co}_{1\text{-}x(z)}\mathrm{Ru}_{x(z)}$ $(10\underline{1}0)$ alloy films are fabricated following a specific $x(z)$ profile, where the concentration x of Ru is varied along the growth direction z. Such fabrication is based on the preliminary studies in homogeneous $\mathrm{Co}_{1\text{-}x}\mathrm{Ru}_x$ $(10\underline{1}0)$, shown also in Chapter 3, in conjunction with Fig. 3.3. These preliminary studies show that T_C decreases in a nearly linear manner as a function of x due to the corresponding decrease in the effective exchange coupling constant [24, 25, 26]. The subsequent $T_C(x)$ dependence allows to accurately design the $T_C^{loc}(z)$ profile in these films, as shown in Fig. 4.2(a).

Hereby, the base layer has been chosen to exhibit a high Curie temperature $T_C^B = 600$ K, such that its magnetic state is fairly constant in the temperature range of $T = 100$ - 300 K [18]. In addition, the films are designed to have $T_C^T = 225$ K and a $T_C^G = 150$ K so that its temperature evolution in the different magnetic regimes can be well observed in the SQUID magnetometer[13].

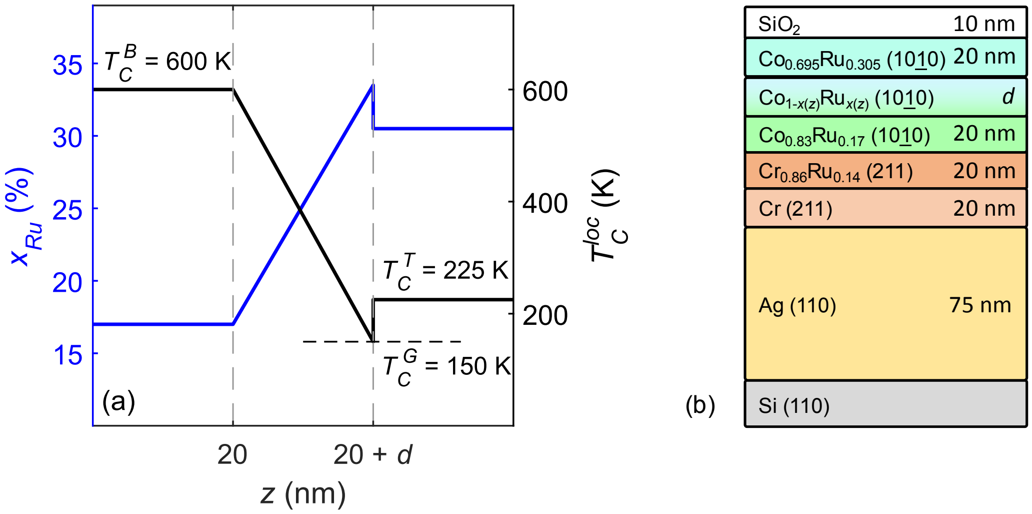

Figure 4.2: (a) Ru concentration x profile as a function of the film depth z in the specifically designed films, shown in blue, and associated T_C^{loc} distribution in black. (b) Schematic of the specific multilayer sequence for the epitaxial growth of the $\mathrm{Co}_{1\text{-}x(z)}\mathrm{Ru}_{x(z)}$ $(10\underline{1}0)$ films

---

[13] The base layer contains an additional 5% Pt content that enhances the overall anisotropy in this FM portion of the film and, hereby, its coercivity. This allows to completely disentangle the magnetization reversal of the two FM portions at intermediate temperatures.

As in Chapter 3, in this work as well epitaxial Co-Ru $(10\underline{1}0)$ alloy thin films are utilized, which exhibit a strong in-plane uniaxial magnetic anisotropy that favors the formation of an easy magnetization axis (EA) along the [0001] direction within the surface plane [24, 25]. Consequently, magnetostatic interactions are essentially immaterial, and laterally uniform magnetization states occur, which enable a quantitatively accurate interpretation of macroscopy magnetization behavior [24, 25]. In such epitaxial films with strong in-plane uniaxial anisotropy, one commonly observes abrupt magnetization reversals as a function of the applied field in conventional magnetometer measurements, which are triggered by the formation of nucleation domains and progress subsequently via rapid domain-wall propagation [27, 28, 29].

Fig. 4.2(b) shows the specific multilayer sequence employed for the epitaxial growth of the $Co_{1-x(z)}Ru_{x(z)}$ $(10\underline{1}0)$ films. All the samples are fabricated by means of sputter-deposition (see Chapter 2). On top of HF-etched oxide-removed Si (110) wafers, a specific underlayer sequence is grown composed of 75 nm Ag (110), 20 nm Cr (211) and 20 nm $Cr_{0.86}Ru_{0.14}$ (211) films [24, 25, 30], that allows for the high-quality epitaxial growth of magnetic $Co_{1-x(z)}Ru_{x(z)}$ $(10\underline{1}0)$ film. 10-nm-thick SiO_2 overcoat layers serve as capping layers to protect the $Co_{1-x(z)}Ru_{x(z)}$ films from oxidation. The alloy layers in the entire multilayer structure are fabricated by co-sputter deposition. Particularly in the case of CoRu, the deposition rate of Co is adjusted during growth to facilitate the growth profile shown in Fig. 4.2(a). Here, samples with different thicknesses d of the exchange-graded layer are fabricated, which will allow for a quantitative analysis on the magnetic interactions between the two FM regions at intermediate temperatures. The actual fabrication of the $Co_{1-x(z)}Ru_{x(z)}$ profile is composed of homogeneous Co-Ru layers with thicknesses ranging 0.5-2 nm, depending on the total thickness of the EGP.

Fig. 4.3 shows the structural analysis conducted for several of these films with different d, which is fundamentally identical to the analysis conducted in Chapter 3. Fig. 4.3(a) shows X-ray diffraction (XRD) θ-2θ scans for each of the so-fabricated films representing different values of thicknesses d for the graded coupling layer. A reference sample without top magnetic layer and $d = 20$ nm has also been fabricated to elucidate the top layer's role in the overall behavior of the EGP films. In Fig. 4.3(a), only the diffraction peaks corresponding to the intended crystallographic

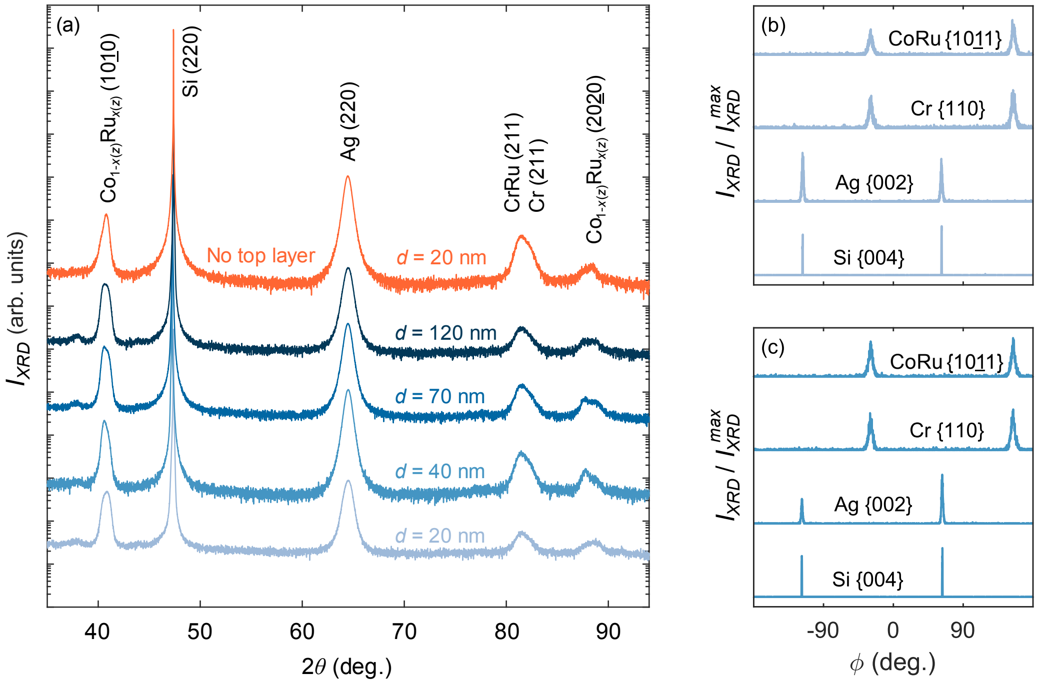

Figure 4.3: (a) XRD θ-2θ scan of several simples with different thickness d ranging from 20 - 70 nm and a reference sample without top layer for d = 20 nm showing the indexed peaks of each of the crystallographic planes of the films only. (b, c) XRD azimuthal scans at the 2θ poles of the Si {004}, Ag {002}, Cr {110}, and CoRu {10$\underline{1}$1} for the d = 20 and 40 nm samples, respectively.

planes for each of the deposited layers are observed. The presence of the CoRu (20$\underline{2}$0) second-order peaks and the absence of peaks corresponding to other crystallographic orientations verify the high quality epitaxial grown of the entire EGP film samples. The peaks corresponding to the CoRu (10$\underline{1}$0) and CoRu (20$\underline{2}$0) show a certain level of broadening and/or splitting due to the continuous alloy composition induced modification of the lattice spacing along the depth of the film, which is another good indication that the epitaxy is maintained throughout the entire depth [2, 3]. Given that the maximum and minimum Ru concentrations are kept constant in all films, no relevant shift is expected for these peaks as a function of d, which is exactly what is observed in Fig. 4.3(a).

For the purpose of unambiguously verifying the epitaxial grown of the Co$_{1-x(z)}$Ru$_{x(z)}$ films, azimuthal XRD ϕ-scans are conducted, which allow to verify the relative crystal orientations between layers. Figs. 4.3(b, c) show two exemplary XRD azimuthal ϕ-scans for the samples with d = 20, 40 nm, respectively. These measurements are performed at crystal planes that are not perpendicular to the film surface, which provides information about the in-plane crystal structure and relative orientations in between layers in our films, as explained in Chapter 3. In Figs. 4.3(b, c), the X-ray intensity, normalized to the maximum value in each corresponding measurement is shown. All the ϕ-scans show two well defined peaks that are 180º apart and whose positions match the stereographic projections of their nominal structure [2, 30]. The Si {004} and Ag {002} scans indicate a parallel alignment of the Si and Ag [001] directions. The 90º angular shift between the Ag and Cr/CrRu peaks indicate that the Cr [1$\underline{1}$0] direction is parallel to the Ag [001] direction, as intended. Finally, the CoRu {10$\underline{1}$1} peaks appear at the same ϕ-values as those for Cr/CrRu {110}, confirming the in-plane alignment of the CoRu [0001] direction, parallel to the Cr/CrRu [1$\underline{1}$0] direction and thus unambiguously verifying the epitaxial nature of our films.

4.4 Results & Discussion

4.4.1 Temperature Dependent Exchange-Bias Fields

In order to quantify the thermodynamic behavior of the specifically fabricated $Co_{1-x(z)}Ru_{x(z)}$ $(10\underline{1}0)$ films, temperature dependent magnetometry measurements are conducted using a superconductive quantum interference device (SQUID) (see Chapter 2). Here, hysteresis loops measurements are conducted in the temperature range of $T = 100$ - 300 K. Specifically, the magnetization component parallel to the field is measured, which is applied in-plane and parallel to the magnetic EA of the samples.

In Fig. 4.4, three hysteresis loops at different temperatures are shown exemplarily for the sample with d = 20 nm. In Figs. 4.4(a, c), a nearly perfect square-like hysteresis loops at T = 100 and 280 K are observed, respectively, showing a single abrupt magnetization reversal at H_c as one would expect for a conventional uniaxial magnetic film along its EA. In Fig. 4.4(a), the complete structure exhibits a FM state at all depths because $T < T_C{}^G$, equivalent to the case of T_3 in Fig. 4.1(a). A substantial decrease of the total magnetic moment in Fig. 4.4(c) is noticeable, which is due to the fact that a large portion of the film is not ferromagnetic at T = 280 K. Here, only the base layer and part of the graded coupling layer are in a FM state because $T_C{}^T < T < T_C{}^B$. Therefore, the film shows typical single film behavior for these two different temperature regimes, even if $T_C{}^{loc}(z)$ is not constant [4, 5].

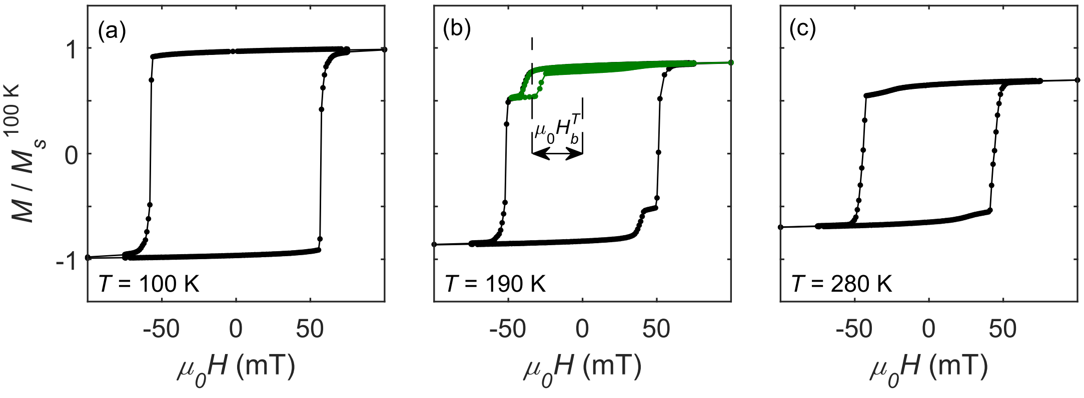

Figure 4.4: Exemplary normalized hysteresis loops measured for the d = 20 nm EGP sample at (a) T = 100 K, (b) 190 K and (c) 280 K, respectively. The green line in (b) represents a minor hysteresis loop, exhibiting a strong bias field $H_b{}^T$ onto the top layer.

At intermediate temperatures, however, shown in Fig. 4.4(b), instead of a single abrupt M reversal process, one observes a two-step reversal. This double step is due to the independent switching of two separated FM regions at intermediate temperatures, as explained in conjunction with Fig. 4.1(a). The first small step corresponds to the reversal of the top layer alone, which is ferromagnetically ordered at this temperature, and whose contribution to the total moment is smaller given that this portion of the film has a T_C^{loc} closer to T. The larger step corresponds then to the reversal of the base FM layer and the adjacent part of the graded coupling layer that is ferromagnetically ordered as well.

In order to test for possible exchange coupling in between the two separate ferromagnetic segments of our EGP films at intermediate temperatures, minor hysteresis loops of the top magnetic layer only are conducted, as shown comparatively in green in Fig. 4.4(b). For this purpose, as starting point, sufficiently high positive H are applied and then decreased down to a certain negative H-value, at which only the top FM layer has switched. Then, the field is increased again to observe the full hysteretic behavior of the top FM layer only. In the minor hysteresis loop of Fig. 4.4(b), one can clearly observe that the hysteresis loop of the top region is shifted with respect to $H = 0$, which verifies the existence of a significant bias field H_b^T acting on the top FM layer only, and which is mediated by the paramagnetic state of the interlayer. This behavior is in accordance with the intended magnetic properties of this specific EGP film structure. It is important to also highlight that the reversal of the FM portion of the graded coupling layer cannot be resolved on its own with our SQUID magnetometer, given that it forms a collective FM state jointly with the bottom FM layer, in the very same way, in which the top layer forms a collective FM state with the rest of the film at sufficiently low temperatures ($T < T_C^G$), at which a full depth correlation of the FM state is established.

Following this procedure, full hysteresis and minor loop measurements are conducted in the entire relevant T-range, that is 100-300K, every 2K in these films. Fig. 4.5(a-c) shows the hysteretic behavior of samples with different thicknesses at $T = 0.9\ T_C^T$. In all the cases, one can observe the two-step magnetization reversal, due to the separate switching of the two different FM regions. The relative size of the reversal of the top layer decreases for increasing thickness d, as the relative

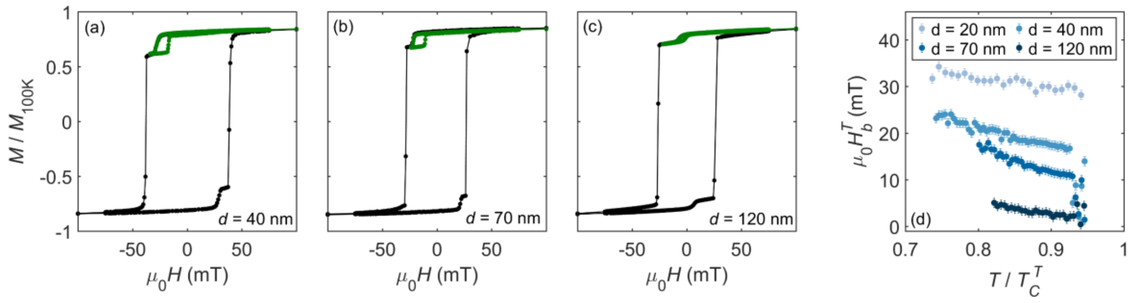

Figure 4.5: (a-c) M vs H hysteretic behaviors of three different samples with different thickness of the graded-layer d at $T = 0.9\ T_C{}^T$. The green lines correspond to the minor loop measurements at the same temperature. (d) $H_b{}^T$ vs. T behavior for several samples with different thicknesses d.

volume of the bottom FM region becomes larger. More relevant though, one can observe in the minor loop measurements, shown in green, the existence of non-zero $H_b{}^T$ acting onto the top FM region in all the cases. Furthermore, in the same relative temperature, such effective bias field seems to be of decreasing magnitude for increasing thickness of the exchange-graded layer.

Fig 4.5(d) shows the $H_b{}^T$ data as a function of T, normalized to $T_C{}^T$, obtained from the minor loop measurements, normalized to the ordering temperature of the top layer. Each individual film with different thickness d shows a monotonously decreasing $H_b{}^T$ for increasing T. Furthermore, for increasing thickness d, the bias field acting onto the top FM region becomes smaller. These results are in excellent qualitative agreement with the intended magnetic behavior of this specifically designed film structure. As the temperature is decreased, the effective thickness of the quasi-PM region decreases. This, in turn, enhances the interaction between FM regions and, therefore, the effective bias field acting onto the top layer. If the thickness d of the exchange-graded layer becomes now larger, then, the overall interaction between FM regions will decrease as well.

For higher T close enough to $T_C{}^T$, the reversal of the top FM region cannot be disentangled from the total moment of the film in an accurate manner, given the moment of the top region is very small. On the other hand, at relevantly lower temperatures, the entire film exhibits a single FM region, and thus, switches synchronously for sufficiently large opposite fields, and no bias field can be determined anymore by means of magnetometry measurements.

4.4.2 Theoretical Comparison and Mean-Field Model

In order to aid an in-depth understanding of these experimental results, an atomistic mean-field model is considered with local spin vectors. Here, following the properties of the epitaxial Co$_{1\text{-}x(z)}$Ru$_{x(z)}$ $(10\underline{1}0)$ thin films, an anisotropic Heisenberg model is used, with the total Hamiltonian of the system being,

$$\mathcal{H} = -\sum_{\{i,j\}} J_{ij}\, \boldsymbol{s}_i \boldsymbol{s}_j + \sum_{i} \boldsymbol{k}_1 [1 - (s_i^x)^2] - \mu_0\, \mu \sum_{i} \boldsymbol{H}_i\, \boldsymbol{s}_i. \tag{4.1}$$

Here, the first energy term in eq. (4.1) is the exchange energy with exchange coupling constant J_{ij} between nearest-neighbors dimensionless spin vectors $\boldsymbol{s}_i$. In this model, J_{ij} remains homogeneous in the plane of the film, but varies along the depth z to reproduce the behavior of the EGP. The second energy term is the first-order uniaxial magnetic anisotropy along the in-plane $\hat{\boldsymbol{x}}$ direction, with anisotropy energy per moment k_1. Here, k_1 is assumed to be concentration independent and, thus constant, along the film depth. The third energy term corresponds to the Zeeman energy, acting on each moment with modulus μ. Such moment μ is also assumed to be constant along the film depth, which corresponds to a simplification given that the saturation moments change with the composition in real thin films. Following the hcp Co-Ru $(10\underline{1}0)$ lattice structure, here $n_{hcp} = 12$ nearest neighbors are considered, with $n_l = 4$ neighboring atoms corresponding to each layer; 4 neighbors in the layer bellow, 4 in-plane and 4 on the layer on top.

In this mean-field calculation, an expansion as $\boldsymbol{s}_i = \langle \boldsymbol{s}_i \rangle + \delta \boldsymbol{s}_i$ is considered, where $\delta \boldsymbol{s}_i$ are the spin-fluctuations and $\langle \boldsymbol{s}_i \rangle$ is the thermodynamic average of $\boldsymbol{s}_i$, which is proportional to $\boldsymbol{M}$. Then, the second-order fluctuation terms $O(\delta s_i\, \delta s_j) \sim O(\delta s^2)$ are neglect such that,

$$\boldsymbol{s}_i \boldsymbol{s}_j \approx -\langle \boldsymbol{s}_i \rangle \langle \boldsymbol{s}_j \rangle + \langle \boldsymbol{s}_i \rangle \boldsymbol{s}_j + \langle \boldsymbol{s}_j \rangle \boldsymbol{s}_i, \tag{4.2}$$

$$(s_i^x)^2 \approx -\langle s_i^x \rangle^2 + 2\, \langle s_i^x \rangle s_i^x. \tag{4.3}$$

Considering in-plane translational invariance only, and rearranging the energy terms, one can obtain the mean-field Hamiltonian of form,

$$\begin{aligned} \mathcal{H}_{MF} = \frac{N n_l}{2} \sum_m [J^e_{m\text{-}1}\, \langle \boldsymbol{s}_{m\text{-}1} \rangle + J_m\, \langle \boldsymbol{s}_m \rangle + J^e_m\, \langle \boldsymbol{s}_{m+1} \rangle] \langle \boldsymbol{s}_m \rangle \\ + N \sum_m K_1 [1 + \langle s_m^x \rangle^2] - \mu_0\, \mu N n_l \sum_m \boldsymbol{H}_{eff,\, m}\, \boldsymbol{s}_m. \end{aligned} \tag{4.4}$$

Here, N represents the number of in-plane atoms and m is now a layer index, with $\boldsymbol{s}_m$ being the spin at the mth layer. The exchange energy terms $J^e_m = [J_m + J_{m+1}]/2$

represent the exchange coupling corresponding to interlayer atoms that are not in the plane of the film, whereas J_m corresponds to the interaction between intralayer atoms. The mean effective-field in the mth layer $\boldsymbol{H}_{eff,m}$ is then,

$$\mu_0 \mu \boldsymbol{H}_{eff,\ m} = -n_l[J^e_{m-1}\ \langle \boldsymbol{s}_{m-1}\rangle + J_m \langle \boldsymbol{s}_m\rangle + J^e_m \langle \boldsymbol{s}_{m+1}\rangle] - 2K_1\langle \boldsymbol{s}_m\rangle\hat{x} - \mu_0 \mu \boldsymbol{H}_m, \qquad (4.5)$$

owning the mean-field Hamiltonian of eqs. (4.4-4.5), one can calculate the free-energy density per unit area of the system as,

$$\mathcal{F} = \mathcal{H}_0 - k_B T \sum_{\mathrm{m}} \log\left\{\frac{\sinh\left(\mu_0 \mu \left|\boldsymbol{H}_{eff,\ m}\right| / k_B T\right)}{\mu_0 \mu \left|\boldsymbol{H}_{eff,\ m}\right| / k_B T}\right\}, \qquad (4.6)$$

with $\mathcal{H}_0$ being a function independent of $\boldsymbol{H}_{eff,\ m}$. Details regarding the evaluation of $\mathcal{F}$ can be found in Appendix B. Now, the magnetization component ς in cartesian coordinates of the mth layer is obtained as,

$$\frac{M^\varsigma_m}{M^0_s} = \langle s^\varsigma_m\rangle = \frac{\partial \mathcal{F}}{\partial\left(\mu_0 H^\varsigma_m\right)} = \mathcal{L}\left[\frac{\mu_0\ \mu\left|\boldsymbol{H}_{eff,\ m}\right|}{k_B T}\right] \frac{H^\varsigma_{eff,\ m}}{\left|\boldsymbol{H}_{eff,\ m}\right|}, \qquad (4.7)$$

where $\mathcal{L}(\mathrm{x}) = \coth(\mathrm{x}) - 1/\mathrm{x}$ is the Langevin function. In this mean-field model, the magnetization vector of each layer depends on the magnetization vectors of the adjacent layers through $\boldsymbol{H}_{eff,m}$. It is also relevant to mention that, if J would be constant along the film depth, then, translational invariance along z could be applied as well and, therefore, one would recover the mean-field expression of the thermodynamic equilibrium behavior of a conventional ferromagnet [31]. Further details regarding the evaluation of this mean-field model can be found in Appendix B.

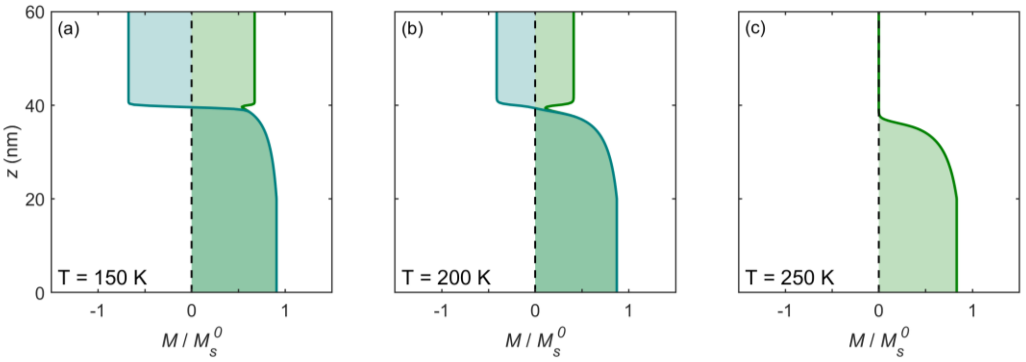

Figure 4.6: Magnetization component parallel to the x-axis along the film depth z obtained by means of the mean-field model at three different temperatures in the three relevant temperature regimes with $\boldsymbol{H} = 0$. The green profile corresponds to an entirely parallel magnetic state, whereas the blue profile antiparallel states of the two FM regions.

Fig. 4.6 show the $M(z)$ profiles of the component parallel to the EA (x-axis) in a thin film with $d = 20$ nm with $\boldsymbol{H} = 0$, and in three exemplary temperatures corresponding to the three characteristic temperature regimes in the film. The calculations are conducted assuming the $J(z)$ profile required to obtain the same $T_C^{loc}(z)$ as the experiments (see Appendix B) and the anisotropy energy of pure Co[14]. The thickness and number of layers are obtained based on the lattice constants of pure Co as well. Fig. 4.6(a), shows in green the $M_m^x(z)$ profile with entirely parallel magnetization state. Firstly, in absence of external field, the entire magnetization profile will order parallel to the EA. Indeed, for the entire set of measurements here conducted $M_m^y(\mathrm{z})$, $M_m^z(\mathrm{z}) = 0$. Here, one observes that the entire structure exhibits long-range ordering even if M changes relevantly along the depth. At intermediate temperatures, shown in Fig. 4.6(b), one observes the formation of two rather separate FM regions, even if in the quasi-PM region, M does exhibit a non-zero ordering due to the proximity of the adjacent FM layers, as expected. At larger temperatures, in Fig. 4.6(c), the top layer is not in a FM state anymore because here, $T > T_C^{loc}(z) = T_C^T$.

At temperatures in which the top layer is in a FM state, namely $T < T_C^T$, one can form $M(z)$ states in which both FM regions are antiparallel, as shown in Figs. 4.6(a, b) by means of the solid blue profiles. This is also true for even lower temperatures, in which the entire structure is FM, and thus, the antiparallel states lead to the formation of an in-plane domain-wall[15]. While not energetically favorable, such formation of domain-walls is possible because the local energy minimum is theoretically stable if the system is initially forced into it.

Then, the change in Zeeman energy onto the top layer, can be obtained from the free energy difference between the parallel $\mathcal{F}_P$ and antiparallel $\mathcal{F}_{AP}$ states as [32],

---

[14] While this is a significant simplification, the here conducted calculations are done in $\boldsymbol{H} = 0$ conditions, such that $\boldsymbol{M}$ aligns parallel to the EA at all depths in order to minimize the anisotropy energy, regardless of the magnitude of k_1.

[15] The stability of this solution to equation (4.7) has been verified in several different ways at all temperatures.

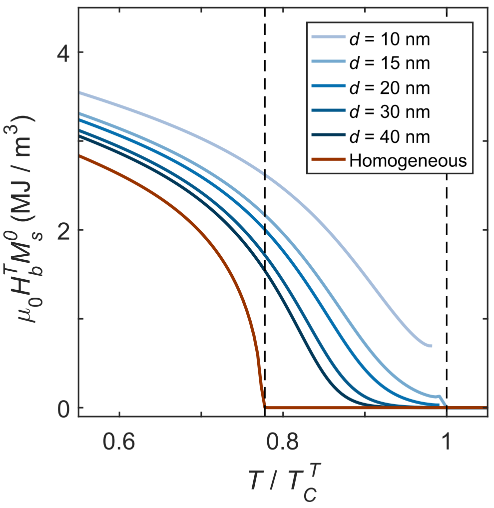

Figure 4.7: (a) Effective H_b^T as a function of T obtained with the atomistic mean-field model, for different thicknesses of the graded-coupling layer. The dark-red line corresponds to a system in which the intermediate layer has a constant $J(z)$, with $T_C^{loc}(z) = T_C^G$ for all intermediate depths.

$$\Delta\mathcal{F} = \mathcal{F}_{AP} - \mathcal{F}_P \approx 2\ d_T \mu_0 H_b^T M_T, \tag{4.8}$$

where d_T and M_T are the thickness and magnetization of the top layer, respectively. Hereby, M_T is obtained as $M_T = M_s^0 \langle \boldsymbol{s}_T \rangle$, with M_s^0 being the maximum magnetization per unit volume. This analysis provides a tool to extract the H_b^T bias fields acting onto the top layer. Fig. 4.7 shows the energy equivalent of H_b^T as a function of temperature for several thicknesses of the graded-coupling layer. The data are presented in energy density units considering homogeneous M_s^0 along the depth of the film. In all these cases, one verifies the existence of a gradual increase on the effective bias field acting onto the top layer. Furthermore, the magnitude of H_b^T decreases for increasing thicknesses d, in agreement with the experimental results in Fig. 4.5. This is because, as the thickness d of the graded-layer increases, the interaction between top and bottom FM regions decreases monotonously.

To show that such $H_b^T(T)$ temperature dependence is really due to the interaction mediated by the exchange-graded profile, Fig. 4.7, shows the effective H_b^T for the same $d = 20$ nm system compared to the H_b^T of a film without a gradient-coupling layer, and which has a homogeneous T_C^G as an intermediate layer instead. Here, one observes the fundamentally different $H_b^T(T)$ acting onto the top layer. While the effective interaction between both FM regions increases with decreasing temperatures in the EGP, the trilayer will exhibit a FM/PM/FM whose effective thickness of the PM region will remain constant. Furthermore, given that the thickness of such PM region is relatively large, the two FM regions will be isolated from each other. Consequently, the effective bias field will only become non-zero at the ordering temperature of the intermediate layer, where the entire structure will exhibit a single FM state.

While the experimental and theoretical results agree in the qualitative behavior, one observes that the $H_b{}^T(T)$ onset in experiments at temperatures close to $T_C{}^T$ is significantly steeper than in simulations. This difference in the quantitative results might be due to the mean-field model itself, in which fluctuations are fundamentally suppressed and, therefore, the local magnetization onsets will differ from those in the real thin-films. Such difference in the $M(z,\ T)$ behaviors would lead then to different $H_b{}^T(T)$, particularly close to $T_C{}^T$. However, experimentally, at temperatures very close to $T_C{}^T$, one cannot disentangle the magnetic behavior of both FM regions because the contribution to the total moment of the top layer is very small. Another relevant approximation in this model is the assumption that all magnetic moments μ have equal magnitude, which might not be the case in the real $Co_{1-x(z)}Ru_{x(z)}$ (1010) thin films.

Despite these approximations, this relatively simple mean-field model allows one to explain accurately the general tendencies of both the magnetization profile along the depth of the film and the proximity-induced bias fields onto the top layer. The here developed theoretical modeling agrees very well with the experimentally obtained results. These results show that one can design specifically thin films with particular EGPs so that both the magnitude and temperature dependence of bias fields acting on certain layers can be controlled accurately.

4.4.3 Temperature Independent Coercivity

In the following, a particular application of the previously obtained results in temperature dependent bias fields is discussed. As explained in Section 4.1, many devices such as MTJs require stable operation points of both the read and write cycles. This can be a challenging task since, in general, coercivity in ferromagnets is a strongly temperature-dependent quantity. Indeed, H_c relies on thermal activation processes that trigger the first-order phase transition of magnetization reversal. Consequently, many approaches are generally considered to suppress, or reduce, the $H_c(T)$ dependence for applications that require specific target values for operations. Such approaches include microstructure modifications via material substitutions [33, 34, 35] or the already discussed exchange-spring-media designs (see Section 3.1) [36, 37, 38, 39]. However, some of these specific materials engineering relies on very specific material choices, that constrain their broadband applicability in real devices. Thus, novel methodologies are still required to suppress or control the temperature dependence of coercivity over extended temperature ranges with flexible material choices.

This particular need connects with the here explored EGPs. In such films, specific FM regions can cause effective temperature-dependent bias fields that, in principle, can allow for a complete suppression of the temperature dependence of H_c. This is exactly the phenomenon that is investigated in this particular set of EGPs. In order to show this effect, full hysteresis loops are measured every 2K in the SQUID magnetometer for the here explored films.

Fig. 4.8(a) shows as a color-coded map the decreasing field branch of the hysteresis loop in the $d = 20$ nm film. In this color map, one identifies an abrupt magnetization reversal at sufficiently large negative H for all temperatures. Such abrupt change in M is represented in the color map by the narrow light-yellow regions, corresponding to $M = 0$, and which separates the positive (red) and negative (blue) magnetization values. For intermediate temperatures, one can also identify a red-to-orange transition, which represents the magnetization-reversal step of the top layer, as explained in conjunction with Fig. 4.4(b). Consequently, the orange region of the map corresponds to the antiparallel alignment of the two separate FM regions of the film. More relevantly, in this map one can observe that the coercive field, at which sample magnetization completely inverts to negative values, does not change monotonously as a function of T. Instead, there is a very significant temperature region, in which H_c remains basically constant. Furthermore, this temperature region of constant H_c fully coincides with the temperature range over which the double step reversal happens, namely, the temperature range of 75K in which two separate FM regions are occur between $T_C{}^G$ and $T_C{}^T$.

Fig. 4.8(b), shows the experimentally determined $H_c(T)$ behavior, extracted from the data in Fig. 4.8(a) for the $d = 20$ nm sample. In addition, for comparison purposes, the behavior of the reference sample without a top layer is also shown in red. Here, one can clearly identify the very wide temperature range of constant

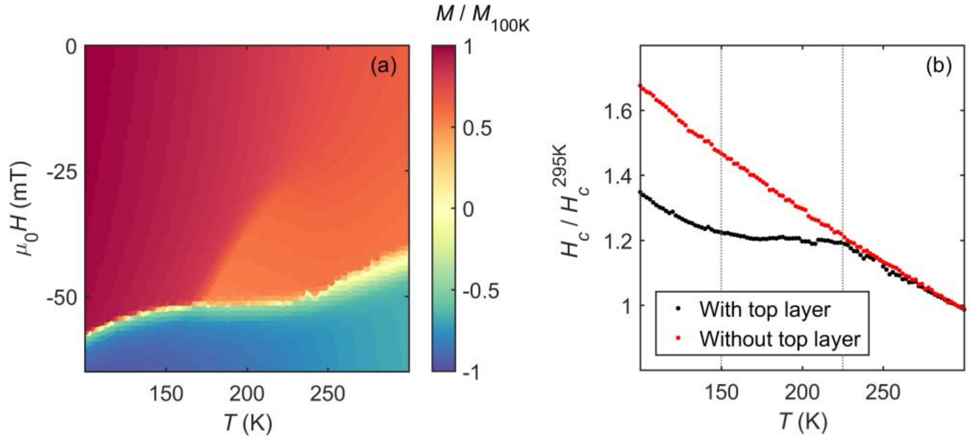

Figure 4.8: (a) Color-coded map of $M(T, H)$ in the decreasing field branch of the hysteresis loop, for the $d = 20$ nm sample. (b) Extracted H_c vs. T behavior for two samples with $d = 20$ nm with and without top layer showing the coercivity plateau.

coercivity, at intermediate temperatures, as indicated by means of the vertical dashed lines. Here, coercivity changes of less than 2% extend over a temperature range of 75 K. In contrast, the reference sample displays very conventional monotonously decreasing $H_c(T)$ behavior at all temperatures and about 20% coercivity change over the exact same temperature range. One can also notice that the EGP sample exhibits a fairly conventional $H_c(T)$ behavior outside the plateau region, namely, at low and high temperatures. These results verify that the observed constant-coercivity plateau is due to the interaction of the top FM layer with the bottom FM section of the film. Indeed, while in the Sections 4.4.1 and 4.4.2, the influence of the bottom onto the top FM regions was studied, at temperatures $T < T_{C}^{T}$, the top FM region also influences the reversal of the bottom FM region when both regions are aligned in an antiparallel state.

Fig 4.9 shows for three samples with different thickness d of the exchange-graded layer the $H_c(T)$ dependence. In all the cases one can clearly observe the slope change of the H_c vs. T behavior. Such change in slope of H_c is observable even in films with rather large thickness d, in which the interaction between FM regions should be smaller.

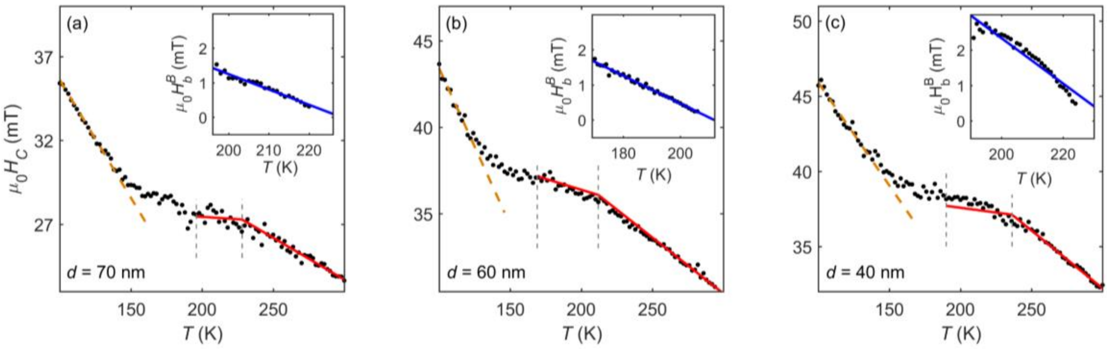

Figure 4.9: H_c vs. T behaviors of several samples with different thickness d. The dashed-orange line represents the low temperature $H_c(T)$ linear expansion. The solid-red line represents the model of eq. (4.12). The inset figures in (a-c) show the corresponding $H_b{}^B(T)$ behavior obtained by means of eq. (4.11).

In order to achieve a deeper understanding of the reversal mechanism in these EGP films, as well as their temperature dependence, a basic model is developed based on the nucleation and domain-wall expansion within the bottom FM portion of the film. Hereby, a sufficiently stable reversal domain formed by nucleation expands by means of domain-wall propagation. Such an expansion occurs on timescales that are much shorter that the measurement itself, leading to the observed sharp M vs. H switch at exactly H_c [26]. Hereby, the formation probability, P, of a stable nucleation domain triggering this magnetization reversal can be written by means of an Arrhenius law as [40],

$$P = p_0 \; e^{-E_B/k_B T}, \tag{4.9}$$

where p_0 is a temperature-independent material-specific constant and E_B is an activation-energy barrier. Hereby, E_B describes the total energy required for the formation of a sufficiently stable reversal nucleation domain of volume V_B that will trigger the reversal. In this FM/PM/FM system, E_B can be expressed as a sum of three energy terms as,

$$E_B = \varepsilon_{DW} A_{DW} - 2\mu_0 H M_B V_B - 2J_g(T) \; A_N \widetilde{M}_B \widetilde{M}_T. \tag{4.10}$$

The first term is the nucleation energy associated with the energy cost of having a domain-wall with energy density ε_{DW} and area A_{DW}. The second is the Zeeman energy gain of the nucleation domain in the bottom FM region with magnetization M_B. The third term in eq. (4.10) represents the energy contribution from the interlayer exchange coupling between the two FM regions in the film that aids for the reversal. Specifically, $J_g(T)$ is the effective interlayer exchange coupling energy density per unit area mediated by the PM region in an area, A_N, of the nucleation domain. $\widetilde{M}_B$ and $\widetilde{M}_T$ represent the magnetization of the bottom and top FM regions, respectively, normalized to their corresponding saturation.

$J_g(T)$ is a nonlinear function that depends on the effective thickness of the intermediate PM region, and thus, on the temperature. Despite this inconvenience, one can actually extract the information of this interlayer energy term from the previously obtained minor-loop measurements of the top layer, shown in Figs. 4.4 and 4.5. Indeed, the third energy term in eq. (4.10) can be represented as an effective field H_b^B acting on M_B, or equivalently, H_b^T acting on M_T, such as,

$$J_g(T) A_N \widetilde{M}_B \widetilde{M}_T = \mu_0 H_b^B M_B V_B = \mu_0 H_b^T M_T V_T. \tag{4.11}$$

Therefore, eq. (4.11) provides a relationship from which one can extract H_b^B from actual H_b^T measurements. The insets of Fig 4.9 show the determined $H_b^B(T)$ data based on the minor loop measurements of the top layer. In such inset figures, one observes the existence of a significant H_b^B acting onto the bottom FM portion of the film. Furthermore, $H_b^B(T)$ has in all the cases a strong temperature dependence that counteracts the conventional $H_c(T)$ behavior, as expected, in the temperature range in which two separate FM regions coexist. The solid-blue lines represent linear least-squares fits to the experimental data, illustrating that $H_b^B(T)$ behaves in an almost linear fashion with a slope α_b. For the different samples, it is observed as expected, that α_b in the $H_b^B(T)$ curves is larger for smaller EGP thicknesses d, because the influence of the top layer onto the bottom portion of the film will be larger for smaller thicknesses of the effective PM region. This behavior verifies that one can compensate the conventional H_c vs. T dependence at will by making a suitable design for the thickness of the graded coupling layer.

Using this model approach, one can consider that the nucleation and subsequent domain-wall expansion get triggered at $P = 1$. Thus, combining eqs. (4.9-4.11), one gets,

$$H_c(T) = H_c(T) \text{ - } \alpha T \text{ - } H_b^B(T), \tag{4.12}$$

where $H_c(0) = \varepsilon_{DW} A_{DW} / 2\mu_0 M_B V_B$ and $\alpha = k_B \ln(p_0) / 2\mu_0 M_B V_B$. M_B is only slowly varying in the 100–300 K temperature range, because $T_C^B = 600$ K is much larger than the actual temperature range of interest. Under the assumption that all geometric factors are basically temperature independent as well, the first two terms in eq. (4.12) predict an approximately linear decrease of H_c as a function of T. This is exactly the behavior observed in the reference sample, shown in Fig. 4.8(b), and also the behavior of all of our samples in the high-T and low-T regimes.

Fig. 4.9, show as red lines the model behavior of eq. (4.12). Here, a linear expansion is considered at high temperatures, representing the first two energy terms in eq. (4.12). At intermediate temperatures, where minor loops can be distinguished, the $H_b^B(T)$ data representing the third term in eq. (4.12) is added. In all the cases, the model explains the $H_c(T)$ behavior very well over the temperature range at which $H_b^B(T)$ can be quantified by means of the minor-loop measurements.

The numerical results of these fits are shown in Table 4.1. Here, the least-squares fitting results of the low- and high-temperature expansions, together with the linear fitting of the $H_b^B(T)$ curve are shown. One observes that α_b representing the slope of $H_b^B(T)$ increases for decreasing thickness of the graded coupling layer, as expected. The here presented model captures the essence of the experimentally observed behavior. Furthermore, at $d = 20$ nm, α_b is basically identical to α at high temperatures, which leads to the compensation effect that creates the coercivity plateau. These results identify the interlayer exchange coupling via the paramagnetic graded-layer portion as the key mechanism that facilitates the intended $H_c(T)$ modification and explains, in a quantitatively accurate manner, the overall magnetization reversal process. For the lowest temperatures, the complete EGP structure exhibits a strongly coupled single FM phase, leading to the reemergence of linear $H_c(T)$ behavior, as shown by the dashed orange lines in Fig. 4.9.

	High T		Bias		Low T	
d (nm)	$\mu_0\alpha$(mT/K)	$\mu_0 H_c(0)$(mT)	$\mu_0\alpha_b$(mT/K)	$\mu_0 H_b^B(0)$(mT)	$\mu_0\alpha$(mT/K)	$\mu_0 H_c(0)$(mT)
20	-0.109 ± 0.006	75 ± 1	-0.108 ± 0.008	26 ± 1	-0.13 ± 0.01	71 ± 1
40	-0.077 ± 0.005	55 ± 1	-0.064 ± 0.006	15 ± 1	-0.13 ± 0.01	60 ± 1
60	-0.065 ± 0.004	50 ± 1	-0.039 ± 0.002	8.3 ± 0.3	-0.18 ± 0.02	62 ± 2
70	-0.049 ± 0.004	38 ± 1	-0.044 ± 0.004	10.1 ± 0.9	-0.13 ± 0.01	48.5 ± 0.6

Table 4.1: Numerical results of the fitting procedures showing the $H_c(T)$ behavior in our samples at low and high temperatures, together with those of the $H_b(T)$ behavior.

4.5 Conclusions & Outlook

In this chapter, the overall magnetization behavior of a ferromagnetic thin film exhibiting a complex EGP has been investigated, both theoretically and experimentally. The here explored profile can lead to the formation of two separate FM regions at intermediate temperatures, that can furthermore interact with each other via proximity effects. Hereby, the interaction between layers is shown to be strongly temperature dependent. This strong temperature dependence can be used, in turn, to achieve temperature independent coercivities in specifically designed films.

Here, H_c changes of less than 2% over a 75-K-wide temperature plateau have been achieved, while conventional films exhibit coercivity changes of 20%. Furthermore, while the temperature region of such $H_c(T)$ plateau is chosen for experimental convenience, it can be engineered for any temperature range, so that possible applications and devices with specific temperature operation ranges can be accommodated, even at room temperature. Furthermore, the here obtained experimental results demonstrate that a wide variety of different $H_c(T)$ dependencies can be engineered by means of a suitable choice of graded-layer thickness and the specific $T_C^{loc}(z)$ profile.

Thus, this work constitutes a proof-of-concept of the capabilities of specifically designed exchange-graded ferromagnetic thin films. As discussed in Chapter 3, the here employed methodology can be utilized for many different kinds of ferromagnetic materials and applications and with a great deal of flexibility in choosing the most relevant temperature-range target. Thus, it could be interesting to explore the capabilities of such graded compositions in materials that could strongly influence the thermal stability and reliability of next-generation devices [41].

Finally, the work here, both in Chapters 3 and 4, focuses tunning the hysteretic behavior of exchange-graded ferromagnetic thin films. However, exchange-graded ferromagnetic structures are being studied as well in the dynamic regime, for applications in the channeling of spin-waves, for magnon-based devices [42, 43]. In this regard, it would be relevant to explore experimentally the spin-wave dynamics of films similar to the ones employed here.

Chapter References

[1] B. J. Kirby, H. F. Belliveau, D. D. Belyea, P. A. Kienzle, A. J. Grutter, P. Riego, A. Berger and C. W. Miller, *Spatial evolution of the ferromagnetic phase transition in an exchange graded film,* Phys. Rev. Lett. **116**, 047203 (2016).

[2] L. Fallarino, B. J. Kirby, M. Pancaldi, P. Riego, A. L. Balk, C. W. Miller, P. Vavassori, and A. Berger, *Magnetic properties of epitaxial CoCr films with depth-dependent exchange-coupling profiles*, Phys. Rev. B **95**, 134445 (2017).

[3] L. Fallarino, P. Riego, B. J. Kirby, C. W. Miller, and A. Berger, *Modulation of Magnetic Properties at the Nanometer Scale in Continuously Graded Ferromagnets*, Materials **11(2)**, 251 (2018).

[4] L. Fallarino, E. López Rojo, M. Quintana, J. S. Salcedo Gallo, B. J. Kirby, and A. Berger, *Modifying Critical Exponents of Magnetic Phase Transitions via Nanoscale Materials Design*, Phys. Rev. Lett. **127**, 147201 (2021).

[5] L.Fallarino, M. Quintana, E. López Rojo, and A. Berger, *Suppression of Coercivity in Nanoscale Graded Magnetic Materials*, Phys. Rev. Appl. **16**, 034038 (2021).

[6] J. S. Salcedo Gallo, A. Berger, M. Quintana, E. Restrepo Parra and L. Fallarino, *Nanoscale control of temperature operation ranges for magnetocaloric applications*, J. Phys. D: Appl. Phys. **54**, 304003 (2021).

[7] S. Ikeda, K. Miura, H. Yamamoto, K. Mizunuma, H. D. Gan, M. Endo, S. Kanai, J. Hayakawa, F.Matsukura, and H. Ohno, *A perpendicular-anisotropy CoFeB–MgO magnetic tunnel junction*, Nat. Mater. **9**, 721 (2010).

[8] J. M. Iwata-Harms, G. Jan, H. Liu, S. Serrano-Guisan, J. Zhu, L. Thomas, R.-Y. Tong, V. Sundar, and P.-K. Wang, *High-temperature thermal stability driven by magnetization dilution in CoFeB free layers for spin-transfer-torque magnetic random access memory*, Sci. Rep. **8**, 14409 (2018).

[9] V. Krizakova, E. Grimaldi, K. Garello, G. Sala, S. Couet, G. Sankar Kar, and P. Gambardella, *Interplay of Voltage Control of Magnetic Anisotropy, Spin-Transfer Torque, and Heat in the Spin-Orbit-Torque Switching of Three-Terminal Magnetic Tunnel Junctions*, Phys. Rev. Appl. **15**, 054055 (2021).

[10] Y. C. Wu, K. Garello, W. Kim, M. Gupta, M. Perumkunnil, V. Kateel, S. Couet, R. Carpenter, S. Rao, S. Van Beek, K.K. Vudya Sethu, F. Yasin, D. Crotti, and G.S. Kar, *Voltage-Gate-Assisted Spin-Orbit-Torque Magnetic Random-Access Memory for High-Density and Low-Power Embedded Applications*, Phys. Rev. Appl. **15**, 064015 (2021).

[11] Y. Takeuchi, E. C. I. Enobio, B. Jinnai, H. Sato, S. Fukami, and H. Ohno, *Temperature dependence of intrinsic critical current in perpendicular easy axis CoFeB/MgO magnetic tunnel junctions*, Appl. Phys. Lett. **119**, 242403 (2021).

[12] H. Sato, E. C. I. Enobio, M. Yamanouchi, S. Ikeda, S. Fukami, S. Kanai, F.Matsukura, and H. Ohno, *Properties of magnetic tunnel junctions with a MgO/CoFeB/Ta/CoFeB/MgO recording structure down to junction diameter of 11 nm*, Appl. Phys. Lett. **105**, 062403 (2014).

[13] L. Zhang, Y. Cheng, W. Kang, L. Torres, Y. Zhang, A. Todri-Sanial, and W. Zhao, *Addressing the thermal issues of STT-MRAM from compact modeling to design techniques*, IEEE Trans. Nanotechnol. **17**, 345 (2018).

[14] N. Dwivedi, A. K. Ott, K. Sasikumar, C. Dou, R. J. Yeo, B. Narayanan, U. Sassi, D. De Fazio, G. Soavi, T. Dutta, O. Balci, S. Shinde, J. Zhang, A. K. Katiyar, P. S. Keatley, A. K. Srivastava, S. K. R. S. Sankaranarayanan, A. C. Ferrari, and C. S. Bhatia, *Graphene overcoats for ultra-high storage density magnetic media*, Nat. Commun. **12**, 2854 (2021).

[15] R. C. Sousa, M. Kerekes, I. L. Prejbeanu, O. Redon, B. Dieny, J. P. Nozières, and P. P. Freitas, *Crossover in heating regimes of thermally assisted magnetic memories*, J. Appl. Phys. **99**, 08N904 (2006).

[16] K. Watanabe, B. Jinnai, S. Fukami, H. Sato, and H. Ohno, *Shape anisotropy revisited in single-digit nanometer magnetic tunnel junctions*, Nat. Commun. **9**, 663 (2018).

[17] B. Jinnai, K. Watanabe, S. Fukami, and H. Ohno, *Scaling magnetic tunnel junction down to single-digit nanometers—Challenges and prospects*, Appl. Phys. Lett. **116**, 160501 (2020).

[18] M. Quintana, A. Meléndez, C. Martín Valderrama, L. Fallarino, and A. Berger, *Temperature-Independent Coercivity in Compositionally Graded Ferromagnetic Multilayers*, Phys. Rev. Applied **18**, 054024 (2022).

[19] U. Gradmann, *Magnetism of surfaces and interfaces*, J. Magn. Magn. Mater. **6**, 173 (1977).

[20] R. Weber, C. Martín Valderrama, L. Fallarino, and A. Berger, *Dependence of the magneto-optical signal on the Co layer thickness asymmetry in Co/Pt/Co films*, Phys. Rev. B **102**, 214434 (2020).

[21] A. F. Kravets, A. N. Timoshevskii, B. Z. Yanchitsky, M. A. Bergmann, J. Buhler, S. Andersson, and V. Korenivski, *Temperature-controlled interlayer exchange coupling in strong/weak ferromagnetic multilayers: A thermomagnetic Curie switch*, Phys. Rev. B **86**, 214413 (2012).

[22] D. M. Polishchuk, A. F. Kravets, Y. O. Tykhonenko-Polishchuk, A. I. Tovstolytkin, and V. Korenivski, *Ferromagnetic resonance and interlayer exchange coupling in magnetic multilayers with compositional gradients*, AIP Advances **7**, 056307 (2017).

[23] A. F. Kravets, D. M. Polishchuk, V. A. Pashchenko, A. I. Tovstolytkin, and V. Korenivski, *Current-driven thermomagnetic switching in magnetic tunnel junctions*, Appl. Phys. Lett. **111**, 262401 (2017).

[24] O. Idigoras, A. K. Suszka, P. Vavassori, B. Obry, B. Hillebrands, P. Landeros, and A. Berger, *Magnetization reversal of in-plane uniaxial Co films and its dependence on epitaxial alignment*, J. Appl. Phys. **115**, 083912 (2014).

[25] O. Idigoras, U. Palomares, A. K. Suszka, L. Fallarino, and A. Berger, *Magnetic properties of room temperature grown epitaxial* $Co_{1-x}Ru_x$*-alloy films*, Appl. Phys. Lett. **103**, 102410 (2013).

[26] P. Riego, L. Fallarino, C. Martínez-Oliver, and A. Berger, *Magnetic anisotropy of uniaxial ferromagnets near the Curie temperature*, Phys. Rev. B **102**, 174436 (2020).

[27] O. Idigoras, P. Vavassori, J.M. Porro, and A. Berger, *Kerr microscopy study of magnetization reversal in uniaxial Co-films*, J. Magn. Magn. Mater. **20**, L57-L60 (2010).

[28] O. Idigoras, A. K. Suszka, P. Vavassori, P. Landeros, J. M. Porro, and A. Berger, *Collapse of hard-axis behavior in uniaxial Co films*, Phys. Rev. B **84**, 132403 (2011).

[29] X. Zhou, N. Vernier, G. Agnus, S. Eimer, W. Lin, and Y. Zhai, *Highly Anisotropic Magnetic Domain Wall Behavior in In-Plane Magnetic Films*, Phys. Rev. Lett. **125**, 237203 (2020).

[30] W. Yang, D. N. Lambeth, and D. E. Laughlin, *Unicrystal Co–alloy media on Si (110)*, J. Appl. Phys. **85**, 4723 (1999).

[31] R. Skomski, *Simple Models of Magnetism* (Oxford University Press, UK, 2008).

[32] W. L. Lim, N. Ebrahim-Zadeh, J. C. Owens, H. G. E. Hentschel, and S. Urazhdin, *Temperature-dependent proximity magnetism in Pt*, Appl. Phys. Lett. **102**, 162404 (2013).

[33] X. Fan, K. Chen, S. Guo, R. Chen, D. Lee, A. Yan, and C. You, *Core–shell Y-substituted Nd–Ce–Fe–B sintered magnets with enhanced coercivity and good thermal stability*, Appl. Phys. Lett. **110**, 172405 (2017).

[34] J. S. Zhang, L. Z. Zhao, X. F. Liao, H. X. Zeng, D. R. Peng, H. Y. Yu, X. C. Zhong, and Z. W. Liu, *Suppressing the* $CeFe_2$ *phase formation and improving the coercivity and thermal stability of Ce-Fe-B alloys by Si substitution*, Intermetallics **107**, 75 (2019).

[35] G. Ding, S. Liao, J. Di, B. Zheng, S. Guo, R. Chen, and Ara Yam, *Microstructure of core-shell NdY-Fe-B sintered magnets with a high coercivity and excellent thermal stability,* Acta Mater. **194**, 547 (2020).

[36] J.-U. Thiele, S. Maat, J. L. Robertson, and E. E. Fullerton, *Magnetic and structural properties of FePt-FeRh exchange spring films for thermally assisted magnetic recording media*, IEEE Trans. Magn. **40**, 2537 (2004).

[37] D. Suess, T. Schrefl, S. Fähler, M. Kirschner, G. Hrkac, F. Dorfbauer, and J. Fidler, Exchange spring media for perpendicular recording, Appl. Phys. Lett. 87, 012504 (2005).

[38] V. Neu, K. Häfner, and L. Schultz, *Dynamic coercivity and thermal stability of epitaxial exchange spring trilayers*, J. Magn. Magn. Mater. **322**, 1613 (2010).

[39] A. Berger, N. Supper, Y. Ikeda, B. Lengsfield, A. Moser, and E. E. Fullerton*, Improved media performance in optimally coupled exchange spring layer media*, Appl. Phys. Lett. **93**, 122502 (2008).

[40] A. Kirilyuk, J. Ferré, V. Grolier, J. P. Jamet, and D. Renard, *Magnetization reversal in ultrathin ferromagnetic films with perpendicular anisotropy*, J. Magn. Magn. Mater. **171**, 45 (1997).

[41] M. Gottwald, J. J. Kan, K. Lee, S. H. Kang, and E. E. Fullerton, *Paramagnetic* Fe_xTa_{1-x} *alloys for engineering of perpendicularly magnetized tunnel junctions*, APL Mater. **1**, 022102 (2013).

[42] L. Fallarino, B. J. Kirby, and E. E. Fullerton, *Graded magnetic materials*, J. Phys. D: Appl. Phys. **54**, 303002 (2021).

[43] R. A. Gallardo, P. Alvarado-Segue, F. Brevis, A. Roldán-Molina, K. Lenz, J. Lindner, and P. Landeros, *Spin-Wave Channeling in Magnetization-Graded Nanostrips*, Nanomaterials **12(16)**, 2785 (2022).

Chapter 5: Scaling Behaviors and Critical Exponents near the Dynamic Phase Transition

In this thesis chapter, the scaling behaviors and critical exponents in the context of the dynamic phase transitions (DPT) are explored experimentally for the first time. For this purpose, first in Section 5.1 the key aspects of the dynamic phase transitions are explained in a comprehensive manner. Here, the similarities and differences between the DPT and the TPT are discussed, including their scaling behaviors in the vicinity of the SOPT. Likewise, in Section 5.2 the equation-of-state of the dynamic order parameter is presented. In Section 5.3, the key experimental methods of this work are explained. This includes the particular sample fabrication and the measurement of the dynamic magnetization behaviors by means of T-MOKE magnetometry. In Section 5.4, the key experimental results regarding the scaling behaviors in the context of the DPT are explained and, finally, in Section 5.5 several conclusions and outlook are discussed.

5.1 Introduction: Dynamic phase transitions

In the previous chapters, relevant aspects of the thermodynamic-equilibrium phase-transition of ferromagnetic materials and thin films have been discussed. In this regard, exchange-graded FM thin films have been shown to exhibit continuous phase transitions in which the order parameter, magnetization, can be controlled upon suitable design of the EGPs.

In this framework, the reversal mechanism of such films has been discussed in Chapters 3 and 4. Indeed, for the type of thin films investigated here and in the limit of very slow field changes, the reversal mechanism was hereby driven by the nucleation of domains with opposite spins, and the subsequent domain wall expansion favored by the external magnetic field.

In general, in magnetization reversal, it is common to encounter non-equilibrium thermodynamic phenomena in which the individual spins in the system rotate towards their most stable spin configuration. Such reversal is associated with the FOPT happening at $T < T_C$ when the system crosses the $H = 0$ line.

Parallel, the concept of thermodynamic phase transition is fundamentally associated with physical systems that are in thermodynamic equilibrium. This is the case, even if the reversal mechanism in FM materials is a non-equilibrium thermodynamic process, because the order parameter is associated to the most energetically stable configuration only. However, one can also find phase-transitions in physical systems that are far from thermodynamic equilibrium [1]. In such non-equilibrium phase transitions, the collective dynamic behaviors of the degrees of freedom in the system change abruptly upon small changes in the dynamic control parameter of the driving force of the dynamics. Relevant examples in this regard can be found in laser emission [2], charge-density waves [3], mechanical crack propagation [4, 5] or superconducting materials [6].

In this regard, a physical system known to exhibit non-equilibrium phase transitions is the Ising model because, fundamentally here, collective behaviors subject to non-equilibrium processes are known to happen, i.e. magnetization reversal. However, given that in most cases, the reversal time-scales are much faster than measurement time-scales, the possible existence of such non-equilibrium phase transitions has been neglected for a long time.

In the 1990s, Tomé and de Oliveira found an abrupt change in the dynamic magnetization behavior in an Ising-like spin system when it is subjected to a time-dependent periodic magnetic field $H(t)$ [7]. The Hamiltonian of such system is,

$$\mathcal{H} = -J \sum_{\{i,j\}} s_i s_j - \mu_0 H(t) \sum_{\mathrm{i}} \mu s_i , \tag{5.1}$$

where J represents the nearest-neighbors exchange interaction and s_i are spin ½ variables located on lattice points. More specifically, they found an abrupt change in the overall $M(t)$ sequences for different $H(t)$ conditions. Ever since then, the so-called dynamic phase-transition (DPT), has been subject of many relevant studies [8, 9, 10, 11, 12, 13, 14], partly because of its similarities with respect to the conventional thermodynamic equilibrium phase transition, to be discussed in this chapter.

In the following chapters of this thesis, several aspects related to previously unexplored phenomena in the DPT will be discussed in detail. In this chapter, the experimental verification of the dynamic critical behavior will be discussed. For this purpose, first, the key aspects of the DPT and the associated scaling behaviors will be explained. In Section 5.2 the experimental exploration of these scaling behaviors will be motivated. Next, in Section 5.3, the experimental methods employed in this thesis for the observation of the DPT will be described. In Section 5.4, the key experimental results will be explained and, finally, in Section 5.5, some concluding remarks and future work will be proposed.

5.1.1 Dynamic Phase Transitions

The DPT consists of an abrupt change in the dynamic $M(t)$ response of a FM to an external periodic $H(t)$ such as,

$$H(t) = H_1 \cos\left(\frac{2\pi t}{P}\right), \tag{5.2}$$

where P is the period and H_1 is the field amplitude [7]. The $M(t)$ trajectory is hereby determined by such external $H(t)$ and the dynamic response of the collective magnetic system, characterized by a metastable relaxation time constant τ_M, and which stablishes the time required for magnetization to switch [15]. In Fig. 5.1(b), the $M(t)$ trajectory is shown in the presence of a slow enough external field, which is shown in Fig. 5.1(a). The $M(t)$ response of Fig. 5.1(a) is hereby obtained by a mean-field model, whose details will be explained in Section 5.1.2, with relative temperature $T/T_C = 0.8$ and $P/\tau_M = 200$. As observed in this figure, if $\tau_M << P$, magnetization will be able to follow the magnetic field oscillations, even if with a certain time-delay with respect to the $H(t)$ oscillations and will describe full hysteresis loops. Such hysteretic behavior is shown in Fig. 5.1(c), where M is plotted against H.

However, for faster dynamics, i.e. P being comparable to τ_M, magnetization will not be able to follow the magnetic field oscillations, and thus M will instead oscillate around a non-zero net M-value [7]. Given that $M(t)$ can oscillate in two opposite directions, two stable dynamic behaviors can be observed, as depicted in Figs 5.1(e, f). Interestingly, such symmetry breaking in the M response happens even in the external magnetic field is centered around a 0 net field value, which is similar to the two equivalent thermodynamic equilibrium ground states of the Ising model in zero field .

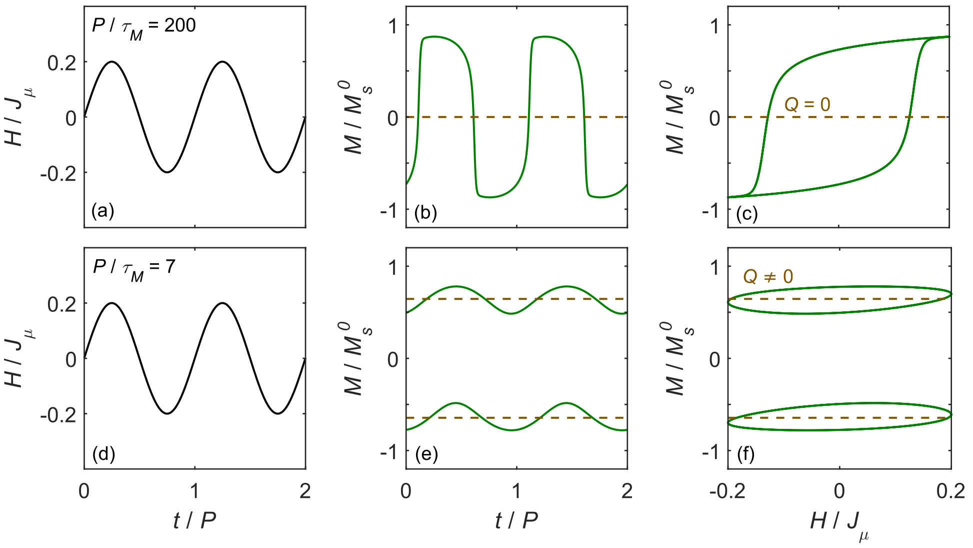

Figure 5.1: (a) Schematic of a slow sinusoidal magnetic field with $H_I/J_\mu = 0.2$ in normalized units and (b) subsequent $M(t)$ time-trace in green with average magnetization $Q = 0$ shown as a brown dashed line. (c) Magnetization represented as a function of H showing the hysteretic behavior. (d) $H(t)$ and (e) subsequent $M(t)$ for much faster dynamics ($P/\tau_M = 7$), showing fundamentally different magnetization dynamics with respect to (b). (f) M represented as a function of H for the data in (e) with $Q \neq 0$.

Thus, Figs. 5.1(b, e) exhibit fundamental differences in their non-equilibrium magnetization behavior. This fundamental change is hereby characterized by the dynamic order parameter Q, defined as the period-averaged magnetization [7]:

$$Q = \int_t^{P+t} M(t')\ \mathrm{d}t'. \tag{5.3}$$

In Figs. 5.1(b, c, e, f), Q is shown by means of brown-dashed lines. For even slower external fields, the $M(t)$ behavior will exhibit conventional hysteresis loops with $Q = 0$ for slower fields.

Fig. 5.2, shows the values of Q as a function of P/τ_M calculated with a MFA (see Section 5.1.2), as shown by the brown points. Here, one can observe that the dynamic order parameter undergoes a unique SOPT at a critical period, P_C. Such a critical point separates a dynamically ordered phase with $Q \neq 0$, called dynamic ferromagnetic (dFM) phase, from a dynamic paramagnetic (dPM) where $Q = 0$ [7].

In the vicinity of P_c, Q is known to follow a power-law behavior as,

$$Q(P \to P_c) \propto (P_c - P)^{\beta_d}, \tag{5.4}$$

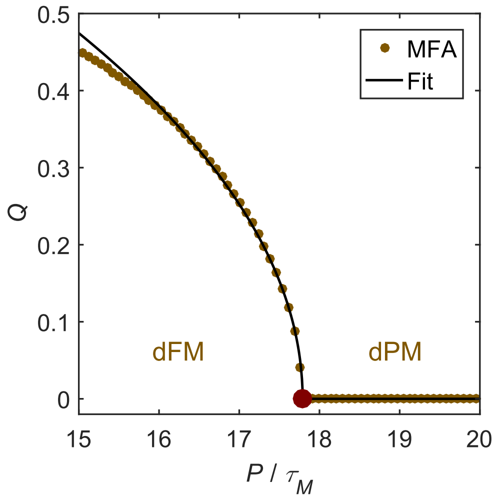

Figure 5.2: Dynamic order parameter Q represented as a function of the field period P. The dark red point separates the dFM, with $Q \neq 0$, from the dPM phase, with $Q = 0$. The brown points are the results from the MFA with $T = 0.8T_C$ and $H_l/J = 0.2$. The solid black line is a least-squares fit to eq. (5.4), exhibiting a critical exponent $\beta_d = 0.5$ in the vicinity of the critical point.

where β_d is a dynamic critical exponent [16, 17]. In Fig. 5.2, the solid-black line is a least-squares fit to eq. (5.4). Here, an excellent agreement between the MFA and the power-law is observed for the Q-values that are closer to P_c. Such fitting procedure leads to a critical exponent $\beta_d = 0.5$, which is identical to the critical exponent β in the thermodynamic equilibrium phase transition in mean-field models. Indeed, it is well known from theoretical studies that β_d corresponds to the same universality class as the conventional critical exponent β [18], which is an intriguing result, given that the TPT and DPT are fundamentally different phenomena [16, 17, 19, 20].

At this point, before explaining further detail of this non-equilibrium phenomenon, it will be relevant to explain key insights on the overall magnetization dynamics to be employed in this work as well. For this particular purpose, a mean-field approximation will be employed.

5.1.2 Non-equilibrium equation of magnetization dynamics within the mean-field approximation

For the most part, the knowledge in dynamic magnetic phase transition has been driven by theoretical studies, in which the $M(t)$ trajectories were analyzed for different field conditions in the entire dynamic phase space. Most relevantly, such studies characterized the magnetization behavior using the 2D Ising model, even though 3D Ising or Heisenberg models have also been considered [8, 9, 11]. For this purpose, either Monte Carlo simulations, MFA-based calculations, or even analytical derivations have been employed.

While this work is primarily experimental, the here obtained results will be compared with simulations for comparison purposes. The modeling technique used throughout this thesis will be the mean-field approach of the 2D Ising model, which is also the approach first employed by T. Tomé and de Oliveira, that allowed for a first demonstration of the DPT [7]. Such model allows for a simple and relatively fast calculations of the $M(t)$ signals in the entire phase space in the vicinity of P_c, and most of the key aspects of such dynamic $M(t)$ behaviors [21, 22, 23]. As a starting point, the magnetization evolution of a mean-field Ising-like system is considered using Glauber stochastic dynamics [15] as,

$$\tau_M \frac{d\langle s\rangle(t)}{dt} = -\langle s\rangle(t) + \tanh\left[\frac{T_C}{T}\frac{\mu_0\mu}{n_T J} H_{eff}(t)\right]. \tag{5.5}$$

Here, $H_{eff}(t)$ is the effective mean-field acting on a spin in the lattice with n_T total nearest neighbors. In this case, $H_{eff}(t)$ is given by the effective exchange field as,

$$H_{eff}(t) = \frac{n_T J}{\mu_0\mu}\langle s\rangle(t) + H(t). \tag{5.6}$$

Throughout this thesis, eq. (5.5) will be evaluated to obtain a steady-state periodic solution of $M(t) = M_s^0\langle s\rangle(t)$ for any given periodic $H(t)$ sequences [21]. In such evaluation, H is taken in dimensionless units H/J_μ, with $J_\mu = n_T J/\mu_0\mu$. In general, throughout this work, $T = 0.8\,T_C$, which is a relative temperature large enough to avoid computational complications at very low temperatures [24, 25].

In order to evaluate (5.5), the corresponding finite differences equation is obtained as,

$$\langle s_k\rangle = F[\langle s_k\rangle] = \frac{1}{1+\tau_M K/P}\left[\tanh\left[\frac{T_C}{T}\frac{H_{eff}(t)}{J_\mu}\right] + \frac{\tau_M K}{P}\langle s_k\rangle\right], \tag{5.7}$$

with K being the typically used number of discrete time points k over a period of discrete-time $\langle s_k\rangle$ and field H_k [11, 21]. Here $K = 300$ is sufficient to describe the dynamic magnetization behavior in the entire dynamic phase space in the vicinity of P_c. For the evaluation of this finite-differences equation, an initial condition $\langle s_k^{i=1}\rangle$ is considered and then, $\langle s_k^{i+1}\rangle$ computed as,

$$\langle s_k^{i+1}\rangle = \langle s_k^i\rangle + c\left[F\left[\langle s_k^i\rangle\right] - \langle s_k^i\rangle\right], \tag{5.8}$$

where $c = 0.5$ represents the fraction of $F[\langle s_k^i\rangle]$ added to the next $\langle s_k^{i+1}\rangle$ iteration in order to keep the convergence stable, even in the points of the dynamic phase space close to the critical point. This process is continued until convergence has been achieved. The condition for the convergence of $M(k)$ in this thesis is set at,

$$\max\left[F\left[\langle s_k^i\rangle\right] - \langle s_k^i\rangle\right] < 10^{-10}, \tag{5.9}$$

which provides sufficiently reliable solutions in the entirety of the explored dynamic phase space. Hereby, the values of the dynamic order parameter are obtained using the discrete analog of eq. (5.3), namely,

$$Q = \frac{1}{K}\sum_{k=1}^{K}\langle s_k\rangle\,. \tag{5.10}$$

Let us compare eq. (5.5), with the behavior expected in thermodynamic equilibrium. For a constant field, in the limit of $t \to \infty$, $M(t)$ will converge to a constant value and $dM(t)/dt \to 0$. Thus, eq. (5.5) becomes,

$$\langle s\rangle = \tanh\left[\frac{T_C}{T}\frac{H_{eff}(t)}{J_\mu}\right], \tag{5.11}$$

which is exactly the expression of the *s*pin ½ mean-field model in thermodynamic equilibrium, that reproduces the TPT with the SOPT at $T = T_C$ [26].

5.1.3 Similarities and differences between the equilibrium and dynamic phase transitions

In Section 5.1.1, the dynamic order parameter Q of the DPT has been defined. Such order parameter describes the occurrence of a SOPT in the dynamical system at a critical period P_c [7]. The occurrence of such SOPT is due to field periods P becoming comparable to the magnetization relaxation times of the system, as explained in conjunction with the mean-field model of Section 5.1.2.

One key difference here between the DPT and TPT is that the existence of this uniquely occurring critical point depends not only on τ_M, but also on the external field amplitude H_1 [8]. This is because larger field amplitudes lead to faster magnetization relaxations, and, therefore, lower periods are required for the observation of the SOPT. In Fig. 5.3, the P_c vs. H_1 dependence is shown in the MFA with $T = 0.8\,T_C$.

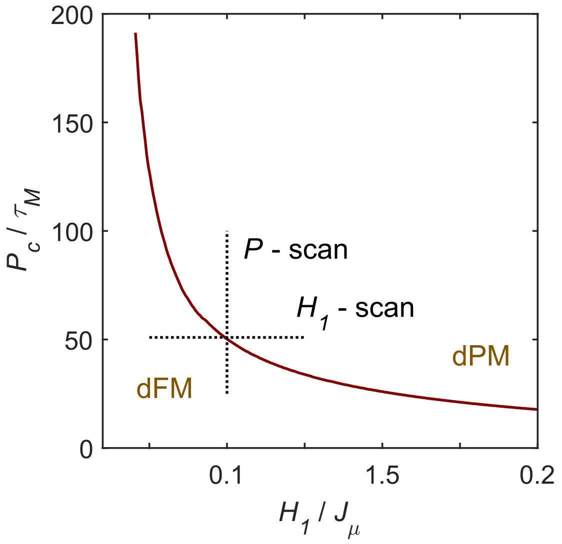

Figure 5.3: Value of P_c, normalize to τ_M, as a function of the field amplitude H_1. The aspects of the dynamic phase space in the vicinity of P_c can be studied by following P- or H_1-scans as shown by means of the dotted-black lines.

Here, P_c exhibits a monotonously decreasing trend with increasing H_1. This is a relevant phenomenon because it allows for the observation of the SOPT in two different ways: changing P while leaving H_1 constant (P-scan), or changing H_1 leaving P constant (H_1-scan). In the H_1-scan, by changing H_1, one shifts P_c until $P = P_c$, which leads to the observation of the SOPT. The critical field at which $P = P_c$ will be referred to as H_1^{crit}. Such two types of scans are schematically represented in Fig. 5.3. The relevance of the second type of scan, i.e. the H_1-scan, will become apparent in the Chapter 6, where broader explorations of the dynamic phase space are conducted.

In spite of these two different ways of observing of the SOPT of Q, all theoretical studies until now have verified that the critical exponent β_d follows the same universality class of the Ising model[16], equivalently to the critical exponent β of the TPT [16, 17, 19, 20, 27]. Such observations made researchers consider the possible existence of a conjugate field for the dynamic order parameter Q. The existence of such conjugate field requires for a symmetry breaking in the $M(t)$ dynamics.

---

[16] Such scaling behavior with critical exponent β_d is observed in the P-scan.

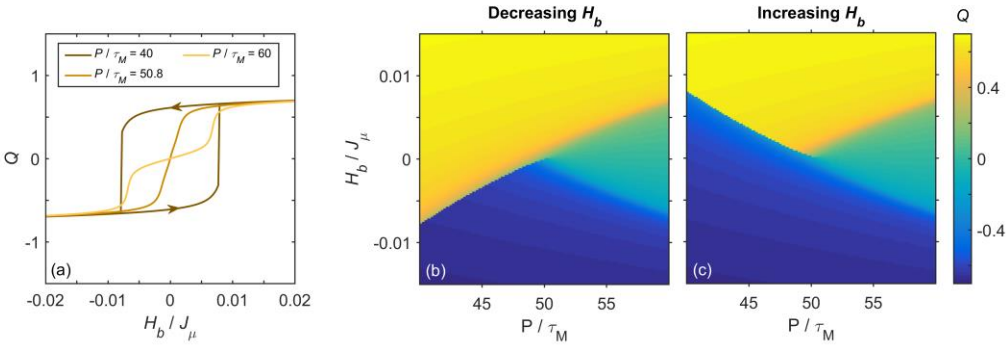

Figure 5.4: (a) Q vs. H_b behavior for three P/τ_M-values corresponding to the dFM phase, the critical point and the dPM phase. (b, c) Color-coded maps of the numerically stable solutions of $Q(P,\ H_b)$ in decreasing and increasing field configurations, showing the bistability regime for lower periods. All the MFA simulations in this figure are done considering $T/T_C = 0.8$ and $H_1/J_\mu = 0.1$.

This symmetry breaking in the $M(t)$ trajectories is known to be a constant bias field H_b, superimposed to simple sinusoidal external field oscillations [28], and is furthermore verified both theoretically and experimentally [29, 30]. So, the entire $H(t)$ driving field is described as,

$$H(t) = H_b + H_1 \ \cos\left(\frac{2\pi t}{P}\right). \tag{5.12}$$

The existence of such a H_b conjugate field implies that, in the dFM phase, Q undergoes a FOPT upon crossing the $H_b = 0$ line, in equivalence to M inverting its sign upon crossing the $H = 0$ line in the thermodynamic equilibrium counterpart. Also, the existence of a bistability regime when the system crosses the $H_b = 0$ line leads to a hysteretic behavior of $Q(H_b)$ in the dFM, while in the dPM phase, $Q(H_b)$ will only change continuously [30].

In Fig 5.4(a), MFA calculations of the $Q(H_b)$ behavior are shown both in the dFM phase, at the critical point (i.e., $P = P_c$) and in the dPM phase. Here, the bistability regime that leads to the hysteretic behavior of Q is observed in the dFM phase only. For $P \geq P_c$, Q undergoes a monotonous behavior only and, at exactly the critical point, i.e., $P/\tau_M = 50.8$ in Fig. 5.4(a), for small enough H_b, Q will follow a power-law behavior as,

$$Q(P = P_c,\ H_b \to 0) \propto H_b^{1/\ \delta_d}. \tag{5.13}$$

where δ_d is a critical exponent [21]. Such scaling behavior was verified by mean-field calculation, showing that δ_d also corresponds to the same universality class as the critical exponent δ in the TPT [18, 22].

The fact that H_b plays the role of the conjugate field of Q implies as well that one can define a 2-dimensional (P, H_b) phase space for the dynamic order parameter, in which the system will undergo first and second order phase transitions. In Figs. 5.4(b, c), the stable and metastable states of Q are represented as a color-coded maps in the entire (P, H_b) phase space. Hereby, Fig. 5.4(b) represents the values of Q obtained while decreasing H_b from saturation (for constant P), whereas 5.4(c) represents Q while increasing H_b. In these color-coded maps one observes both the behavior of Q in the dFM and dPM phases, as well as the bistability regime for $P/\tau_M < 50.8$, represented by the regions of the phase space that exhibit different Q-values between Figs. 5.4(b, c) which leads to the $Q(H_b)$ hysteresis [30]. In the dPM phase, for $P/\tau_M > 50.8$, Q exhibits the same monotonous behavior as a function of H_b in both maps, represented by the continuous change from blue to green and from green to yellow.

In Fig. 5.5(a), only the stable states of $Q(P, H_b)$ are shown as a color-coded map. Here, the black line corresponds to the FOPT, while the dark-red dot corresponds to the SOPT. The entire phase space behavior of Q is antisymmetric

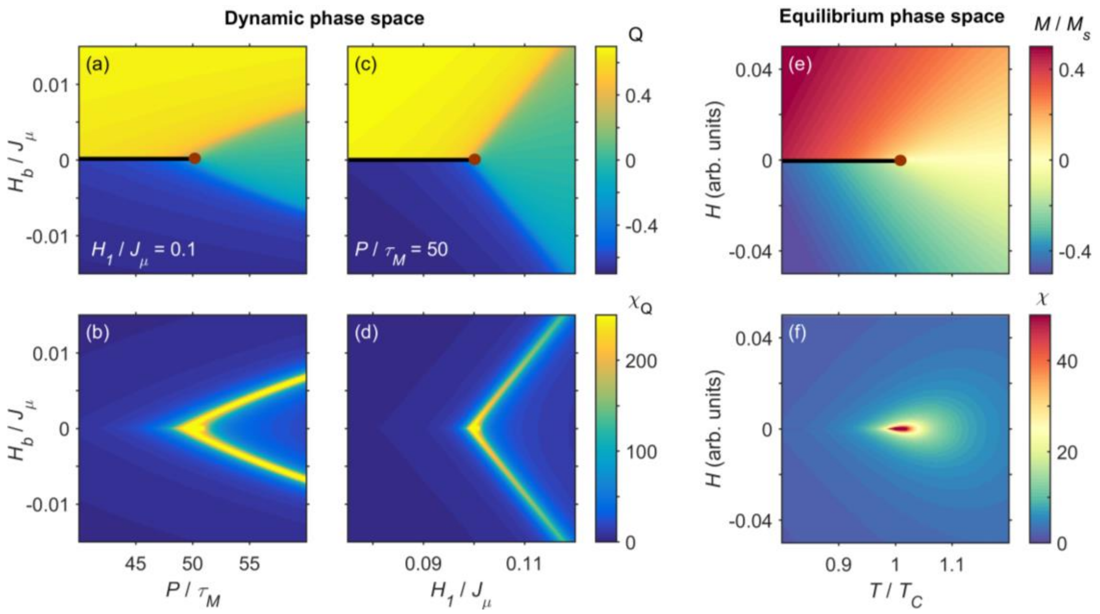

Figure 5.5: (a, b) Exemplary color-coded maps of the phase-space behavior of $Q(P, H_b)$ and the associated dynamic susceptibility $\chi_Q(P, H_b)$, showing the metamagnetic anomalies as bright yellow sidebands in the dPM phase. (c,d) Color-coded maps of the phase-space behavior of $Q(H_1, H_b)$ and associated $\chi_Q(H_1, H_b)$. (e, f) Color-coded maps of the equilibrium thermodynamic $M(T, H)$ in the vicinity of T_C, shown for comparison purposes. The dark-red point corresponds to the SOPT and the black-solid line corresponds to the FOPT in all the plots. The color bars apply to the color maps to the left of the bar.

with respect to H_b, namely $Q(H_b) = -Q(-H_b)$. This particular point is analog to the time-reversal symmetry of $M(H) = -M(-H)$ in the equilibrium phase space [18]. In Fig. 5.5(c), the stable states of $Q(H_I, H_b)$ are represented comparatively. Here, the key aspects of the dynamic phase space behavior of Q are also observed, including the existence of a FOPT at $H_b = 0$ in the FM phase and SOPT at $H_I^{crit}/J_\mu = 0.101$.

All the properties of the phase space behavior of $Q(P, H_b)$ described until now, including all the theoretically verified scaling relations of eqs. (5.4, 5.13), are basically identical to those of the equilibrium phase space behavior of $M(T, H)$ [8, 18]. There are however significant differences between both phenomena. Indeed, in the dPM phase, $Q(H_b)$ can exhibit rather steep, but still continuous, changes that happen at opposite $\pm H_b$-values [23]. Such changes are readily shown exemplarily in the yellow line of Fig. 5.4(a). In the entire dynamic phase space in Fig. 5.5(a), such steep, but still continuous, changes of Q are shown in the changes from blue to green and green to yellow in the dPM phase. A deeper understanding of this particular behavior can be obtained by inspecting the dynamic susceptibility χ_Q, defined as,

$$\chi_Q = \left.\frac{\partial Q}{\partial H_b}\right|_P . \tag{5.14}$$

In Figs. 5.5(b, d), the phase space behavior of χ_Q is shown as color-coded maps. Here, one observes that the large changes in the $Q(H_b)$-curves lead to very significant χ_Q-values in two branches in the dPM where the significant changes of Q from low to high values occur. The so-called metamagnetic anomalies were first observed experimentally by Riego et. al. [23], later verified theoretically by different groups [31, 32, 33, 34]. These anomalous metamagnetic sidebands can also be observed in the dynamic fluctuations, defined as,

$$\sigma_Q = \sqrt{\langle Q^2 \rangle - \langle Q \rangle^2}, \tag{5.15}$$

even if these are not shown here because, in MFA, fluctuations are fundamentally suppressed and therefore $\sigma_Q = 0$ in the entire dynamic phase space [23].

Figs. 5.5(e,f) show comparatively the phase space behavior of $M(T, H)$ and the conventional susceptibility $\chi(T, H)$ in a parameter space range that is analogous to that of Figs. 5.5(a-d). The here presented behavior is described by the Arrott-Noakes equation-of-state,

$$\left(\frac{H}{M}\right)^{1/\gamma} = \frac{T - T_C}{T_1} + \left(\frac{M}{M_1}\right)^{1/\beta}, \tag{5.16}$$

as described in Chapter 1, assuming critical exponents of a mean-field approximation, namely, $\beta = 0.5$ and $\gamma = 1$ [35]. The susceptibility $\chi(T, H)$ map of Fig. 5.5(f), indicates the complete absence of metamagnetic tendencies in the PM phase. This is a fundamental difference between the phase space behaviors of Q and M in the vicinity of the DPT and TPT, respectively.

5.2 Motivation: Scaling Behaviors Near the Second-Order Phase Transition

In Section 5.1, the key aspects of the DPT have been discussed. As mentioned, the dynamic order parameter shows critical scaling in the vicinity of Pc with critical exponents β_d and δ_d that correspond to the universality class of the Ising model [22]. Each of these scaling relations have been verified in several theoretical works independently.

However, the experimental observation of the DPT has only been available recently by means of specifically designed experiments, which nonetheless, have allowed for the verification of key insights of the DPT, such as the bistability regime of Q in the dFM phase [30] or the temperature dependence of Q for different T/T_C-ratios [14]. However, no work until now has managed to quantify accurately such dynamic critical exponents, which exactly the key purpose of this chapter.

The lack of experimental verification of such Q-scaling is mainly due to the existence of metamagnetic anomalies in the dPM phase, even in the close vicinity of the SOPT, which constrain the critical regime to a rather limited parameter space [8, 23]. Thus, in order to experimentally quantify this critical behavior, one must first find a suitable sample design and parameter space, in which metamagnetic tendencies are sufficiently suppressed.

Provided that no metamagnetic anomalies are observed and both the scalings of eqs. (5.4, 5.13) are indeed fulfilled, then one could postulate that Q should follow an Arrott-Noakes type of equation-of-state in the vicinity of the critical point, in full analogy to the Arrott-Noakes equation-of-state of the TPT [18, 35]. Thus, the behavior of the dynamic order parameter would be described as,

$$\left(\frac{H_b}{Q}\right)^{1/\gamma_d} = \frac{P - P_C}{P_1} + \left(\frac{Q}{Q_1}\right)^{1/\beta_d}, \tag{5.17}$$

where Q_1 and P_1 are material specific constants. Eq. (5.17) describes the scaling of Q both as a function of P and H_b in the vicinity of P_c with the critical exponents β_d and γ_d, with $\delta_d = 1 + \gamma_d/\beta_d$ (see Appendix A). The here proposed equation-of-state for the dynamic order parameter has not been explored in the past, neither theoretically nor experimentally.

In order to conduct such experimental verification of the scaling behaviors of Q one requires, on the one hand, from thin films that can mimic Ising-like behaviors of eq. (5.1), which is the model in which the DPT were theorized in the first place. On the other hand, magneto-optical setups with sufficient M-sensitivity for real-time monitoring of the $M(t)$ traces are required. In this framework, while the experimental observation of many relevant aspects of the DPT has been verified already, the experimental verification of the scaling behaviors of Q is still an open problem.

5.3 Experimental Methods & Sample Fabrication

In order to reproduce experimentally the theoretical predictions in the scaling of the dynamic order parameter, one needs thin films that can mimic the 2D-Ising like behavior. In order to reproduce experimentally such behavior, one can employ film whose magnetization dynamics is more accurately described by anisotropic Heisenberg-like models, given that both Heisenberg and Ising models are of the same symmetry class. However, in general, anisotropies and demagnetizing fields play a significant role in the magnetization reversal. For example, in perpendicularly magnetized systems, such as Co/Pt multilayers, demagnetizing fields will favor the formation of magnetic domains prior the abrupt magnetization reversal and, thus, smear out the sharp FOPT of ferromagnets [29].

With the purpose of obtaining thin films that can reproduce 2D Ising like behavior, a sample recipe similar to the ones in Chapters 3 and 4 is employed. Here, thin epitaxial Co (10$\underline{1}$0) films with thicknesses ranging 0.8-20 nm are grown by means of sputter deposition following the multilayer sequence shown in Fig 3.2, even if the main focus of this particular work is going to be the sample with 0.8 nm [36, 37, 38]. The reason for the choice of this particular crystal structure is also similar to the reasons explained in Chapters 3 and 4. Here, the single crystal Co film exhibits a strong in-plane anisotropy along the in-plane (0001) direction, which leads to an in-plane geometry in which demagnetizing fields are negligible. In field conditions in which $\boldsymbol{H}$ is applied parallel to the EA, i.e., the (0001) direction, then, the magnetic anisotropy will play no role into the dynamics of the system and, thus, the magnetization behavior will be comparable to that of an Ising-type film. In these conditions, spins have only two opposite stable states and global magnetization rotations are not relevant processes, leading to a simple abrupt magnetization reversal, required for the observation of the DPT [13, 14, 23, 30, 39].

In order to fabricate such single crystal thin films, on HF-etched Si (110) chips, a series of underlayer films are grown, namely, a 75-nm-thick Ag (110) film and a 20-nm-thick Cr (211) film, that serve as templates for the epitaxial growth of Co (10$\underline{1}$0) layers [37]. The 0.8 nm Co (10$\underline{1}$0) film is sandwiched between two non-magnetic Co$_{60}$Cr$_{40}$ films of 5 nm. This avoids the possible existence of surface effects that are relevant for such low thicknesses, such as surface anisotropies or DMI, while also keeping the epitaxial growth of the entire Co$_{60}$Cr$_{40}$/Co/Co$_{60}$Cr$_{40}$

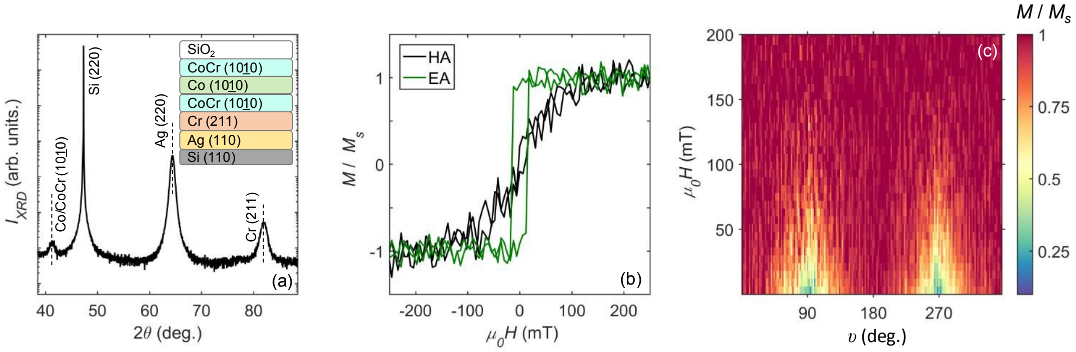

Figure 5.6: (a) XRD θ-2θ scan of the epitaxial thin film, showing the peaks corresponding to each of the intended crystallographic planes of the multilayer stack. The inset shows the particular multilayer sequence employed for the epitaxial growth of the Co (10$\underline{1}$0) film. (b) M vs. H VSM hysteresis loop measurements for the same film showing the easy and hard axis behaviors for orthogonal sample orientations. (c) Color-coded map of the equilibrium $M(\upsilon, H)$ measured showing the expected 180º symmetry for films with in-plane uniaxial magnetic anisotropy.

(1010) structure. A 10-nm-thick SiO$_2$ layer on top prevents the oxidation of entire structure. In Fig. 5.5(a), the θ-2θ XRD scan of the ultrathin film with thickness of the Co layer of 0.8 nm is shown. Here, the peaks corresponding to the crystallographic planes of each of the grown layers are observed. Such peaks, as well as the absence of peaks corresponding to different crystallographic planes allow us to confirm the epitaxial growth of the entire multilayer sequence, also for the low-thickness Co film with is embedded in the Co$_{60}$Cr$_{40}$/Co/Co$_{60}$Cr$_{40}$ (10$\underline{1}$0) stack. The SiO$_2$ capping layer is amorphous and, thus, shows no peaks in the XRD measurement.

In order to verify the expected in-plane uniaxial magnetic anisotropy of the Co (10$\underline{1}$0) layer, a VSM magnetometry characterization is conducted at room temperature (see Chapter 2). Here, the hysteretic behavior of $M(H)$ is measured in equilibrium for different angle orientations υ between the EA and the field direction. Fig. 5.6(b) shows the hysteresis loops corresponding to the EA and HA being parallel to the field direction. The hysteresis loop corresponding to the EA shows the expected square-like behavior, with the corresponding abrupt change at the magnetization reversal point. The loop corresponding to the HA shows a continuous change of M with H in agreement with the coherent rotation of the macrospin, which is the behavior expected in this particular case. This result demonstrates the anisotropic Heisenberg nature of the FM thin film, making it suitable to study the DPT for Ising-type film structures.

To further verify the expected in-plane uniaxial magnetic anisotropy, the entire $M(\upsilon, H)$ behavior is represented as a color-coded map in Fig. 5.6(c). For each angle υ, the measurements are conducted in a decreasing field sequence after saturating magnetization along any given direction. Here the expected 180º periodicity that corresponds to uniaxial magnetic behavior in the film is observed. At 90º and 270º magnetization rotates continuously from the field direction to the EA at $H = 0$, which is the behavior expected in the HA [40].

While samples of different Co thickness have been fabricated and measured for this particular study, the work here will focus on this Co film with 0.8 nm. Firstly, in principle a very thin film is required for the observation of the 2D Ising-like behavior. Co films with even lower thicknesses are shown to exhibit T_C that are lower than room temperature and, thus, cannot be measured with the room temperature T-MOKE setup. Contrarily, thicker films are shown to always exhibit substantial metamagnetic anomalies, even in the close vicinity of P in the dPM phase.

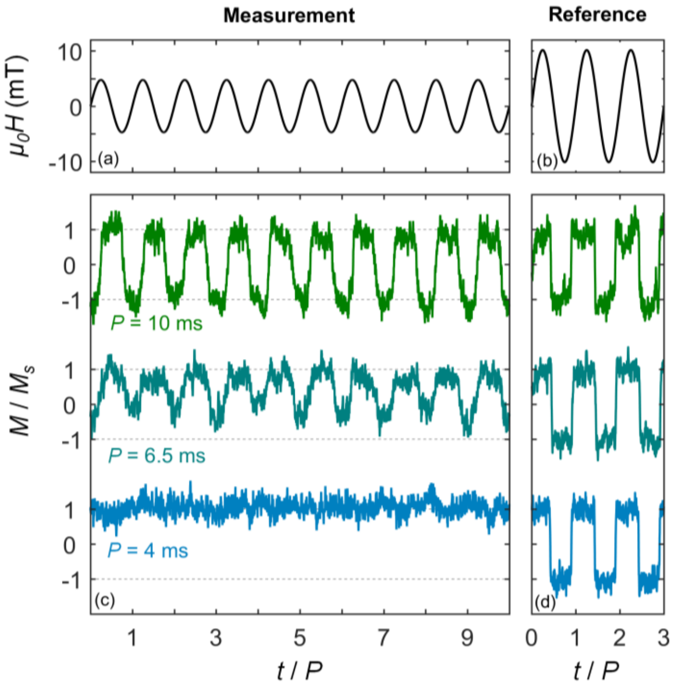

Figure 5.7: Exemplary T-MOKE measurement set. (a, b) Example of externally applied magnetic field with field amplitude $\mu_0 H_1 = 4.76$ mT and reference field signal with larger amplitude $\mu_0 H_1 = 10.1$ mT. (c) $M(t)$ signals measured for $H(t)$ sequences the field amplitude in (a) and different P showing the fundamentally different dynamic behaviors of M. (d) Corresponding MOKE reference signals with the external field as in (b), used to normalize each individual measurement set to M_s.

In order to experimentally investigate the dynamic magnetization behavior in these films with such low thicknesses, a transverse magneto-optical Kerr effect (T-MOKE) setup is employed due to its excellent sensitivity for real-time and low MOKE signals [41, 42, 43, 44, 45]. The details regarding the specifics of the tool can be found in Chapter 2. Here, the sample is placed in such a way that the EA is parallel to the direction of $\boldsymbol{H}$, which in the case of the T-MOKE tool is transversal direction. Consequently, there is going to be a field-aligned M-component only that will exhibit the expected bimodal behavior of the Ising model [13, 14].

Fig. 5.7 shows three exemplary MOKE signal traces with different field conditions for the sample with thickness of 0.8 nm. This sample exhibits a small relative intensity change of $\Delta I/I \sim 0.2\%$ upon magnetization reversal, which is however still sufficient to accurately quantify the real-time magnetization behavior for such a low thickness sample. The $M(t)$ signals are tracked in the presence of a sinusoidal magnetic fields sequence of amplitude $\mu_0 H_1 = 4.76 \pm 0.1$ mT and three different periods in the vicinity of P_c. To properly identify relative magnetization changes in our T-MOKE setup, reference measurements are conducted before and after each field sequence with stronger field amplitudes, as observed in Fig. 5.7(b). Such reference field sequences lead to abrupt and periodic magnetization reversal cycles that occur at any given field P, as seen in Fig. 5.7(d). The subsequently obtained reference $M(t)$ measurements are utilized to normalize the entire set of $M(t)$ signals to M_s. Given the monotonously decreasing P_c vs. H_1 dependence (see Fig. 5.3), H_1 is chosen so that P_c falls in the millisecond range, and thus, both Q and the dynamic fluctuations can be measured with our T-MOKE setup with a sufficient signal-to-noise ratio [13, 14].

The first signal in green in Fig. 5.7(c), corresponds to P = 10 ms. Here, periodically occurring reversals of M are observed, which lead to a nearly square-type $M(t)$ signal. Such signal leads to a $Q = 0$ value, in agreement with the behavior expected in the dPM phase. In the second curve, in turquoise, the results for an intermediate P = 6.5 ms are shown. In these conditions, $M(t)$ does not reach a negative saturation, but instead it exhibits fluctuations in each subsequent field cycle periods. This dynamic behavior agrees with the behavior expected in points of the dynamic phase space where P is similar to P_c [16, 28]. Finally, for even faster dynamics with P = 4 ms, shown in blue, M remains basically in a positively saturated state throughout the magnetic field cycle. In these conditions, $Q \neq 0$, which is the behavior expected in the dFM phase.

These preliminary results imply that one can effectively access both the dPM and dFM phases in such thin films, as well as the critical regime close to P_c, where large dynamic fluctuations are observed. In order to quantify the entire dynamic phase space, a series of measurements are conducted in which $M(t)$ signals are recorded for different field conditions in a consistent manner.

In such series of $H(t)$ sequences, H_1 is left constant while P and H_b are swept in the vicinity of the critical point. For every individual P-value, H_b stepwise decreases and subsequently increases after every 200 field oscillation periods in steps that, in this particular case, are of 0.015 mT[17]. Such H_b-sweep measurements are then repeated 5 times, which allows for an accurate quantification of the bistability regime of the dFM phase. From the 200 field oscillations measured under stable conditions, only the last 100 are considered for the numerical analysis of the $M(t)$ signals to avoid transient behaviors in $H(t)$. This implies that, for each (P, H_b) point in the dynamic phase space, 500 Q_i-values are extracted in each of the decreasing and increasing H_b sequences.

---

[17] Throughout this thesis, the H_b step size is chosen so that the relative H_b/H_1-ratios are kept similar between different phase space measurements.

5.4 Results & Discussion

In the following, the results for the 0.8 nm Co (10$\underline{1}$0) film will be discussed. Fig. 5.8 shows as a color-coded map the phase-space behavior of Q in the vicinity of the critical point for $\mu_0 H_1 = 4.76 \pm 0.01$ mT, quantified following procedure explained in the previous section. Here, all the key aspects of the phase-space behavior of $Q(P, H_b)$ are reproduced, as explained in Section 5.1. In the dFM phase, two equivalent dynamic states are observed with opposite $\pm Q$-values for positive and negative H_b represented by the yellow and blue regions in the map. The sharp FOPT is hereby observed right at $\mu_0 H_b = 0$ mT. In the dPM phase, Q changes in a continuous fashion as a function of H_b, as observed by the continuous color change. Thus, Q can be precisely observed in the immediate vicinity of the DPT for our ultrathin film even if this sample exhibits extremely small MOKE-signals.

Now, to properly characterize the scaling behavior of Q by utilizing eq. (5.17), and subsequently quantify critical exponents, a consistent scaling regime close to P_c must be selected. In Fig. 5.8(b), the experimentally determined σ_Q-values are represented in the same (P, H_b) phase-space region of Fig. 5.8(a). Here, first, the absence of any relevant metamagnetic fluctuations in our selected parameter space is verified, which is very different from what has been observed in thicker films.

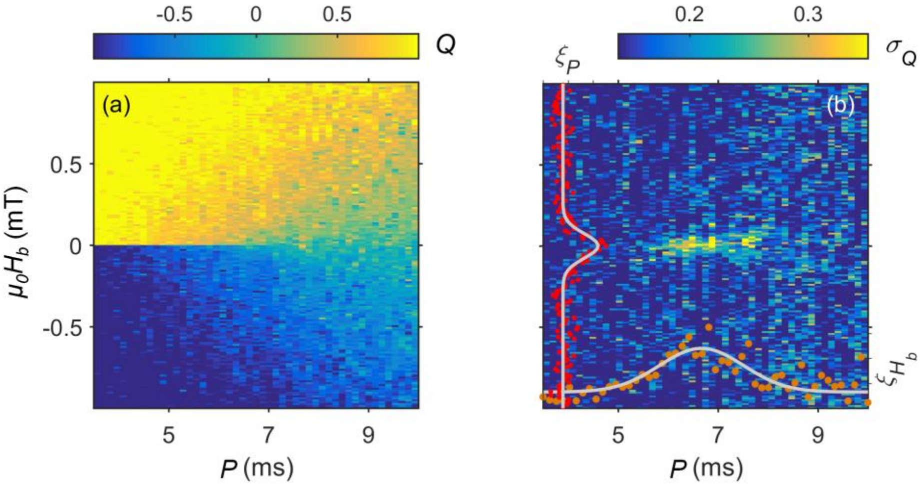

Figure 5.8: (a) Color-coded map of the $Q(P, H_b)$ phase space behavior in the vicinity of the SOPT, measured in an ultrathin Co (10$\underline{1}$0) film with $\mu_0 H_1 = 4.76 \pm 0.01$ mT. (b) Associated dynamic fluctuations σ_Q in the same (P, H_b) phase space, exhibiting the critical regime at points close enough to P_c. Red and orange points represent the statistical evaluation of ξ_P and ξ_H, respectively, and the solid-grey lines represent the subsequent least-squares fits to Gaussian distributions that allow for a quantification of the critical regime.

More importantly, though, σ_Q becomes large only in a narrow region of the dynamic phase space close to the SOPT, as one can see from the approximately ellipse-shaped yellow region for small $|H_b|$-values in the center of the figure. Such a region with large σ_Q-values is associated with the existence of critical fluctuations, which is the expected behavior in the vicinity of P_c, in analogy with the thermal fluctuations of M close to T_C.

A statistical analysis of σ_Q along the P- and H_b-axes is conducted to precisely quantify the region that exhibits large dynamic fluctuations. Such statistical analysis is conducted by numerically integrating $\xi_H = \int \sigma_Q \, dP$ and $\xi_P = \int \sigma_Q \, dH_b$ along the P- and H_b-axes respectively, which are also shown as insets points in Fig. 5.8(b). These data reveal gaussian-like distributions of ξ_H and ξ_P, as shown by means of the solid-grey lines in Fig. 5.8(b), which exhibit standard deviations of $L_H = 0.107$ mT and $L_P = 1.2$ ms. These L_H and L_P quantities characterize the critical regime in the close vicinity of P_c and are taken systematically for the analysis of the critical behaviors of Q. In particular, here a criterion of utilizing a $\pm 3L_H$ and $\pm 3L_P$ phase-space segment has been applied to identify the relevant region, in which to analyze the scaling behavior of Q.

In Fig. 5.9, the results on the scaling behavior of Q are shown. In Figs. 5.9(a-c), the experimental phase-space behavior of $Q(P, H_b)$ are shown as color-coded maps for three different values of H_I in the critical region only, which was identified in the above discussed manner. All the explored cases for different H_I-values exhibit well distinguished FM and PM phases, and all key aspects of the phase-space behavior of Q, as discussed in conjunction with Fig. 5.8. In these three different maps, a monotonously decreasing trend of P_c with H_I can be identified as well, which agrees with the expected theoretical behavior that was discussed in conjunction with Fig. 5.3 [13, 14, 39].

In order to quantify the Q-scaling of these experimental results, one assumes now that each of these sets of data fulfills the dynamic analog of the Arrott-Noakes equation-of-state, namely eq. (5.17). Here, instead of just assuming an ideal scaling of Q, the possible existence of local lateral imperfections in the film is considered [46, 47]. Hereby, local imperfections should lead to the existence of narrow P_c-

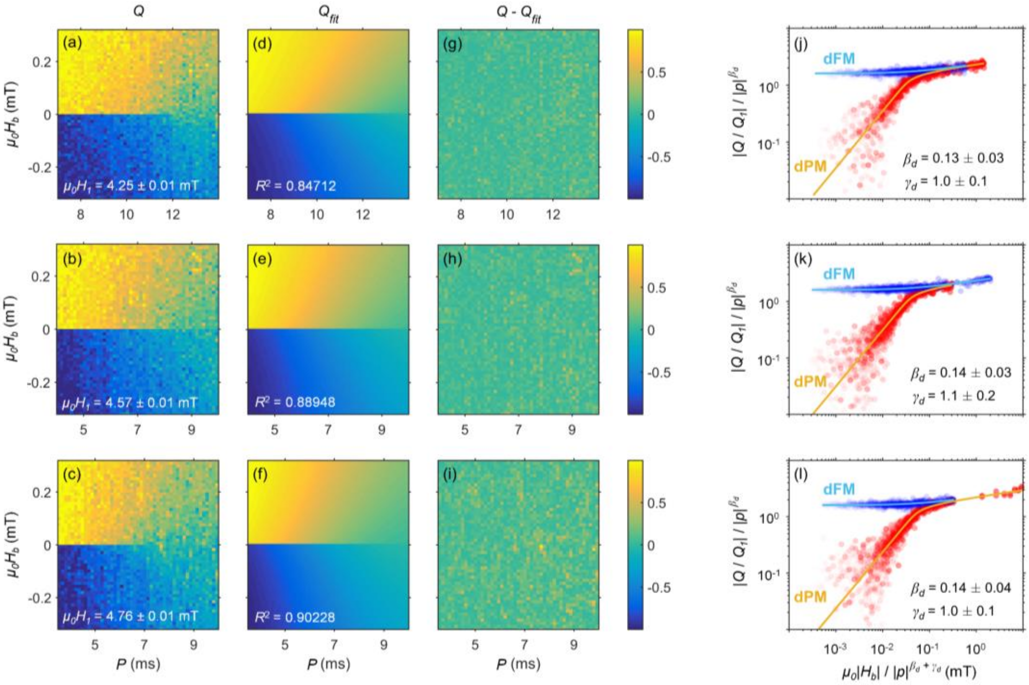

Figure 5.9: (a-c) Color-coded maps of the experimental $Q(P,\ H_b)$ phase space behavior in the critical regime for three different H_1-values. (d-f) Color-coded maps of results from the least-squares fitting to eqs. (5.18, 5.19) to the data in (a-c). (g-i) Color-coded maps of the least-squares fitting residual, showing negligible systematic deviations. The color bars in the right-hand side of (g-i) apply to each entire row. (j-l) Arrott plots of the renormalized $|Q/Q_1|/|p|^{\beta_d}$ vs. $\mu_0|H_b|/|p|^{\beta_d+\gamma_d}$ showing the actual scaling of Q. Experimental data are represented by red (PM) and blue (FM) points. The transparency level of each point indicates $|p|$, being more transparent points closer to P_C. The solid light-blue and orange lines represent the ideal scaling.

distributions characterized by an average critical point $\widetilde{P}_c$, and a standard deviation ΔP_c.

In order to encompass such P_c distribution onto the dynamic Arrott-Noakes equation-of-state, the following procedure is considered. Each $Q(P,\ H_b)$ point in the dynamic phase space is calculated as [46, 47],

$$Q(P,\ H_b) = \int_0^{\infty} Q'(P,\ H_b,\ P_c)\, \rho_D(P_c)\ dP_c, \tag{5.18}$$

where $\rho_D(P_c)$ describes the Gaussian distribution of P_c as,

$$\rho_D(P_c) = \frac{1}{\sqrt{2\pi}}\ \mathrm{e}^{-\frac{1}{2}\left(\frac{\widetilde{P}_c\ -\ P_c}{\Delta P_c}\right)^2}. \tag{5.19}$$

The values of $Q'(P,\ H_b,\ P_c)$ in eq. (5.18) are obtained numerically from eq. (5.17) with an error better than 10^{-11}. Likewise, the integration limits in eq. (5.18) are set numerically such that the integration interval is $P_c = \widetilde{P}_c \pm 3\Delta P_c$. Using this model, we fit each of the dynamic behaviors of $Q(P, H_b)$ of Figs. 5.9(a-c). The fitting procedure is repeated self-consistently in order to maintain the same critical regime with respect to each subsequent calculation of $\widetilde{P_c}$ until the convergence is achieved.

Figs. 5.9(d-f) show as color-coded maps the least-squares fitting results of the here presented model. In these figures, one observes that all the key characteristics of the $Q(P, H_b)$ data are very precisely reproduced and the fit-function of eqs. (5.17)-(5.19) is in excellent agreement with the experimental data. In order to confirm the applicability of the model, the residual differences between experimental data and fit results are represented in Figs. 5.9(g-i). Here, negligible systematic deviations are observed, and only white-noise is clearly visible in the entire phase-space, further validating the quality of our results. Coefficients of determination $R^2 > 0.84$ are obtained for each of the data fits, with all deviations caused by white noise, only.

In analogy to the TPT Arrott-Noakes equation, this particular data analysis allows one to generate scaling plots of a properly renormalized order parameter, given by $|Q/Q_1|/|p|^{\beta_d}$, vs. a renormalized bias field quantity defined as $\mu_0|H_b|/|p|^{\beta_d+\gamma_d}$, with $p = (P - \widetilde{P_c})/P_1$ (see Appendix A). In such a data representation, all experimental data in the dynamic phase-space of Figs. 5.9(a-c) should collapse onto only two different curves. Furthermore, each of these curves should correspond to the points either in the PM or FM phases. In the here proposed fitting function, however, the existence of a non-zero ΔP_c implies that there is no renormalized field that can collapse all the points onto two curves. Alternatively, the residues from Figs. 5.9(g-i) are mapped onto the ideal case in which $\Delta P_c = 0$ and $P_c = \widetilde{P_c}$.

The results from this procedure are shown in Figs. 5.9(j-l). Here, the experimental data are represented by means of red (PM) and blue (FM) points. Here, one verifies that the data clearly collapse onto two branches, clearly following the trend of the scaling function, represented by means of the cyan and orange lines, respectively. One key observation from this particular Arrott representation is that the data extends over four decades in the renormalized H_b and about two decades in the renormalized Q, confirming scaling in a very significant parameter space. The points in the PM phase with lower $\mu_0|H_b|/|p|^{\beta_d+\gamma_d}$-values exhibit larger deviations because they correspond to points with low Q-values and, thus, they exhibit larger relative errors.

Given that the scaling of Q in the vicinity of the SOPT is confirmed, one is now in position to look into the results on the critical exponents. The extensive data analysis here results in an average critical exponent $\beta_d = 0.14 \pm 0.04$, which is in excellent agreement with the theoretically predicted critical exponent of the 2D Ising Model (see Table 5.1) [18]. This is true as well for each of the individual data sets measured at different H_1-values. The results for γ_d show rather significant deviation deviations with respect to the 2D Ising Model. This is probably associated with the very large theoretical values of δ_d, which lead to extremely sharp onset behaviors of Q at very low H_b-values in the close vicinity of P_c. Here, the field resolution is limited by the noise level with which we can keep H_1 and H_b constant and, thus, the H_b-axis is difficult to access with higher precision. Still, this is the first experimental observation of the scaling behavior of the dynamic order parameter of an ultrathin ferromagnetic thin film and the results are shown to be in very good agreement with the 2D Ising Model, as expected.

In order to compare now the critical exponents of the DPT with those of the TPT, the thermodynamic equilibrium behavior has been studied in the same film by means of SQUID magnetometry (see Chapter 2). Here, the $M(T, H)$ phase space behavior is measured by sweeping T in the vicinity of T_C while keeping H constant, as shown in Fig. 5.10(a). Here, one clearly observes the abrupt SOPT at $T_C \sim 370$K, as expected, which allows to accurately quantify the critical regime of the TPT.

A procedure equivalent to the DPT is conducted in order to calculate the equilibrium critical exponents of the TPT, as well as considering the possible existence of T_C-distributions in the film [46, 47]. Thus, $M'(T, H, T_C)$ is calculated using the Noakes-Arrott equation,

$$\left(\frac{H}{M'}\right)^{1/\gamma} = \frac{T - T_C}{T_1} + \left(\frac{M'}{M_1}\right)^{1/\beta}, \tag{5.20}$$

where T_1 and M_1 are material specific constants. Then, a T_C-distribution is considered with an average $\widetilde{T_C}$ and standard deviation ΔT_C. Thus,

$$M(T, H) = \int_0^\infty M'(T, H, T_C)\, \rho_T(T_C)\ dT_C, \tag{5.21}$$

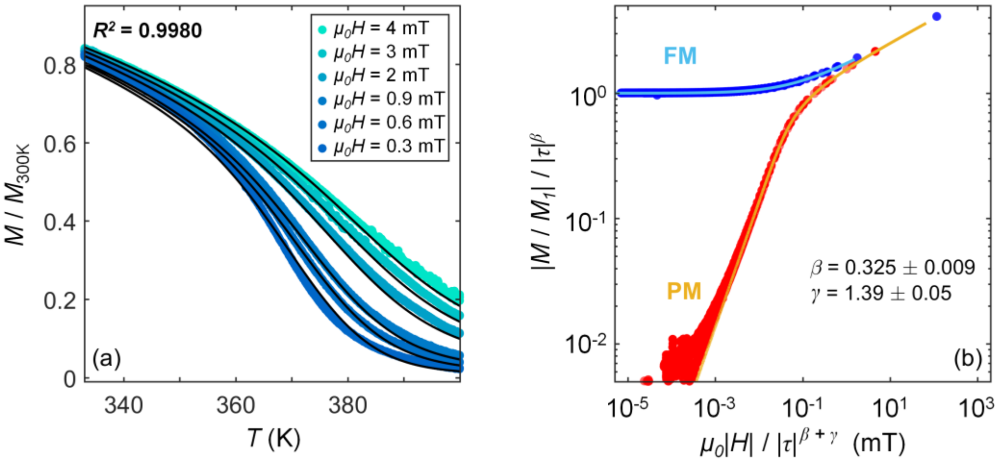

Figure 5.10: (a) Equilibrium thermodynamic M vs. T data for several constant H-values. Colored points represent experimental data and solid-black lines represent the single least-squares fit of the entire data set to eqs. (5.20-5.22). (b) Arrott plot of the renormalized $|M/M_1|/|\tau|^{\beta}$ as a function of the renormalized $\mu_0|H|/|\tau|^{\beta+\gamma}$. The blue and red points represent the data of (a) in the FM and PM phases respectively. The light blue- and orange-solid lines represent the extracted scaling function of M.

where,

$$\rho_T(T_C) = \frac{1}{\sqrt{2\pi}}\, e^{-\frac{1}{2}\left(\frac{\widetilde{T}_C - T_C}{\Delta T_C}\right)^2}. \tag{5.22}$$

The specifics of the numerical analysis in such non-linear equations are essentially identical to those of the DPT. Eq. (5.20) is numerically evaluated with a precision better than 10^{-11}.

The magnetometry data of Fig. 5.10(a) are assumed to follow eq. (5.20)-(5.22), and a least squares fitting procedure is conducted. Here, excellent fitting is obtained, as seen in Fig. 5.10(a), with $R^2 = 0.9980$. Fig. 5.10(b) shows the renormalized magnetization $|M/M_1|/|\tau|^{\beta}$ vs. the renormalized field $\mu_0|H|/|\tau|^{\beta+\gamma}$, being $\tau = (T - \widetilde{T}_C)/T_1$. Here, two very clear separate curves are seen, with very clear distinction between the points in the PM and FM phases, in analogy to the case in Figs. 5.9(j-l). Both curves collapse over six decades in the renormalized field axis and two in the renormalized magnetization, which is an even broader scaling range, if compared to the DPT, which is related to better signal-to-noise ratio.

The results from the fitting of these data lead to critical exponents of $\beta = 0.325 \pm 0.009$ and $\gamma = 1.39 \pm 0.05$. Surprisingly, the here obtained exponents agree

$\mu_0 H_1$ (mT)	β_d	γ_d	P_c (ms)	ΔP_c (ms)	R^2
4.25 ± 0.01	0.13 ± 0.03	1.0 ± 0.1	10.2 ± 0.5	2.9 ± 0.1	0.84712
4.57 ± 0.01	0.14 ± 0.03	1.1 ± 0.2	6.5 ± 0.4	3.0 ± 0.3	0.88948
4.76 ± 0.01	0.14 ± 0.04	1.0 ±0.1	5.6 ± 0.4	2.9 ± 0.2	0.90228
Avg.	0.14 ± 0.04	1.0 ± 0.1			
	β	γ	T_C (K)	ΔT_C (K)	
Therm. Eq.	0.325 ± 0.009	1.39 ± 0.05	369.9 ± 0.2	13.0 ± 0.2	0.9980
2D Ising	0.125	1.75			
3D Ising	0.3264	1.237			

Table 5.1: Experimentally obtained critical exponents of the DPT and TPT. The theoretical exponents are shown comparatively in the bottom part of the table.

rather well with those of the 3D Ising model, as one can see comparatively in Table 5.1 [18]. Thus, the DPT and TPT seem to exhibit fundamentally different dimensionalities in our sample. This is an intriguing result, given that, until now, all theoretical works have predicted that the TPT and DPT correspond to the same universality [16, 17, 19, 20].

In order to explain these seemingly inconsistent results, one should have a closer look at the dimensionalities in the system as well as the typical parameter space utilized in experiments. In the TPT case, the relative temperature range in which measurements are generally done, is in the ±10% range of T_C. However, from prior work, it is also known that the overall scaling-behavior of M and the associated critical exponents change from 2D to 3D behavior in the 4-11 monolayer thickness range [48, 49, 50, 51]. In this temperature and thickness range, the thermodynamic correlation length is comparable to the thickness of the film. In order to observe pure 2D scaling behavior of the equilibrium M, one should consider a much smaller T-range in the vicinity of T_C, because only in this smaller T-range is the correlation length consistently larger than the film thickness. However, such a reduction of the T-range is not meaningful, because any real thin film will exhibit a small but non-zero T_C distribution that will hide the 2D behavior closer to T_C. Particularly in this case, the extracted ΔT_C-values indicate that an analysis bellow ±10% of T_C is not meaningful and, thus, the observed 3D Ising-like critical exponents are not entirely unexpected.

Consequently, while the utilized parameter space leads to a 3D-like thermodynamic behavior, which hides the 2D nature of the sample in the TPT measurements, this is not the case for the DPT. The observation of 2D dynamic critical exponents should then be related to a fundamentally different crossover length-scales, at which a 2D to 3D dimensional crossover occurs. The non-equilibrium reversal of this film is dominated by a nucleation process in which the domain-wall width is considerably larger than the thickness. Considering the properties of our film, the domain-wall width is estimated to be $l \sim \sqrt{A/K_1} \sim 100$ nm, with A being the exchange stiffness and K_1 the first-order anisotropy energy [52]. The here estimated domain-wall width is two orders of magnitude larger than the thickness of the film. Therefore, the cluster formation with opposite spins and the subsequent domain-wall expansion will happen purely in the film plane in a 2D manner, because at the given length-scales the domain can only expand two-dimensionally. This qualitative argument on the magnetization reversal mechanism explains why one observes dynamic critical exponents that are consistent with the 2D Ising model, while in the same critical range, the thermodynamic equilibrium exponents correspond to those of the 3D case. Thus, this qualitative explanation suggests two fundamentally very different crossover length-scales for the TPT and the DPT, at which 3D to 2D dimensional crossover behavior occurs for finite thickness films.

5.5 Conclusions & Outlook

In this chapter, the scaling behavior of the dynamic order parameter Q near dynamic phase transitions has been quantified experimentally for the first time. For this purpose, a non-equilibrium thermodynamic analog of the Arrott-Noakes equation-of-state has been proposed, which encompasses the theoretically predicted scaling behavior of Q, and which is formally identical to the thermal equilibrium case for M.

The here obtained results for ultrathin Co (10$\underline{1}$0) films show that the observed Q-scaling is of the universality class of the 2D Ising model, as expected, while the M-scaling in thermodynamic equilibrium corresponds to the universality class of the 3D Ising model, instead. These incidentally observed differences are probably due to fundamentally different dimensional crossover length-scales between the DPT and the TPT, an aspect that has not been studied in the past, neither theoretically nor experimentally.

In this regard, this work leads to interesting questions regarding such dimensional crossover relations of the DPT. It is reasonable to expect that FM films with larger thicknesses in the range of 100 nm will exhibit critical exponents in agreement with the 3D Ising model. However, accessing the critical regime in such films would require setups with sufficient P and H_1 sensitivities due to the appearance of metamagnetic anomalies in the dPM phase in the vicinity of the critical point.

The periodically occurring DW nucleation and subsequent expansion seems to play a crucial role in the dynamics of the system and its dimensionality. In this context, this work would benefit from a theoretical analysis using Monte Carlo simulations of the DPT for thin films of different thicknesses.

Chapter References

[1] M. C. Cross and P. C. Hohenberg, *Pattern formation outside of equilibrium*, Rev. Mod. Phys. **65**, 851 (1993).

[2] J. Kröll, J. Darmo, S. S. Dhillon, X. Marcadet, M. Calligaro, C. Sirtori, and K. Unterrainer, *Phase-resolved measurements of stimulated emission in a laser*, Nature **449**, 698-701 (2007).

[3] N. Ogawa, Y. Murakami, and K. Miyano, *Charge-density-wave phase reconstruction in the photoinduced dynamic phase transition in* $K_{0.3}MoO_3$, Phys. Rev. B **65**, 155107 (2002).

[4] D. Bonamy, S. Santucci, & L. Ponson, *Crackling Dynamics in Material Failure as the Signature of a Self-Organized Dynamic Phase Transition*, Phys. Rev. Lett. **101**, 045501 (2008).

[5] A. Shekhawat, S. Zapperi, & J. P. Sethna, *From Damage Percolation to Crack Nucleation Through Finite Size Criticality*, Phys. Rev. Lett. **110**, 185505 (2013).

[6] P.H. Kes, N. Kokubo, R. Besseling, *Vortex matter driven through mesoscopic channels*, Physica C **408-410**, 478-481 (2004).

[7] T. Tomé and M. J. de Oliveira, *Dynamic phase transition in the kinetic Ising model under a time-dependent oscillating field*, Phys. Rev. A **41**, 4251 (1990).

[8] P. Riego, P. Vavassori, and A. Berger, *Towards an understanding of dynamic phase transitions*, Physica B **549**, 13-23 (2018).

[9] G. Korniss, P. A. Rikvold, and M. A. Novotny, *Absence of first-order transition and tricritical point in the dynamic phase diagram of a spatially extended bistable system in an oscillating field*, Phys. Rev. E **66**, 056127 (2002).

[10] H. Jang, M. J. Grimson, and C. K. Hall, *Dynamic phase transitions in thin ferromagnetic films*, Phys. Rev. B **67**, 094411 (2003).

[11] P. Riego and A. Berger, *Nonuniversal surface behavior of dynamic phase transitions*, Phys. Rev. E **91**, 062141 (2015).

[12] E. Vatansever and N. G. Fytas, *Dynamic phase transitions in the presence of quenched randomness*, Phys. Rev. E **97**, 062146 (2018).

[13] J. M. Marín Ramírez, E. Oblak, P. Riego, G. Campillo, J. Osorio, O. Arnache, and A. Berger, *Experimental exploration of dynamic phase transitions and associated metamagnetic fluctuations for materials with different Curie temperatures*, Phys. Rev. E **102**, 022804 (2020).

[14] M. Quintana, E. Oblak, J. M. Marín Ramírez, and A. Berger, *Experimental exploration of the vector nature of the dynamic order parameter near dynamic magnetic phase transitions*, Phys. Rev. B **102**, 094436 (2020).

[15] R. J. Glauber, *Time-Dependent Statistics of the Ising Model*, J. Math. Phys. **4**, 294 (1963).

[16] P. A. Rikvold, H. Tomita, S. Miyashita, and S. W. Sides, *Metastable lifetimes in a kinetic Ising model: Dependence on field and system size*, Phys. Rev. E **49**, 5080 (1994).

[17] S. W. Sides, P. A. Rikvold, and M. A. Novotny, *Kinetic Ising Model in an Oscillating Field: Finite-Size Scaling at the Dynamic Phase Transition*, Phys. Rev. Lett. **81**, 834 (1998).

[18] N. Goldenfeld, *Lectures on Phase Transitions and the Renormalization Group* (CRC Press, 1992).

[19] S. W. Sides, P. A. Rikvold, and M. A. Novotny, *Kinetic Ising model in an oscillating field: Avrami theory for the hysteretic response and finite-size scaling for the dynamic phase transition*, Phys. Rev. E **59**, 2710 (1999).

[20] G. Korniss, C. J. White, P. A. Rikvold, and M. A. Novotny, *Dynamic phase transition, universality, and finite-size scaling in the two-dimensional kinetic Ising model in an oscillating field*, Phys. Rev. E **63**, 016120 (2000).

[21] O. Idigoras, P. Vavassori, and A. Berger, *Mean field theory of dynamic phase transitions in ferromagnets*, Physica B 407, 1377-1380 (2012).

[22] R. A. Gallardo, O. Idigoras, P. Landeros, and A. Berger, *Analytical derivation of critical exponents of the dynamic phase transition in the mean-field approximation*, Phys. Rev. E **86**, 051101 (2012).

[23] P. Riego, P. Vavassori, and A. Berger, *Metamagnetic Anomalies near Dynamic Phase Transitions*, Phys. Rev. Lett. **118**, 117202 (2017).

[24] G. Berkolaiko and M. Grinfeld, *Type of dynamic phase transition in bistable equations*, Phys. Rev. E **76**, 061110 (2007).

[25] X. Shi and G. Wei, *Effective-field theory on the transverse Ising model under a time oscillating longitudinal field*, Phys. Lett. A **374**, 1885 (2010).

[26] S. Blundell, *Magnetism in Condensed Matter* (Oxford University Press, Great Britain, 2001).

[27] A. Vasilopoulos, Z. D. Vatansever, E. Vatansever, and N. G. Fytas, *Monte Carlo study of the two-dimensional kinetic Blume-Capel model in a quenched random crystal field*, Phys. Rev. E **104**, 024108 (2021).

[28] D. T. Robb. P. A. Rikvold, A. Berger, and M. A. Novotny, *Conjugate field and fluctuation-dissipation relation for the dynamic phase transition in the two-dimensional kinetic Ising model*, Phys. Rev. E 76, 021124 (2007).

[29] D. T. Robb, Y. H. Xu, O. Hellwig, J. McCord, A. Berger, M. A. Novotny, and P. A. Rikvold, *Evidence for a dynamic phase transition in [Co/Pt]$_3$ magnetic multilayers*, Phys. Rev. B **78**, 134422 (2008).

[30] A. Berger, O. Idigoras, and P. Vavassori, *Transient Behavior of the Dynamically Ordered Phase in Uniaxial Cobalt Films*, Phys. Rev. Lett. **111**, 190602 (2013).

[31] G. M. Buendía and P. A. Rikvold, *Fluctuations in a model ferromagnetic film driven by a slowly oscillating field with a constant bias*, Phys. Rev. B **96**, 134306 (2017).

[32] X. Shi and P. Liu, *Metamagnetic anomalies in the kinetic Ising model*, Physica A **536**, 120998 (2019).

[33] Y. Yüksel, Ü. Akıncı, E. Vatansever, *Metamagnetic anomalies in the kinetic Blume–Capel model with arbitrary spin*, Physica A **603**, 127867 (2022).

[34] Y. Yüksel, *Dynamic phase transition properties and metamagnetic anomalies of kinetic Ising model in the presence of additive white noise*, Physica A **580**, 126172 (2021).

[35] A. Arrott & J. E. Noakes, *Approximate Equation of State For Nickel Near its Critical Temperature*, Phys. Rev. Lett. **19**, 786 (1967).

[36] W. Yang, D. N. Lambeth and D. E. Laughlin, *Uniaxial Co–alloy media on Si(110)*, J. Appl. Phys. **85**, 4723–4725 (1999).

[37] O. Idigoras, A. K. Suszka, P. Vavassori, B. Obry, B. Hillebrands, P. Landeros, A. Berger, *Magnetization reversal of in-plane uniaxial Co films and its dependence on epitaxial alignment*, J. Appl. Phys. **115**, 083912 (2014).

[38] O. Idigoras, U. Palomares, A. K. Suszka, L. Fallarino, and A. Berger, *Magnetic properties of room temperature grown epitaxial $Co_{1-x}Ru_x$-alloy films*, Appl. Phys. Lett. **103**, 102410 (2013).

[39] M. Quintana and A. Berger, *General existence and determination of conjugate fields in dynamically ordered magnetic systems*, Phys. Rev. E **104**, 044125 (2021).

[40] E. C. Stoner and E. P. Wohlfarth, *A mechanism of magnetic hysteresis in heterogeneous alloys*, Philos. Trans. R. Soc. London **240**, 599 (1948).

[41] Z. Q. Qiu and S. D. Bader, *Surface magneto-optic Kerr effect*, Rev Sci Instrum **71**, 1243–1255 (2000).

[42] E. Oblak, P. Riego, L. Fallarino, A. Martínez-de-Guerenu, F. Arizti and A. Berger, *Ultrasensitive transverse magneto-optical Kerr effect measurements by means of effective polarization change detection*, J. Phys. D: Appl. Phys. **50**, 23LT01 (2017).

[43] E. Oblak, P. Riego, A. García-Manso, A. Martínez-de-Guerenu, F. Arizti, I. Artetxe and A. Berger, *Ultrasensitive transverse magneto-optical Kerr effect measurements using an effective ellipsometric detection scheme,* J. Phys. D: Appl. Phys. **53**, 205001 (2020).

[44] C. Martín Valderrama, M. Quintana, A. Martínez-de-Guerenu, T. Yamauchi, Y. Hamada, Y. Kurokawa, H. Yuasa, and A. Berger, *Insertion layer magnetism detection and analysis using transverse magneto-optical Kerr effect (T-MOKE) ellipsometry*, J. Phys. D: Appl. Phys. **54**, 435002 (2021).

[45] C. Martín Valderrama, M. Quintana, A. Martínez-de-Guerenu, T. Yamauchi, Y. Hamada, Y. Kurokawa, H. Yuasa, and A. Berger, *Sensitivity and reproducibility of transverse magneto-optical Kerr effect (T-MOKE) ellipsometry*, J. Phys. D: Appl. Phys. **55**, 435007 (2022).

[46] P. Alvarez-Alonso, J. L. Sánchez Llamazares, C. F. Sánchez-Valdés, G. J. Cuello, V. Franco, P. Gorria, and J. A. Blanco, *On the broadening of the magnetic entropy change due to Curie temperature distribution*, Journal of Applied Physics **115**, 17A929 (2014).

[47] J. Waters, A. Berger, D. Kramer, H. Fangohr, and O. Hovorka, *Identification of Curie temperature distributions in magnetic particulate systems*, J. Phys. D: Appl. Phys. **50**, 35LT01 (2017).

[48] Y. Li and K. Baberschke, *Dimensional crossover in ultrathin Ni(111) films on W(110)*, Phys. Rev. Lett. **68**, 1208 (1992).

[49] A. Aspelmeier, F. Gerhardter, and K. Baberschke, *Magnetism and structure of ultrathin Gd films*, J. Magn. Magn. Mater. 132, 22-30 (1994).

[50] F. Huang, M. T. Kief, G. J. Mankey, and R. F. Willis, *Magnetism in the few-monolayers limit: A surface magneto-optic Kerr-effect study of the magnetic behavior of ultrathin films of Co, Ni, and Co-Ni alloys on Cu(100) and Cu(111)*, Phys. Rev. B **49**, 3962 (1994).

[51] P. Cossio, J. Mazo-Zuluaga, J. Restrepo, *Critical behavior of ferromagnetic Ising thin films*, Physica B **384**, 227-229 (2006).

[52] A. Hubert, R. Schäfer, *Magnetic Domains, The analysis of Magnetic Microstructures* (Springer-Verlag Berlin Heidelberg New York, 1998).

Chapter 6: Generalized Conjugate Field of the Dynamic Order Parameter in DPTs

In this chapter, a revision of the conjugate field definition of the dynamic order parameter within the DPT is conducted. For this purpose, a mean-field model is employed to characterize the phase space behavior of Q in the vicinity of the SOPT in magnetic field sequences without half-wave asymmetry. In Section 6.1, the reasons for the necessity of a generalized conjugate field are justified and, in Section 6.2, the work of this chapter is motivated. In Section 6.3, the key theoretical and experimental results are discussed in a detailed manner. This includes a formal definition of a generalized conjugate field, its experimental verification, and the verification of the scaling behaviors in the vicinity of the critical point. Finally, in Section 6.4, several conclusions and outlook are discussed.

6.1 Introduction: Time-Reversal Symmetry within the DPT

In the previous chapter, the main aspects of the dynamic-phase transitions have been discussed [1, 2]. The critical behavior of the dynamic order parameter Q in the entire (P, H_b) phase-space has been experimentally explored by means of T-MOKE measurements [3, 4, 5, 6] on specifically designed thin films [7], which has allowed for the experimental quantification of the dynamic critical exponents.

However, one major assumption in the previous chapter was that the time-dependent component of $H(t)$ is a sinusoidal magnetic field, which in general does not have to be the case [8, 9, 10]. For example, many Monte Carlo simulation studies employ square $H(t)$ sequences in their characterization of the $M(t)$ trajectories, instead of the here employed sinusoidal fields [11, 12, 13, 14, 15]. In general, field sequences composed of different waveforms can in principle lead to distinct $M(t)$ dynamics, that can furthermore influence the dynamic phase space behavior of Q. In the most general case, an external field sequence is characterized by,

$$H(t) = H_b + H_{din}(t), \tag{6.1}$$

with $H_{din}(t)$ being the time-dependent component of $H(t)$, which for both experiments and calculations in Chapter 5 was a simple sinusoidal magnetic field of amplitude H_1 and period P. This generalization of the $H(t)$ dynamics is particularly relevant in the context of the conjugate field of Q. As mentioned in the previous chapter, the discovery that H_b corresponds to the conjugate field of Q was first proposed by Robb et. al. [16], and later verified experimentally [17, 18] and by means of mean-field calculations [19, 20]. Also, theoretical works have verified that, at least for sinusoidal and square $H_{din}(t)$ field sequences, H_b is the conjugate field of Q. However, a more recent study showed that even Fourier components superimposed to simple sinusoidal field sequences can also contribute to the conjugate field of Q [8].

To illustrate this, let us consider the following: Fig. 6.1 shows the phase space behavior of $Q(H_1, H_b)$ and $\chi_Q(H_1, H_b)$ as color-coded maps for field sequences with different $H_{din}(t)$ waveform. The data are obtained with the MFA model described in Chapter 5 [19, 21, 22], considering $T/T_C = 0.8$ and $P/\tau_M = 50$. Figs. 6.1(a-c) show the $Q(H_1, H_b)$ phase-space behaviors with $H_{din}(t)$ waveforms composed of triangular-, sinusoidal- and square-like waveforms, respectively, superimposed to

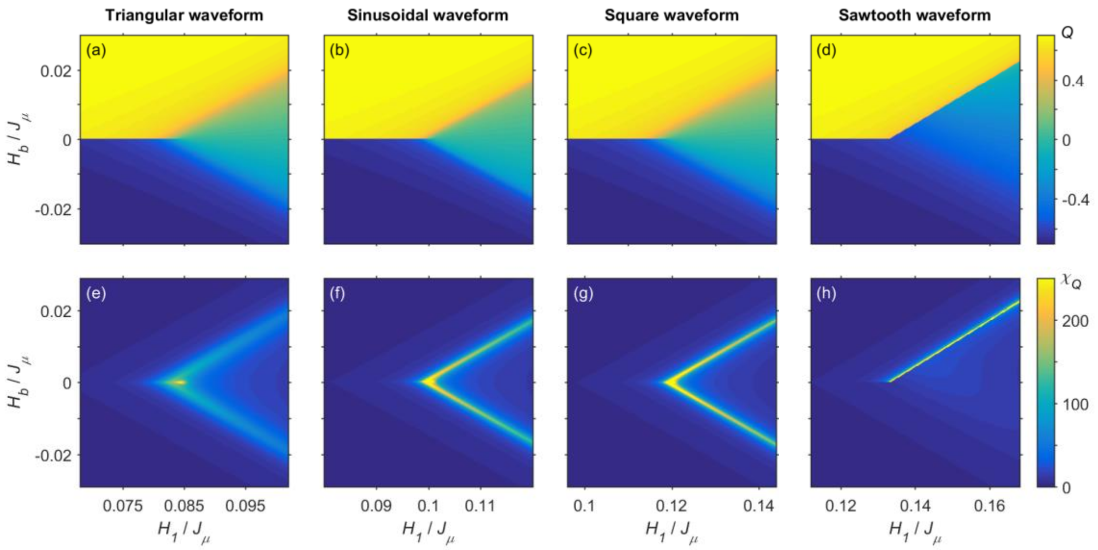

Figure 6.1: (a-d) Color-coded maps of the $Q(H_1, H_b)$ phase-space behavior with triangular, sinusoidal, square, and sawtooth like $H(t)$ waveforms. (e-h) Color-coded maps of the $\chi_Q(H_1, H_b)$ phase space behavior corresponding to (a-d). The color bars on the right-hand side of the figure apply to the entire row.

H_b[18]. Here, Figs. 6.1(a-c) are shown to describe rather similar behaviors of Q in the entire dynamic phase space. In these cases, the existence of a critical point at a critical field value H_1^{crit} is observed, which separates the dFM from the dPM phase. The specific H_1^{crit}-value are different for distinct waveforms utilizing the same amplitude. For example, square field sequences induce steeper changes in $M(t)$, which will lead then to faster dynamics, and thus, smaller P_c-values if compared with the sinusoidal and triangular field sequences. These different dynamics also seem to influence the strength of the metamagnetic anomalies, represented by means of χ_Q in Figs. 6.1(e-g). Here, more abrupt field changes, as in the case of the square $H_{din}(t)$ in Fig. 6.1(g) seem to strengthen the magnitude of metamagnetic anomalies.

More relevant though, the dynamic order parameter in Figs. 6.1(a-c) exhibits time-reversal symmetry implying,

$$Q(H_1,\ H_b) = -Q(H_1,\ -H_b), \tag{6.2}$$

in the entire dynamic phase space. This time-reversal symmetry is also analog to the conventional time-reversal symmetry of ferromagnets in thermal equilibrium, in which $M(T,\ H) = -M(T,\ -H)$ [23, 24].

This particular property of the dynamic phase space is partly due to the symmetries of $H(t)$ itself. The $H(t)$ waveforms in Figs. 6.1(a-c) share a common feature: $H_{din}(t)$ has the so-called half-wave asymmetry (HWA), namely,

$$H_{din}(\mathrm{t}) = -H_{din}(\mathrm{t} + \mathrm{P}/2). \tag{6.3}$$

The HWA implies that, in the dPM phase, $M(t)$ will describe a periodic reversal, that will naturally lead to $M(t) = -M(t + P/2)$ as well, and thus, $Q = 0$ exactly. In the conventional dynamic phase space, it is H_b the field component that breaks the symmetry of eq. (6.3) and that leads to $Q \neq 0$ [16, 20].

Figs. 6.1(d, h) show now the phase space behavior of $Q(H_1,\ H_b)$ and $\chi_Q(H_1,\ H_b)$ in a sawtooth like field sequence. Here, while a critical point is still noticeable, one can observe that the phase space behavior of Q is strongly modified. First, one observes that, for $H_b = 0$, $Q \neq 0$ in the dPM phase, as seen from the light-blue

---

[18] Here, the field amplitude H_1 is taken as the maximum field value in each sequence with $H_b = 0$.

portion of the conventional dPM phase. Second, this modification of the conventional dPM phase, leads to a strong suppression of one branch of the metamagnetic anomalies, corresponding to negative H_b, as seen in Fig. 6.1(h). Interestingly, this strong modification of the $Q(H_1, H_b)$ phase space does not seem to relevantly affect the dFM phase, as seen from the yellow and blue portions of the map. The reason for this strong modification of the dynamic phase space behavior of Q, particularly in the dPM phase, is because a sawtooth-like $H(t)$ waveform does not have the half-wave asymmetry of eq. (6.3), and thus, the periodically happening $M(t)$ reversal is different in both directions. More relevant though, given that the time-reversal symmetry of the $Q(H_1, H_b)$ phase space is lost, i.e., eq. (6.2) is not fulfilled, then, these results must imply that H_b is not the conjugate field of Q upon applying the most general $H(t)$ sequence.

Most of the studies in DPTs involving the conjugate field of Q, only consider a rather limited subset of $H_{din}(t)$ components. Thus, there is rather limited knowledge on the existence of general conjugate fields for arbitrary $H(t)$ sequences [25, 26], which is the specific aspect that will be explored in this chapter of the thesis [27].

6.2 Motivation & Field Sequence Description

As seen in Section 6.1, for an arbitrary periodic $H_{din}(t)$ magnetic field sequence, the phase space behavior of $Q(H_1, H_b)$ does not need to exhibit time-reversal symmetry. This implies that, in general, H_b does not need to be the conjugate field of the dynamic order parameter Q in the DPT.

In this chapter, a revision of the concept of the conjugate field in the DPT will be conducted in a detailed manner. Here, the existence of a generalized conjugate field of the dynamic order parameter H^* will be investigated. For this purpose, a series of specific simulations and experiments will be conducted.

In Section 6.1, it has been observed that the loss of HWA seems to affect most relevantly the dPM phase. Given that this is the case, the $Q(H_1, H_b)$ phase space will be primarily analyzed here instead of the previously used $Q(P, H_b)$ phase space. In this way, broader explorations of the entire phase space are feasible.

One must also notice that the HWA of eq. (6.3) implies that even $H(t)$ Fourier components are fundamentally suppressed. Indeed, as pointed out by Robb et. al. [8], it is the existence of non-zero even Fourier components that can cause a net effect on H^*. Thus, in order to investigate the possible existence of H^* in a consistent manner, an in-phase second harmonic field component will be included into the overall $H(t)$ field sequence, such that,

$$H(t) = H_b + H_1 \cos\left(\frac{2\pi t}{P}\right) + H_2 \cos\left(\frac{4\pi t}{P}\right), \tag{6.4}$$

with H_2 being the field amplitude of the second harmonic field component. The existence of a non-zero H_2, implies that the HWA is going to be lost, which provides as simple way to continuously deform the overall $H(t)$ sequences by analyzing the overall $Q(H_1, H_b)$ phase space behaviors for ever increasing H_2-values.

6.3 Results & Discussion

6.3.1 Theoretical modeling and definition of a generalized conjugate field

In this section, the effects of a $H_2 \neq 0$ component onto the overall phase space behavior of Q close to the critical point will be analyzed theoretically with help of the MFA model [19, 22]. Likewise, the question regarding the general existence of a conjugate H^* field in the presence of both H_b and H_2 will be addressed.

If it exists, a general formulation of H^* needs to be consistent with time-reversal symmetry in the entire dynamic phase space as,

$$Q(P,\ H^*) = -Q(P,\ -H^*), \tag{6.5}$$

as explained in Section 6.2. Given that $H^* = H_b$ in absence of H_2, then H* should be compatible with an expansion around the $H^* = H_b$ case, at least for sufficiently small H_2-values. In order to characterize the viability of such an expansion, the impact of a H_2-term onto the dPM phase for fixed P/τ_M and H_1/J_μ-values is studied first. The analysis starts here because, in this phase space region, deviations from the $H^* = H_b$ case seem to be far more substantial than in the dFM phase, according to the initial results of Figs. 6.1(d, h).

In Fig. 6.2(a), several examples of Q vs. H_b dependence are displayed in the dPM phase for several values of H_2/J_μ, assuming $P/\tau_M = 50$ and $H_1/J_\mu = 0.1$. For the $H_2 = 0$ case, i.e., the solid-yellow line in Fig. 6.2(a), Q describes the conventional behavior in the dPM phase. Here, Q monotonously increases with H_b and exhibits the antisymmetry of eq. (6.2), with $Q(H_b = 0) = 0$. Both the conventional (low-Q) and anomalous (high-Q) dPM regions are separated by the metamagnetic on-set regions, which is the behavior expected for metamagnetic anomalies.

For non-zero H_2 amplitudes of $H(t)$, the anomalous dPM regions with high values of Q differ only minimally from the $H_2 = 0$ case in the way Q approaches its near saturation value as a function of H_b. However, at lower H_b-values the behavior in the conventional dPM phase differs substantially, as seen from the darker-solid lines in Fig. 6.2(a). Here, Q shows an offset plateau of increasing magnitude with H_2. For negative values of H_2, Q displays opposite behavior with negative plateau values for Q, as demonstrated by the dashed lines in Fig. 6.2(a). The deviations from the $H_2 = 0$ case come from the fact that the driving force of the dynamics is

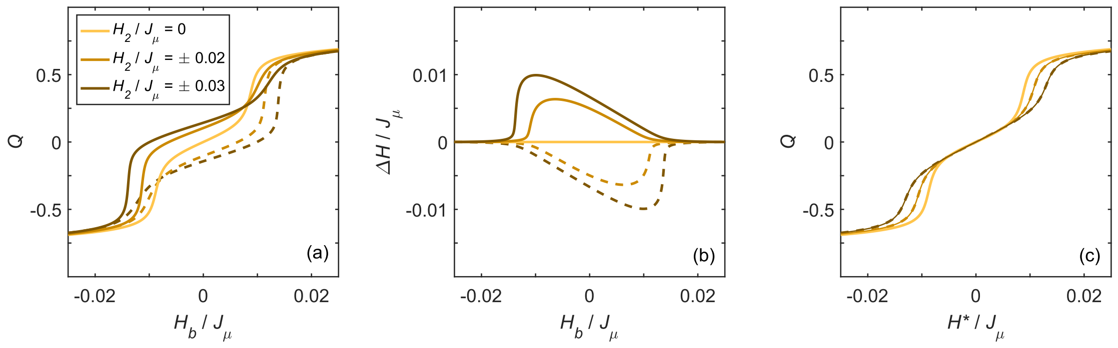

Figure 6.2: (a) MFA calculations of Q vs. H_b for different H_2 values assuming $P/\tau_M = 50$ and $H_1/J_\mu = 0.1$. (b) Subsequently calculated deviations ΔH vs. H_b required for the recovery of time-reversal symmetry for the same values of H_2 shown in (a). (c) Q vs. $H^* = H_b + \Delta H$ for the data sets shown in (a) and (b), showing that time-reversal symmetry is restored [27].

asymmetric and thus, the resulting magnetization dynamics is asymmetric too. As a result, the $M(t)$ dynamics behaves as if an effective bias effect would be acting onto $M(t)$. The $H_2 \neq 0$ component also affects the shape of the metamagnetic anomalies. Here, we observe a shift of the metamagnetic onset regions as well as a broadening in the change of Q with H_b in only one of the two metamagnetic transition regions.

The fact that the time-reversal symmetry of the Q vs. H_b curve is not preserved in the PM region implies that $H^* \neq H_b$ upon the application of additional harmonic components with $H_2 \neq 0$ in the driving $H(t)$. To verify the possible existence of a generalized $H^*(H_b, H_2)$ expression, the deviation $\Delta H(H_b, H_2)$ of H^* from the pure bias field value H_b are defined, such that [27],

$$H^* = H_b + \Delta H(H_b, H_2). \tag{6.6}$$

This ΔH deviation is the absolute change in H_b necessary to recover eq. (6.5), which can be obtained as the net bias shift in-between two opposite values of Q, namely [27]

$$\Delta H = \frac{1}{2}[H_b(Q) + H_b(\text{-}Q)], \tag{6.7}$$

where Q implicitly depends on H_b and H_2. In Fig. 6.2(b), ΔH is shown as a function of H_b for the cases displayed in Fig. 6.2(a). Hereby, ΔH is calculated taking each $H_b(Q)$-value, and finding the opposite $H_b(\text{-}Q)$ using a linear interpolation method. We observe that ΔH describes an asymmetric, nearly triangular shape as a function of H_b whose magnitude has the sign of H_2, so that it vanishes for $H_2 = 0$ as expected. Also, ΔH approaches zero in the regions corresponding to the anomalous PM region,

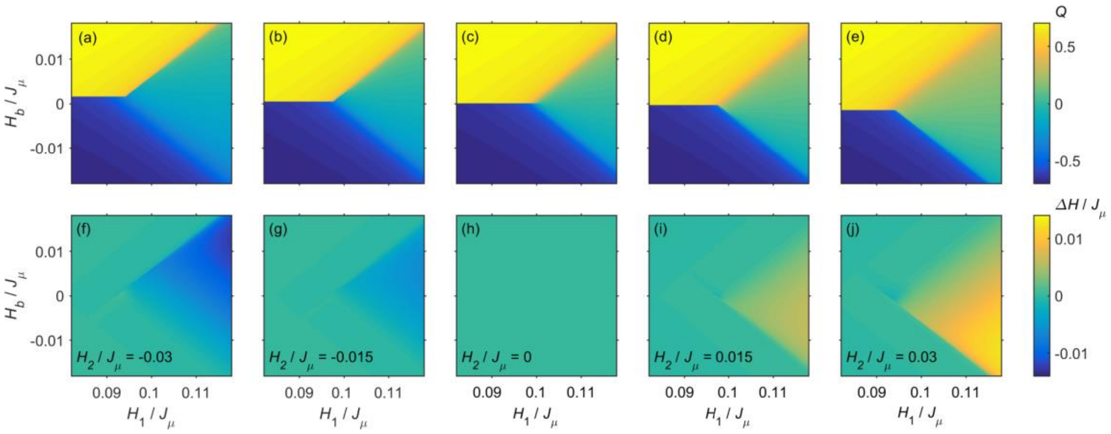

Figure 6.3: (a-e) Color-coded maps of the $Q(H_1,\ H_b)$ phase space for different H_2-values obtained with the MFA model, assuming $P/\tau_M = 50$. (f-j) Color-coded maps of ΔH, calculated by means of eq. (6.7), for the results in (a-e). The color scales on the right-hand side of the figure apply to the entirety of each row [27].

which implies that the nearly saturated Q state is not substantially affected by H_2, at least in this segment of the phase space. This is also in agreement with the initial observation in Figs. 6.1(d, h) that regions with large values of Q do not seem to be affected by the loss of HWA in the $H(t)$ signals.

Fig. 6.1(c) shows the same set of Q data in Fig. 6.1(a) now as a function of H^*, calculated by means of eqs. (6.6, 6.7). Here, one can observe that the antisymmetry is completely restored for all selected H_2 amplitudes. The values of Q with opposite H_2 collapse onto the same curve if plotted against the H^*-axis. These results indeed verify that a generalized conjugate field H^* can be computed by means of eqs. (6.6, 6.7), at least in the PM phase, so that time-reversal symmetry is restored.

To provide a complete description of the effects of H_2, also in the dFM phase, the entire $Q(H_1,\ H_b)$ phase space in the vicinity of the SOPT is presented for several values of H_2 in Figs. 6.3(a-e). The $\mu_0 H_2 = 0$ case of Fig. 6.3(c) shows the conventional $Q(H_1,\ H_b)$ phase space behavior, already described in Fig. 6.1(b) [28]. Here, the time-reversal symmetry is strictly preserved in the complete phase space with $H^* = H_b$, as expected.

For non-zero H_2-values, the dFM phase remains almost unchanged as seen from the yellow and blue regions in the maps. The only exceptions here are the exact location of the critical point and the precise placement of the phase line that separates the dynamically stable states, which will be discussed later. In the anomalous dPM regions, the large values of Q at larger $|H_b|$ are also not substantially affected by a non-zero H_2 component.

However, in the conventional dPM phase Q shows a clear offset behavior that increases in size with H_2, which is identified by the gradual color change from darker to lighter green in between Figs. 6.3(a-e) in the conventional dPM regions of the phase space. The change of Q in this region of the phase space agrees with the results in Fig. 6.2(a), in which this offset behavior was displayed for one specific H_1/J section.

As mentioned before, there is a shift of the critical point for increasing $|H_2|$. For the $|H_2|/J_\mu = 0.03$ case, for instance, H_1^{crit} is ~4% smaller than in the $H_2/J_\mu = 0$ case. This shift is due to the fact that the maximum field amplitude due to the superposition of the H_1 and H_2 components is larger, and thus only a smaller H_1 amplitude is required to drive the system into the dPM phase [28]. These findings demonstrate that the addition of secondary harmonic field components to the usual magnetic field sequence affects both H^* and the critical point of the overall $Q(H_1, H_b)$ phase space, contrary to the previous reports [8]. Further details in this regard will be discussed in Section 6.3.2 in conjunction with the corresponding experimental results.

Given that H_b does not properly represent the conjugate field in the phase space now, the phase line dividing the stable states of Q in Figs. 6.3(a-e) is ill-defined in the H_b-domain [18]. This is because, fundamentally, the FOPT occurs when the system crosses the zero-conjugate-field value, that in this case, is not represented with $H_b = 0$, but $H^* = 0$. So, for simplicity the shift of the critical point in the (H_1, H_b) domain is utilized here, which can be easily identified, to decide where the transition of all dynamically stable states occurs along the H_b-axis for all $H_1 < H_1^{crit}$ values. Correspondingly, this shift of the critical point away from the $H_b = 0$ point for non-vanishing H_2-values leads to a shifting of the line dividing the positive and negative states of Q in the entire FM phase. This shift is, however, very modest in size and can only be spotted upon very close inspection of Fig. 6.3(a-e).

Figs. 6.3(f-j) show the corresponding deviations ΔH, according to eq. (6.7), required to transform H_b into H^* for each H_1/J_μ, H_b/J_μ point in the dynamic phase space. As expected, the deviations are zero within the numerical precision of our computations in the complete phase space for $H_2 = 0$, as seen in Fig. 6.3(h). As H_2 becomes non-zero, the deviations become increasingly large in the conventional dPM phase only and exhibit the same sign as H_2 itself. These results are a generalization of the corresponding results in Fig. 6.2(b) represented also as a function of H_1. The values of ΔH in both the anomalous dPM region and the dFM phase are at least two orders of magnitude smaller (but still non-zero) in comparison with the central portion of the dPM region. These results agree with the fact that the dFM phase space remains basically unaltered, with the only exception being the phase line dividing the stable states.

To sum up, the addition of secondary Fourier components to the $H(t)$ magnetic field signal plays a substantial role only in the conventional dPM phase, as well as for the exact location of the critical point. The secondary even harmonic field H_2 acts effectively as an additional bias field $\Delta \mathrm{H}$ that works in sync or against H_b itself. Despite this effect, a generalized conjugate field H^* can be constructed in the presence of non-zero H_2 components that break the HWA. Such H^* can be constructed by establishing the effective field required to recover the time-reversal symmetry. For this purpose, the characteristic of the needed correction to H_b have been discussed here for the entirety of the relevant phase space.

6.3.2 Experimental results & model comparison

To verify the theoretical predictions of Section 6.3.1, the experimental phase space behavior of $Q(H_1, H_b)$ in a Co $(10\underline{1}0)$ sample will be analyzed in the presence of a second order H_2-component [27]. In Chapter 5, a 0.8 nm thick sample was measured because this particular film exhibited negligible metamagnetic tendencies that allowed for the scaling analysis of the critical point. Contrarily, here a 20 nm thick Co $(10\underline{1}0)$ sample has been measured. The reason for this choice is that the here proposed correction should be compatible with the existence of metamagnetic anomalies [29] while, also, thicker films will exhibit larger signal-to-noise ratios, which will allow for a more accurate magneto-optical detection and detailed data analysis.

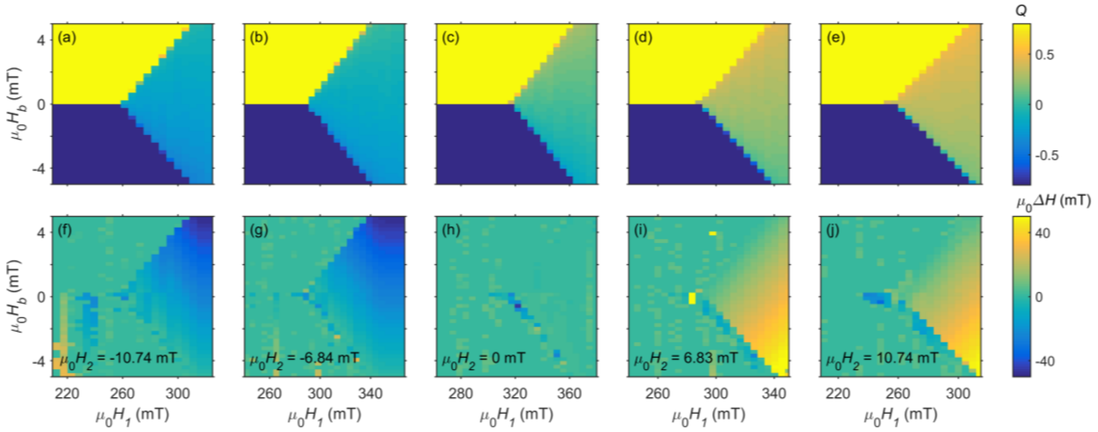

Figure 6.4: (a-e) Color-coded maps of the phase space behavior of $Q(H_1, H_b)$ with different H_2-values and obtained experimentally for a 20-nm-thick Co (10$\underline{1}$0) thin film. (f-j) Color-coded maps of the subsequently obtained $\Delta H(H_1, H_b)$-values. The color bars on the right-hand side of the figure apply to each entire row [27].

The measurements are conducted in the T-MOKE setup (see Chapter 2) at room temperature with the fundamental period of the field oscillations being $P =$ 10 ms [30, 31]. In Fig. 6.4(a-e), the experimental phase space behavior of Q as a function of both H_1 and H_b is shown for several values of H_2. In all these cases, the order parameter shows a qualitative identical behavior to the simulations in Figs. 6.3(a-e). For the $H_2 = 0$ mT case in Fig. 6.4(c), the $Q(H_1, H_b)$ phase space behavior is characterized by a critical point at $\mu_0 H_1^{crit} = 31.49$ mT dividing both the dFM and the dPM phases. In the dFM phase, for $H_1 < H_1^{crit}$, one observes two well defined opposite regions separated by the $H_b = 0$ phase line. In the dPM phase, $Q = 0$ within the experimental precision for $H_b = 0$ and reaches values near saturation for sufficiently large values of H_b in the anomalous dPM phase. Also, in the experiments here, the metamagnetic anomalies happen in a rather narrow range of H_b field values that are of the order of the resolution grid along the H_b-axis in our wide phase space area measurements, as seen by the seemingly abrupt yellow-to-green and green-to-blue transition regions.

For different H_2-values in Figs. 6.4(a-e), the phase transition and the phase space behavior of $Q(H_1, H_b)$ is not fundamentally changed. In all these cases, one observes dFM and dPM phases clearly divided by certain critical field amplitude H_1^{crit}. However, one can most evidently observe here that the values of Q in the conventional dPM regime increase monotonously with H_2, in good agreement with the simulations shown in Fig. 6.3(a-e). Furthermore, the critical field amplitude decreases substantially with $|H_2|$, leading to $\mu_0 H_1^{crit} = 25.54$ mT for $\mu_0 H_2 = \pm 10.47$ mT, for instance, which is fundamentally consistent with the results in Section 6.3.1, even if it represents a yet more substantial decrease than what occurs in our simulations. In the dFM phase, any deviation from the $H_2 = 0$ case is smaller than the experimental H_b resolution grid. Correspondingly, possible shifts of the phase line dividing the stable states in the dFM phase are below our H_b resolution here. Nonetheless, it is clearly observed that all core characteristics of the phase space behavior of Q are in excellent qualitative agreement with the simulations in Section 6.3.1. As in the simulations, one observes also here that the secondary field component affects mainly the conventional dPM phase, as well as the critical field amplitude whose relative difference is found to be larger than in the simulations.

Figs. 6.4(f-j) show as color-coded maps the corresponding experimental $\Delta H(H_1, H_b)$ values, determined by using eq. (6.7) in the entire measured phase space and for the same H_2 amplitudes used for Figs. 6.4(a-e). For the $\mu_0 H_2 = 0$ mT case in Fig. 6.4(h), ΔH is effectively zero in the entire analyzed phase space, except for the region with very large metamagnetic fluctuations, which is a consequence of the experimental resolution limit along the H_b-axis and thus leads to an enhanced noise level for the determined ΔH-values. As H_2 is varied, ΔH shows a qualitative identical phase space behavior to the one found in the simulations, as can be seen in Figs. 6.4(f-j). Here, one also observes that the higher order induced bias ΔH is only relevant in the conventional dPM phase. An asymmetric shape can be identified as a function of H_b, whose magnitude increases monotonously with H_2, also in good agreement with the results in Figs. 6.3(f-j). At the same time, ΔH is smaller than the fluctuation level of our measurements in the dFM phase, and thus are equal to zero within the experimental precision.

In order to achieve a deeper understanding of these results, specific aspects of the experimental data will be compared to the simulations obtained in Section 6.3.1. Fig. 6.5(a), shows Q along a cut of the phase space in the dPM state, in which $H_1 = 1.08\ H_1^{crit}$ while H_b is varied for three different values of H_2. Here, the change of Q due to the presence of H_2 is significant in the conventional dPM region only, which is in excellent qualitative agreement with the mean-field simulations shown in Fig. 6.2(a). It is also noticeable that the H_b-range of the conventional dPM regime is similar in these three cases, which is associated with the fixed H_1/H_1^{crit}-ratio chosen for this purpose. A substantial impact of the H_2 amplitude onto the general

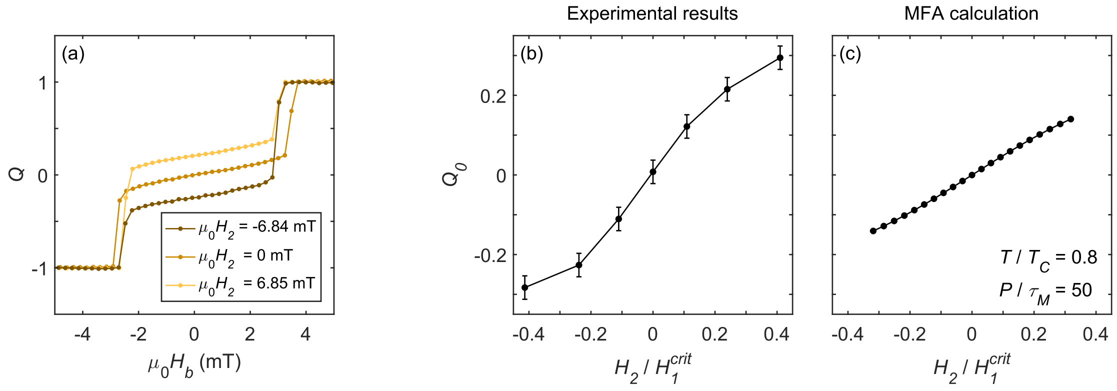

Figure 6.5: (a) Experimentally obtained Q vs. H_b in the dPM phase for several H_2 and $H_1 = 1.08$ H_1^{crit}. (b, c) Experimental and MFA calculation of $Q_0 = Q(H_b = 0)$ for $H_1 = 1.08$ H_1^{crit}. The H_2 data are normalized to H_1^{crit} for comparison purposes [27].

occurrence of the metamagnetic anomalies is observed only in creating an asymmetry in the Q-change that is associated with them, which is essentially the same behavior as seen in the calculation. In contrast to the calculations, however, an asymmetric broadening of only one of the metamagnetic onset region is not observed, which might be associated with the limited H_b-resolution that was experimentally achieved.

The effective plateau effect in Q is now compared in both simulations and experiments. For this, the plateau is quantified by means of Q_0, which is the average value of Q at $H_b = 0$ for the same H_1/H_1^{crit}-ratio as a function of H_2. This particular quantity is represented exemplarily with bigger points in Fig. 6.5(a). Fig. 6.5(b) shows the experimental Q_0 as a function of H_2 for the same section of the phase space, namely, $H_1 = 1.08$ H_1^{crit}. The H_2-axis is normalized to H_1^{crit} for comparison with the theoretical data, shown in Fig. 6.5(c). For small H_2 amplitudes, Q_0 shows a linear dependence with H_2 and becomes sub-linear only for larger enough $|H_2|$ amplitudes. This analysis is fully consistent with the results of our simulations shown in Fig. 6.5(c) that displays a very similar qualitative behavior. The slope of Q_0 with H_2, shown in Fig. 6.5(b, c) seems to differ in between simulations and experiments by about 30%. These quantitative differences might be due to the fact that experiments and simulations are done in a very different P/τ_M and T/T_C parameter ranges and thus both systems show very different relaxation time scales which could potentially affect the relative effect of a non-zero H_2 onto the overall dynamics. Also, simulations here correspond to a mean-field model, in which spin-fluctuations are neglected.

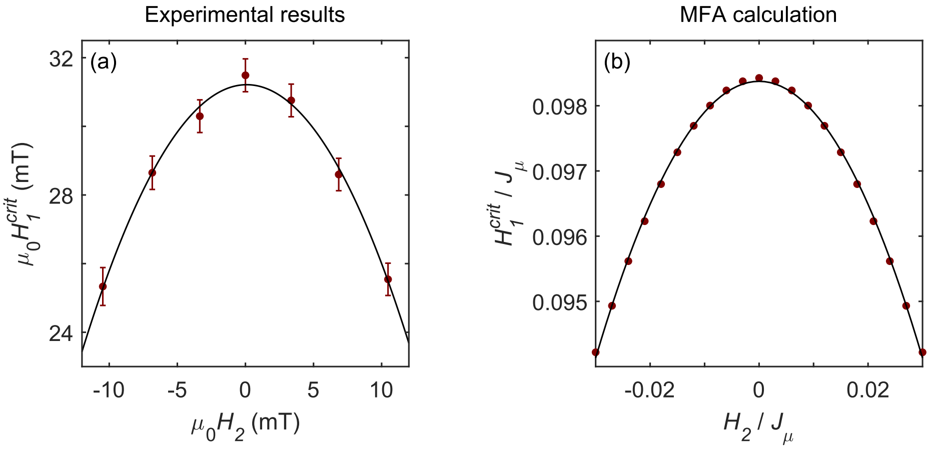

Figure 6.6: (a) Experimental and (b) theoretical critical field H_1^{crit} vs. H_2. In both figures, dark-red dots represent the actual data and the solid-black line represent least-squares fits to a parabolic function [27].

Another aspect analyzed in detail is the H_2 dependence of the critical point. Figs. 6.6(a, b) show the experimental and theoretical H_1^{crit}-values as a function of H_2. In both cases a quadratic decrease of the critical field amplitude as a function of H_2 is identified. The solid-black lines represent a least-squares fitting to a parabolic function centered around $H_2 = 0$, providing in both cases a very large coefficient of determination $R^2 > 0.995$. As $|H_2|$ increases while keeping H_1 constant, the total field amplitude also increases. Correspondingly, the total amplitude of $H(t)$ can become larger than H_1^{crit} for the H_2-free case, and the system will transition into the dynamic dPM phase, even if H_1 alone is smaller than the critical field amplitude [28]. Thus, by increasing H_2, while keeping H_1 constant, H_1^{crit} will decrease monotonously. Here, the H_1^{crit} vs. H_2 dependence is quadratic, at least for a substantial range of H_2.

Given the one-to-one correspondence in between H_1^{crit} and P_c determining the location of the critical point, as explained in Chapter 5, one can deduce that for increasing H_2, P_c should decrease in a similar fashion as H_1^{crit}, which is different from what was previously reported [8]. To our understanding, the reason for this discrepancy with previous theoretical work, in which no relevant P_c vs. H_2 dependence was observed, is the fact that the values of H_2 amplitudes used in this previous study were too small in comparison to the fundamental amplitude to detect any substantial change in P_c [8].

To complete this comparative analysis for both experiments and simulations and provide an overall perspective, it is worthwhile to have a closer look at ΔH.

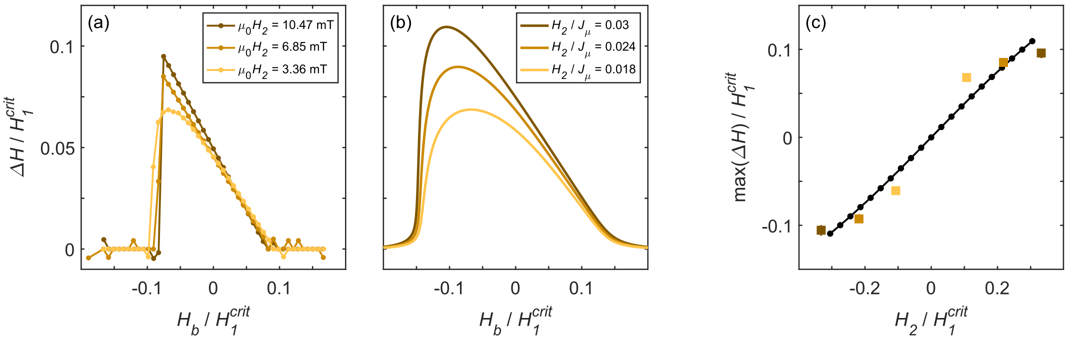

Figure 6.7: (a) Experimental and (b) theoretical ΔH as a function of H_b in the dPM phase with $H_1 = 1.08\ \mathrm{H_1^{crit}}$. All the data is normalized to H_1^{crit} for comparison purposes. (c) Maximum ΔH as a function of H_2 showing the monotonously increasing deviations in the dPM phase with $H_1 = 1.08\ H_1^{crit}$. Black data correspond to MFA calculations while colored squares correspond to experimental data [27].

Fig. 6.7(a) shows $\Delta H/H_1^{crit}$ as a function of the bias field H_b normalized to H_1^{crit} for several H_2 amplitudes at the same fixed $H_1 = 1.08\ H_1^{crit}$ condition of the phase space. Here, the three curves show triangular shapes whose width is nearly identical in all three cases. The range of significant ΔH deviations fully coincides with the conventional dPM regime. Fig. 6.7(b) shows as a comparison theoretical $\Delta H/H_1^{crit}$ vs. H_b/H_1^{crit}-data for the same $H_1/H_1^{crit} = 1.08$ ratio. In these cases, we also observe an asymmetric near triangular shape, with magnitudes that are very similar to those in Fig. 6.7(a). Here, the behavior close to the maximum is far smoother if compared with experimental data due to the higher H_b-resolution achievable in theoretical studies. The relative width of ΔH differs in between simulations and experiments. This is due to the fact that different effective P/τ_M-values are being used, which lead to different stability ranges of the conventional PM region in the normalized dynamic phase space [28, 29].

Figs. 6.7(a, b) show that the width of ΔH in the renormalized space is identical for all H_2-amplitudes. Thus, the widening of ΔH with H_2 in the PM phase space that was observed in Fig 6.2(b) is simply due to the H_1^{crit} vs. H_2 dependence rather than a genuine widening of the conventional dPM region itself. In other words, H_2 affects the magnitude of the critical point without disturbing the overall dPM phase layout in the properly renormalized H_1/H_1^{crit}-scale.

In Fig. 6.7(c), the maximum of $\Delta H/H_1^{crit}$ is shown as a function H_2/H_1^{crit}. Here, the black dots represent MFA calculation, whereas the colored squares represent the experimental values, whose error bars are comparable to the size of the squares. The MFA calculations, show an almost linear increase with H_2, in agreement with the almost linear increase of Q_0 with H_2 shown in Fig. 6.5(c). Both experiments and simulations agree well in the magnitude of $\Delta H/H_1^{crit}$. For larger H_2/H_1^{crit}-values, the experimental max(ΔH)/H_1^{crit} seem to exhibit more of a tendency towards saturation than can be seen in simulations. This might be associated with the fact that the experimental $\Delta H/H_1^{crit}$ vs. H_b/H_1^{crit} curves appear somewhat truncated and thus, their actual measured maximum might be slightly reduced in comparison to the respective theoretical curves for large H_2 amplitudes.

As concluding remarks from this analysis, both the simulations and experiments point towards very specific symmetries of ΔH, as well as the phase space behavior of Q in presence of a general $H(t)$ sequence. In absence of H_2, the inversion of $H_b \rightarrow -H_b$ in the magnetic field signal leads to exactly $Q \rightarrow -Q$, i.e., the time-reversal symmetry. At the same time, in absence of H_b, it is observed that the inversion of $H_2 \rightarrow -H_2$ also leads to $Q \rightarrow -Q$, as one can exemplarily see in Figs. 6.5(b, c). However, if now both H_b and H_2 are non-zero, then the opposite $Q \rightarrow -Q$ state is accessed with $H_b \rightarrow -H_b$ and $H_2 \rightarrow -H_2$. This antisymmetric feature is necessarily preserved in the deviations so that $\Delta H(H_b, H_2) = -\Delta H(-H_b, -H_2)$, which is what we observe in the entirety of our investigation. Following this observation, it is easy to show that $H^*(H_b, H_2) = -H^*(-H_b, -H_2)$, which in and by itself is not a trivial observation.

6.3.3 Scaling properties in the presence of a generalized conjugate field

In sections 6.3.1 and 6.3.2, a generalized conjugate field has been constructed for arbitrary periodic $H(t)$ waveforms, which is fundamentally defined such that the time-reversal symmetry of the $Q(P, H^*)$ phase space is restored. Furthermore, such generalized H^* has been experimentally quantified in the entire dynamic phase space in the vicinity of the critical point, and shows good agreement with the theoretical calculations within the MFA model.

However, there is still one key piece missing in the verification of H^* as a conjugate field of Q, namely, the quantification of the scaling behaviors of Q in the (P, H^*) phase space. Indeed, if H^* really represents the conjugate field of Q, then, as described in Chapter 5, at exactly $P = P_c$ [20],

$$Q \propto (H^{*})^{1/\delta_d}. \tag{6.8}$$

Thus, in the vicinity of P_c, the entire phase space behavior of Q should be described by the dynamic analog of the Arrott-Noakes equation-of-state as [32],

$$\left(\frac{H^{*}}{Q}\right)^{1/\gamma_d} = \frac{P - P_C}{P_1} + \left(\frac{Q}{Q_1}\right)^{1/\beta_d}. \tag{6.9}$$

In order to verify the scaling behaviors of Q in the dynamic phase space with the generalized conjugate field, extended high-resolution MFA simulations were conducted. For this purpose, the phase space behavior of $Q(P, H_b)$ is quantified for several H_2-values and for P and H_1 conditions, in which metamagnetic anomalies are basically inexistent. First, the absence of metamagnetic anomalies in the vicinity of P_c is required because such metamagnetic tendencies are a deformation of the dynamic phase space, that is absent in eq. (6.9), as explained in Chapter 5. Hereby, the $Q(P, H_b)$ phase space behavior in this section is calculated with $T/T_C = 0.8$ and $H_1/J_\mu = 0.2$, which leads to sufficiently fast dynamics to significantly suppress metamagnetic anomalies in mean-field calculations [28, 29].

Fig. 6.8(a) shows as a color map $Q(P, H_b)$ with $H_2 = 0$ and Fig. 6.8(b) shows the corresponding χ_Q. Here, the absence of any relevant metamagnetic anomalies is verified, which makes these data suitable for the scaling analysis. Fig. 6.8(b) also shows that the critical regime, i.e. the yellow region with very large χ_Q-values is only significant in a narrow region of the dynamic phase space that extends over $L_P = 0.3\tau_M$ in the P-axis and $L_H = 3\ 10^{-4}\ J_\mu$ in the H^{*}-axis. Once more, following

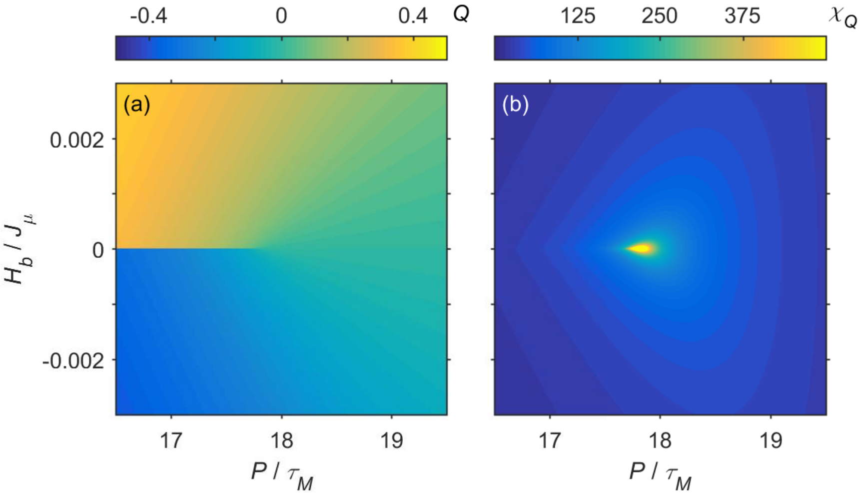

Figure 6.8: (a) Color-coded map of the phase space behavior of $Q(P, H_b)$ in the close vicinity of P_c with $T/T_C = 0.8$ and $H_1/J_\mu = 0.2$ (b) Color-coded map of χ_Q in the same phase space as (a), showing negligible metamagnetic tendencies in the dPM phase.

the criterion established in Chapter 5, the phase-space segment utilized to calculate the scaling of Q, is determined by $\pm 3L_H$ and $\pm 3L_P$ in the vicinity of P_c. While, in principle, the presence of a non-zero H_2-component could substantially modify such critical regime, the L_P and L_H-values of the $H_2 = 0$ case are utilized for all the different maps in the following.

Figures 6.9(a-c) show the $Q(P, H^*)$ phase space behaviors for several different H_2-values in the critical regime previously established. In the here presented cases, all key aspects of the dynamic phase space are clearly observed, including the time-reversal symmetry restored upon utilizing H^*. Hereby, the existence of a non-zero H_2 component, does not seem to substantially modify the $Q(P, H^*)$ phase space behavior, which look basically identical. This is true even if H_2 is of the same order of magnitude as H_b in the critical regime stablished by L_H.

Now, each of these data sets are assumed to follow eq. (6.9) independently. In contrast to the experimental results of Chapter 5, it is not necessary to consider

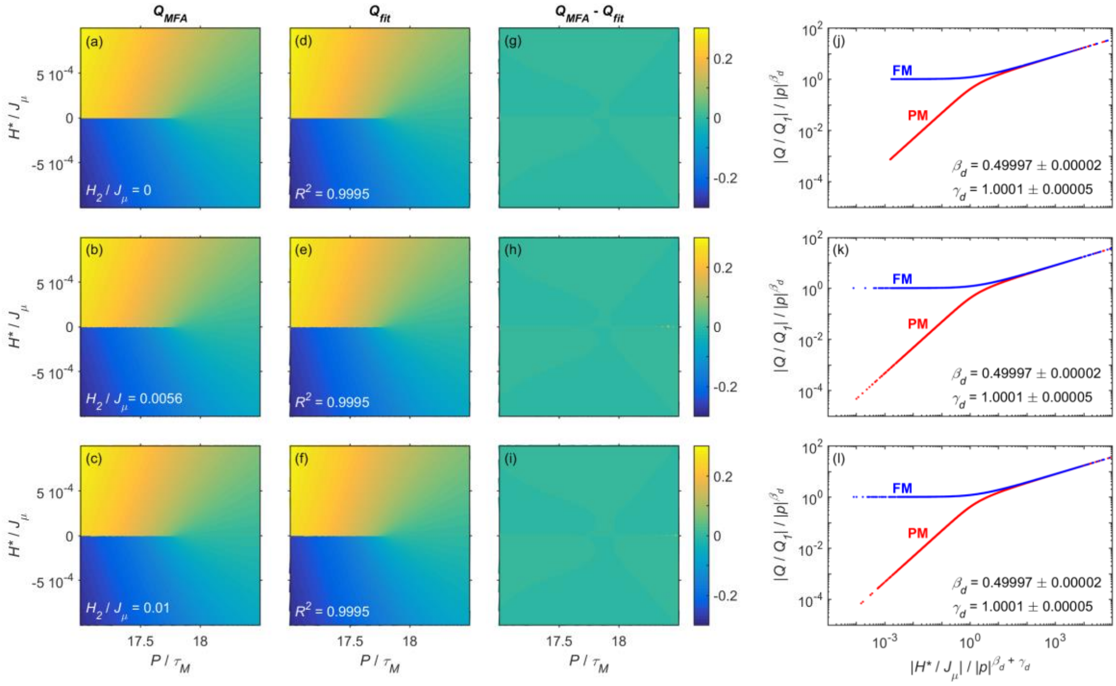

Figure 6.9: (a-c) Color-coded maps of $Q(P, H^*)$ for several H_2-values in the here determined critical regime. (d-f) Color-coded maps of the least squares fittings to the data in (a-c) using eq. (6.9). (g-i) Color-coded maps of the residual from the fitting procedures showing negligible deviations. Color bars in the right-hand side of (g-i) apply to all the color maps on their left in each row. (j,l) Arrott plot of the renormalized order parameter $|Q/Q_1|/|p|^{\beta_d}$ vs. $|H^*/J_\mu|/|p|^{\gamma_d+\beta_d}$. Blue points represent the data of the dFM phase while red points represent the data of the dPM phase.

P_c-distributions here. While the MFA calculations do exhibit some systematic deviations very close to P_c, they correspond to discretization limitations, that do not impact the fit relevantly [33, 34]. Given the non-linearity of eq. (6.9), instead of fitting $Q(P, H^*)$, which would require numerical calculations of Q in the entire phase space, here, P is fitted as a function of H^* and Q as,

$$P(H^*,\ Q) = P_c + P_1\left[\left(\frac{H^*}{Q}\right)^{1/\gamma_d} - \left(\frac{Q}{Q_1}\right)^{1/\beta_d}\right], \tag{6.10}$$

which gives a simple closed expression for this particular analysis. Figs. 6.9(d-f) show the least-squares fits of eq. (6.10). Here, one observes that the key aspects of the $Q(P, H^*)$ phase space are in excellent agreement with the MFA calculations. These results lead to a coefficient of determination values $R^2 > 0.9995$ in all the cases, which is an excellent indicator of the quality of the results. Figs. 6.9(g-i) show the residual differences between the MFA calculations data and fits. Given that P is the dependent variable in the fitting, the residual differences ΔQ are calculated by error propagation as,

$$Q_{MFA} - Q_{fit} = \Delta Q = \frac{1}{P_1\left[\frac{-H^{*1/\gamma_d}}{\gamma_d}\ Q^{\frac{-1-\gamma_d}{\gamma_d}} - \frac{1}{\beta_d\ Q_1^{1/\beta_d}}\ Q^{\frac{1-\beta_d}{\beta_d}}\right]}\Delta P. \tag{6.11}$$

Here, the residual differences show negligible systematic deviations in the entirety of the dynamic phase space, which provides further insight on the quality of the results.

Provided the quality of the least-squares fits, the renormalized order parameter $|Q/Q_1|/|p|^{\beta_d}$ is now represented as a function the renormalized bias field $|H^*/J_\mu|/|p|^{\gamma_d+\beta_d}$ in Figs. 6.9(j-l), in order to observe the scaling of Q in the vicinity of P_c (see Appendix C). This procedure is identical to the analysis conducted in Chapter 5, Fig. 5.9. Such figures show an excellent scaling of the renormalized Q, both in the curves corresponding to the dPM phase (red) and the dFM phase (blue). Furthermore, the scaling extends over eight decades in the renormalized field and five in the renormalized order parameter in all of the here presented cases.

These results provide critical exponents $\beta_d = 0.5$ and $\gamma_d = 1$, which are the critical exponents expected in mean-field models and, particularly, in the $H_2 = 0$ case where $H^* = H_b$ exactly. Therefore, these results prove the existence of generalized conjugate fields H^* for arbitrary $H(t)$ field sequences without HWA.

H_2/J_μ	β_d	γ_d	P_c/τ_M	R^2
0,0000	0,49997 ± 0.00002	1,0001 ± 0.00005	17,7803 ± 0.0002	0,99951
0,0011	0,49997 ± 0.00002	1,0002 ± 0.00005	17,7802 ± 0.0002	0,99951
0,0022	0,49997 ± 0.00002	1,0002 ± 0.00005	17,7800 ± 0.0003	0,99951
0,0033	0,49997 ± 0.00002	1,0002 ± 0.00005	17,7795 ± 0.0003	0,99951
0,0044	0,49998 ± 0.00002	1,0001 ± 0.00005	17,7789 ± 0.0002	0,99951
0,0056	0,49997 ± 0.00002	1,0001 ± 0.00005	17,7781 ± 0.0002	0,99952
0,0067	0,49997 ± 0.00002	1,0002 ± 0.00005	17,7772 ± 0.0003	0,99952
0,0078	0,49998 ± 0.00002	1,0002 ± 0.00005	17,7760 ± 0.0003	0,99952
0,0089	0,49997 ± 0.00002	1,0001 ± 0.00005	17,7747 ± 0.0002	0,99953
0,0100	0,49997 ± 0.00002	1,0001 ± 0.00005	17,7732 ± 0.0002	0,99953

Table 6.1: Results of the scaling analysis of $Q(P, H^*)$ for different H_2-values.

The critical exponents β_d and γ_d are shown to be of the same universality class as in the case of $H(t)$ sequences with HWA.

The analysis in Fig. 6.9, which show exemplarily the scaling results for three H_2-values, are repeated for further data sets with additional H_2-amplitudes. The results of these analyses are represented in Table Table 6.1. In all the cases, excellent scaling is observed with $R^2 > 0.9995$ and critical exponents that match those of the mean-field model, further verifying the quality of the results. Likewise, one observes the monotonous decrease of P_c as a function of H_2, as explained in conjunction with Fig. 6.6. It is also interesting to mention that the critical regime does not seem to become narrower for larger H_2-amplitudes. Instead, R^2 seems to monotonously increase with H_2, even if only minimally. In order to observe further deviations, one would probably have to consider larger asymmetries in $H_{din}(t)$, for which larger H_2/H_1-ratios would be required.

6.4 Conclusions & Outlook

In this chapter, the existence and characteristics of a generalized conjugate field H^* of the dynamic order parameter Q within the DPT has been studied for arbitrary magnetic field sequences that do not necessarily have half-wave asymmetry. For this purpose, Ising-like spin systems have been studied, both experimentally and theoretically, in the presence of magnetic field sequences with three different Fourier components: a fundamental harmonic frequency, a constant bias field, and a second harmonic field component.

The second harmonic field contribution acts as an additional bias field whose effects are most relevant in the conventional dPM phase. A properly defined H^* leads to a complete restoration of the time-reversal symmetry in the entire dynamic phase space. The here proposed procedure to calculate such a conjugate field, considering an expansion around the conventional bias field value, is applicable to any arbitrary magnetic field sequences, independently on the number of even Fourier components within $H(t)$.

Together with the additional bias field induced by the second harmonic Fourier component of $H(t)$, a shift of the critical point has also been observed and quantified. This shift happens because, overall, the presence of such field component leads to a stronger effective field amplitude, that leads to a change in P_c. Thus, while the odd $H(t)$ Fourier components do not contribute to H^*, given that they do not break the HWA, the even components contribute both to the effective field amplitude and H^*. It is reasonable to expect, likewise, a decreasing relevance of further Fourier components for the dynamics of the system, possibly with an order dependent decreasing relevance given that the corresponding periods are increasingly further away from the periods close to the critical region.

Finally, the scaling behaviors of Q in the (P, H^*) phase space has been investigated theoretically. Here, it has been found that Q still undergoes the expected scaling with critical exponents that are of the same universality class of the mean-field Ising model, as expected.

Thus, the issue of generalized conjugate fields in the DPT has been investigated in a comprehensive manner. The conjugate field of the dynamic order parameter is not solely composed of the bias field in the most general scenario.

Instead, this generalized conjugate field can be determined from sufficiently complete phase space data. As an outlook, it would be relevant to verify whether even more complex $H(t)$ field sequences still allow for the definition of H^* and its practical computation.

Chapter References

[1] T. Tomé and M. J. de Oliveira, *Dynamic phase transition in the kinetic Ising model under a time-dependent oscillating field*, Phys. Rev. A **41**, 4251 (1990).

[2] P. Riego, P. Vavassori, and A. Berger, *Towards an understanding of dynamic phase transitions*, Physica B **549**, 13-23 (2018).

[3] E. Oblak, P. Riego, L. Fallarino, A. Martínez-de-Guerenu, F. Arizti and A. Berger, *Ultrasensitive transverse magneto-optical Kerr effect measurements by means of effective polarization change detection*, J. Phys. D: Appl. Phys. **50**, 23LT01 (2017).

[4] E. Oblak, P. Riego, A. García-Manso, A. Martínez-de-Guerenu, F. Arizti, I. Artetxe and A. Berger, *Ultrasensitive transverse magneto-optical Kerr effect measurements using an effective ellipsometric detection scheme,* J. Phys. D: Appl. Phys. **53**, 205001 (2020).

[5] C. Martín Valderrama, M. Quintana, A. Martínez-de-Guerenu, T. Yamauchi, Y. Hamada, Y. Kurokawa, H. Yuasa, and A. Berger, *Insertion layer magnetism detection and analysis using transverse magneto-optical Kerr effect (T-MOKE) ellipsometry*, J. Phys. D: Appl. Phys. **54**, 435002 (2021).

[6] C. Martín Valderrama, M. Quintana, A. Martínez-de-Guerenu, T. Yamauchi, Y. Hamada, Y. Kurokawa, H. Yuasa, and A. Berger, *Sensitivity and reproducibility of transverse magneto-optical Kerr effect (T-MOKE) ellipsometry*, J. Phys. D: Appl. Phys. **55**, 435007 (2022).

[7] O. Idigoras, A. K. Suszka, P. Vavassori, B. Obry, B. Hillebrands, P. Landeros, A. Berger, *Magnetization reversal of in-plane uniaxial Co films and its dependence on epitaxial alignment*, J. Appl. Phys. **115**, 083912 (2014).

[8] D. T. Robb and A. Ostrander, *Extended order parameter and conjugate field for the dynamic phase transition in a Ginzburg-Landau mean-field model in an oscillating field*, Phys. Rev. E **89**, 022114 (2014).

[9] Z. Huang, Z. Chen, F. Zhang and Y. Du, *Dynamic phase transition in the Heisenberg model under a time-dependent oscillating field*, Phys. Lett. A **338**, 485-493 (2005).

[10] N. Fujiwaraa, T. Kobayashi, and H. Fujisaka, *Dynamic phase transition in a rotating external field*, Phys. Rev. E **75**, 026202 (2007).

[11] P. A. Rikvold, H. Tomita, S. Miyashita, and S. W. Sides, *Metastable lifetimes in a kinetic Ising model: Dependence on field and system size*, Phys. Rev. E **49**, 5080 (1994).

[12] S. W. Sides, P. A. Rikvold, and M. A. Novotny, *Kinetic Ising Model in an Oscillating Field: Finite-Size Scaling at the Dynamic Phase Transition*, Phys. Rev. Lett. **81**, 834 (1998).

[13] S. W. Sides, P. A. Rikvold, and M. A. Novotny, *Kinetic Ising model in an oscillating field: Avrami theory for the hysteretic response and finite-size scaling for the dynamic phase transition*, Phys. Rev. E **59**, 2710 (1999).

[14] M. Acharyya, *Nonequilibrium phase transition in the kinetic Ising model: Divergences of fluctuations and responses near the transition point*, Phys. Rev. E **56**, 1234 (1997).

[15] M. Acharyya, *Multiple dynamic transitions in an anisotropic Heisenberg ferromagnet driven by polarized magnetic field*, Phys. Rev. E **69**, 027105 (2004).

[16] D. T. Robb. P. A. Rikvold, A. Berger, and M. A. Novotny, *Conjugate field and fluctuation-dissipation relation for the dynamic phase transition in the two-dimensional kinetic Ising model*, Phys. Rev. E 76, 021124 (2007).

[17] D. T. Robb, Y. H. Xu, O. Hellwig, J. McCord, A. Berger, M. A. Novotny, and P. A. Rikvold, *Evidence for a dynamic phase transition in [Co/Pt]3 magnetic multilayers*, Phys. Rev. B **78**, 134422 (2008).

[18] A. Berger, O. Idigoras, and P. Vavassori, *Transient Behavior of the Dynamically Ordered Phase in Uniaxial Cobalt Films*, Phys. Rev. Lett. **111**, 190602 (2013).

[19] O. Idigoras, P. Vavassori, and A. Berger, *Mean field theory of dynamic phase transitions in ferromagnets*, Physica B 407, 1377-1380 (2012).

[20] R. A. Gallardo, O. Idigoras, P. Landeros, and A. Berger, *Analytical derivation of critical exponents of the dynamic phase transition in the mean-field approximation*, Phys. Rev. E **86**, 051101 (2012).

[21] R. J. Glauber, *Time-Dependent Statistics of the Ising Model*, J. Math. Phys. **4**, 294 (1963).

[22] T. Tomé and M. J. de Oliveira, *Dynamic phase transition in the kinetic Ising model under a time-dependent oscillating field*, Phys. Rev. A **41**, 4251 (1990).

[23] S. Blundell, *Magnetism in Condensed Matter* (Oxford University Press, Great Britain, 2001).

[24] N. Goldenfeld, *Lectures on Phase Transitions and the Renormalization Group* (CRC Press, 1992).

[25] E. Vatansever and N. G. Fytas, *Dynamic phase transitions in the presence of quenched randomness*, Phys. Rev. E **97**, 062146 (2018).

[26] Y. Yüksel, *Dynamic phase transition properties and metamagnetic anomalies of kinetic Ising model in the presence of additive white noise*, Physica A **580**, 126172 (2021).

[27] M. Quintana and A. Berger, *General existence and determination of conjugate fields in dynamically ordered magnetic systems*, Phys. Rev. E **104**, 044125 (2021).

[28] P. Riego, P. Vavassori, and A. Berger, *Towards an understanding of dynamic phase transitions*, Physica B **549**, 13-23 (2018).

[29] P. Riego, P. Vavassori, and A. Berger, *Metamagnetic Anomalies near Dynamic Phase Transitions*, Phys. Rev. Lett. **118**, 117202 (2017).

[30] J. M. Marín Ramírez, E. Oblak, P. Riego, G. Campillo, J. Osorio, O. Arnache, and A. Berger, *Experimental exploration of dynamic phase transitions and associated metamagnetic fluctuations for materials with different Curie temperatures*, Phys. Rev. E **102**, 022804 (2020).

[31] M. Quintana, E. Oblak, J. M. Marín Ramírez, and A. Berger, *Experimental exploration of the vector nature of the dynamic order parameter near dynamic magnetic phase transitions*, Phys. Rev. B **102**, 094436 (2020).

[32] A. Arrott & J. E. Noakes, *Approximate Equation of State For Nickel Near its Critical Temperature*, Phys. Rev. Lett. **19**, 786 (1967).

[33] G. Berkolaiko and M. Grinfeld, *Type of dynamic phase transition in bistable equations*, Phys. Rev. E **76**, 061110 (2007).

[34] X. Shi and G. Wei, *Effective-field theory on the transverse Ising model under a time oscillating longitudinal field*, Phys. Lett. A **374**, 1885 (2010).

Chapter 7: Conclusions & Outlook

In this work, aspects related to the occurrence of magnetic phase transitions in nanoscale-designed ferromagnetic thin films have been investigated in a detailed manner. Here, different types of phase transition have been studied both experimentally and theoretically. From this work, several general conclusions can be drawn.

Firstly, it has been shown that thin films exhibiting exchange-graded profiles provide an excellent basis for tuning many aspects of FM materials' behavior that are otherwise extremely difficult or basically impossible to control. Such exchange-profiles lead to thermodynamic behaviors dominated by a local Curie temperature profile on sizes in the 1-2 nm length-scale, leading to the formation of separate quasi-PM/FM regions that can expand or reduce with temperature. This is a counterintuitive observation given that ferromagnetism is a long-range collective phenomenon. The quasi-PM phase occurs in regions where T is larger than T_C^{loc} and, while formally ferromagnetically ordered, because the order parameter is non-zero, behaves as if it is in a PM state for all practical purposes.

In this regard, it has been shown that EGPs can be designed to modify in a continuous fashion the occurrence of the TPT and the subsequent equilibrium critical exponents, hereby circumventing universality. Given that critical exponents can otherwise only be tuned at surfaces, this experimental observation provides an intriguing basis for further theoretical and experimental research in all-interfaced materials, with gradual changes of exchange energy. Not only that, the here explored EGPs are shown to exhibit hysteresis-free behaviors over extended temperature ranges, making them possibly relevant for a number of technologies including, for instance, magnetic-refrigeration.

The EGPs envisioned and demonstrated in Chapter 4 are a proof-of-concept of complex depth-dependent profiles' capabilities towards data storage technologies. Here, separate FM regions in the film are shown to exhibit strong temperature dependent interactions with each other, leading to temperature dependent bias fields over extended temperature ranges. In this regard, it has been shown that such profiles can be used to tune the temperature dependence of coercivity, leading to a coercivity plateaus over extended T-ranges of 75 K.

Beyond these results, one key aspect that is worthwhile mentioning is that there is nothing unique about the here employed Co-Ru alloy combinations, as long as the non-magnetic dopant causes an effective reduction of the exchange-energy. Exchange-graded profiles are known to be compatible with Ni-Cu or Co-Cr alloys, for example, and they should be compatible with materials commonly employed in magnetic devices. Furthermore, the profiles can be designed in such a way that they operate at any given temperature, making them suitable for applications both at cryogenic or room temperatures and further enhancing the significance of EGPs' applicability.

At this point, given the fact that the profiles explored in Chapter 4 are envisioned for thin film technologies, it would be most relevant to explore if and how EGPs are compatible with RKKY-type interactions. Here, by adding a purely NM layer, such as Ru, together with a EGP, one could obtain separate FM regions exhibiting ferromagnetic and/or antiferromagnetic coupling strengths. Hereby, such type of antiferromagnetic coupling could be strongly temperature dependent as well, which could be potentially relevant for certain applications.

Chapters 5 and 6 explored the occurrence of dynamic phase transitions in FM homogeneous thin films. In Chapter 5, it has been experimentally observed in ultrathin Co films that the scaling behaviors and critical exponents in such DPT are compatible with those of the 2D Ising model, as expected. However, for the same film thickness they are shown to differ from those of the TPT of a 2D Ising system, and instead agree with those of the 3D Ising model. The here obtained results point towards different length-scales at which a dimensional crossover occurs for the TPT and DPT, which is a phenomenon not explored so far, neither theoretically nor experimentally. In this regard it would be most relevant to conduct further theoretical research in Monte-Carlo simulations to provide further insights about such crossover dimensionality relations, as well as the correlation length in the DPT.

Experimentally, it would be significant to explore if such dimensionality crossover can be observed in thin film systems with larger thickness. This is not a trivial task because thicker films are known to exhibit metamagnetic anomalies, that constrain the critical regime to rather narrow P-ranges. One could conduct similar experiments in perpendicularly magnetized systems, given that, here, the

DW width is generally smaller and, thus, the dimensional crossover could occur at lower thicknesses.

Parallel, the existence of arbitrary conjugate fields in the DPT has also been explored. Here, it has been shown that one can construct a generalized conjugate field for any time-dependent field sequence, even if they do not have half-wave asymmetry. The conducted theoretical analysis within the mean-field model perfectly matches the experimental results and, furthermore, shows that the critical exponents in the rescaled conjugate field agree with the expected mean-field model values, further verifying the significance of these results.

Finally, provided the here obtained results, it would be most relevant to learn if EGPs also lead to a modification of the dynamic phase space behavior of Q and particularly, the dynamic critical exponents. Indeed, while the attention of the EGP work in this thesis was focused on their thermodynamic equilibrium properties, their dynamic behaviors could be explored in a rather similar way. This is because the key experimental properties of films with EGPs, such as M_s or H_c can be designed similarly, so that the dynamic magnetization behaviors can be investigated with the same type of tools and procedures, and with the same level of data quality.

Appendix A: Stoner-Wohlfarth Model

The Stoner-Wohlfarth model considers a homogeneous magnetic state in which collinear spins generate a magnetization vector $\boldsymbol{M}$ of constant modulus. Hereby, $\boldsymbol{M}$ can rotate as the magnetic field strength H changes. In the original Stoner-Wohlfarth model, the ferromagnet is assumed to have a first-order uniaxial magnetic anisotropy energy density K_1. Here, a second-order energy density K_2 is considered as well to better mimic the second order magnetic anisotropy of Co. Thus, assuming all the field axes are in the same plane, that is in the plane of a thin film in this case, then the free energy density of the system is,

$$\mathcal{F} = -\mu_0 H M_s \cos(\varphi) + K_1 \sin^2(\nu - \varphi) + K_2 \sin^4(\nu - \varphi), \tag{A.1}$$

where ν is the angle between easy magnetization axis and field direction, and φ represents the angle between the magnetization vector and field direction. Here, in absence of external magnetic field, i.e. $H = 0$, the energy of the system is minimized if $\varphi = \nu$, namely, if magnetization vector is parallel to the EA. More generally, in presence of $H \neq 0$, the magnetization direction can be obtained by minimizing the energy density of the system, as,

$$\frac{\partial \mathcal{F}}{\partial \varphi} = \mu_0 H M_s \sin(\varphi) - K_1 \sin(2(\nu - \varphi)) - 4 K_2 \sin^3(\nu - \varphi) \cos(\nu - \varphi) = 0\,, \tag{A.2}$$

For the quantification of the equilibrium state, the existence of a metastable local energy minimum requires for the second derivative to be positive, namely,

$$\begin{aligned} \frac{\partial^2 \mathcal{F}}{\partial \varphi^2} = {} & -\mu_0 H M_s \cos(\varphi) + 2K_1 \cos(2(\nu - \varphi)) \\ & - 4K_2 \sin^2(\nu - \varphi)\left[\sin^2(\nu - \varphi) - 3\cos^2(\nu - \varphi)\right] > 0 \end{aligned} \tag{A.3}$$

Eq. (A.2) is solved for φ following the Newton-Raphson method with a precision better than 10^{-8}. The evaluation of the $M(\nu, H)$ component parallel to the field direction shown in Chapter 3 is then computed by considering $M = M_s \cos\varphi$.

Appendix B: Atomistic Model of Graded FM Thin Films

Here, the detailed derivation of the thermodynamic behavior of exchange-graded ferromagnetic thin films in the mean-field Heisenberg model is derived. As a starting point, the Hamiltonian of the system is considered as,

$$\mathcal{H} = -\sum_{\{i,j\}} J_{ij}\ \boldsymbol{s}_i\boldsymbol{s}_j + \sum_{i} k_1[1-(s_i^x)^2] - \mu_0\sum_{i} \boldsymbol{H}_i\ \mu_i\boldsymbol{s}_i\,. \tag{B.1}$$

The first term in the Hamiltonian corresponds to the nearest-neighbors exchange-energy, with exchange-coupling constant J_{ij} that, in this particular case, varies as a function of the depth of the film, and therefore as a function of the location of the pair of adjacent dimensionless spin vectors $\boldsymbol{s}_i$ and $\boldsymbol{s}_j$. The second energy term is the first-order uniaxial anisotropy, with anisotropy energy k_1, set in-plane along the direction $\hat{\boldsymbol{x}}$ without loss of generality. Here, k_1 is assumed to be constant along the film depth. The third energy term is the Zeeman energy with an external field $\boldsymbol{H}_i$ acting on the spin $\boldsymbol{s}_i$. The magnetic moments magnitude $\mu_i = \mu$ are assumed to be homogeneous along the film depth as well, which is a simplification with respect to real Co-Ru alloys. In this model, the demagnetizing factors are essentially negligible given the in-plane geometry of the system.

In order to study the mean-field equations, an expansion as $\boldsymbol{s}_i = \langle \boldsymbol{s}_i \rangle + \delta\boldsymbol{s}_i$ is considered, where $\delta\boldsymbol{s}_i$ are the spin-fluctuations. Then, the second order fluctuation terms $O(\delta\boldsymbol{s}_i\ \delta\boldsymbol{s}_j) \sim O(\delta\boldsymbol{s}^2)$ are neglected such that,

$$\begin{aligned} \boldsymbol{s}_i\boldsymbol{s}_j &= (\langle \boldsymbol{s}_i\rangle + \delta\boldsymbol{s}_i)\big(\langle \boldsymbol{s}_j\rangle + \delta\boldsymbol{s}_j\big) \\ &= \langle \boldsymbol{s}_i\rangle\langle \boldsymbol{s}_j\rangle + \langle \boldsymbol{s}_i\rangle\delta\boldsymbol{s}_j + \langle \boldsymbol{s}_j\rangle\delta\boldsymbol{s}_i + \delta\boldsymbol{s}_i\delta\boldsymbol{s}_j \\ &\approx -\langle \mathrm{s_i}\rangle\langle \mathrm{s_j}\rangle + \langle \mathrm{s_i}\rangle\mathrm{s_j} + \langle \mathrm{s_j}\rangle\mathrm{s_i}, \end{aligned} \tag{B.2}$$

$$\begin{aligned} (s_i^x)^2 &= (\langle s_i^x\rangle + \delta s_i^x)^2 \\ &= \langle s_i^x\rangle^2 + 2\langle s_i^x\rangle\delta s_i^x + \delta s_i^{x2} \\ &\approx -\langle s_i^x\rangle^2 + 2\,\langle s_i^x\rangle s_i^x. \end{aligned} \tag{B.3}$$

These approximations lead to the mean-field Hamiltonian $\mathcal{H}_{MF}$ of the form,

$$\begin{aligned} \mathcal{H}_{MF} = &\sum_{\{i,j\}} J_{ij}\ \langle \boldsymbol{s}_i\rangle\langle \boldsymbol{s}_j\rangle - \sum_{\{i,j\}} J_{ij}\ \big(\langle \boldsymbol{s}_i\rangle\boldsymbol{s}_j + \langle \boldsymbol{s}_j\rangle\boldsymbol{s}_i\big) + \sum_{i} k_1[1+\langle s_i^x\rangle^2] \\ &- \sum_{i} 2k_1\langle s_i^x\rangle s_i^x - \mu_0\,\mu\sum_{i} \boldsymbol{H}_i\ \boldsymbol{s}_i\,. \end{aligned} \tag{B.4}$$

Given that the behavior $\langle \boldsymbol{s}_i \rangle$ at different layers varies, one can only assume in-plane translational invariance. This means that $\langle \boldsymbol{s}_i \rangle = \langle \boldsymbol{s}_j \rangle = \langle \boldsymbol{s}_m \rangle$ only if $\boldsymbol{s}_i$ and $\boldsymbol{s}_j$ are spins that interact in the same mth plane. At this point, the summations are reformulated over the i and j coefficients. The here explored system is that of hcp Co $(10\underline{1}0)$, in which each layer has $n_{hcp} = 12$ nearest neighbors, with $n_l = 4$ atoms per layer; 4 of the layer below, 4 in the same plane, and 4 of the layer on top. The film each layer has N atoms, representing the lateral extent of the film. In these conditions, all the terms in the Hamiltonian become only function of the mth layer only, and thus,

$$\begin{aligned}\mathcal{H}_{\boldsymbol{MF}} = {} & \frac{Nn_l}{2}\sum_m [J^e_{m\text{-}1}\langle \boldsymbol{s}_{m\text{-}1}\rangle + J_m\langle \boldsymbol{s}_m\rangle + J^e_m\langle \boldsymbol{s}_{m+1}\rangle]\langle \boldsymbol{s}_m\rangle \\ & + N\sum_m k_1[1 + \langle s^x_m\rangle^2] - Nn_l\sum_m [J^e_{m\text{-}1}\langle \boldsymbol{s}_{m\text{-}1}\rangle + J_m\langle \boldsymbol{s}_m\rangle + J^e_m\langle \boldsymbol{s}_{m+1}\rangle]\boldsymbol{s}_m \\ & - 2N\sum_m \boldsymbol{k}_1\langle s^x_m\rangle s^x_m - \mu_0\,\mu\, N\sum_m \boldsymbol{H}_m\cdot \boldsymbol{s}_m\,,\end{aligned} \tag{B.5}$$

where $J^e_m = [J_m + J_{m+1}]/2$ represents the exchange coupling strength between interlayer atoms and J_m the coupling strength between intralayer atoms. Considering the lateral uniformity, they depend only on the film depth, and not on the lateral dimension. The terms in $\boldsymbol{s}_m$ are rearranged, so that they are under the influence of an effective mean-field $\boldsymbol{H}_{eff,m}$ of the form,

$$\mu_0\,\mu\boldsymbol{H}_{eff,\,m} = -n_l\,[J^e_{m\text{-}1}\langle \boldsymbol{s}_{m\text{-}1}\rangle + J_m\langle \boldsymbol{s}_m\rangle + J^e_m\langle \boldsymbol{s}_{m+1}\rangle] - 2\boldsymbol{k}_1\langle \boldsymbol{s}_m\rangle\widehat{x} - \mu_0\,\mu\boldsymbol{H}_m\,, \tag{B.6}$$

and thus, the Hamiltonian simplifies to,

$$\begin{aligned}\mathcal{H}_{\boldsymbol{MF}} = {} & \frac{Nn_l}{2}\sum_m [J^e_{m\text{-}1}\langle \boldsymbol{s}_{m\text{-}1}\rangle + J_m\langle \boldsymbol{s}_m\rangle + J^e_m\langle \boldsymbol{s}_{m+1}\rangle]\langle \boldsymbol{s}_m\rangle \\ & + N\sum_m \boldsymbol{k}_1[1 + \langle s^x_m\rangle^2] - \mu_0\,\mu N n_l\sum_m \boldsymbol{H}_{eff,\,m}\cdot \boldsymbol{s}_m\,.\end{aligned} \tag{B.7}$$

Equation (B.7) represents the mean-field Hamiltonian shown in eq. (4.4) in the main text. In order to compute the thermodynamic behavior of magnetization the partition function $\mathcal{Z}$ of the system is considered as,

$$\mathcal{Z} = \sum_{\{\boldsymbol{s}_m\}} \mathrm{e}^{-\mathcal{H}_{\mathrm{MF}}/k_B T}, \tag{B.8}$$

where $\{\boldsymbol{s}_m\}$ indicates the sum over all the microstates of all the m layers. Then, the free-energy density per unit area is expressed as,

$$\begin{aligned}\mathcal{F} &= -\,k_B T \log \mathcal{Z}\\ &= \sum_m \left[\frac{n_l}{2}\,[J_{m\text{-}1}\,\langle \boldsymbol{s}_{m\text{-}1}\rangle + J_m\,\langle \boldsymbol{s}_m\rangle + J_{m+1}\,\langle \boldsymbol{s}_{m+1}\rangle]\langle \boldsymbol{s}_m\rangle \;+\; \boldsymbol{k_1}[1+\langle s_m^x\rangle^2]\right]\\ &\quad -\,k_B T \log\left\{\sum_{\{\boldsymbol{s}_m\}} \mathrm{e}^{-\frac{\sum_{\mathrm{m}} \boldsymbol{H}_{eff,\,m}\,\boldsymbol{s}_m}{k_B T}}\right\}. \end{aligned} \qquad \text{(B.9)}$$

For convenience, $\mathcal{H}_0$ is defined as the first sum in eq. (B.9), that do not depend on $\boldsymbol{s}_m$, so that one obtains,

$$\mathcal{F} = \mathcal{H}_0 \;-\; k_B T\;\log\left\{\sum_{\{\boldsymbol{s}_m\}}\prod_m \mathrm{e}^{-\frac{\mu_0\,\mu\boldsymbol{H}_{eff,\,m}\,\boldsymbol{s}_m}{k_B T}}\right\}. \qquad \text{(B.10)}$$

The sum over all the microstates of the system can be made in the continuous limit, owning that $\boldsymbol{H}_{eff,\,m}\;\boldsymbol{s}_m = \left|\boldsymbol{H}_{eff,\,m}\right|\;|s_m|\cos\theta_m$. Thus, one obtains,

$$\begin{aligned}\sum_{\{\boldsymbol{s}_m\}}\prod_m \mathrm{e}^{-\frac{\mu_0\,\mu\boldsymbol{H}_{eff,\,m}\,\boldsymbol{s}_m}{k_B T}} &= \frac{1}{(4\pi)^M}\prod_m \int_0^{2\pi}\mathrm{d}\varphi_m \int_0^{\pi}\mathrm{d}\theta_m\;\mathrm{e}^{-\frac{\mu_0\,\mu H_{eff,\,m}\,s_m}{k_B T}\cos\theta_m}\sin\theta_m\\ &= \prod_m \frac{\sinh\left(\mu_0\,\mu\left|\boldsymbol{H}_{eff,\,m}\right|\,/k_B T\right)}{\mu_0\,\mu\left|\boldsymbol{H}_{eff,\,m}\right|\,/k_B T}. \end{aligned} \qquad \text{(B.11)}$$

Finally, one inserts eq. (B.11) into (B.10) as,

$$\mathcal{F} = \mathcal{H}_0 - k_B T \sum_m \log\left\{\frac{\sinh\left(\mu_0\,\mu\left|\boldsymbol{H}_{eff,\,m}\right|\,/k_B T\right)}{\mu_0\,\mu\left|\boldsymbol{H}_{eff,\,m}\right|\,/k_B T}\right\}. \qquad \text{(B.12)}$$

In order to calculate the magnetization component ς of the mth layer, one calculates the derivatives of $\mathcal{F}$ as,

$$\begin{aligned}\frac{M_m^{\varsigma}}{M_s^{0}} = \langle s_m^{\varsigma}\rangle = -\frac{\partial\mathcal{F}}{\partial\left(\mu_0 H_m^{\varsigma}\right)} &= \left[\coth\left(\frac{\mu_0\;\mu\left|\boldsymbol{H}_{eff,\,m}\right|}{k_B T}\right) - \frac{k_B T}{\mu_0\;\mu\left|\boldsymbol{H}_{eff,\,m}\right|}\right]\frac{H_{eff,\,m}^{\varsigma}}{\left|\boldsymbol{H}_{eff,\,m}\right|}\\ &= \mathcal{L}\left[\frac{\mu_0\;\mu\left|\boldsymbol{H}_{eff,\,m}\right|}{k_B T}\right]\;\frac{H_{eff,\,m}^{\varsigma}}{\left|\boldsymbol{H}_{eff,\,m}\right|}, \end{aligned} \qquad \text{(B.13)}$$

where $\mathcal{L}(\mathrm{x}) = \coth(\mathrm{x}) - 1/\mathrm{x}$ represents the Langevin function and $\boldsymbol{H}_{eff,m}$ is evaluated by means of eq. (B.6). With this equation, one can compute the 'local' Curie temperature, assuming a linear expansion. It is easy to show that,

$$T_C^{m} = \frac{1}{3k_B}[n_l\,(J_{m\text{-}1} + J_m + J_{m+1}) + 2\boldsymbol{k_1}]. \qquad \text{(B.14)}$$

In order to calculate numerically the magnetization profile, one considers a starting condition $M_m^{\varsigma,\;i=0}$ and evaluate iteratively eq. (B.13) as,

$$\langle s_m^{\varsigma,\ i} \rangle = \langle s_m^{\varsigma,\ i\text{-}1} \rangle + c \left\{ \mathcal{L} \left[\frac{\left| \boldsymbol{H}_{\mathit{eff},m}^{\mathit{i\text{-}1}} \right|}{k_B T} \right] \frac{H_{\mathit{eff},\ m}^{\varsigma,\ \mathit{i\text{-}1}}}{\left| \boldsymbol{H}_{\mathit{eff},m}^{\mathit{i\text{-}1}} \right|} \text{-} \langle s_m^{\varsigma,\ i\text{-}1} \rangle \right\}, \tag{B.15}$$

where $c = 0.5$ is a parameter that contributes to keep the convergence of the solution stable at all temperatures.

Appendix C: Scaling behavior associated with the dynamic Arrott-Noakes equation-of-state

In this appendix, a brief revision of the scaling behavior of Q in the vicinity of P_c is conducted. The dynamic Arrott-Noakes equation-of-state is postulated as,

$$\left(\frac{H^*}{Q}\right)^{1/\gamma_d} = \frac{P - P_c}{P_1} + \left(\frac{Q}{Q_1}\right)^{1/\beta_d}. \tag{C.1}$$

Here, P_1 and Q_1 are material specific constants, H^* is the generalized conjugate field of Q, P is the period of the external magnetic field strength and P_c is the critical period in which the system undergoes a SOPT. Also, β_d and γ_d are critical exponents, that depend only on the dimensionality of the system. This expression is formally identical to the Arrott-Noakes equation-of-state in thermodynamic equilibrium,

$$\left(\frac{H}{M}\right)^{1/\gamma} = \frac{T - T_C}{T_1} + \left(\frac{M}{M_1}\right)^{1/\beta}, \tag{C.2}$$

where T_1 and M_1 are material specific constants, H is the external magnetic field strength, T is the temperature of the system and T_C the Curie temperature. Likewise, β and γ are equilibrium critical exponents that are of the same universality class as β_d and γ_d. In this appendix, the description of the scaling behaviors of Q is conducted in the vicinity of the SOPT happening at P_c. Such description is formally identical to the scaling behavior of M in the vicinity of T_C. Thus, while here the case of the DPT is explored, this description is formally equivalent to the TPT using the analog quantities.

In the dFM phase, for $H^* \to 0$, the left-hand side of eq. (C.1) vanishes, and thus we rewrite,

$$Q = Q_1\left(\frac{P - P_C}{P_1}\right)^{\beta_d}. \tag{C.3}$$

Eq. (C.3) represents the scaling of Q as a function of P in the dFM phase, as explained in conjunction with eq. (5.4) in chapter 5. Likewise, at exactly $P = P_c$, then the first term in the right-hand side of eq. (C.1) vanishes and,

$$\left(\frac{H^*}{Q}\right)^{1/\gamma_d} = \left(\frac{Q}{Q_1}\right)^{1/\beta_d}, \tag{C.4}$$

which can be rewritten as,

$$Q = Q_1^{\frac{\gamma_d}{\gamma_d+\beta_d}}\, H^{*\frac{\beta_d}{\gamma_d+\beta_d}} = Q_1^{1\text{-}\frac{1}{\delta_d}}\, H^{*\frac{1}{\delta_d}}, \tag{C.5}$$

with $\delta_d - 1 = \gamma_d/\beta_d$. Eq. (C.5) is therefore, identical to eqs. (5.13) and (6.7) in chapters 5 and 6, respectively.

Also, eq. (C.1) allows for a re-scaling of properly defined quantities. To show this, first, for simplicity, $p = (P_C \text{ - } P)/P_1$ is defined. Eq. (C.1) is rewritten as,

$$\frac{H^*}{Q} = \left[\left(\frac{Q}{Q_1}\right)^{1/\beta_d} + p\right]^{\gamma_d}. \tag{C.6}$$

Here, $p > 0$ in the FM phase and $p < 0$ in the PM phase, which leads to the two separate curves in the scaled quantities that can be written jointly as,

$$\frac{H^*}{p^{\gamma_d}} = Q_1 \frac{Q}{Q_1}\left[\frac{1}{p}\left(\frac{Q}{Q_1}\right)^{1/\beta_d} \pm 1\right]^{\gamma_d}. \tag{C.7}$$

If we divide by p^{β_d}, one obtains,

$$\frac{H^*}{p^{\gamma_d+\beta_d}} = Q_1\left(\frac{Q}{Q_1 p^{\beta_d}}\right)\left[\left(\frac{Q}{Q_1 p^{\beta_d}}\right)^{1/\beta_d} \pm 1\right]^{\gamma_d}. \tag{C.8}$$

With $h_s = H^*/p^{\gamma_d+\beta_d}$ and $q_s = Q/Q_1 p^{\beta_d}$ as the rescaled conjugate field and order parameter, respectively, a simplified version of eq. (C.1) can be written as,

$$h_s = Q_1 q_s \left[q_s^{1/\beta_d} \pm 1\right]^{\gamma_d}. \tag{C.9}$$

In eq. (C.9), q_s depends implicitly on h_s. If represented against each other on the logarithmic scale, this expression leads to two separate curves, which correspond to the dFM and dPM phases, as seen in Figs. (5.9) and (6.9).

List of Abbreviations

Abbreviations that occur in the immediate context of a statement only are not listed here.

AC	Alternating Current
CPL	Circularly Polarized Light
DC	Direct Current
dFM	Dynamic Ferromagnetic
DMI	Dzyaloshinskii-Moriya Interaction
dPM	Dynamic Paramagnetic
DPT	Dynamic Phase Transition
DW	Domain-Wall
EA	Easy-Axis
EGP	Exchange-Graded Profile
FM	Ferromagnetic
HA	Hard-Axis
hcp	Hexagonal Close Packed
L-MOKE	Longitudinal Magneto-Optical Kerr Effect
MCA	Magneto-Crystalline Anisotropy
MFA	Mean-Field Approximation
MOKE	Magneto-Optical Kerr Effect
MOFE	Magneto-Optical Faraday Effect
NM	Nonmagnetic
PM	Paramagnetic
P-MOKE	Polar Magneto-Optical Kerr Effect
QWP	Quarter Wave-Plate
SQUID	Superconducting Quantum Interference Device
T-MOKE	Transverse Magneto-Optical Kerr Effect
TPT	Thermodynamic Phase Transition
UHV	Ultra-High Vacuum
VSM	Vibrating Sample Magnetometry
XRD	X-Ray Diffraction
XRR	X-Ray Reflectivity

List of Variables

Variables that occur in the immediate context of a statement only are not listed here. Bold symbols indicate vectors.

$\mathcal{F}$	Helmholtz free energy of a system
$\mathcal{H}$	Hamiltonian of a system
$\mathcal{Z}$	Partition function
α_{MO}	Longitudinal magneto-optical component of the reflection matrix
β	Thermodynamic critical exponent in the TPT at $H = 0$ and $T \rightarrow T_C$
β_d	Dynamic critical exponent in the DPT at $H^* = 0$ and $P \rightarrow P_C$
β_{MO}	Transverse magneto-optical component of the reflection matrix
γ	Thermodynamic critical exponent in the TPT associated with χ at $T \rightarrow T_C$.
γ_d	Dynamic critical exponent in the DPT associated with χ at $P \rightarrow P_C$.
γ_{MO}	Polar magneto-optical component of the reflection matrix
δ	Thermodynamic critical exponent in the TPT at $T = T_C$ and $H \rightarrow 0$.
δ_d	Dynamic critical exponent in the DPT at $P = P_C$ and $H^* \rightarrow 0$.
ΔT_C	Curie temperature distribution standard deviation
ΔP_C	Critical point distribution standard deviation
θ	Angle of reflection with respect to the film surface
θ_c	Critical angle for total reflection
λ	Photon wavelength
$\boldsymbol{\mu}$	Magnetic moment vector
μ_0	Vacuum permeability
ρ_T	Curie temperature distribution
ρ_A	Room-temperature density of a given material A
ρ_D	Critical period distribution
σ	Thermodynamic magnetic fluctuations
σ_Q	Dynamic fluctuations
τ	Reduced temperature
τ_M	Metastable relaxation time constant
ν	Angle between EA and field direction
φ	Angle between magnetization vector and field direction
χ	Thermodynamic Magnetic Susceptibility
χ_d	Dynamic Magnetic Susceptibility
ω	Angle of incident light with respect to the film surface

d	Thickness of a given thin film layer
$\boldsymbol{H}$	External magnetic field strength vector
H^*	Generalized conjugate field of the dynamic order parameter in the DPT
$H_{1,2}$	First and second harmonic magnetic field amplitudes
H_b	Magnetic bias field
H_c	Coercive magnetic field
$H_{i,j}^{dip}$	Dipolar magnetic field strength induced in the ith spin by the jth spin
H_K	Anisotropy field strength
I_D	Light-intensity obtained in a photodetector
I_{XRD}	X-ray light intensity obtained in diffraction
J	Exchange coupling strength
J_μ	Material specific field strength for dimensionless analysis in the DPT
J_g	Interlayer coupling strength in EGPs mediated by a PM region
$k_{1,2}$	First- or second-order uniaxial magnetic anisotropy energy constants
$K_{1,2}$	First- or second-order thermodynamic magnetic anisotropy energy densities
k_B	Boltzmann constant
$\boldsymbol{M}$	Magnetization vector
M_r	Remanence magnetization
M_s	Saturation magnetization
M_s^0	Zero-temperature saturation magnetization
n_{hcp}	Total number of nearest neighbors in an hcp lattice structure
n_l	Number of nearest-neighbors in certain layer
p	Reduced period in the DPT
P	External magnetic field period
P_C	Critical period in the DPT
Q	Dynamic order parameter in the DPT
Q_i	Total X-ray momentum transfer
Q_{MO}	Magneto-optical coupling constant
R	Reflection matrix of a system
$r_{\{s,p\}}$	Reflection matrix elements
$\boldsymbol{s}_i$	Spin-vector of the ith localized magnetic moment
s_g	Local Curie temperature change in V-shaped EPGs
T	Temperature
T_C	Curie temperature
T_C^{loc}	Local Curie temperature

Acknowledgements

It feels very difficult for me to express my gratitude to all the people that accompanied me in this nice four-year journey… but I will try.

Firstly, this thesis has been possible thanks to the constant help and support of my supervisor, Andreas Berger. Thank you for showing me everything I know now about magnetism. I admire your professionality and leadership and I'm truly thankful for your guidance during this whole experience, both in the good and the bad times.

I'm grateful to Txema Pitarke, for giving me such a nice opportunity to work and conduct my experiments at the CIC nanoGUNE, as well as for his kindness as Tutor.

I would like to acknowledge all my present and past colleagues of the Nanomagnetism group in nanoGUNE for the excellent work environment during my Ph.D. Particularly, I want to thank Lorenzo Fallarino. I learned many many things from you. It would not have been possible without your constant support and predisposition to help. I would also like to thank Carmen Martín Valderrama because of the countless hours of intense work. I have also learned many things from you. Keep it easy.

Likewise, I thank my colleagues Paolo, Matteo, Naëmi, Ramon, Terunori, Emanuela, Mikel, Pablo, Naga, and our visitors Juan, Irene, Adrián, Claudio, Fernando and Prof. Yuasa. Your support, kindness, knowledge, and experience has been essential accomplishing this work.

I would like to acknowledge all the excellent technical team members in nanoGUNE, because science would not be possible without them. Specially, I most thankful to our group technician Cesar Antonio Rufo for the long hours inside the cleanroom preparing samples, as well as Ralph Gay, and Roger Llopis. Likewise, I'd like to mention all the human resources team in nanoGUNE, with special thanks to Uxue, Itziar, Yurdana and Ainara for their kindness.

This Ph.D. has been conducted in an excellent work environment with caring and incredibly smart people. I would like to acknowledge all my colleagues in nanoGUNE, with particular mention to all the 3,000 members of the Nanodevices group. Needless to say, I thank María for the countless coffee breaks and always* positive attitude. I'd also like to thank Nerea, Juanma, Inge, Francesco, Diogo,

José, Gabriele, Isabel, Andrea, Yaiza, Manu, Fran, Ana, Marina… I apologize to everyone not listed.

I am most thankful to the Spanish Ministry of Science, Innovation and Universities for funding my Ph.D. The funding also allowed me to spend an excellent three-month period at the Helmholtz Zentrum Dresden Rossendorf in Germany, for which I am also thankful.

In this regard, I also want to express my eternal gratitude to Prof. Denys Makarov for giving me such a nice opportunity to work in his group during this period. I'm thankful for your hard work and such a nice work environment, even in the most difficult times. Likewise, I want to give thanks to José, for being my travel companion, and my colleagues in the HZRD, Oleksii, Oleksandr, Shahrukh, Sergio, Pavlo, Denise, Ihor… Vielen Dank!

I'm also thankful to Dr. Satoshi Tomita and Prof. Denys Makarov for reading this thesis and giving their feedback for the international doctoral mention. Thank you for having taken the time for this work.

I'm truly thankful for my family and friends in San Sebastian: Ander, Sara, Jonmi, Vanessa; as well as my family and friends (from the beautiful city of) Bilbao: Mario, Unai, Iñigo, Gorka. I also want to thank my friends of the monkey community for providing me with laughs, optimism, smiles and sincerity. In that order.

Last but not least, this thesis would not have been possible without the continuous help of my parents, Miguel Ángel and Mentxu that, amongst other things, provided me with the education necessary to get to this point, and for which I could not be more thankful. Os quiero.